University of Warsaw
Faculty of Physics

Doctor of Philosophy Dissertation

Towards Ultracold Molecules Containing Transition-Metal and Lanthanide Atoms: Interatomic Interactions and Ultracold Collisions

by

Klaudia Kinga Zaremba-Kopczyk

Thesis supervisor:
dr hab. Michał Tomza, prof. UW

Warsaw, September 2023

Abstract

"Towards ultracold molecules containing transition-metal and lanthanide atoms: Interatomic interactions and ultracold collisions"

The past three decades of rapid development in laser cooling and trapping techniques have allowed to produce ultracold quantum matter that can be controlled, manipulated, and measured with unprecedented precision. Ultracold atoms and molecules have emerged as a versatile platform for exploring novel quantum phenomena, and have found application in research areas such as condensed-matter physics, quantum computing, controlled chemistry, and precision tests of fundamental physics.

In recent years, there has been a growing interest in the properties of ultracold quantum gases with strong dipolar interactions, such as ultracold gases of highly-magnetic atoms and polar molecules. Ultracold quantum mixtures containing transition-metal or lanthanide atoms offer prospects for the formation of polar molecules with large both electric and magnetic dipole moments. An interplay between long-range interactions of both electric and magnetic nature should allow for applications of such molecules in, among others, quantum simulations of many-body systems and observation of novel exotic quantum phases, while their complex electronic structure could be utilized in precision measurements of fundamental constants.

The doctoral thesis presents a theoretical investigation of interatomic interactions and collisions in ultracold mixtures containing transition-metal (such as Cr, Zn, Cd) and lanthanide atoms (such as Eu, Dy, Er) and analyzes the prospects for the formation of ultracold diatomic molecules containing these atoms. The present research involves calculations of interaction potentials with the use of *ab initio* quantum chemistry methods and quantum scattering calculations for ultracold atom-atom collisions in external magnetic fields.

The thesis is divided into four main parts. The first part gives an introduction to ultracold matter and presents the state of the art in the research of ultracold molecules and dipolar quantum gases. The second part provides the theoretical and methodological foundations for the work presented in the third, main part of the thesis. The third part of the thesis comprises a series of thematically linked publications and preprints devoted to studies of interatomic interactions and collisions in ultracold mixtures containing transition-metal and lanthanide atoms. The presented papers investigate the following research problems: atom-atom collisions in ultracold quantum gases of europium atoms and ultracold quantum mixtures of europium and alkali-metal atoms (Li, Rb), the electronic structure of van der Waals molecules consisting of a zinc or cadmium atom interacting with an alkali-metal (Li, Na, K, Rb, Cs, Fr) or alkaline-earth-metal (Be, Mg, Ca, Sr, Ba, Ra) atom, the electronic structure of LiCr molecule and atom-atom collisions in ultracold mixtures of chromium and lithium atoms, and the long-range interactions in ultracold mixtures of dysprosium or erbium atoms with alkali-metal (Li, Na, K, Rb, Cs, Fr) or alkaline-earth-metal (Be, Mg, Ca, Sr, Ba) atoms. The last, fourth part of the thesis provides a brief summary of the obtained results and outlines the prospects for further research.

Streszczenie

"W kierunku ultrazimnych cząsteczek zawierających atomy metali przejściowych i lantanowców: oddziaływania międzyatomowe i ultrazimne zderzenia"

Ostatnie trzy dekady dynamicznego rozwoju technik laserowego chłodzenia i pułapkowania atomów umożliwiły produkcję ultrazimnej kwantowej materii, która może być z ogromną precyzją kontrolowana i mierzona. Ultrazimne atomy i cząsteczki tworzą doskonałą platformę do badania nowych zjawisk kwantowych i znalazły swoje zastosowanie w takich obszarach badań jak fizyka materii skondensowanej, obliczenia kwantowe, kontrolowana chemia, czy precyzyjne testy fundamentalnych praw fizyki.

W ostatnich latach uwagę badaczy przyciągnęły tzw. ultrazimne gazy dipolowe, w których atomy lub cząsteczki wykazują silne oddziaływania dipol-dipol – takie ultrazimne gazy mogą tworzyć zarówno wysokomagnetyczne atomy, jak i polarne cząsteczki. Ultrazimne kwantowe mieszaniny zawierające atomy metali przejściowych lub lantanowców oferują perspektywy utworzenia polarnych cząsteczek posiadających zarówno duży elektryczny, jak i magnetyczny moment dipolowy. Obecne w takich mieszaninach połączenie dalekozasięgowych oddziaływań o elektrycznym i magnetycznym charakterze pozwoli na stworzenie nowych symulatorów kwantowych i obserwację egzotycznych faz kwantowych, natomiast złożona struktura elektronowa takich cząsteczek mogłaby zostać wykorzystana w precyzyjnych pomiarach stałych fundamentalnych.

Niniejsza rozprawa doktorska przedstawia teoretyczne badania międzyatomowych oddziaływań i zderzeń w ultrazimnych mieszaninach zawierających atomy metali przejściowych (takich jak Cr, Zn, Cd) i lantanowców (takich jak Eu, Dy, Er) oraz analizuje perspektywy tworzenia ultrazimnych dwuatomowych cząsteczek zawierających te atomy. Prezentowane badania obejmują obliczenia potencjałów oddziaływania metodami *ab initio* chemii kwantowej oraz obliczenia rozpraszania kwantowego dla ultrazimnych zderzeń atom-atom w zewnętrznych polach magnetycznych.

Praca podzielona jest na cztery główne części. Pierwsza część stanowi wprowadzenie do ultrazimnej materii i przedstawia aktualny stan badań nad ultrazimnymi cząsteczkami i dipolowymi gazami kwantowymi. W drugiej części przedstawiono podstawy teoretyczne i metody badawcze zastosowane w celu uzyskania wyników przedstawionych w trzeciej, głównej części rozprawy. Trzecią część rozprawy stanowi seria powiązanych tematycznie publikacji i przeddruków poświęconych badaniom oddziaływań i zderzeń międzyatomowych w ultrazimnych mieszaninach zawierających atomy metali przejściowych i lantanowców. W prezentowanych publikacjach i przeddrukach poruszane są następujące problemy badawcze: zderzenia atom-atom w ultrazimnych gazach kwantowych atomów europu i ultrazimnych mieszaninach europu i metali alkalicznych (Li, Rb), struktura elektronowa cząsteczek van der Waalsa składających się z atomu cynku lub kadmu oddziałującego z atomem metalu alkalicznego (Li, Na, K, Rb, Cs, Fr) lub metalu ziem alkalicznych (Be, Mg, Ca, Sr, Ba, Ra), struktura elektronowa cząsteczki LiCr i zderzenia atom-atom w ultrazimnych mieszaninach chromu i litu, a także oddziaływania dalekozasięgowe w ultrazimnych mieszaninach atomów dysprozu lub erbu z atomami metali alkalicznych (Li, Na, K, Rb, Cs, Fr) lub metali ziem alkalicznych (Be, Mg, Ca, Sr, Ba). Ostatnia, czwarta część pracy zawiera krótkie podsumowanie uzyskanych wyników oraz rysuje perspektywy dalszych badań.

Acknowledgments

First and foremost, I would like to express my gratitude to my supervisor, Michał Tomza, for the scientific guidance and support he has provided me throughout my time as his student. I am thankful to Michał for the time invested in my scientific growth and for always generously sharing his expertise and advice.

I thank all members of the Quantum Molecular Systems group for creating a supportive and stimulating work atmosphere. Over the course of my PhD studies, I stumbled upon many issues when running electronic structure calculations, and I deeply appreciate all the help I received to resolve them. I would particularly like to acknowledge Marcin Gronowski for the willingness to share his expertise and invaluable support.

In the summer of 2017, I had the opportunity to visit the group of Piotr Żuchowski at the Nicolaus Copernicus University in Toruń. I thank Piotr for introducing me to the theory of quantum scattering for ultracold atoms. During my 4-week stay in Toruń, I had a chance to start working on my PhD thesis project while still being a Master's student.

I would like to express my gratitude to Maxence Lepers for the opportunity to visit his group at Université de Bourgogne Franche-Comté in Dijon in 2021-2022 and willingness to share his scientific knowledge with me. Thanks to Quantum Interactions and Control lab members, especially Gohar, Astghik, Xavier, and Rodolphe for a warm welcome in Dijon and creating a great atmosphere during my stay.

Thanks to all the physicists and chemists, with whom I had the opportunity to study, discuss, and participate in schools and conferences.

Last but not least, I am indebted to my family and friends for their enthusiastic support throughout this journey.

This work was financially supported by the National Science Center in Poland (Preludium grant no. 2019/35/N/ST4/04504). The Poland's high-performance computing infrastructure PL-Grid (HPC Centers: ACK Cyfronet AGH) is gratefully acknowledged for providing computer facilities and support within computational grant no. PLG/2021/015237.

Contents

Preface

The advent of methods to cool and trap atoms with laser light in the 1980s sparked a revolution in the field of atomic, molecular, and optical (AMO) physics and eventually led to the first experimental observation of a Bose-Einstein condensate (BEC) with dilute alkali-metal-atom gases in 1995 [1–3] – a phenomenon predicted by S. Bose [4] and A. Einstein [5] over 70 years earlier. The experimental breakthroughs of atom cooling and trapping, the realization of an atomic BEC, and, further, the development of laser-based precision spectroscopy and quantum control were all recognized by Nobel Prizes in Physics – in 1997 (awarded to S. Chu [6], C. N. Cohen-Tannoudji [7], and W. D. Phillips [8]), 2001 (awarded to E. A. Cornell [9], W. Ketterle [10], and C. E. Wieman [9]), 2005 (awarded to J. L. Hall [11] and T. W. Hänsch [12], and R. J. Glauber [13]), and 2012 (awarded to S. Haroche [14] and D. J. Wineland [15]). Over the past three decades, exceptional controllability of matter and light has been achieved, allowing to produce cold (< 1 K) and ultracold (< 1 mK) atomic and molecular samples whose properties can be precisely tailored with electromagnetic fields.

A variety of atomic species of increasingly complex internal structure has already been brought to quantum degeneracy and employed in sophisticated ultracold experiments: starting from alkali-metal atoms [1–3; 16–20], through alkaline-earth-metal [21–24] and transition-metal atoms [25; 26], to lanthanide atoms [27–34]. After the successful production of single-species atomic quantum gases, research on ultracold matter has soon expanded onto double-degenerate quantum mixtures [35; 36], ultracold molecules [37–41], and hybrid systems of ultracold atoms with ions [42; 43]. Ultracold quantum gases serve as an unequaled platform for studies of quantum matter and light-matter interactions due to their unprecedented controllability and have found applications in, among others, quantum computation [44; 45] and quantum simulations of many-body physics [46–48], controlled chemistry [49; 50], and fundamental physics [51; 52].

In recent years, there has been a growing interest in ultracold quantum gases of highly magnetic atoms, such as transition-metal atom chromium and lanthanide atoms like europium, erbium, holmium, or dysprosium. Quantum mixtures containing transition-metal or lanthanide atoms offer prospects for the formation of ground-state polar molecules with large both electric and magnetic dipole moments. An interplay between long-range interactions of both electric and magnetic nature should allow for novel applications in, among others, quantum simulations of many-body systems [50], while the complex electronic structure of such molecules could serve as a sensitive probe in precision measurements [51]. Heteronuclear mixtures of highly magnetic atoms are promising systems for the exploration of polaron physics [53–55], Efimov physics [56], exotic Fulde-Ferrell-Larkin-Ovchinnikov (FFLO) states [57; 58], and binary supersolids [59]. Degenerate mixtures of Dy and K atoms [60–62], Dy and Er atoms [63–65], Er and Li atoms [66], Cr and Li atoms [67; 68], and Er and Yb atoms [69] are currently being investigated experimentally.

An increased interest in the properties of ultracold quantum gases with strong dipolar interactions, such as ultracold gases of highly magnetic atoms and polar molecules, motivated us to theoretically investigate the interatomic interactions and ultracold collisions in mixtures containing transition-metal (such as Cr, Zn, Cd) and lanthanide atoms (such as Eu, Dy, Er) and analyze the prospects for the formation of diatomic molecules containing these atoms. The results of this study form the content of the present PhD thesis and include:

- the analysis of magnetically tunable Feshbach resonances between ultracold europium atoms and between europium and alkali-metal (Li, Rb) atoms, calculated with the use of multichannel quantum scattering formalism,
- investigation of the properties (potential energy curves, permanent electric dipole moments, and spectroscopic constants) of diatomic molecules consisting of either a Zn or Cd atom interacting with an alkali-metal (Li, Na, K, Rb, Cs, Fr) or alkaline-earth-metal (Be, Mg, Ca, Sr, Ba, Ra) atom, calculated with the use of the *ab initio* electronic-structure coupled-clusters method,
- calculation of the potential energy curves and the permanent and transition electric dipole moments for the electronic states of the LiCr molecule correlated to the four lowest atomic dissociation limits (with the use of coupled-clusters and multireference configuration interaction methods), analysis of magnetically tunable Feshbach resonances in the Cr+Li mixtures (obtained using multichannel quantum scattering calculations), analysis of the prospects for the formation of polar and highly magnetic LiCr molecules via magneto- and photoassociation, proposal of the precision measurements of the variation of electron-to-proton mass ratio using ultracold LiCr molecules,
- derivation and numerical calculations of the C_6 coefficients characterizing the van der Waals interactions between Dy or Er atoms in the two lowest energy levels and the ground-state alkali-metal (Li, Na, K, Rb, Cs, Fr) or alkaline-earth-metal (Be, Mg, Ca, Sr, Ba) atoms.

The present dissertation is based on a series of thematically linked publications and preprints:

- Paper I: K. Zaremba-Kopczyk, P. Żuchowski, and M. Tomza, *Magnetically tunable Feshbach resonances in ultracold gases of europium atoms and mixtures of europium and alkali-metal atoms*, Phys. Rev. A 98, 032704 (2018), DOI: 10.1103/PhysRevA.98.032704 [70],
- Paper II: K. Zaremba-Kopczyk and M. Tomza, *Van der Waals molecules consisting of a zinc or cadmium atom interacting with an alkali-metal or alkaline-earth-metal atom*, Phys. Rev. A 104, 042816 (2021), DOI: 10.1103/PhysRevA.104.042816 [71],
- Paper III: K. Zaremba-Kopczyk, M. Gronowski, and M. Tomza, *Ultracold mixtures of Cr and Li atoms: theoretical prospects for controlled atomic collisions, LiCr molecule formation, and molecular precision measurements*, preprint,
- Paper IV: K. Zaremba-Kopczyk, M. Tomza, and M. Lepers, *Van der Waals coefficients for interactions of dysprosium and erbium atoms with alkali-metal and alkaline-earth-metal atoms*, preprint.

and is outlined as follows. **Chapter 1** gives a brief introduction to ultracold matter, describes the methods for the production of ultracold quantum gases, and presents the state of the art in the research of ultracold molecules and dipolar quantum gases. **Chapter 2** provides the theoretical and methodological foundations for the work presented in Papers I – IV. It begins by describing the electronic and rovibrational structure of diatomic molecules within the adiabatic approximation. Next, we describe the *ab initio* quantum chemistry methods employed in our electronic structure calculations (Papers I – III), as well as the coupled-channels formalism underlying the quantum scattering calculations (Paper I and Paper III). The last section of Chapter 2 is devoted to the description of long-range interactions between ultracold atoms and sets the ground for the calculations presented in Paper IV. Papers I – IV, complemented by the commentary about the motivation behind each work and the PhD Candidate's contribution to each paper, comprise the core of the thesis and are presented in **Chapter 3**. Finally, in **Chapter 4** we provide a brief summary of the obtained results and outline prospects for further research.

Chapter 1

Introduction

1.1 Ultracold matter

The production of ultracold atoms and molecules has revolutionized modern physics and chemistry, allowing to investigate quantum properties of matter at an unattainable otherwise level. Since thermal fluctuations are suppressed at ultralow temperatures, ultracold quantum matter can be controlled, manipulated, and measured with unprecedented precision.

Ultracold quantum gases are very dilute systems, with gas densities obtained experimentally typically ranging from 10^{12} to 10^{15} cm^{-3}. In a dilute gas, the mean interparticle distance $n^{-1/3}$ greatly exceeds the range of the interparticle interaction R_{int}:

$$n^{-1/3} \gg R_{\text{int}} \,,$$

where n denotes the gas density and R_{int} is the characteristic radius of the interparticle interaction (R_{int} marks a transition point between the short-range and the long-range asymptotic behavior of the s-wave scattering wave function and is determined by the shape of the interaction potential [72]).

At ultralow temperatures, the thermal de Broglie wavelength λ_{th} of particles greatly exceeds R_{int}:

$$\lambda_{\text{th}} = \sqrt{\frac{2\pi\hbar^2}{m k_{\text{B}} T}} \gg R_{\text{int}} \,,$$

with $\hbar$ and k_{B} denoting the reduced Planck and Boltzmann constants, respectively, m denoting the particle mass, and T being the gas temperature. Therefore, the ultracold regime is achieved when $R_{\text{int}}\lambda_{\text{th}}^{-1} \ll 1$, which roughly corresponds to temperatures below 1 mK.

An ultracold gas enters the quantum-degenerate regime when the thermal de Broglie wavelength λ_{th} becomes comparable to the mean interparticle distance $n^{-1/3}$, so that:

$$n\lambda_{\text{th}}^3 \gtrsim 1 \,,$$

where $n\lambda_{\text{th}}^3$ is the phase-space density of the gas. Depending on the statistics of constituent particles (bosons or fermions), the ground-state of an ultracold quantum gas is either a Bose-Einstein condensate or a Fermi sea. In the case of an ideal BEC, all particles occupy the same, lowest-lying single-particle quantum state, while in the case of a Fermi sea, the particles populate the lowest allowed by the Pauli exclusion principle single-particle levels, up to the Fermi energy. For an ideal gas of bosonic particles in a three-dimensional box, the BEC is formed when the phase-space density exceeds the critical value of 2.612. Because $n\lambda_{\text{th}}^3 \propto nT^{-3/2}$, very low temperatures are required to reach quantum degeneracy since, at the same time, gas density needs to be low enough to avoid losses due to inelastic collisions. For atomic quantum gases obtained experimentally, the temperatures of degeneracy commonly range from 100 nK to 1 μK.

Since ultracold quantum gases are very dilute, it is usually sufficient to only consider pair interactions and collisions in their description. At ultralow temperatures, the lowest angular-momentum (l) collisions dominate, and for identical bosons only even values of l are possible, while for identical fermions – only odd values. For bosonic gases, only s-wave scattering between particles can take place in the ultracold regime (unless the so-called shape resonances with bound states of $l \neq 0$ exist), which allows us to replace the actual interaction potential by a pseudopotential, which, following Ref. [73], reads:

$$V(\boldsymbol{r}) = \frac{2\pi\hbar^2 a}{\mu}\delta(\boldsymbol{R})\frac{\partial}{\partial R}R\,, \tag{1.1}$$

where μ is the reduced mass of the system, $\boldsymbol{R}$ is the vector between the positions of the particles, and a is the s-wave scattering length. Since for identical fermions the s-wave collisions are forbidden due to the Pauli exclusion principle, the p-wave collisions dominate.

The magnitude and sign of the s-wave scattering length can be tuned by means of the so-called Feshbach resonances [74]; Feshbach resonances serve as a powerful tool to control the interaction strength in ultracold gases and allow us to enter the strongly-interacting regime and explore the many-body physics of strongly-correlated systems (the physics of Feshbach resonances will be discussed in more detail in Secs. 1.3.1 and 2.3.3).

1.2 Production of ultracold atomic gases

The production of ultracold atomic quantum matter is realized through laser cooling of an atomic ensemble in a magneto-optical trap (MOT), followed by evaporative cooling in a magnetic or an optical dipole trap. The mechanisms for neutral atom trapping involve [75]:

- radiation-pressure trapping [76], which uses the force exerted on an atom in the process of incoherent photon scattering (due to spontaneous emission when operating with near-resonant light) to counteract external forces and create a stable trapping potential; radiation-pressure traps have typical depths of up to a few kelvins and allow to cool a gas of atoms down to temperatures of a few tens of microkelvins; their performance is limited by strong optical excitations,

- magnetic trapping [77], which employs the interaction between an atom's magnetic dipole moment and an external magnetic field gradient to create a state-dependent shift in the energy of the atom; magnetic traps are shallow, with typical depths of the order of 100 mK,

- optical dipole trapping [78], which results from the interaction between an atom's induced electric dipole moment with far-detuned light (therefore, as opposed to radiation-pressure traps, optical excitations can be kept extremely low); the trap depths are typically below 1 mK; this type of trapping mechanism is the weakest among the three, but offers the flexibility to realize a variety of trapping geometries (e.g., multi-well potentials, periodic potentials of optical lattices).

Radiation-pressure trapping is typically applied during the first stage of an ultracold gas production, when the atomic ensemble is pre-cooled to temperatures in the microkelvin range with the use of a MOT. The laser cooling mechanism primarily exploits the momentum conservation law during repeated cycles of near-resonant absorption of a photon and its subsequent spontaneous emission (see Fig. 1.1). In the Doppler cooling scheme, the laser is *red-detuned* (tuned to a frequency below the resonant frequency) from the atomic transition frequency. As the atom moves towards the laser, it sees the counterpropagating photons as *blue-shifted* due to the Doppler effect and can absorb the *resonant* ones. The photon absorption transitions the atom to an excited electronic state and makes it lose momentum in the direction of the photon

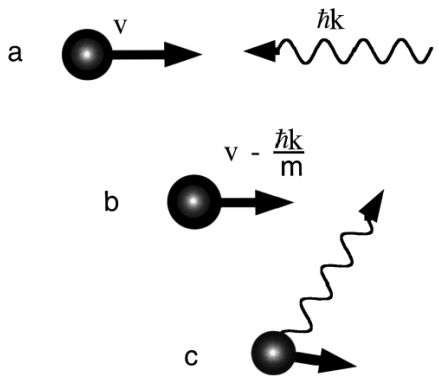

Figure 1.1: A depiction of the laser cooling scheme, as presented in W. D. Phillips's Nobel Lecture [8]: a) an atom with velocity $\boldsymbol{v}$ absorbs a photon with momentum $\hbar\boldsymbol{k}$ ($\boldsymbol{k}$ denotes the wave vector of the photon); b) the atom (of mass m) is slowed by $\hbar k/m$ in the direction of the incident beam; c) the photon is emitted in a random direction and, on average, the atom moves slower than in a).

propagation. Subsequent spontaneous emission of the photon causes a recoil of the atom in a random direction. After many absorption-emission cycles, the atom recoil is averaged to zero due to a random walk in the momentum space. The lowest temperature obtainable within the Doppler cooling scheme, T_{Doppler}, is limited by the atomic transition's natural linewidth, Γ:

$$T_{\mathrm{Doppler}} = \frac{\hbar\Gamma}{2k_{\mathrm{B}}}\,.$$

Over time, sub-Doppler cooling schemes have been elaborated, such as the polarization-gradient cooling, Raman cooling, or resolved-sideband Raman cooling, which are described in Ref. [75].

The pre-cooled atoms are next transferred from a MOT to a magnetic or an optical dipole trap to perform evaporative cooling. During evaporative cooling, weakly-confined atoms with high kinetic energies are removed as the trap depth is adiabatically decreased. This process gradually reduces the average temperature of an ensemble and eventually allows to reach quantum degeneracy.

1.3 Ultracold molecules

1.3.1 Production of ultracold molecules

Up till now the extension of laser cooling and trapping techniques from atoms to molecules poses a significant challenge. This is due to the fact that molecules, as compared to atoms, possess additional degrees of freedom that give rise to a richer energy level structure (i.e., the additional presence of rotational and vibrational levels associated with each electronic state, see Fig. 2.1 in Sec. 2.1.2). The dense spectrum of energy levels makes the molecules more prone to various loss mechanisms what significantly complicates the cooling process and quantum state manipulation.

On the other hand, the very complexity of molecular structure offers a diverse landscape for probing fundamental physics, exploring strongly-correlated quantum matter and exotic quantum phases, quantum computing, or investigating the dynamics of chemical reactions [79]. Therefore, much effort has been put into the development of methods to produce cold and ultracold molecular samples. These methods employ two main approaches: direct (cooling of molecules using external fields or other cold species) and indirect (association of pre-cooled atoms into molecules).

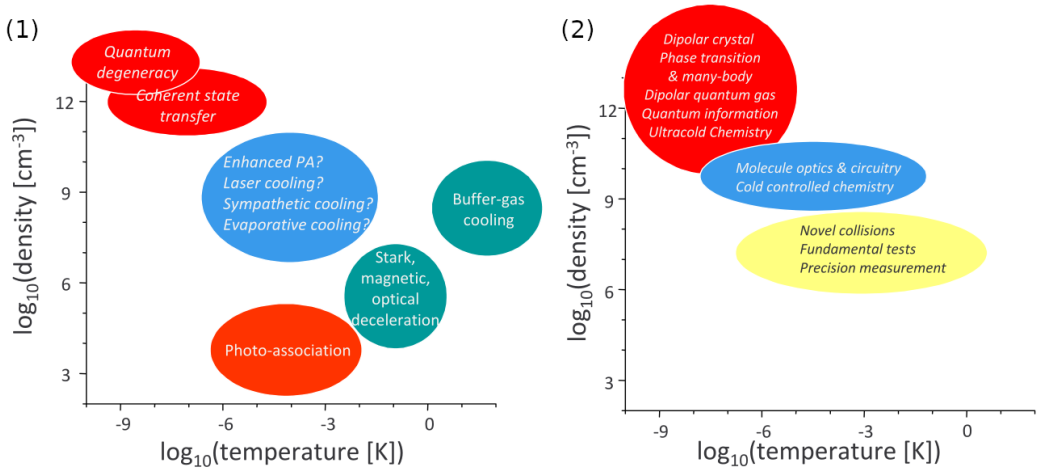

Figure 1.2: (1) Methods for the production of cold and ultracold molecules in different regions of temperature T and phase-space density n. (2) Potential applications of cold and ultracold molecules, along with the required values of T and n. Image source: Ref. [79].

Indirect methods

Indirect methods are so far the most efficient ones to produce ultracold quantum gases of (diatomic) molecules – they allow to obtain samples with the highest phase space densities and control over molecular degrees of freedom. In this approach, ultracold atoms are associated into molecules using magnetoassociation via Feshbach resonances (FRs) [80] and photoassociation (PA) [81] followed by stimulated Raman adiabatic passage (STIRAP) [82]. The methods, however, only allow to synthesize molecules from atomic species that are amendable to laser cooling and trapping. So far, mainly bialkali homo- and heteronuclear dimers [37–41; 83–92] have been produced, although the association of alkaline-earth-metal- [93–95] and lanthanide-containing molecules has also been demonstrated [96; 97].

1. **Magnetoassociation followed by STIRAP**

   One way to produce an ultracold molecular quantum gas is magnetoassociation via Feshbach resonances. In this method, pairs of ultracold atoms are associated into weakly-bound Feshbach molecules by ramping an applied magnetic field across a FR (see Fig. 1.3). Weakly-bound Feshbach molecules can be then transferred into deeply-bound molecular

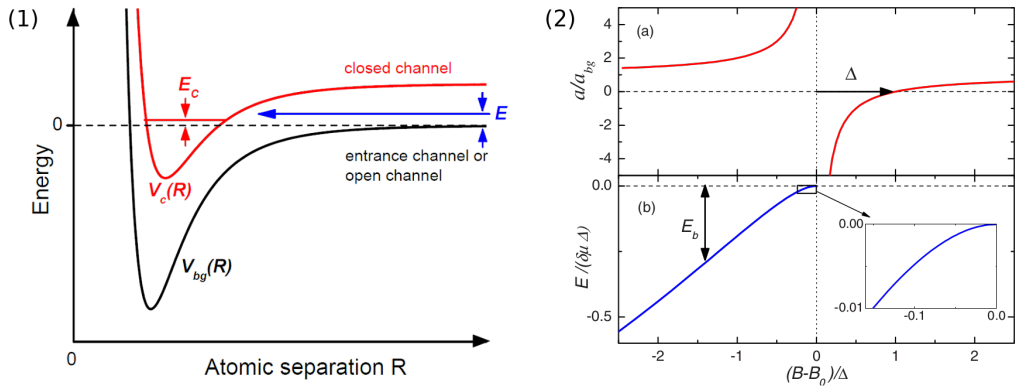

Figure 1.3: Two-channel model for a magnetic Feshbach resonance. (1) A FR occurs when two atoms colliding at energy E in the entrance channel resonantly couple to a molecular bound state with energy E_c in the closed channel. (2) The scattering length (a) and the molecular bound state energy (b) as a function of the magnetic field near the FR. Images taken from Ref. [74].

states by STIRAP as presented in Fig. 1.5b). In the process, a pair of Raman lasers is used to coherently transfer the molecules between quantum states via a third intermediate state. The proper choice of the intermediate state is key as it must have a favorable function overlap with both the initial and the final molecular state [82].

Magnetoassociation via Feshbach resonances has been employed to produce ultracold homonuclear bialkali dimers: Li_2 [98; 99], Na_2 [100], K_2 [40; 101], Rb_2 [37; 102], and Cs_2 [84] and a variety of heteronuclear bialkali dimers, such as: LiK [103], LiCs [104], NaK [105], NaRb [90; 106], KRb [83], or RbCs [86; 87]. The production of lanthanide-containing dimers, such as Er_2 [96] and DyK [97] has also been demonstrated recently. Heteronuclear molecules are produced out of an atomic quantum gas mixture as illustrated in Fig. 1.4.

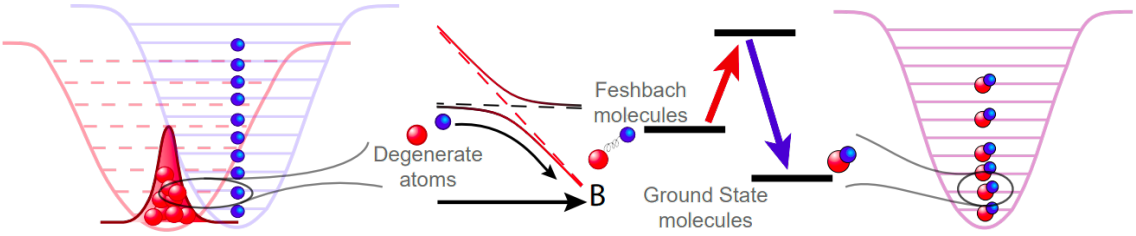

Figure 1.4: Production of ultracold heteronuclear molecules out of a binary quantum gas. Beginning with degenerate gases of two atomic species, Feshbach molecules are created by sweeping a magnetic field through a FR. Next, the weakly-bound molecules are coherently transferred to the ground state by STIRAP. Image from Ref. [92].

2. **Photoassociation**

Photoassociation is a process in which two colliding atoms A and B in an unbound scattering state are excited into a weakly-bound molecular state AB^* (see Fig. 1.5). The process is driven by resonant light with angular frequency ω:

$$A + B + \hbar\omega \longrightarrow AB^* \,.$$

Since the lifetime of a molecule in an excited state is finite, the weakly-bound molecule AB^* subsequently spontaneously decays into a stable ground-state molecule:

$$AB^* + \hbar\omega' \longrightarrow AB$$

or dissociates back into a pair of atoms, depending on the overlap between the vibrational wave function of the photoassociated molecule and the wave functions of the ground-state levels.

Since PA is followed by spontaneous decay, the final distribution of the population may span multiple rovibrational levels, depending on the transition selection rules and Franck-Condon overlap. Therefore, coherent population transfer needs to be applied (e.g., via STIRAP) to ensure a complete population transfer of the weakly-bound molecules into a target quantum state [81].

PA has been applied to produce ultracold homonuclear (Li_2 [107], Na_2 [108], K_2 [109], Rb_2 [110], and Cs_2 [111]) and heteronuclear (LiK [112], LiRb [113], NaK [114], KRb [85; 115], NaCs [116], RbCs [117]) alkali-metal molecules, as well as molecules containing non-magnetic closed-shell atoms, such as alkaline-earth-metal atoms (Ca_2 [118] and Sr_2 [93; 95; 119]) and lanthanides (YbLi [120], YbRb [121], CsYb [122], Yb_2 [123]).

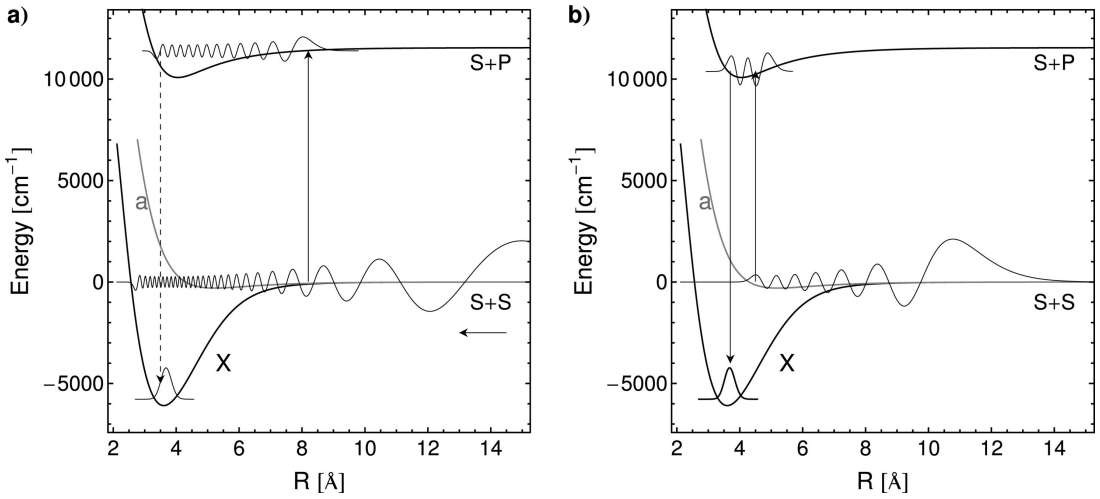

Figure 1.5: Schematic depiction of a cold ground-state molecule formation by a) photoassociation b) magnetoassociation followed by STIRAP. a) In photoassociation, a free pair of atoms is coupled to a weakly-bound excited molecular state at long range (solid arrow), followed by radiative stabilization via spontaneous decay at short range (dashed arrow). b) In magnetoassociation, a molecule is first created in a vibrational state near the dissociation threshold using a magnetic FR. The molecule is then transferred to a lower-bound state by STIRAP (solid arrows). Image source: Ref. [81].

Direct methods

For many years, direct laser cooling of molecules down to ultralow temperatures has been considered as nearly impossible, and indirect techniques are to this day the most effective means to produce molecular quantum matter. Indirect methods, however, exclude many chemically relevant species from formation – such as monohydrides, nitrides, oxides, fluorides, chlorides, or organic molecules [79]. Direct methods in which molecules are cooled from molecular beam temperatures (decelerated supersonic beams, buffer-gas cooling) can only produce molecules in the low energy regime (1 mK – 1 K) [124]. However, a major breakthrough was made in 2010, when direct laser cooling of a diatomic molecule (SrF) to millikelvin temperatures was demonstrated for the first time [125]. In 2017, sub-Doppler temperature regime was achieved with the laser-cooled CaF [126], and the past few years have brought rapid progress in the laser cooling and trapping of molecules (including polyatomic ones) to sub-Doppler temperatures in the microkelvin range.

1. **Molecular beam deceleration**

   Molecular beam deceleration is used to prepare cold, velocity-controlled molecular beams. It begins by a supersonic expansion of a molecular beam (a mixture of molecules of interest and a buffer gas – composed of chemically inert atoms, typically helium – is expanded from high pressure into vacuum) and its subsequent deceleration using electric (Stark decelerator) [124], magnetic (Zeeman slower) [127], or optical fields [128]. During the supersonic expansion, molecules undergo many elastic collisions with the buffer-gas atoms and lose most of their vibrational and rotational energy. Therefore, once injected into a decelerator, the molecules are vibrationally and rotationally cold in the moving frame despite moving at a speed of 300 – 2000 m/s in the laboratory frame. In decelerators employing the Stark and Zeeman effects, a beam of molecules is slowed by a rapidly switching, inhomogeneous electric or magnetic field, respectively, while optical decelerators use deep periodic optical lattice potentials to slow the molecules through oscillatory motion.

   Multiple molecular species have already been Stark-decelerated, for example: CO [129], NH_3/ND_3 [130], OH [131], SrF [132], H_2CO [133], NH [134], SO_2 [135], LiH [136], CaF [137],

and benzene [138]. Zeeman-effect-based deceleration was demonstrated, for example, for: O_2 [139], NH [140], CaOH [127], and YbOH [141].

2. **Buffer-gas and sympathetic cooling**

Buffer-gas and sympathetic cooling both employ collisional thermalization of molecules with an atomic-gas coolant. In buffer-gas cooling, molecules thermalize via collisions with cryogenic buffer gas (helium or neon), reaching temperatures in the kelvin regime. As the cooling process does not depend on molecular properties like the energy level structure and electric dipole moment, it can be applied to a large variety of molecular species. A wide range of cold molecules have already been produced via buffer-gas cooling, spanning small polyatomic molecules such as ND_3 [142; 143] and H_2CO [142], heavy molecules like ThO [144; 145], and radicals NH [146], SrF [147], CaH [148], BaF [149], or CaF [150].

Sympathetic cooling uses a reservoir of ultracold atoms to cool atoms and molecules to ultralow temperatures. In the first step, the species of interest are cryogenically precooled or beam-decelerated. Sympathetic cooling has been successfully applied to produce ultracold gases of atoms through interspecies collisions [17; 151]. However, in order for sympathetic cooling to be effective, elastic cross section must significantly dominate the inelastic cross sections [152], which is difficult to achieve with atom-molecule systems. Theoretical proposals for the production of ultracold molecules by sympathetic cooling have been presented, for example for OH with Rb acting as a coolant [153], NH_3 with alkali-metal and alkaline-earth-metal atoms [154], NH/OH with Mg [155; 156], or CaF with Li/Rb [157], but not yet fully realized experimentally. Signatures of sympathetic cooling, however, were observed in Na–NaLi system [158].

3. **Laser cooling and trapping**

A class of molecules eligible for direct cooling and trapping was identified in the first proposal of a molecular MOT [159], namely, the molecules have to be characterized with diagonal Franck-Condon factors (FCFs), no net nuclear spin, and the ground or lowest metastable state needs to have a higher angular momentum than the first electronically excited state. Diatomic molecules such as metal oxides, sulfides, carbides, hydrides, and halides were proposed to meet these criteria.

Several diatomic molecules (SrF [160–162], CaF [126; 163; 164], YbF [165] and YO [166]) have already been trapped and cooled in a MOT to sub-Doppler temperatures. In 2017, laser cooling of a polyatomic molecule, SrOH [167], was demonstrated for the first time, and the achievement of sub-Doppler regime was demonstrated with CaOH in 2022 [168]. Direct laser cooling has also recently been extended to more complex polyatomic molecules, such as $CaOCH_3$ [169].

4. **Evaporative cooling**

Evaporative cooling, described earlier in Sec. 1.2, can be also applied to molecular species. Molecules from the high-energy tail in a thermal distribution are removed by adiabatic lowering of the trap depth. Subsequent elastic molecule-molecule collisions rethermalize the ensemble to a lower temperature. Similarly to sympathetic cooling, the performance of evaporative cooling is ultimately limited by the ratio of elastic-to-inelastic two-body collision rates.

Evaporative cooling of molecules was demonstrated for the first time in 2012 with hydroxyl radicals [170] and recently allowed to produce quantum degenerate gases of bialkali dimers: KRb [171] and NaK [172]. Molecular dipolar BECs of NaCs [173] and NaRb [174] should also be realized very soon.

1.3.2 Applications and prospects

Ultracold molecules with their rich internal structure, large polarizabilities, and strong coupling to microwave fields offer a rich playground for studying strongly-correlated quantum systems. They have emerged as a platform connecting a variety of research areas, including chemistry [50], particle physics and cosmology [51], condensed matter physics [48], and quantum information [175]. Here we give a brief overview of the current and prospective applications of ultracold molecules.

Controlled chemistry

Studies on cold and ultracold molecules have provided detailed insights into molecular interactions and chemical reactivity, including reaction pathways, resonance phenomena, and reactive collisions [50]. At low and ultralow temperatures, the energy scales of long-range interactions are comparable to or greater than the collision energies, what dramatically changes the reaction dynamics [176]. As reactants approach the short range, the particle rearrangements occur. Because ultracold reactants can be controlled with the accuracy of a single quantum state, each stage of the short-range reaction dynamics can be tracked and studied.

A remarkable example of control over a chemical reaction was presented in the seminal work by Ospelkaus *et al.* [177], where the dynamics of the ultracold bimolecular reaction KRb + KRb $\rightarrow$ K_2 + Rb_2 was studied. When the fermionic $^{40}K^{87}Rb$ molecules were all prepared in their absolute ground state, *s*-wave scattering was prohibited, and at the given collision energy the reaction KRb + KRb $\rightarrow$ K_2 + Rb_2 required tunneling through the *p*-wave centrifugal barrier. Next, half of the molecules were transferred to another hyperfine state, allowing for the *s*-wave scattering and hence increasing the reaction rate by nearly an order of magnitude. In a subsequent experiment, it was possible to directly observe all reactants, intermediates, and products of the reaction KRb + KRb $\rightarrow$ $K_2Rb_2^*$ $\rightarrow$ K_2 + Rb_2 [178].

Many-body physics and quantum simulations

The realization of atomic Bose-Einstein condensates and degenerate Fermi gases opened a window to the exploration of strongly correlated many-body systems and quantum simulations. In the early experiments on degenerate atomic gases, it was possible to demonstrate, for example, a transition between a superfluid and a Mott-insulating phase with bosonic atoms confined in an optical lattice [179], the Bardeen-Cooper-Schrieffer–Bose-Einstein condensation (BCS-BEC) crossover – between a BCS state of weakly-attractive fermionic atoms and a BEC of weakly-bound bosonic molecules [99; 101], or the realization of a a fermionic Mott insulator [180]. Atoms loaded into optical lattices (artificial periodic potentials formed by the interference of counterpropagating laser beams, see Ref. [48]) have allowed for quantum simulations of solid-state-like systems with different geometries, strength of interactions, and disorder [48].

In the realm of many-body physics, ultracold molecules offer opportunities to explore phenomena such as novel exotic forms of superfluidity [181], supersolidity [182], or quantum magnetism [183; 184]. Moreover, owing to the additional degrees of freedom and possibly strong long-range interactions, molecules offer a more versatile platform for building synthetic quantum matter as compared to atoms. Exemplary advanced quantum materials that could be emulated with ultracold molecules loaded into optical lattices are depicted in Fig. 1.6.

Precision measurements and tests of fundamental physical laws

Heavy, multielectron molecules offer enhanced possibilities in terms of applications in fundamental research, such as tests of fundamental symmetries, searches for spatio-temporal variations of fundamental constants, tests of quantum electrodynamics, tests of general relativity, or searches for dark matter, dark energy, and extra forces [51; 52; 185]. Moreover, cold and ultracold atoms,

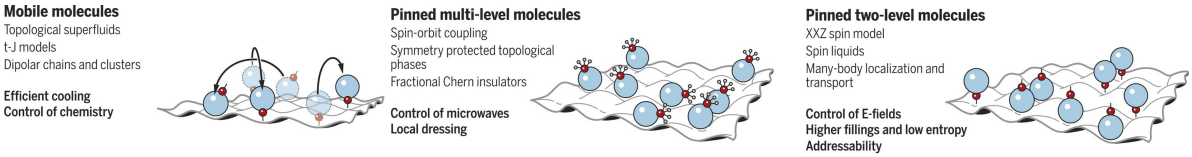

Figure 1.6: Prospective quantum materials assembled with ultracold molecules. Image source: Ref. [50].

ions, and molecules serve as ideal systems for high-resolution spectroscopy due to the reduced Doppler broadening of spectral lines at low and ultralow temperatures.

Atoms like dysprosium [186] and multiple highly-charged atomic ions [52] have already been applied in searches of physics beyond the Standard Model and setting constraints on temporal variations of the fine-structure constant α and the proton-to-electron mass ratio m_p/m_e. The complex electronic structure of molecules and molecular ions allows for even greater sensitivity to the variations of fundamental constants such as α [187] and m_p/m_e [188–190], and offer potential improvement in constraining the value of the electron electric dipole moment (eEDM) [191; 192] or investigation of parity (P) and time-reversal (T) violation [167; 193; 194]. Polar paramagnetic molecules have been proposed to offer enhanced sensitivity to eEDM, while diamagnetic molecules – to P and T violation [51]. Additionally, weakly-bound Feshbach molecules have been shown to be extremely sensitive to the variations of the m_p/m_e [187].

1.4 Dipolar quantum gases

This section gives an overview of the achievements in the field of ultracold dipolar quantum gases, i.e., quantum gases whose constituents interact via strong dipole-dipole interactions (DDIs). The DDIs have a long-range ($\propto 1/r^3$) and anisotropic (d-wave symmetry) character, and their relative strength (with respect to short-range and isotropic interactions) can often be tuned with external fields [195]. The interaction potential of two polarized dipoles reads:

$$V_{\mathrm{dd}}(r) = \frac{C_{\mathrm{dd}}}{4\pi}\frac{(1-\cos^2\theta)}{r^3}\,,$$

where $|\boldsymbol{r}| = r$ is the distance between the dipoles, θ gives the angle between $|\boldsymbol{r}|$ and the polarization axis, and C_{dd} is the dipole coupling constant, which is equal to $\mu_0\mu^2$ for particles having a permanent magnetic dipole moment (μ_0 denotes the vacuum magnetic permeability) and d^2/ϵ_0 for particles with a permanent electric dipole moment d (ϵ_0 denotes the vacuum permittivity). Since θ varies from 0 to $\pi/2$, the factor $1-\cos^2\theta$ takes values between -2 and 1. Therefore, the DDI is repulsive for particles in a side-by-side alignment and attractive in a head-to-tail configuration. The dipolar coupling is much larger for particles having an electric dipole moment as compared to those with a magnetic dipole moment since:

$$\frac{\mu_0\mu^2}{d^2/\epsilon_0} \sim \alpha^2 \sim 10^{-4}\,,$$

where α is the fine-structure constant. Another quantity often used in measuring the absolute strength of the DDI (for a particle of mass m) is the so-called dipolar length a_{dd}, defined as:

$$a_{\mathrm{dd}} = \frac{C_{\mathrm{dd}}m}{12\pi\hbar^2}\,.$$

Dipolar quantum gases of highly magnetic atoms

In recent years, particular attention has been drawn to dipolar quantum gases of highly magnetic atoms such as chromium Cr($^7S_3$), erbium Er($^3H_6$), and dysprosium Dy($^5I_8$) with magnetic

dipole moments of 6, 7, and 10 Bohr magnetons μ_B, respectively. Dipolar quantum gases have enabled access to novel many-body quantum phases and realization of complex spin models [196]. Pioneering experiments on atomic quantum gases with strong DDIs, realized in the group of T. Pfau, involved the use of Cr atoms and allowed to demonstrate, e.g., the d-wave collapse of a dipolar BEC [197–199]. Even more spectacular *dipolarity* effects have been observed later with Dy and Er atoms, such as the emergence of quantum chaos in ultracold collisions [200; 201], Fermi surface deformation [202], self-bound droplets of a dilute magnetic quantum liquid [203], Rosensweig instability of a quantum ferroffuid [204], realization of extended Bose-Hubbard models [205], and supersolidity [206–208].

What distinguishes highly magnetic lanthanides possessing both large electronic spin and large electronic orbital angular momentum, such as dysprosium and erbium, is the large anisotropy of interactions, having its source not only in the long-range magnetic DDIs, stemming from the atoms' large magnetic moments, but also in the anisotropic contributions to the van der Waals (vdW) interactions, resultant of the large orbital angular momentum of valence electrons that occupy a partially filled $4f$ electron shell shielded by a closed $6s$ shell [209]. This anisotropy leads to rich, dense, and chaotic spectra of magnetic Feshbach resonances in collisions between highly magnetic atoms in non-S electronic ground states [200; 201], far different from Feshbach resonance spectra observed in collisions between S-state alkali-metal and alkaline-earth-metal atoms [74]. The complexity of interatomic interactions, and consequent complexity of collisional spectra, is what causes the investigation of such systems and explanation of their properties very challenging.

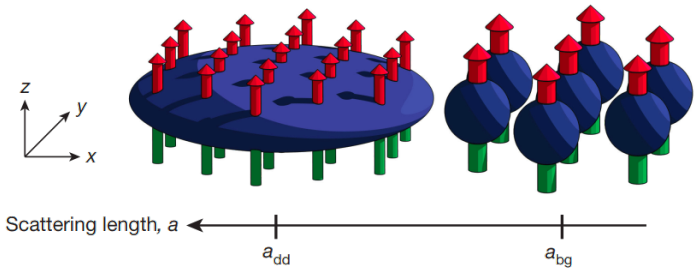

Figure 1.7: A schematic of the experimental procedure for observing Rosensweig instability in a dipolar quantum gas as presented in Ref. [204]. A strongly dipolar BEC in prepared in a pancake-shaped trap (left). By tuning the scattering length with a Feshbach resonance, such that the dipolar attraction dominates the repulsive contact interaction, an instability of a dipolar gas is induced and the atoms cluster to droplets (right).

So far, degenerate quantum gases of highly magnetic transition-metal and lanthanide atoms, such as Cr ($^7S_3$; $6\,\mu_B$) [25; 26], Eu ($^8S_{7/2}$; $7\,\mu_B$) [34], Er ($^3H_6$; $7\,\mu_B$) [32; 33], and Dy ($^5I_8$; $10\,\mu_B$) [30; 31] have been realized experimentally. Magneto-optical trapping of Ho($^4I^o_{15/2}$; $9\,\mu_B$) [210] and Tm($^2F_{7/2}$; $4\,\mu_B$) [211] atoms has also been demonstrated.

Dipolar quantum gases of polar molecules

Another way to realize a quantum gas with significant DDIs is to use particles having a large permanent electric dipole moment. Therefore, molecules are ideal candidates for studying dipolar effects, provided that they: *i.* are heteronuclear and possess a significant permanent EDM, *ii.* are prepared in a low rovibrational state and are stable against collisional relaxation, *iii.* an external electric field is applied to orient the molecules in the laboratory frame [212]. The experimentally available ultracold molecular systems with a large EDM include: KRb, NaK, RbCs, NaRb, KCs, LiCs, NaLi, SrF, CaF, YO, HO (see Sec. 1.3.1).

Ultracold quantum mixtures containing highly magnetic atoms

Heteronuclear mixtures containing highly magnetic atoms have been proposed as a platform to study polaron physics in systems with dominant dipolar interactions [53–55], Efimov physics [56], exotic FFLO states in systems with significant mass imbalance [57; 58], and binary supersolids [59]. Experiments on degenerate mixtures of Dy and K atoms [60–62], Dy and Er atoms [63–65], Er and Li atoms [66], Cr and Li atoms [67; 68], and Er and Yb atoms [69] are currently being realized, making the theoretical proposals more and more feasible.

One particular feature that motivates the experiments on Fermi-Fermi mixtures such as ^{161}Dy+^{40}K [60–62] and ^{53}Cr+^{6}Li [67; 68] is the favorable mass imbalance of constituent atoms ($8.17 \leq M/m \leq 13.6$), that, according to theoretical predictions, should allow for the access to novel superfluid states with exotic pairing mechanisms like the FFLO and Sarma phases [57; 58; 213; 214]. In addition, mass-imbalanced fermionic mixtures have been predicted to exhibit exotic few-body effects like p-wave atom-dimer interactions [215–217] or non-Efimovian weakly-bound trimer, tetramer, and pentamer states [218; 219].

Ultracold quantum mixtures of highly magnetic transition-metal or lanthanide atoms interacting with open-shell or closed-shell S-state atoms offer prospects for the formation of ground-state polar molecules with large both electric and magnetic dipole moments (the production of DyK Feshbach molecules was recently reported in Ref. [97]). The interplay between magnetic and electric DDIs specific to such molecules should allow to build novel quantum simulators and explore different regimes of quantum magnetism [50; 220]. Moreover, the complex electronic structure of molecules containing transition-metal or lanthanide atoms, including a very rich structure of the excited electronic states, provides enhanced sensitivities in precision tests of fundamental physics [51; 189].

Therefore, the electronic structure of molecules containing highly magnetic transition-metal and lanthanide atoms, such as Cr– [221; 222] and Eu–alkali-metal and alkaline-earth-metal dimers [223] have been theoretically investigated alongside the collisional properties of ultracold heteronuclear mixtures: Cr+Li [Paper III], Cr+Rb [221], Cr+Ca^+/Sr^+/Ba^+/Yb^+ [224], Eu+Li/Rb [Paper I], Er+Li [225], Er+Yb [226; 227], Er+Sr [227], and Dy+Sr/Yb [227]. The *ab initio* studies of interatomic interactions in homonuclear dimers of highly magnetic lanthanide atoms such as Eu_2 [228], Ho_2 [229], Er_2 [230], and Tm_2 [230] have also been reported.

Chapter 2

Methodology

The present Chapter discusses the theory underlying the calculations presented in Papers I – IV. Hartree atomic units ($m_e = 1, e = 1, \hbar = 1, 4\pi\epsilon_0 = 1$; e denotes the electron charge) are used throughout the Chapter.

2.1 Electronic and rovibrational structure of diatomic molecules

2.1.1 Adiabatic and Born-Oppenheimer approximations

The separation of variables method is frequently employed to simplify complex Schrödinger equations for systems with many variables and underlies one of the most important and fundamental approximations used in quantum chemistry and molecular physics – the adiabatic approximation. In the adiabatic approximation, and its universally used variation – the Born-Oppenheimer (BO) approximation, we assume that the electronic degrees of freedom can be decoupled from the nuclear ones. The assumption relies on the fact that the atomic nuclei move much slower than the electrons (due to their $10^3 - 10^5$ times larger mass), and therefore the electrons can instantaneously adapt to a new configuration of the nuclei.

In the non-relativistic approach, the total Hamiltonian of a molecule – a system composed of n electrons and N nuclei bound by Coulomb interactions – can be written as:

$$H = H_{\mathrm{el}} + T_{\mathrm{n}} \tag{2.1}$$

with

$$H_{\mathrm{el}} = T_{\mathrm{el}} + V\,, \tag{2.2}$$

where we have defined the electronic Hamiltonian, H_{el}; T_{el} and T_{n} denote the electronic and nuclear kinetic energy operators, respectively, and V is the electrostatic potential energy operator. In the space-fixed frame, the above terms can be expressed as:

$$T_{\mathrm{el}} = -\frac{1}{2}\sum_{i=1}^{n} \boldsymbol{\nabla}_i^2\,, \tag{2.3}$$

$$T_{\mathrm{n}} = -\sum_{I=1}^{N} \frac{1}{2M_I}\boldsymbol{\nabla}_I^2\,, \tag{2.4}$$

$$V = \sum_{i<j}^{n} \frac{1}{|\boldsymbol{r}_i - \boldsymbol{r}_j|} - \sum_{i=1}^{n}\sum_{I=1}^{N} \frac{Z_I}{|\boldsymbol{r}_i - \boldsymbol{R}_I|} + \sum_{I<J}^{N} \frac{Z_I Z_J}{|\boldsymbol{R}_I - \boldsymbol{R}_J|}\,, \tag{2.5}$$

where $\boldsymbol{\nabla}_i$ is the gradient operator for electron i ($\boldsymbol{\nabla}_I$ for nucleus I), $\boldsymbol{r}_i$ denotes a position vector of electron i ($\boldsymbol{R}_I$ – a position vector of nucleus I), and M_I and Z_I denote the mass and

charge of nucleus I, respectively. The consecutive terms of the V operator describe the electron-electron, electron-nucleus, and nucleus-nucleus Coulomb interactions. Our aim is to solve the time-independent Schrödinger equation for the molecular Hamiltonian H defined in Eq. (2.1):

$$H\Psi_{\mathrm{tot}}(\boldsymbol{r},\boldsymbol{R}) = E\Psi_{\mathrm{tot}}(\boldsymbol{r},\boldsymbol{R})\,. \tag{2.6}$$

The total molecular wave function $\Psi_{\mathrm{tot}}(\boldsymbol{r},\boldsymbol{R})$ depends on the positions of all electrons and nuclei: $\boldsymbol{r} \equiv \{\boldsymbol{r}_i\}$ and $\boldsymbol{R} \equiv \{\boldsymbol{R}_I\}$. To simplify the solution of Eq. (2.6), $\Psi_{\mathrm{tot}}(\boldsymbol{r},\boldsymbol{R})$ is first expanded in terms of the electronic $\psi_k(\boldsymbol{r};R)$ and nuclear $\chi_k(\boldsymbol{R})$ wave functions:

$$\Psi_{\mathrm{tot}}(\boldsymbol{r},\boldsymbol{R}) = \sum_k \psi_k(\boldsymbol{r};R)\chi_k(\boldsymbol{R})\,, \tag{2.7}$$

where the summation is over all electronic states k. The wave function $\psi_k(\boldsymbol{r};R)$ depends directly on the positions of the electrons and parametrically on the frozen positions of the nuclei. The above expansion is referred to as the Born-Huang expansion [231], and is equivalent to the decomposition of Ψ_{tot} in the complete basis of the electronic Hamiltonian, H_{el} (2.2). In the adiabatic and Born-Oppenheimer approximations, we next assume that the electron cloud adiabatically follows the nuclear motion, and we limit the expansion in Eq. (2.7) to a single term:

$$\Psi_k(\boldsymbol{r},\boldsymbol{R}) = \psi_k(\boldsymbol{r};R)\chi_k(\boldsymbol{R})\,, \tag{2.8}$$

which holds provided that the electronic state k is well-separated from other electronic states.

The assumption that electronic and nuclear motions can be decoupled allows us to solve the electronic and nuclear Schrödinger equations separately. The electronic Schrödinger equation reads:

$$H_{\mathrm{el}}\psi_k(\boldsymbol{r};R) = E_k^{\mathrm{el}}(R)\psi_k(\boldsymbol{r};R)\,, \tag{2.9}$$

where the energy of the electronic state $E_k^{\mathrm{el}}(R)$ depends parametrically on the internuclear distance R. By solving Eq. (2.9) for all possible positions of the nuclei, one obtains the potential energy curve (PEC) for the nuclear motion. It is worth noting here that the basic concepts of quantum chemistry, such as PEC and the notion of electronic structure, are implicit to the adiabatic and BO approximations.

The nuclear dynamics is governed by the nuclear Schrödinger equation:

$$\Big(T_{\mathrm{n}} + E_{\mathrm{el}}^k(R) + T'_{kk}(R)\Big)\chi_k(\boldsymbol{R}) = E\chi_k(\boldsymbol{R})\,, \tag{2.10}$$

where $T'_{kk} = \langle\psi_k|\,T_{\mathrm{n}}|\psi_k\rangle$ is the adiabatic correction (diagonal Born-Oppenheimer correction, DBOC) to the BO potential $E_{\mathrm{el}}^k(R)$, and is usually very small and neglected in the electronic structure calculations. In the adiabatic approximation, the PEC for the nuclear motion is given by:

$$U_k(R) = E_k^{\mathrm{el}}(R) + T'_{kk}(R)\,, \tag{2.11}$$

while the BO approximation completely neglects the T'_{kk} term. If two electronic eigenstates k, k' are close in energy, $E_k^{\mathrm{el}}(R) \approx E_{k'}^{\mathrm{el}}(R)$, the nuclear wave packet is no longer localized on one PEC. In this case, the adiabatic (or BO) approximation breaks down and non-adiabatic coupling terms, involving integrals of the type $\langle\psi_{k'}|\,\boldsymbol{\nabla}_I\psi_k\rangle$, need to be taken into account [232].

Once the BO approximation is applied and PECs are calculated, one can define the interaction energy between atoms forming a molecule. In the supermolecule approach, the interaction energy (E_{int}) is defined as the difference between the total energy of a complex (E_{AB}) and the energies of isolated monomers (E_A, E_B). For a diatomic molecule AB composed of atoms A and B, it can be calculated as:

$$E_{\mathrm{int}}(R) = E_{AB}(R) - E_A(\infty) - E_B(\infty)\,. \tag{2.12}$$

2.1.2 Rovibrational structure of diatomic molecules

Let us discuss the solution of the nuclear Schrödinger equation introduced in Eq. (2.10) for a diatomic molecule composed of monomers A and B. We assume that the center-of-mass (COM) motion has been separated out and PECs are known. The Hamiltonian describing the internal energy of the dimer in a given electronic state k reads:

$$H_{\mathrm{n}} = -\frac{1}{2\mu}\boldsymbol{\nabla}_R^2 + U_k(R)\,, \tag{2.13}$$

where $\mu = \frac{M_A M_B}{M_A+M_B}$ is the reduced mass of the nuclei, $\boldsymbol{R} = \boldsymbol{R}_A - \boldsymbol{R}_B$, and $U_k(R)$ has been defined in Eq. (2.11). We again apply the separation of variables technique to separate the vibrations of the molecule from its rotations around the COM. To this end, we express the nuclear (rovibrational) wave function $\chi_k(\boldsymbol{R})$ in terms of a product of a spherical function $Y(\theta,\varphi)$ describing the rotations (with co-latitude angle θ and the longitudinal angle φ) and function $\phi_k(R)$ describing the vibrations:

$$\chi_k(\boldsymbol{R}) = Y(\theta,\varphi)\frac{\phi_k(R)}{R}\,. \tag{2.14}$$

After inserting $\chi_k(\boldsymbol{R})$ (2.14) into the nuclear motion equation defined in Eq. (2.13), we find that $Y(\theta,\varphi) \equiv Y_J^M(\theta,\varphi)$ is a spherical harmonic function being the solution to the quantum rigid rotor problem with respective eigenvalues $\frac{J(J+1)}{2\mu R^2}$ (where J is the angular momentum of the molecule and M denotes its projection onto the quantization axis). The equation describing the molecular vibrations then reads:

$$\left(-\frac{1}{2\mu}\boldsymbol{\nabla}_R^2 + V_{kJ}^{\mathrm{eff}}(R)\right)\phi_{kvJ}(R) = E_{kvJ}\phi_{kvJ}(R)\,, \tag{2.15}$$

where

$$V_{kJ}^{\mathrm{eff}}(R) = U_k(R) + \frac{J(J+1)}{2\mu R^2} \tag{2.16}$$

is the effective potential including the centrifugal term, $\frac{J(J+1)}{2\mu R^2}$, which is responsible for the elongation of bond length as J increases and the rotational motion gets faster. We can see that $\phi_k(R) \equiv \phi_{kvJ}(R)$, thus rotations and oscillations of a molecule cannot be fully separated.

For the lowest-lying vibrational levels of a given electronic state, the molecular vibrations can be modeled by a quantum harmonic oscillator with vibrational energies E_v:

$$E_v = \omega_e\left(v+\frac{1}{2}\right)\,, \tag{2.17}$$

where ω_e denotes the harmonic constant, proportional to the second derivative of the electronic potential $U_k(R)$ at equilibrium distance $R = R_e$. A more accurate approximation to the vibrational energy levels include the anharmonicity term:

$$E_v = \omega_e\left(v+\frac{1}{2}\right) - \omega_e x_e\left(v+\frac{1}{2}\right)^2\,, \tag{2.18}$$

where x_e is the first anharmonicity constant – proportional to the third derivative of the potential.

The vibrational bound states $\phi_{kvJ}(R)$ with energies E_{kvJ} can be obtained by solving the equation Eq. (2.15) numerically using the discrete variable representation (DVR) method. There are multiple variations of the method [234], but we will illustrate its principles for a simple case of an equally spaced quadrature [234–236]. The vibrational wave function $\phi_{kvJ}(R)$ will be represented on a grid of equidistant points $\{R_i\}$:

$$R_i = R_{\mathrm{min}} + i\frac{(R_{\mathrm{max}} - R_{\mathrm{min}})}{N}, \qquad i = 1,\,...,\,N-1\,. \tag{2.19}$$

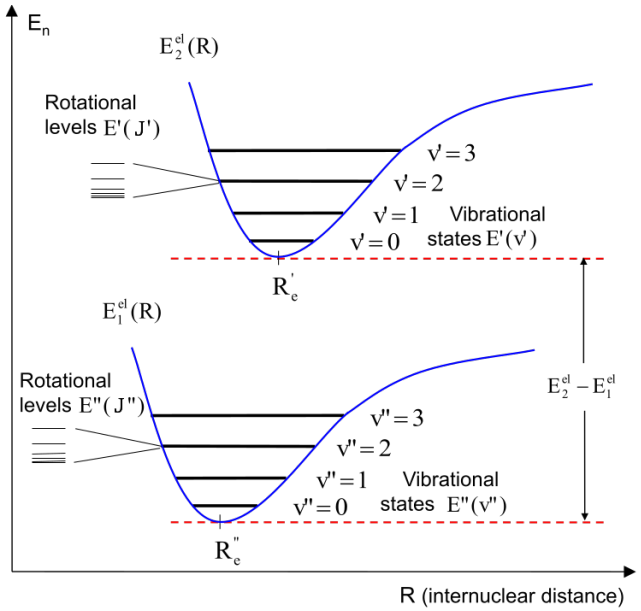

Figure 2.1: Depiction of the electronic, vibrational, and rotational energy levels' structure for a diatomic molecule [233].

The set of functions, orthonormal in the $(R_{\min}, R_{\max})$ interval (the wave function vanishes at the endpoints $R_{\min}$ and $R_{\max}$), that generate the quadrature is given by:

$$f_i(R) = \sqrt{\frac{2}{R_{\max} - R_{\min}}} \sin\left(\frac{i\pi(R - R_{\min})}{R_{\max} - R_{\min}}\right), \qquad i = 1, ..., N-1\,; \tag{2.20}$$

this set of functions is referred to as the DVR primitive functions and is equivalent to the particle-in-a-box eigenfunctions. For this choice of primitive functions, the DVR basis set reads:

$$\phi_\alpha(R) = \frac{2}{\sqrt{N(R_{\max} - R_{\min})}} \sum_{i=1}^{N-1} \sin\left(\frac{i\pi\alpha}{N}\right) \sin\left(\frac{i\pi(R - R_{\min})}{R_{\max} - R_{\min}}\right), \qquad \alpha = 1, ..., N-1\,. \tag{2.21}$$

We are solving the eigenproblem (2.15) in the DVR functions basis. The Hamiltonian matrix element reads:

$$H_{\alpha\beta} = T_{\alpha\beta} + V_{kJ}^{\text{eff}}(R_\alpha)\delta_{\alpha\beta}\,, \tag{2.22}$$

where the diagonal and non-diagonal kinetic energy matrix elements, $T_{\alpha\alpha}$ and $T_{\alpha\beta}$ $(\alpha \neq \beta)$, respectively, are given by [236]:

$$T_{\alpha\alpha} = \frac{1}{2\mu} \frac{\pi^2}{2(R_{\max} - R_{\min})^2} \left(\frac{3N^2 + 1}{3} - \frac{1}{\sin^2(\frac{\alpha\pi}{N})}\right) \tag{2.23}$$

and

$$T_{\alpha\beta} = \frac{1}{2\mu} \frac{\pi^2(-1)^{\alpha-\beta}}{2(R_{\max} - R_{\min})^2} \left(\frac{1}{\sin^2[\frac{\pi(\alpha-\beta)}{2N}]} - \frac{1}{\sin^2[\frac{\pi(\alpha+\beta)}{2N}]}\right). \tag{2.24}$$

The Hamiltonian (2.22) is diagonalized numerically to obtain the vibrational bound states $\phi_{kvJ}(R_\alpha)$ with respective binding energies E_{kvJ}.

2.2 *Ab initio* methods for electronic structure calculations

For most quantum-mechanical systems, obtaining the exact solution to the Schrödinger equation is impossible. The *ab initio* (= *derived from first principles*) electronic structure methods have

been developed to provide accurate estimates of molecular structure and properties. State-of-the-art quantum chemistry methods allow for the calculation of atomic and molecular properties at an unprecedented level of precision without any prior experimental knowledge.

2.2.1 Self-consistent field methods

A powerful tool to obtain approximate solutions to the Schrödinger equation is the variational method based on the variational principle, which for an arbitrary function Φ can be written as:

$$E[\Phi] = \frac{\langle \Phi | H \Phi \rangle}{\langle \Phi | \Phi \rangle} \geq E_0 \,, \tag{2.25}$$

where E_0 is the exact ground-state energy (the variational method can also be adapted to give bounds on the energies of the excited states [237]). Approximate ground-state solution is derived by minimizing the energy functional $E[\Phi]$ with a reasonable ansatz for the wave function Φ.

The first step in electronic structure calculations typically involves applying the Hartree-Fock (HF) approximation to the atomic or molecular Schrödinger equation. The HF method is also known as the self-consistent field (SCF) method. In this method, the trial wave function for a system of n electrons, Φ_{HF}, is a normalized Slater determinant:

$$\Phi_{\mathrm{HF}} = \frac{1}{\sqrt{n!}} \begin{vmatrix} \phi_1(1) & \phi_2(1) & \cdots & \phi_n(1) \\ \phi_1(2) & \phi_2(2) & \cdots & \phi_n(2) \\ \vdots & \vdots & \ddots & \vdots \\ \phi_1(n) & \phi_2(n) & \cdots & \phi_n(n) \end{vmatrix} , \tag{2.26}$$

which is an antisymmetrized product of one-electron wave functions called spinorbitals, $\phi_i(j)$ (where $j \equiv \tau_j \equiv (\boldsymbol{r}_j, \sigma_j)$ with $\sigma_j = \pm 1/2$ denoting the spin coordinate). The electronic Hamiltonian introduced in Eq. (2.2) can be rewritten as the sum of zero-, one- and two-electron terms:

$$H_{\mathrm{el}} = \sum_i^n h_i + \sum_{i<j}^n \frac{1}{r_{ij}} + \sum_{I<J}^N \frac{Z_I Z_J}{R_{IJ}} \,, \tag{2.27}$$

where $r_{ij} \equiv |\boldsymbol{r}_i - \boldsymbol{r}_j|$ and $R_{IJ} \equiv |\boldsymbol{R}_I - \boldsymbol{R}_J|$, and h_i is the one-electron Hamiltonian describing the kinetic energy of electron i and its interaction with the nuclei:

$$h_i = -\frac{1}{2} \boldsymbol{\nabla}_i^2 - \sum_{I=1}^N \frac{Z_I}{r_{iI}} \,, \tag{2.28}$$

with $r_{iI} \equiv |\boldsymbol{r}_i - \boldsymbol{R}_I|$. For further analysis, we can introduce the sum of one-electron energy operators $h = \sum_i h_i$, and the Coulomb (J_j) and exchange (K_j) operators, which are defined through their action on a spinorbital $\phi_i(k)$ in the following way:

$$J_j \phi_i(k) = \left(\int \frac{\phi_j^*(l) \phi_j(l)}{r_{kl}} \mathrm{d}\tau_l \right) \phi_i(k) \,, \tag{2.29}$$

$$K_j \phi_i(k) = \left(\int \frac{\phi_j^*(l) \phi_i(l)}{r_{kl}} \mathrm{d}\tau_l \right) \phi_j(k) \,. \tag{2.30}$$

Let us also define the total Coulomb and exchange operators:

$$J = \sum_i J_i \,, \tag{2.31}$$

$$K = \sum_i K_i \,. \tag{2.32}$$

By calculating the expectation value of $E[\Phi_{\mathrm{HF}}] = \langle \Phi_{\mathrm{HF}} | H_{\mathrm{el}} | \Phi_{\mathrm{HF}} \rangle$, we obtain the energy functional:

$$E[\Phi_{\mathrm{HF}}] = \sum_{i=1}^{n} h_{ii} + \frac{1}{2} \sum_{i,j=1}^{n} (J_{ij} - K_{ij}) \,, \tag{2.33}$$

where $h_{ii} = \langle \phi_i | h | \phi_i \rangle$ is the one-electron integral, while J_{ij} and K_{ij} are the two-electron integrals describing, respectively, the Coulomb repulsion between electrons and the exchange energy due to the antisymmetry of the total wave function. They are defined as follows:

$$J_{ij} = \langle \phi_i \phi_j | \phi_i \phi_j \rangle \,, \tag{2.34}$$

$$K_{ij} = \langle \phi_i \phi_j | \phi_j \phi_i \rangle \,, \tag{2.35}$$

where

$$\langle \phi_i \phi_j | \phi_k \phi_l \rangle = \sum_{\sigma_1, \sigma_2 = -1/2}^{1/2} \int \int \mathrm{d}^3 r_1 \mathrm{d}^3 r_2 \frac{\phi_i^*(\boldsymbol{r}_1, \sigma_1) \phi_j^*(\boldsymbol{r}_2, \sigma_2) \phi_k(\boldsymbol{r}_1, \sigma_1) \phi_l(\boldsymbol{r}_2, \sigma_2)}{r_{12}} \,. \tag{2.36}$$

In the HF method, we want to obtain the spinorbitals ϕ_i that minimize the energy functional $E[\Phi_{\mathrm{HF}}]$. This is achieved by solving the Fock operator eigenproblem:

$$F \phi_i(k) = \varepsilon_i \phi_i(k) \,, \tag{2.37}$$

where F is defined as follows:

$$F = h + J - K \,. \tag{2.38}$$

The energy of an electron in a spinorbital ϕ_i can therefore be expressed as:

$$\varepsilon_i = h_{ii} + \sum_{j} (J_{ij} - K_{ij}) \,, \tag{2.39}$$

which can be interpreted as the energy of an electron moving in a mean field created by all other electrons and the nuclei (the HF method does not take into consideration the electron correlation). The energy of an atomic or a molecular system within the Hartree-Fock approximation can be eventually written as:

$$E_{\mathrm{HF}} = \sum_{i=1}^{n} \varepsilon_i - \frac{1}{2} \sum_{i,j=1}^{n} (J_{ij} - K_{ij}). \tag{2.40}$$

Even though the HF approach introduces a substantial simplification of the original molecular Hamiltonian eigenproblem, obtaining an exact numerical solution to the HF equations (2.37) requires computational power and poses a challenge for most molecular systems. In practical implementations, the molecular orbitals (MOs), $\psi_i(\boldsymbol{r})$, are approximated by a linear combination of atomic orbitals (LCAO) $\zeta_j(k)$ of a known analytical form (typically, the orbitals are of Gaussian type):

$$\psi_i(\boldsymbol{r}) = \sum_{j=1}^{m} C_{ij} \zeta_j(\boldsymbol{r}) \,, \tag{2.41}$$

where $m \geq n$. Within the LCAO scheme, the energy is minimized with respect to the expansion coefficients C_{ij}, which yields the Roothaan-Hall equations:

$$\mathbf{FC} = \mathbf{SC}\epsilon \,, \tag{2.42}$$

where $\mathbf{F}$ is the Fock matrix with elements $F_{kl} = \langle\zeta_k|F|\zeta_l\rangle$, $\mathbf{S}$ is the overlap matrix with elements $S_{kl} = \langle\zeta_k|\zeta_l\rangle$, $\mathbf{C}$ is the matrix of expansion coefficients C_{kl}, and ϵ is a diagonal matrix of the orbital energies. By inserting the LCAO expansion, we obtain the energy functional:

$$E[\mathbf{C}] = \sum_{p,q} D_{pq} h_{pq} + \frac{1}{2} \sum_{p,q} \sum_{r,s} \left(D_{pq} D_{rs} - D_{pr} D_{qs}\right) \langle\zeta_p \zeta_r|\zeta_q \zeta_s\rangle \,, \tag{2.43}$$

where we have introduced the density matrix $\mathbf{D} = \mathbf{C}\mathbf{C}^{\mathbf{T}}$ with matrix elements $D_{pq} = \sum_i^m C_{pi} C_{qi}$.

In a self-consistent field procedure, an initial guess of the density matrix is first made. The Fock matrix is then constructed and diagonalized to obtain a set of MOs, which are in the next step used to construct an improved density matrix. The procedure is repeated until the density matrix stops changing and the energy difference from one iteration to another is below a predefined threshold.

The main limitation of the Hartree-Fock method is that it does not take into account the electron correlation – both dynamical and non-dynamical. The dynamical correlation in responsible for the instantaneous electron-electron repulsions (i.e., the cusp condition as $r_{ij} \to 0$), while the non-dynamical one accounts for the nearly-degenerate electron configurations and plays a crucial role in the description of bond formation and bond breaking processes. The non-dynamical correlation can be factored in using the multi-configuration self-consistent field (MCSCF) approach, where several configurations are explicitly included in the SCF procedure [238].

2.2.2 Configuration interaction methods

The dynamical electron correlation may be recovered by going beyond the ansatz of a single-determinant Hartree-Fock wave function. In the configuration interaction (CI) method, the total wave function is represented as a combination of Slater determinants constructed from the one-electron basis. The method gives an exact solution to the electronic Schrödinger equation if the expansion includes all possible Slater determinants (obtained by exciting all possible electrons to all possible virtual orbitals). In this case, the total wave function (the full configuration interaction (FCI) wave function) can be written as:

$$|\Psi_{\mathrm{FCI}}\rangle = (1 + \hat{C})\,|\Phi_{\mathrm{HF}}\rangle \tag{2.44}$$

with the correlation operator $\hat{C}$ defined as:

$$\hat{C} = \sum_{ai} C_i^a \hat{a}_a^\dagger \hat{a}_i + \sum_{abij} C_{ij}^{ab} \hat{a}_a^\dagger \hat{a}_b^\dagger \hat{a}_j \hat{a}_i + \ldots \,, \tag{2.45}$$

where $\hat{a}_i^\dagger$ and $\hat{a}_j$ are the creation and annihilation operators of spinorbitals i and j, respectively, while C_i^a, C_{ij}^{ab}, etc., are the expansion coefficients computed using the variational principle or by direct diagonalization.

Since the number of determinants included in the FCI expansion grows factorially with the number of electrons and basis functions, full CI calculations are only possible for few-electron systems. In practice, the expansion (2.45) is often truncated to only account for a limited number of the lowest-order excitations (for example, the CISD method is limited to single (S) and double (D) excitations). This, however, introduces the main limitation of the CI approach – truncation of the correlation operator by excitation level leads to the lack of size consistency and size extensivity of the method. The lack of size consistency poses a particular problem at large internuclear distances, where the computed molecular energies lose physical meaning.

In a multireference configuration interaction (MRCI) method, the CI wave function is constructed by including excitations not only from the ground-state electronic configuration, but also from chosen excited states [239].

2.2.3 Coupled-cluster methods

The main limitations of the CI methods are the lack of size consistency and size extensivity and slow convergence towards the FCI limit. These problems are resolved by the coupled-clusters (CC) method based on an exponential ansatz wave function:

$$|\Psi_{\mathrm{CC}}\rangle = e^{\hat{T}} |\Phi_{\mathrm{HF}}\rangle \,, \tag{2.46}$$

where $e^{\hat{T}}$ is the exponent of the cluster operator $\hat{T}$. The cluster operator $\hat{T}$ is a sum of operators corresponding to all single, double, ..., and n-fold excitations:

$$\hat{T} = \hat{T}_1 + \hat{T}_2 + ... + \hat{T}_n \,. \tag{2.47}$$

These operators can be expressed as:

$$\begin{aligned} \hat{T}_1 &= \sum_{ai} t_i^a \hat{a}_a^\dagger \hat{a}_i \\ \hat{T}_2 &= \frac{1}{4} \sum_{abij} t_{ij}^{ab} \hat{a}_a^\dagger \hat{a}_b^\dagger \hat{a}_j \hat{a}_i \\ &\vdots \\ \hat{T}_n &= \frac{1}{(n!)^2} \sum_{i_1 i_2 ... i_n} \sum_{a_1 a_2 ... a_n} t_{i_1 i_2 ... i_n}^{a_1 a_2 ... a_n} \hat{a}_{a_1}^\dagger \hat{a}_{a_2}^\dagger ... \hat{a}_{a_n}^\dagger \hat{a}_{i_n} ... \hat{a}_{i_2} \hat{a}_{i_1} \,, \end{aligned} \tag{2.48}$$

where t are the cluster amplitudes. The Ψ_{CC} wave function in Eq. (2.46) without truncation of excitations is equivalent to a full CI wave function Ψ_{CI} from Eq. (2.44). The expansion coefficients can be related as follows:

$$\begin{aligned} C_i^a &= t_i^a \,, \\ C_{ij}^{ab} &= t_{ij}^{ab} + t_i^a t_j^b - t_i^b t_j^a \,, \end{aligned} \tag{2.49}$$

etc. Unlike the CI method, the CC method is not variational. The energy of the system calculated within the CC approach reads:

$$E_{\mathrm{CC}} = \frac{\langle \Phi_{\mathrm{HF}}| \, e^{-\hat{T}} H e^{\hat{T}} \, |\Phi_{\mathrm{HF}}\rangle}{\langle \Phi_{\mathrm{HF}} | \Phi_{\mathrm{HF}} \rangle}. \tag{2.50}$$

When the cluster operator $\hat{T}$ includes all terms up to $\hat{T}_n$, we obtain the exact (within a given basis set) solution to the electronic Schrödinger equation. For multielectron systems, the cluster operator expansion has to be truncated at an excitation level smaller than n. The truncation of the cluster operator, however, does not lead to mixing of cluster amplitudes for monomers at an infinite distance, making the CC method inherently size consistent.

Among the CC methods frequently employed in real electronic structure computations one could mention the CCSD method, which corresponds to $\hat{T} = \hat{T}_1 + \hat{T}_2$, or the CCSDT method – corresponding to $\hat{T} = \hat{T}_1 + \hat{T}_2 + \hat{T}_3$. The CCSD(T) method – the coupled-clusters method restricted to single, double and non-iterative (calculated based on perturbation theory) triple excitations is considered to be the gold standard of quantum chemistry.

2.2.4 Basis sets

In the LCAO-MO approach, introduced in Sec. 2.2.1, a set of atomic orbitals is used in the expansion of molecular orbitals (see Eq. (2.41)). As a consequence of atomic symmetry, AOs always take the form:

$$\zeta(\boldsymbol{r}) = R(r) Y_l^m(\theta, \varphi) \,, \tag{2.51}$$

where the radial function $R(r)$ is known exactly only for one-electron systems. The exact function satisfies the cusp condition due to the singularity of the interaction potential at the nucleus, i.e.:

$$\left.\frac{\mathrm{d}R}{\mathrm{d}r}\right|_{r=0} = -ZR(0)\,. \tag{2.52}$$

At large distances, an electron sees the remainder of the molecule as a structureless charge. Therefore, just like in the case of a hydrogen atom, the wave function of the electron will decay exponentially. This behavior is satisfied by the so-called Slater-type orbitals (STOs) [240]:

$$\chi^{\mathrm{STO}}(\boldsymbol{r}) = P(r)Y_l^m(\theta,\varphi)e^{-\alpha r}\,, \tag{2.53}$$

where the radial polynomial $P(r)$ can take different forms. However, due to the difficulty associated with the evaluation of multi-center integrals using STOs, they are rarely used in the *ab initio* calculations nowadays. Gaussian-type orbitals (GTOs) have been introduced to remediate the problem with multi-center integrals: owing to the so-called Gaussian product rule, the four-center integrals can be reduced to a finite sum of two-center integrals, and, in the next step, to a finite sum of one-center integrals [241]. GTOs can be written in a form similar to STOs:

$$\chi^{\mathrm{GTO}}(\boldsymbol{r}) = P(r)Y_l^m(\theta,\varphi)e^{-\alpha r^2}\,. \tag{2.54}$$

Even though GTOs are less *physical* than STOs, and a larger number of basis functions is needed to reproduce the behavior of a real atomic orbital, they allow for a much faster computation of molecular integrals. The poor description of the cusp behavior is resolved by the contraction of GTOs, i.e., rather than using primitive Gaussian functions in the AO expansion, linear combinations of Gaussians are used:

$$\chi_k^{\mathrm{CGTO}}(\boldsymbol{r}) = \sum_i C_{ik}\chi_i^{\mathrm{GTO}}(\boldsymbol{r})\,. \tag{2.55}$$

Different contraction schemes may be adapted to factor in the electron correlation effects. Correlation-consistent basis sets of type cc-pVXZ developed by Dunning and coworkers [242] are constructed by adding higher angular momentum functions to account for a more complex electron density distribution caused by correlation.

A basis set suitable for accurate molecular calculations requires more than just describing the atoms effectively. It must also flexibly accommodate atomic deformations during molecule formation and incorporate adjustments due to external perturbations for calculating molecular properties. Achieving this flexibility involves adding diffuse and polarization functions to the basis set [243].

An atom in a molecule experiences the field from surrounding atoms, therefore causing a shift in the charge density. Polarization functions are employed to reshape the atomic orbitals with respect to the configuration adopted in an atom. Polarization functions supply the basis set with functions of higher angular momenta than those of occupied orbitals in the atomic SCF calculation. They have their radial maxima in the region of valence electrons.

Another enhancement frequently incorporated into Gaussian-type basis sets are the so-called diffuse functions. These functions are characterized by shallow Gaussian profiles that better capture the tail of atomic orbitals. They play a crucial role in accurately describing the behavior of electrons in larger and more flexible molecular systems, including anions and polar molecules. They are also necessary for the computation of excited states.

Dunning basis sets are typically labeled with 'cc-pVXZ', where 'cc-p' stands for 'correlation-consistent polarized', 'V' stands for 'valence' (meaning that the basis set focuses on the description of valence correlation effects), 'X' indicates the cardinal number of the basis set (single, double, triple, etc.), and 'Z' (zeta) refers to a set of Gaussian-type functions. Augmented versions of the basis sets with added diffuse functions are typically labeled with with 'aug-' preceding 'cc-pVXZ'.

The basis sets developed by Dunning systematically achieve the convergence of post-HF calculations towards the complete basis set (CBS) limit. The CBS extrapolation formula allows to estimate the energy of a system at the limit of an infinitely large basis set size. For the correlation energy, the following general form of the extrapolation formula is assumed:

$$E_{\mathrm{corr}}(\infty) = E_{\mathrm{corr}}(X) + AX^{-\alpha}\,. \tag{2.56}$$

In most chemical applications, relative energies are more important than absolute energies. Within the supermolecule approach (2.12), the interaction energy is computed as a difference between the total energy of a complex and the energies of constituent monomers. As practically all *ab initio* computations are performed using finite basis sets, the calculation of E_{int} is susceptible to the basis set superposition error (BSSE). This is because MOs are linear combinations of AOs and, when the energy of the whole complex is computed, the monomers 'borrow' functions from each other, leading to an expansion of their basis set. This problem can be addressed by applying the Boys-Bernardi counterpoise correction, i.e., by using 'ghost' functions (empty basis functions of another monomer) in the computations of monomer energies [244].

2.2.5 Relativistic effects

Relativistic effects strongly affect the physical and chemical properties of heavy, multi-electron atoms, such as the transition metals, lanthanides, and actinides. Rigorous treatment of relativistic effects requires solving the Dirac-Coulomb equation, which is not a standard practice in routine quantum chemistry calculations due to its four-component nature and computational demands. Instead, various approximations and methods like the Breit-Pauli approximation, Douglas-Kroll-Hess (DKH) method, effective core pseudopotentials (ECPs), and different levels of relativistic corrections within the established techniques have been implemented to incorporate relativistic effects into quantum chemical calculations [245; 246].

The Dirac Hamiltonian for an electron moving in an external potential V reads [245]:

$$H_{\mathrm{D}} = c\boldsymbol{\alpha}\cdot\boldsymbol{\pi} + c^2\beta + V = \begin{pmatrix} V + c^2 & c\boldsymbol{\sigma}\cdot\boldsymbol{\pi} \\ c\boldsymbol{\sigma}\cdot\boldsymbol{\pi} & V - c^2 \end{pmatrix}\,, \tag{2.57}$$

where c is the speed of light (≈ 137 in Hartree units), $\boldsymbol{\alpha}$ and β are the standard symbols for the 4x4 Dirac matrices, $\boldsymbol{\sigma} = [\mathbb{1}, \sigma_x, \sigma_y, \sigma_z]$ denotes a vector of Pauli matrices, and $\boldsymbol{\pi} = \boldsymbol{p} + \boldsymbol{A}$ with the electron momentum $\boldsymbol{p} = -i\boldsymbol{\nabla}$ and vector potential $\boldsymbol{A}$. The above equation is a one-electron equation and needs to be augmented to treat many-electron systems. For example, the Dirac-Coulomb-Breit Hamiltonian (or the Breit-Pauli Hamiltonian) allows to treat systems of two or more electrons.

Breit-Pauli approximation

The Breit-Pauli approximation is a non-relativistic approximation to the Dirac equation. It assumes that the energy scales associated with relativistic effects are much smaller than the typical energy differences between atomic or molecular states, which allows to treat relativistic effects as perturbations to the non-relativistic Hamiltonian. The dominant relativistic corrections in heavier many-electron systems are the mass-velocity term, the Darwin term, and the spin-orbit (SO) coupling term. Within the Breit-Pauli approximation, the modified Schrödinger equation reads [246]:

$$(H_0 + H_{\mathrm{MV}} + H_{\mathrm{Darwin}} + H_{\mathrm{SO}})\Psi = E\Psi\,, \tag{2.58}$$

where $H_0 = T + V$ is the non-relativistic Hamiltonian, and the consecutive operators describe the scalar relativistic effects (H_{MV} is the mass-velocity term and H_{Darwin} is the Darwin term) and the spin-orbit coupling (H_{SO}):

$$H_{\mathrm{MV}} = -\frac{p^4}{8c^2}\,, \tag{2.59}$$

$$H_{\text{Darwin}} = -\frac{p^2 V}{8c^2}\,, \tag{2.60}$$

$$H_{\text{SO}} = \frac{i\boldsymbol{\sigma}(\boldsymbol{p}V)\times\boldsymbol{p}}{4c^2}\,. \tag{2.61}$$

The mass-velocity correction describes the overall increase in the effective mass of an electron moving at high speeds due to special relativity. The Darwin correction arises from the interaction between the electron's charge distribution and the rapidly changing electric field of the nucleus caused by its motion (*Zitterbewegung*).

The magnetic field generated by the electron's motion about the nucleus becomes velocity-dependent due to special relativity and interacts with the electron's spin. This interaction couples the electron's spin angular momentum with its orbital angular momentum, giving rise to the SO coupling. It leads to the energy level splittings between states that have different total angular momenta and the emergence of fine structure effects in atomic and molecular spectra, particularly for heavy elements – the strength of the SO coupling strongly depends on the nuclear charge ($\sim Z^4$). In molecules, SO coupling introduces interactions between the electronic states of different multiplicities, which has implications for optical properties of the molecules, e.g., by opening avoided crossings.

Douglas-Kroll-Hess method

The idea behind the DKH method is to define a unitary operator that removes the off-diagonal blocks of the Dirac Hamiltonian (2.57) and splits the Dirac equation into large and small components, H_+ and H_- [247; 248]:

$$H_{\text{DKH}} = U H_{\text{D}} U^\dagger = \begin{pmatrix} H_+ & 0 \\ 0 & H_- \end{pmatrix}\,, \tag{2.62}$$

where the upper and lower blocks correspond to the positive and negative energy branches of the full Dirac spectrum, respectively. Since the negative energy branch is not of interest for chemistry, it can be discarded. Hence, the upper block will define the equation for the two-component DKH wave function, Ψ_{DKH}:

$$H_+ \Psi_{\text{DKH}} = E \Psi_{\text{DKH}}\,. \tag{2.63}$$

Finding the unitary matrix that allows for such transformation is no less complicated than solving the Dirac equation itself. Therefore, in practice, the decoupling is done up to a certain level of precision. As proposed by Douglass and Kroll [247], the unitary operator can be decomposed into a sequence of simpler transformations:

$$U = ...U_2 U_1 U_0\,, \tag{2.64}$$

where U_0 is the transformation that decouples the free-particle Dirac equation:

$$U_0 = A_p(1+\beta R_p) = \begin{pmatrix} A_p & A_p R_p \\ -A_p R_p & A_p \end{pmatrix} \tag{2.65}$$

with

$$A_p = \sqrt{\frac{E_p + c^2}{2E_p}} \tag{2.66}$$

and

$$R_p = \frac{c\boldsymbol{\sigma}\cdot\boldsymbol{p}}{E_p + c^2} = \boldsymbol{\sigma}\boldsymbol{P}_p\,, \tag{2.67}$$

where $E_p = \sqrt{c^4 + p^2c^2}$. The first-order DKH Hamiltonian thus reads:

$$H_{\text{DKH1}} = U_0 H_{\text{D}} U_0^\dagger = E_p + A_p[V + \boldsymbol{\sigma}\boldsymbol{P}_p V \boldsymbol{\sigma}\boldsymbol{P}_p]A_p\,, \tag{2.68}$$

where the potential energy operator is transformed into momentum space, $V \equiv V(\boldsymbol{p}, \boldsymbol{p})$. The additional decoupling transformations U_i, required in the presence of an external potential, take the form:

$$U_i = \sqrt{1 + W_i^2} + W_i \,, \tag{2.69}$$

where W_i is an anti-Hermitian operator of the i-th order in the external potential operator $V^{(i)}$; the form of W_i has been discussed by Heß and coworkers [249; 250]. For example, the standard expression for the W_1 operator is given by:

$$W_1 = \frac{A_p R_p V(\boldsymbol{p}, \boldsymbol{p}') A_{p'} - A_p V(\boldsymbol{p}, \boldsymbol{p}') R_{p'} A_{p'}}{E_p + E_{p'}} \,, \tag{2.70}$$

yielding the second-order DKH Hamiltonian:

$$H_{\mathrm{DKH2}} = H_{\mathrm{DKH1}} + \frac{1}{2}\{W_1, \{W_1, E_p\}\} \,, \tag{2.71}$$

where $\{a, b\}$ denotes the anticommutator of operators a and b.

Effective Core Potentials

The frozen core approximation and effective core potentials are another way to include relativistic effects in the non-relativistic framework. In the frozen core approximation, it is assumed that the core electrons' contribution to the total electron correlation energy is constant, whereas ECPs reproduce the behavior of chemically inert core electrons with a simplified pseudopotentials and treat only the outermost electrons explicitly. What justifies this approach is the fact the chemical bonding arises from the reorganization of the highest-lying orbitals while the core orbitals in heavy elements remain hardly affected. ECPs allow to restrict the computations to a smaller number of electrons while maintaining the accuracy comparable to all-electron calculations. The effective core potentials can incorporate not only the effects of the core electrons, but also the relativistic effects, such as the mass-velocity and Darwin effects into the potential [251].

2.3 Description of ultracold collisions

2.3.1 Basics of quantum scattering

Let us first consider the collision of two isotropic particles whose interaction is governed by the isotropic potential $V(r)$. We are solving the Schrödinger equation describing their relative motion:

$$\left(-\frac{1}{2\mu}\boldsymbol{\nabla}_{\boldsymbol{r}}^2 + V(r)\right)\psi(\boldsymbol{r}) = E\psi(\boldsymbol{r}). \tag{2.72}$$

Since the potential is isotropic, there is no coupling between the partial waves, and $\psi(\boldsymbol{r})$ can be decomposed into a sum over products of radial functions $R_l(r)$ and spherical harmonics $Y_l^m(\theta, \varphi)$:

$$\psi(\boldsymbol{r}) = \sum_{l,m} \frac{R_l(r)}{r} Y_l^m(\theta, \varphi) \,, \tag{2.73}$$

where l is the relative angular momentum with its projection m onto a space-fixed z-axis. Now we consider only the radial part of Eq. (2.72):

$$\left(-\frac{1}{2\mu}\frac{\mathrm{d}^2}{\mathrm{d}r^2} + \frac{l(l+1)}{2\mu r^2} + V(r)\right) R_l(r) = E R_l(r) \,, \tag{2.74}$$

where the second term corresponds to the centrifugal barrier, which is repulsive for $l > 0$ and vanishes for the s-wave. The equation (2.74) has a spectrum of N_l bound states with discrete energies E_l for $E < 0$, and a continuous spectrum of scattering states with $E > 0$.

Consider now the case when $r \to \infty$ and $V(r \to \infty) \to 0$. We can now neglect the two latter terms of Eq. (2.74). The particles are then described by a plane wave with relative kinetic energy $E = k^2/2\mu$ and relative momentum $\boldsymbol{k}$. The first term of of Eq. (2.74) yields $\frac{\mathrm{d}^2 R}{\mathrm{d}r^2} = -k^2 R(r)$, leading us to the asymptotic solution expressed in terms of spherical Bessel and Neumann functions, $j_l(kr)$ and $n_l(kr)$, respectively:

$$\lim_{r\to\infty} R_l(r) \to kr\left(A_l j_l(kr) + B_l n_l(kr)\right) \tag{2.75}$$

with

$$\lim_{r\to\infty} j_l(kr) \to \frac{\sin\left(kr - \frac{l\pi}{2}\right)}{kr} \tag{2.76}$$

and

$$\lim_{r\to\infty} n_l(kr) \to -\frac{\cos\left(kr - \frac{l\pi}{2}\right)}{kr}\,, \tag{2.77}$$

where A_l and B_l are l-dependent normalization constants that we obtain by imposing another boundary condition, $R_l(0) = 0$, i.e., the wave function vanishes at the origin. By inserting (2.76) and (2.77) into Eq. (2.75), we can obtain the normalized radial wave function in the long-range limit:

$$\lim_{r\to\infty} R_l(r) \to \sqrt{\frac{2\mu}{\pi k}}\left(\sin\left(kr - \frac{l\pi}{2}\right) + K_l \cos\left(kr - \frac{l\pi}{2}\right)\right)\,, \tag{2.78}$$

where K_l is the K-matrix defined as:

$$K_l = -\tan\delta_l(k) \tag{2.79}$$

with δ_l denoting the phase shift, which gives all the information about the scattering process, defined as:

$$\delta_l = \arctan\left(-\frac{B_l}{A_l}\right)\,. \tag{2.80}$$

Another important quantity in the scattering problems is the S-matrix, which is related to the phase shift δ_l and K-matrix in the following way:

$$S_l = e^{2i\delta_l} = \frac{1 + iK_l}{1 - iK_l}\,. \tag{2.81}$$

We can now also introduce the scattering amplitude $f(k,\theta)$:

$$f(k,\theta) = \frac{1}{2ik}\sum_l (2l+1)(e^{i\delta_l} - 1)P_l(\cos\theta)\,, \tag{2.82}$$

with $P_l(\cos\theta)$ denoting the Legendre polynomials, and the scattering cross section $\sigma(k)$:

$$\sigma(k) = \sum_{l=0}^{\infty} \sigma_l(k) \tag{2.83}$$

with

$$\sigma_l(k) = \frac{4\pi}{k^2}(2l+1)\sin^2\delta_l(k) = \frac{4\pi}{k^2}(2l+1)|1 - S_l|^2\,. \tag{2.84}$$

In the low energy regime, when the relative energy of the incident particle is much lower than the centrifugal barrier, we can assume that the scattering takes place in the lowest partial wave only, $l = 0$. As $k \to 0$, the scattering cross section yields:

$$\lim_{k\to\infty} \sigma_0(k) = 4\pi a^2\,, \tag{2.85}$$

where a denotes the s-wave scattering length, which is given by [252]:

$$a = -\lim_{k\to\infty} \frac{\tan\delta_0(k)}{k}\,. \tag{2.86}$$

2.3.2 Multichannel scattering theory

In a simple two-particle scattering scenario, there is typically just one channel, which represents the initial state of the particles and their final state after the scattering event. However, in more complex scenarios involving multiple degrees of freedom, there can be multiple possible final states that the particles can scatter into. Each of these will constitute a separate scattering channel.

In general, the atoms used in ultracold experiments have a spin structure. The Hamiltonian describing the nuclear motion of two atoms, A and B, possessing a hyperfine structure and colliding in an external magnetic field reads [253; 254]:

$$\hat{H} = -\frac{\hbar^2}{2\mu}\frac{1}{R}\frac{d^2}{dR^2}R + \frac{\hat{L}^2}{2\mu R^2} + \sum_{S,M_S} V_S(R)|S,M_S\rangle\langle S,M_S| + \hat{H}_A + \hat{H}_B + \hat{H}_{ss}\,, \tag{2.87}$$

where R denotes the internuclear distance, $\hat{L}$ – the rotational angular momentum operator, μ is the reduced mass of the system, $V_S(R)$ describes the Born-Oppenheimer potential energy curves for a state of a given total electronic spin S, and $|S,M_S\rangle\langle S,M_S|$ is the projection operator on the state with spin S and its projection M_S. The atomic Hamiltonians, $\hat{H}_j$ $(i = A, B)$, comprise the hyperfine and Zeeman interactions and are given by:

$$\hat{H}_j = a_j\hat{i}_j\cdot\hat{s}_j + \left(g_e\mu_{\mathrm{B}}\hat{s}_{j,z} + g_j\mu_{\mathrm{N}}\hat{i}_{j,z}\right)B_z\,, \tag{2.88}$$

where $\hat{s}_j$ and $\hat{i}_j$ denote the electronic and nuclear spin operators, a_j is the hyperfine coupling constant, B_z is the magnetic field strength, $g_{e/j}$ is the electron/nuclear g factor, and $\mu_{\mathrm{B/N}}$ is the Bohr/nuclear magneton, respectively. The last term of Eq. (2.87) describes the magnetic dipole-dipole interaction between the electronic spins:

$$\hat{H}_{ss} = \frac{\alpha^2}{R^3}\left(\hat{s}_A\cdot\hat{s}_B - 3\hat{s}_{A,z}\hat{s}_{B,z}\right)\,, \tag{2.89}$$

where α is the fine structure constant.

The total scattering wave function and Hamiltonian can be constructed in a in a fully uncoupled basis set:

$$|i_A,m_{i_A}\rangle|s_A,m_{s_A}\rangle|i_B,m_{i_B}\rangle|s_B,m_{s_B}\rangle|L,m_L\rangle\,, \tag{2.90}$$

where m_{x_j} is the projection of the angular momentum x_j on the space-fixed z-axis. The expansion includes all possible spin configurations for which the projection of the total angular momentum $M_{\mathrm{tot}} = m_{f_A} + m_{f_B} + m_L = m_{i_A} + m_{s_A} + m_{i_B} + m_{s_B} + m_L$ is conserved. The Hamiltonian is then transformed to the basis of atomic hyperfine eigenstates, which is asymptotically diagonal. The coupled-channels equations can be solved using a renormalized Numerov propagator as described in Ref. [255]: the wave function ratio Ψ_{i+1}/Ψ_i at the i-th grid step is propagated starting from short interatomic distances within the classically forbidden region, where the amplitude of the scattering wave function is negligible, to large interatomic separations, where the electronic and dipole-dipole interaction potentials become insignificant in comparison to the collision energy.

Subsequently, the K and S matrices are extracted by imposing the long-range scattering boundary conditions in terms of Bessel functions, and the scattering lengths are obtained using the S-matrices as described in the previous section.

2.3.3 Physics of Feshbach resonances

The notion of a Feshbach resonance has already been introduced in Sec. 1.3.1. The aim of this section is to outline the elementary properties of FRs. For a comprehensive analysis we refer the Reader to, e.g., Refs. [74; 80].

The basic idea behind a FR can be explained using Fig. 1.3 presented in Sec. 1.3.1. We are limiting our analysis to the case of magnetically tuned Feshbach resonances, although optically induced FRs are also possible [74]. Consider two molecular potential energy curves, $V_{bg}(R)$ and $V_c(R)$, where the former refers to the background potential that asymptotically connects to two free atoms in an ultracold gas, whereas the latter represents the closed (energetically inaccessible) channel. In the collision process, the background potential $V_{bg}(R)$ represents an energetically accessible pathway for two atoms colliding at a small energy E, therefore is referred to as the entrance channel. The closed channel can support bound molecular states close to the dissociation threshold of the open channel. A FR occurs when the bound molecular state in the closed channel energetically approaches the scattering state when varying the magnetic field. The energy difference between the two states can be tuned by means of the Zeeman effect, provided that the magnetic moments of the separated atoms and the molecular bound state differ (for future reference, let us denote this difference as $\delta\mu$).

The coupled two-channel Hamiltonian describing the relative motion of two colliding atoms can be represented by a 2x2 matrix:

$$H_{\mathrm{2B}} = \begin{pmatrix} -\frac{\hbar^2}{2\mu}\boldsymbol{\nabla}^2 + V_{bg}(R) & W(R) \\ W(R) & -\frac{\hbar^2}{2\mu}\boldsymbol{\nabla}^2 + V_c(R,B) \end{pmatrix}, \tag{2.91}$$

where the off-diagonal potential $W(R)$ describes the spin-exchange or dipole-dipole interaction that is responsible for the interchannel coupling. We assume that the zero of energy is shifted to the energy E of the dissociated atoms for all values of the magnetic field. In the absence of coupling, the eigenstates of a two-channel Hamiltonian are given by diabatic states $(\psi_{1,j}, 0)$ and $(0, \psi_{2,j})$, where $\psi_{i,j}$ denotes the eigenstates of the Hamiltonian for channel i. The coupling results in mixing between these states. As a consequence, the H_{2B} eigenstates will have components from each channel, and therefore will be referred to as dressed (or adiabatic) states.

Fig. 1.3 (2b) shows the behavior of the weakly-bound molecular state energy in the vicinity of a FR. Close to the resonance position B_0, the open and closed channels are strongly coupled, and the scattering length a is large and positive (at B_0 the scattering length diverges). In this case, there exists a dressed molecular state with binding energy:

$$E_b = \frac{1}{2\mu a^2}, \tag{2.92}$$

where E_b depends quadratically on the magnetic detuning, $B - B_0$. Since the molecular state is weakly bound, it can spontaneously dissociate back into a pair of unbound atoms as a result of resonant couplings to the two-atom scattering states. The decay rate of the molecules is determined from the Fermi's golden rule [256]:

$$\Gamma(E_b) = 2|\delta\mu\Delta|\sqrt{m a_{bg}^2 E_b}, \tag{2.93}$$

where Δ denotes the width of a resonance, which is related to the strength of the coupling between the bound and scattering states, a_{bg} is the background scattering associated with $V_{bg}(R)$, and m denotes the atomic mass. Far from the resonance, the energy of the bare molecular state varies linearly with B, with a slope determined by the difference in magnetic moments of the open and closed channels, $\delta\mu$.

Magnetically tunable FRs allow to control the sign and magnitude of the scattering length a according to the expression [257]:

$$a(B) = a_{bg}\left(1 - \frac{\Delta}{B - B_0}\right). \tag{2.94}$$

This functional form can be numerically fitted to the calculated scattering lengths in the vicinity of resonance poles in order to characterize FRs in a given system.

2.4 Long-range interactions between ultracold atoms

2.4.1 Definition of the long range

Whether an interaction is of long-range character depends on a system under consideration and the context of our study. For example, from the ultracold collisions point of view, a long-range interaction is one that can be *felt* beyond the centrifugal barrier. In the absence of DDIs, ground-state neutral atoms interact via short-range vdW interactions with the leading term $\propto 1/R^6$. In contrast, the DDIs have a long-range behavior, decaying as $1/R^3$, and can be either attractive or repulsive depending on the relative orientation of the dipoles.

At low collision energies, the centrifugal barrier $\frac{l(l+1)}{2\mu R^2}$ (see Eq. (2.74)) prevents the atoms from interacting in higher ($l > 0$) partial waves. For a power-law potential decaying as $1/R^n$, the scattering phase shift $\delta_l(k) \propto k^{2l+1}$ for $l < \frac{n-3}{2}$ and $\delta_l(k) \propto k^{n-2}$ otherwise [196]. Therefore, for $n < 4$, all partial waves contribute to the scattering process and the interaction is of long-range character, whereas for $n \geq 4$, the interaction is purely s-wave and short-ranged.

For the remainder of this section, rather than using the long-range definition from the perspective of ultracold collisions, we will define the long range as a distance at which the overlap between atomic electron clouds is negligible.

2.4.2 Perturbative calculation of long-range interactions

Consider two distant electrostatic potential distributions A and B whose centers of mass are separated by distance R. In the body-fixed frame and using spherical coordinates, the multipolar expansion of the interaction energy for the two distributions can be written as [258]:

$$V_{\mathrm{AB}}(R) = \sum_{l_A,l_B=0}^{+\infty} \sum_{m=-l_<}^{+l_<} \frac{f_{l_A l_B m}}{R^{1+l_A+l_B}} Q_{l_A,m}(A) Q_{l_B,-m}(B)\,, \tag{2.95}$$

where l_A and l_B describe the tensor rank related to the multipole moments $Q_{l_A,m}(A)$ and $Q_{l_B,-m}(B)$ of the charge distributions A and B, respectively, and $-l_< \leq m \leq l_<$, where $l_< = \min(l_A, l_B)$. The multipole moments are defined in the following way:

$$Q_{l_A,m}(A) = \sqrt{\frac{4\pi}{2l_A+1}} \sum_{i\in A} q_i r_i^{l_A} Y_l^{m_A}(\theta_i, \varphi_i)\,, \tag{2.96}$$

where r_i denotes the position of the i-th charge q_i. The number factor $f_{l_A l_B m}$ is given by:

$$f_{l_A l_B m} = (-1)^{l_B} \sqrt{\frac{(2l_A+2l_B)!}{(2l_A)!(2l_B)!}} C^{l_A+l_B,0}_{l_A m l_B -m} \tag{2.97}$$

with $C^{a\alpha}_{b\beta c\gamma}$ denoting a Clebsch-Gordan coefficient.

Let A and B be two distant atoms characterized by total angular momenta J_A and J_B with their projections on the quantization axis M_A and M_B, respectively. We use the uncoupled basis set of $|\beta_A J_A M_A \beta_B J_B M_B A\rangle$ to derive the matrix elements describing their interaction, where β denotes all remaining quantum numbers describing the state of a given atom. Since atoms are electrically neutral, there is no first-order correction resulting from their interaction. However, the charge distribution within the atomic electron clouds undergoes fluctuations, causing the atoms to acquire momentary multipole moments. These multipole moments can then interact, effectively causing the atoms to attract each other. The matrix element describing the second-

order energy correction arising from this interaction reads:

$$\langle \beta_A J_A M'_A \beta_B J_B M'_B | V_{\rm AB}^{(2)} | \beta_A J_A M_A \beta_B J_B M_B \rangle = - \sum_{l_A l_B l'_A l'_B} \frac{(-1)^{l_B+l'_B+2J_A+2J_B}}{R^{2+l_A+l_B+l'_A+l'_B}}$$
$$\times \sqrt{\frac{(2l_A+2l_B+1)!(2l'_A+2l'_B+1)!}{(2l_A)!(2l_B)!(2l'_A)!(2l'_B)!}} \sum_{k_A k_B k q} (-1)^{k_A+k_B}(2k_A+1)(2k_B+1)$$
$$\times C^{k0}_{l_A+l_B,0,l'_A+l'_B,0} C^{k0}_{k_A q k_B - q} \begin{Bmatrix} l'_B & l_B & k_B \\ l'_A & l_A & k_A \\ l'_A+l'_B & l_A+l_B & k \end{Bmatrix} \sum_{\beta''_A J''_A \beta''_B J''_B} \frac{C^{J_A M'_A}_{J_A M_A k_A q_A} C^{J_B M'_B}_{J_B M_B k_B q_B}}{\sqrt{(2J_A+1)(2J_B+1)}} \quad (2.98)$$
$$\times \frac{\langle \beta_A J_A || Q_{l_A} || \beta''_A J''_A \rangle \langle \beta''_A J''_A || Q_{l'_A} || \beta_A J_A \rangle \langle \beta_B J_B || Q_{l_B} || \beta''_B J''_B \rangle \langle \beta''_B J''_B || Q_{l'_B} || \beta_B J_B \rangle}{E_{\beta''_A J''_A} - E_{\beta_A J_A} + E_{\beta''_B J''_B} - E_{\beta_B J_B}}$$
$$\times \begin{Bmatrix} l'_A & l_A & k_A \\ J_A & J_A & J''_A \end{Bmatrix} \begin{Bmatrix} l'_B & l_B & k_B \\ J_B & J_B & J''_B \end{Bmatrix},$$

where $E_{\beta_{\{A,B\}} J_{\{A,B\}}}$ is the energy of level $|\beta_{\{A,B\}} J_{\{A,B\}}\rangle$, and $\langle \beta_{\{A,B\}} J_{\{A,B\}} || Q_{l_{\{A,B\}}} || \beta''_{\{A,B\}} J''_{\{A,B\}} \rangle$ is the reduced transition multipole moment between $|\beta_{\{A,B\}} J_{\{A,B\}}\rangle$ and $|\beta''_{\{A,B\}} J''_{\{A,B\}}\rangle$ levels, related to the transition multipole moment $\langle \beta_{\{A,B\}} J_{\{A,B\}} M_{\{A,B\}} | Q_{l_{\{A,B\}}} | \beta''_{\{A,B\}} J''_{\{A,B\}} M''_{\{A,B\}} \rangle$ through the Wigner-Eckart theorem:

$$\left\langle \beta' J' M' \right| Q_{lm} \left| \beta J M \right\rangle = \frac{C^{J'M'}_{JMlm}}{\sqrt{2J'+1}} \langle \beta' J' || Q_l || \beta J \rangle \,. \quad (2.99)$$

The selection rules impose that $M_A + M_B = M'_A + M'_B$. The pairs $(k_A,\, k_B)$ and the value of k are constrained by the values of $(l_A,\, l'_A,\, l_B,\, l'_B)$ and define the possible ranks of the tensorial terms; q_A, q_B, and q are limited by the values of k_A, k_B, and k [258]. The first curly brackets contain a Wigner $9j$ symbol, whereas the latter two contain a Wigner $6j$ symbol.

The leading term of Eq. (2.98) describes the induced-dipole–induced-dipole interaction ($l_A = l_B = l'_A = l'_B = 1$) and decays as $1/R^6$. By writing the energy correction as $-C_6/R^6$, we can extract the leading van der Waals coefficient C_6:

$$C_6 = 30(-1)^{2J_A+2J_B} \sum_{k_A k_B k q} (-1)^{k_A+k_B}(2k_A+1)(2k_B+1) C^{k0}_{2020} C^{k0}_{k_A q k_B - q}$$
$$\times \begin{Bmatrix} 1 & 1 & k_B \\ 1 & 1 & k_A \\ 2 & 2 & k \end{Bmatrix} \sum_{\beta''_A J''_A \beta''_B J''_B} \frac{C^{J_A M'_A}_{J_A M_A k_A q_A} C^{J_B M'_B}_{J_B M_B k_B q_B}}{\sqrt{(2J_A+1)(2J_B+1)}} \begin{Bmatrix} 1 & 1 & k_A \\ J_A & J_A & J''_A \end{Bmatrix} \begin{Bmatrix} 1 & 1 & k_B \\ J_B & J_B & J''_B \end{Bmatrix} \quad (2.100)$$
$$\times \frac{\langle \beta_A J_A || Q_{l_A} || \beta''_A J''_A \rangle \langle \beta''_A J''_A || Q_{l'_A} || \beta_A J_A \rangle \langle \beta_B J_B || Q_{l_B} || \beta''_B J''_B \rangle \langle \beta''_B J''_B || Q_{l'_B} || \beta_B J_B \rangle}{E_{\beta''_A J''_A} - E_{\beta_A J_A} + E_{\beta''_B J''_B} - E_{\beta_B J_B}} \,.$$

A derivation for a particular case of an S-state atom possessing only electronic spin interacting with a non-S-state atom possessing both electronic spin and orbital angular momentum is presented in Paper IV.

If the charges within distributions A and B move along closed orbits, it can be shown that the magnetostatic force exerted by A on B derives from a potential energy [258]. Therefore, for distant charge distributions, the magnetic interaction can also be written in terms of a multipolar expansion similar to Eq. (2.95) by replacing $1/4\pi\epsilon_0$ (equal to 1 in atomic units) with $\mu_0/4\pi$ (equal to α^2 in atomic units). Hence, for two atoms A and B with respective spins $\boldsymbol{S}_A$ and $\boldsymbol{S}_B$, the magnetic DII is given by:

$$\hat{V}^{\rm mdd}_{AB} = \frac{\alpha^2}{R^3} \left(\boldsymbol{S}_A \cdot \boldsymbol{S}_B - 3(\boldsymbol{S}_A \cdot \hat{\boldsymbol{R}})(\boldsymbol{S}_B \cdot \hat{\boldsymbol{R}}) \right) \quad (2.101)$$

with $\hat{\boldsymbol{R}}$ denoting the unit vector: $\boldsymbol{R} = R\hat{\boldsymbol{R}}$.

Chapter 3

Main results of the thesis

The core of the present PhD work comprises a series of thematically linked publications and preprints:

[Paper I]: K. Zaremba-Kopczyk, P. Żuchowski, and M. Tomza, *Magnetically tunable Feshbach resonances in ultracold gases of europium atoms and mixtures of europium and alkali-metal atoms*, Phys. Rev. A 98, 032704 (2018), DOI: 10.1103/PhysRevA.98.032704.

[Paper II]: K. Zaremba-Kopczyk and M. Tomza, *Van der Waals molecules consisting of a zinc or cadmium atom interacting with an alkali-metal or alkaline-earth-metal atom*, Phys. Rev. A 104, 042816 (2021), DOI: 10.1103/PhysRevA.104.042816.

Paper III: K. Zaremba-Kopczyk, M. Gronowski, and M. Tomza, *Ultracold mixtures of Cr and Li atoms: theoretical prospects for controlled atomic collisions, LiCr molecule formation, and molecular precision measurements* (preprint).

Paper IV: K. Zaremba-Kopczyk, M. Tomza, and M. Lepers, *Van der Waals coefficients for interactions of dysprosium and erbium atoms with alkali-metal and alkaline-earth-metal atoms* (preprint).

3.1 Paper I: *Magnetically tunable Feshbach resonances in ultracold gases of europium atoms and mixtures of europium and alkali-metal atoms*

Paper I

"Magnetically tunable Feshbach resonances in ultracold gases of europium atoms and mixtures of europium and alkali-metal atoms"

Klaudia Zaremba-Kopczyk, Piotr S. Żuchowski, and Michał Tomza

Phys. Rev. A 98, 032704 (2018)

Commentary

Ultracold gases of europium atoms represent a promising system for experiments exploiting strong dipole-dipole interactions. In contrast to the ground-state of dysprosium or erbium used in current experiments on magnetic quantum gases, the ground-state of europium is an S-state. The large magnetic dipole moment of Eu atoms results solely from their large electron spin. Therefore, the use of europium could potentially allow for the realization of many-body phenomena, such as magnetic polaron or Efimov physics, that may be extremely difficult to realize with Dy and Er ultracold quantum gases (the dense and chaotic spectra of magnetic Feshbach resonances in ultracold collisions between those atoms significantly hinder the controllability of the atoms' internal degrees of freedom). Moreover, a BEC of europium atoms has been realized in the group of M. Kozuma just recently [34], paving the way for exploring the many-body physics in non-chaotic systems with strong DDIs.

For the above reasons, we investigated magnetically tunable Feshbach resonances between ultracold europium atoms and between europium and alkali-metal atoms using multichannel quantum scattering calculations. We analyzed the prospects for the control of scattering properties, observation of quantum chaotic behavior, and magnetoassociation into ultracold polar and paramagnetic molecules. In the work presented in [Paper I], the PhD Candidate: performed all numerical calculations for europium-containing ultracold gases, generated all numerical data presented in the article, participated in the results analysis and interpretation, and prepared all figures and tables presented in the article.

Magnetically tunable Feshbach resonances in ultracold gases of europium atoms and mixtures of europium and alkali-metal atoms

Klaudia Zaremba-Kopczyk,[1] Piotr S. Żuchowski,[2] and Michał Tomza[1,*]
[1]*Faculty of Physics, University of Warsaw, Pasteura 5, 02-093 Warsaw, Poland*
[2]*Faculty of Physics, Astronomy and Informatics, Nicolaus Copernicus University in Torun, Grudziadzka 5, 87-100 Toruń, Poland*

(Received 6 June 2018; published 14 September 2018)

We investigate magnetically tunable Feshbach resonances between ultracold europium atoms and between europium and alkali-metal atoms using multichannel quantum scattering calculations. For ultracold gases of europium atoms both homonuclear ^{153}Eu + ^{153}Eu and heteronuclear ^{151}Eu + ^{153}Eu systems are studied. Calculations for mixtures of europium and alkali-metal atoms are carried out for prototype systems of ^{153}Eu + ^{87}Rb and ^{153}Eu + ^{7}Li. We analyze the prospects for the control of scattering properties, observation of quantum chaotic behavior, and magnetoassociation into ultracold polar and paramagnetic molecules. We show that favorable resonances can be expected at experimentally feasible magnetic-field strengths below 1000 G for all investigated atomic combinations. For Eu atoms, a rich spectrum of resonances is expected as a result of the competition between relatively weak short-range spin-exchange and strong long-range magnetic dipole-dipole interactions, where the dipolar interaction induces measurable resonances. A high density of resonances is expected at magnetic-field strengths below 200 G without pronounced quantum chaos signatures. The present results may be useful for the realization and application of dipolar atomic and molecular quantum gases based on europium atoms in many-body physics.

DOI: 10.1103/PhysRevA.98.032704

I. INTRODUCTION

Magnetically tunable Feshbach resonances are a universal and useful tool to control collisional properties in ultracold quantum gases [1,2]. They have been essential for the realization of a plethora of ground-breaking experiments in quantum many-body physics [3,4]. Magnetic Feshbach resonances are expected between any open-shell atoms, but first applications involved ultracold alkali-metal atoms [5]. Nevertheless, they were also observed and employed in experiments with ultracold Cr atoms [6–10], and recently with ultracold Er and Dy atoms [11–17]. Moreover, they were measured in mixtures of Yb atoms in the metastable ^3P state with the ground-state Yb [18,19] or Li [20] atoms, and in a mixture of the ground-state closed-shell Sr and open-shell Rb atoms [21,22].

Ultracold gases of dipolar atoms are especially interesting because the rich physics of different quantum phases and spin models can be realized with them [23,24]. Therefore, atoms in complex electronic states with large both spin and orbital electronic angular momenta, such as Er and Dy, have been cooled down to low and ultralow temperatures. Tremendous successes have already been accomplished with these atoms, just to mention the observation of quantum chaos in ultracold collisions [25], Fermi surface deformation [26], self-bound quantum droplets [27], Rosensweig instability [28], and extended Bose-Hubbard models [29]. The spin dynamics of impurities in a bath of strongly magnetic atoms and magnetic polaron physics [30,31] wait for realization.

The first highly dipolar atoms obtained at ultralow temperatures were Cr ($^7S_3$), Dy ($^5I_8$), and Er ($^3H_6$); however, several other transition-metal or lanthanide atoms may potentially be used. For example, magneto-optical cooling and trapping of Tm ($^2F_{7/2}$) [32] and Ho ($^4I_{15/2}$) [33] were also realized. Another lanthanide candidate is Eu ($^8S_{7/2}$). The buffer-gas cooling and magnetic trapping of Eu atoms were demonstrated [34–36], and recently magneto-optical cooling and trapping of optically pumped metastable Eu ($^{10}D_{13/2}$) atoms were achieved [37]. Further cooling to the quantum degeneracy should not be more challenging than the already demonstrated production of ultracold gases of other lanthanide atoms with more complex electronic structure [11–14]. In contrast to Er and Dy atoms, ground-state Eu atoms do not have any electronic orbital angular momentum ($l = 0$), and their large magnetic dipole moment is solely related to the large electronic spin angular momentum ($s = 7/2$) of seven unpaired f-shell electrons. Eu atoms, thus, are more similar to Cr atoms than to other lanthanides. However, they possess 17% larger dipole moment than Cr, which combined with three times larger mass of Eu as compared to Cr will result in four times stronger dipole-dipole interactions in ultracold gases of Eu atoms as compared to Cr atoms, but four times weaker interactions as compared to Dy and Er atoms (the strength of the dipolar interaction is $a_{\mathrm{dd}} \sim d^2 m$, where d is the dipole moment and m is the mass of atoms [23]).

Heteronuclear molecules possessing a permanent electric dipole moment are another promising candidate for numerous applications, ranging from ultracold controlled chemistry to quantum computation and quantum simulation of many-body physics [38–40]. Heteronuclear molecules formed of atoms

*michal.tomza@fuw.edu.pl

with large magnetic dipole moments could possess large both magnetic and electric dipole moments useful for investigating the interplay between the electric and magnetic dipolar interactions and phases in ultracold gases. Therefore, the chromium–alkali-metal-atom molecules such as CrRb [41], chromium–closed-shell-atom molecules such as CrSr and CrYb [42], europium–alkali-metal-atom molecules such as EuK, EuRb, and EuCs [43], and erbium-lithium molecules ErLi [44] were theoretically investigated and shown to possess large both electric and magnetic dipole moments. Experimentally, the magnetoassociation into ultracold Er_2 dimers [45] and photoassociation into spin-polarized Cr_2 dimers [46] were demonstrated. Ultracold mixtures of Dy and K atoms [47] and Dy and Er atoms [48] were also obtained, opening the way for the formation of ultracold highly magnetic and polar molecules in nontrivial electronic states. The extraordinarily rich, dense, and chaotic spectra of magnetic Feshbach resonances for Dy and Er atoms [16,17,49] may, however, make the magnetoassociation into heteronuclear molecules and investigation of magnetic polaron or Efimov physics difficult. The use of ultracold Eu atoms may be a remedy.

Here we investigate magnetically tunable Feshbach resonances between ultracold europium atoms and between europium and alkali-metal atoms using multichannel quantum scattering calculations. We study both homonuclear ^{153}Eu + ^{153}Eu and heteronuclear ^{151}Eu + ^{153}Eu systems of europium atoms, and ^{153}Eu + ^{87}Rb and ^{153}Eu + ^{7}Li combinations as prototype systems of mixtures of europium and alkali-metal atoms. We show that resonances favorable for the control of scattering properties and magnetoassociation into ultracold polar and paramagnetic molecules can be expected at experimentally feasible magnetic-field strengths below 1000 G for all investigated atomic combinations. The density of s-wave resonances strongly depends on the projection of the total angular momentum on the magnetic field. For Eu atoms, the dipolar interaction induces measurable resonances, and a high density of resonances without pronounced quantum chaos signatures is expected at magnetic-field strengths below 200 G.

The plan of this paper is as follows. Section II describes the used theoretical methods. Section III presents and discusses the numerical results and physical implications of our findings. Section IV summarizes our paper and presents future possible applications and extensions.

II. COMPUTATIONAL DETAILS

Europium atoms in the electronic ground state have very large electronic spin angular momentum ($s = 7/2$), but they do not have any electronic orbital angular momentum ($l = 0$). This results in the $^8S_{7/2}$ term. Lithium and rubidium atoms, as all alkali-metal atoms, have simpler structures described by the $^2S_{1/2}$ term. Characteristics of all investigated atoms are collected in Table I, and atomic hyperfine energy levels as a function of the magnetic field are presented for ^{7}Li, ^{87}Rb, and ^{153}Eu in Fig. 1. Coupling of the electronic spin with the nuclear spin, which is $i = 5/2$ for both isotopes of Eu, results in a very rich hyperfine structure for these atoms. Interestingly, hyperfine coupling constants for Eu are small and negative. They are between one to two orders of magnitude smaller than for alkali-metal atoms; therefore, the regime dominated by the Zeeman interaction with the linear dependence of hyperfine energy levels on the magnetic field can be observed for Eu atoms at relatively small strengths of the magnetic field (cf. Fig. 1). A negative value of the hyperfine coupling constant means the inverse order of hyperfine levels; thus the hyperfine ground state of Eu atoms has angular momentum of $f = 6$.

TABLE I. Terms $^{2s+1}l_j$, electronic spins s, nuclear spins i, possible total angular momenta f, and hyperfine coupling constants $a_{\rm hf}$ for the investigated atoms.

Atom	$^{2s+1}l_j$	s	i	f	$a_{\rm hf}$ (MHz)
^{7}Li	$^2S_{1/2}$	1/2	3/2	1, 2	401.752 [50]
^{87}Rb	$^2S_{1/2}$	1/2	3/2	1, 2	3417.34 [50]
^{151}Eu	$^8S_{7/2}$	7/2	5/2	1, . . . , 6	−20.052 [51]
^{153}Eu	$^8S_{7/2}$	7/2	5/2	1, . . . , 6	−8.853 [51]

The Hamiltonian describing the nuclear motion of two colliding atoms, $A + B$, reads

$$\hat{H} = -\frac{\hbar^2}{2\mu}\frac{1}{R}\frac{d^2}{dR^2}R + \frac{\hat{L}^2}{2\mu R^2} + \sum_{S,M_S} V_S(R)|S, M_S\rangle\langle S, M_S| + \hat{H}_A + \hat{H}_B + \hat{H}_{ss}, \quad (1)$$

where R is the interatomic distance, $\hat{L}$ is the rotational angular momentum operator, μ is the reduced mass, $V_S(R)$ is the potential-energy curve for the state with the total electronic spin S, and $|S, M_S\rangle\langle S, M_S|$ is the projection operator on the states with the total electronic spin S and its projection M_S. The atomic Hamiltonians, $\hat{H}_j$ ($j = A, B$), including hyperfine and Zeeman interactions are given by

$$\hat{H}_j = a_j \hat{i}_j \cdot \hat{s}_j + (g_e \mu_B \hat{s}_{j,z} + g_j \mu_N \hat{i}_{j,z}) B_z, \quad (2)$$

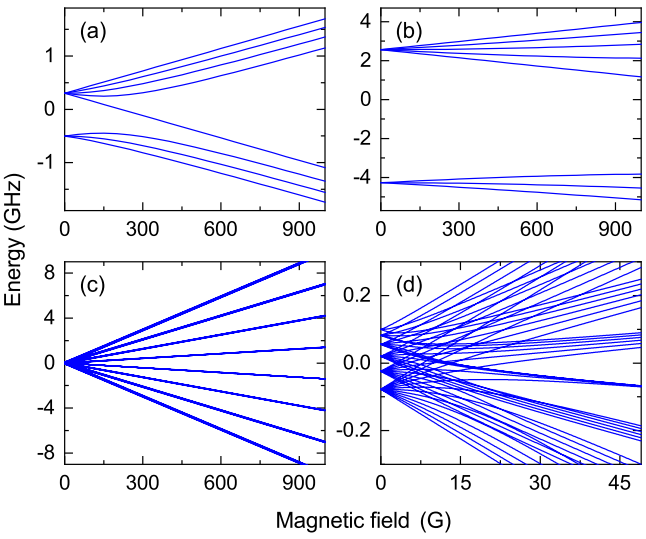

FIG. 1. Hyperfine energy levels for (a) ^{7}Li, (b) ^{87}Rb, and (c),(d) ^{153}Eu atoms as a function of the magnetic field. Panel (d) shows an enlarged part of panel (c) for the small magnetic field.

where $\hat{s}_j$ and $\hat{i}_j$ are the electronic and nuclear spin angular momentum operators, a_j is the hyperfine coupling constant, B_z is the magnetic-field strength, g_e and g_j are the electron and nuclear g factor, and μ_B and μ_N are the Bohr and nuclear magneton, respectively. For Eu atoms we neglect the hyperfine electric quadrupole coupling because it is much smaller than the leading hyperfine magnetic dipole coupling. The magnetic dipole-dipole interaction between electronic spins is

$$\hat{H}_{ss} = \frac{\alpha^2}{R^3}\left(\hat{s}_A \cdot \hat{s}_B - 3\hat{s}_{A,z}\hat{s}_{B,z}\right), \tag{3}$$

where α is the hyperfine coupling constant.

We perform *ab initio* quantum scattering calculations using the coupled-channel formalism as implemented in Refs. [53–55]. We construct the total scattering wave function and Hamiltonian in a fully uncoupled basis set,

$$\left|i_A, m_{i_A}\right\rangle\left|s_A, m_{s_A}\right\rangle\left|i_B, m_{i_B}\right\rangle\left|s_B, m_{s_B}\right\rangle|L, m_L\rangle, \tag{4}$$

where m_j is the projection of the angular momentum j on the space-fixed z axis, including all possible spin configurations, but assuming the projection of the total angular momentum $M_{\rm tot} = m_{f_A} + m_{f_B} + m_L = m_{i_A} + m_{s_A} + m_{i_B} + m_{s_B} + m_L$ to be conserved. Next, we transform the Hamiltonian to the basis of atomic hyperfine eigenstates, which is asymptotically diagonal. For homonuclear collisions of Eu atoms we impose properly the bosonic symmetry by transforming the wave function and Hamiltonian to the basis with well-defined total electronic spin S, nuclear spin I, and rotational L angular momenta, and restricting the Hilbert space to its bosonic sector [53,56]. We solve the coupled-channel equations using a renormalized Numerov propagator [57] with step-size doubling and about 100 step points per de Broglie wavelength. The wave function ratio Ψ_{i+1}/Ψ_i at the ith grid step is propagated from small finite interatomic separations in the classically forbidden region where the scattering wave-function amplitude is negligible to large interatomic separations where electronic and dipolar potentials are negligible as compared to the collision energy. Then the K and S matrices are extracted by imposing the long-range scattering boundary conditions in terms of Bessel functions. The scattering lengths are obtained from the S matrices for the lowest entrance channels $a_0 = (1 - S_{00})(1 + S_{00})/(ik)$, where $k = \sqrt{2\mu E/\hbar^2}$ and E is the collision energy. Feshbach resonances are characterized by their positions B_0, widths Δ, and background scattering lengths $a_{\rm bg}$, obtained by numerical fitting of the functional form $a(B) = a_{\rm bg}[1 - \Delta/(B - B_0)]$ to the calculated scattering lengths in the vicinity of resonance poles. All calculations are carried out for the collision energy of 100 nK.

Interaction between ^8S-state Eu and ^2S-state Li or Rb atoms results in two molecular electronic states of the $^7\Sigma^-$ and $^9\Sigma^-$ symmetries which have total electronic spin of $S = 3$ and 4, respectively. Interaction between two ^8S-state Eu atoms results in eight electronic states of the $^1\Sigma_g^+$, $^3\Sigma_u^+$, $^5\Sigma_g^+$, $^7\Sigma_u^+$, $^9\Sigma_g^+$, $^{11}\Sigma_u^+$, $^{13}\Sigma_g^+$, and $^{15}\Sigma_u^+$ symmetries with the total electronic spin S from zero to 7, respectively. The energy differences between molecular electronic states with different total electronic spin result from the exchange interaction.

For the Eu + Rb and Eu + Li systems we use potential-energy curves calculated in Ref. [43]. Analytical potential-energy functions $V_S(R)$ are fitted to *ab initio* data separately for $S = 3$ and 4 assuming the same long-range van der Waals coefficients C_6 reported in Ref. [43]. For Eu + Eu system we use potential-energy curves calculated in Ref. [52]. For this system, however, it was shown that the exchange interaction is small, and a family of potential-energy curves with different total electronic spin S can be reproduced assuming the Heisenberg spin-exchange model of the spin-exchange interaction between f-shell electrons of Eu atoms [52]. As a result, the potential-energy curves for the Eu + Eu system read

$$V_S(R) = V_{S=7}(R) + J(R)[56 - S(S+1)]/2, \tag{5}$$

where functions $V_{S=7}(R)$ and $J(R)$ were calculated using *ab initio* methods in Ref. [52], and here we fit an analytical formula to them.

Morse–long-range potential-energy functions [58] are used to represent $V_S(R)$. They are given by

$$V_S(R) = D_e\left[1 - \frac{u_{\rm LR}(R)}{u_{\rm LR}(R_e)}\exp[-\phi(R)y_p(R)]\right]^2 - D_e, \tag{6}$$

where D_e and r_e are the well depth and equilibrium distance of the interaction potential, respectively. The long-range part of the interaction potential is given by

$$u_{\rm LR}(R) = -\frac{C_6}{R^6}, \tag{7}$$

whereas other functions are of the form

$$\begin{aligned} y_p(R) &= \frac{R^p - R_e^p}{R^p + R_e^p}, \\ \phi(R) &= \varphi_\infty\, y_p(R) + (1 - y_p(R))\sum_{i=0}^{4}\varphi_i y_q^i(R), \end{aligned} \tag{8}$$

with $\varphi_\infty = \ln\left(\frac{2D_e}{u_{\rm LR}(R_e)}\right)$, $p = 4$, and $q = 4$. D_e, R_e, and C_6 are directly taken as reported in Refs. [43,52]. The free parameters in the potential-energy functions, φ_i ($i = 0$–4), are determined by numerical fitting to the *ab initio* points from Refs. [43,52]. The obtained parameter values are presented in Table II. The R-dependent spin coupling constant $J(R)$ of the underlying Heisenberg model for the Eu + Eu system can be accurately approximated by the function

$$J(R) = \alpha/\cosh[\beta(R - R_0)], \tag{9}$$

where $\alpha = -0.53915\ {\rm cm}^{-1}$, $\beta = 0.79223\ {\rm bohr}^{-1}$, and $R_0 = 7.8760$ bohr are obtained by numerical fitting to the *ab initio* points from Ref. [52]. Such a function has a proper, exponentially decaying with R, asymptotic behavior.

We set the scattering lengths a_S of the employed potential-energy curves by scaling them with appropriate factors λ, $V_S(R) \to \lambda V_S(R)$, taking values in the range of 0.97–1.03. We express the scattering lengths in the units of characteristic length scales of the van der Waals interaction, R_6, given by

$$R_6 = \left(\frac{2\mu C_6}{\hbar^2}\right)^{1/4}. \tag{10}$$

It takes values 84 bohr, 166 bohr, and 178 bohr for ^{153}Eu + ^{7}Li, ^{153}Eu + ^{87}Rb, and ^{153}Eu + ^{151}Eu, respectively. The corresponding characteristic energy scale is given by

TABLE II. Parameter values of the used Morse–long-range potential-energy functions fitted to *ab initio* data from Refs. [43,52]. D_e is in cm^{-1} and other parameters are in atomic units or are dimensionless.

	Eu + Li		Eu + Rb		Eu + Eu
Parameter	$V_{S=3}$	$V_{S=4}$	$V_{S=3}$	$V_{S=4}$	$V_{S=7}$
D_e	2971.0	2443.2	1239.1	1047.1	704.32
R_e	6.5561	6.7288	8.6393	8.7904	9.2919
φ_0	−1.1665	−0.96262	−0.80406	−0.75536	−0.78004
φ_1	0.24492	0.37826	−0.28015	−0.23809	−0.49552
φ_2	1.2024	0.49243	−0.71864	−0.66458	−0.28324
φ_3	−1.1880	−1.3791	−0.88769	−0.54075	0.36690
φ_4	−4.2923	−2.9548	−1.2472	−0.84187	−0.45423
C_6	2066	2066	3779	3779	3610

$E_6 = \hbar^2/(2\mu R_6^2)$, and is 1.8 mK, 56 μK, and 36 μK for the above mixtures.

III. NUMERICAL RESULTS AND DISCUSSION

Before we discuss the results for magnetically tunable Feshbach resonances, we will analyze the hyperfine structures of the investigated mixtures and their impact on the scattering properties. Figure 2 presents hyperfine energy levels for mixtures of ^{153}Eu + ^{7}Li, ^{153}Eu + ^{87}Rb, and ^{153}Eu + ^{151}Eu atoms with $M_{\rm tot} = 0$ as a function of the magnetic field. Black lines show atomic thresholds which are the result of combining the atomic hyperfine energy levels, presented in Fig. 1, summing to selected $M_{\rm tot}$. The colorful (gray scale) lines are the atomic thresholds shifted by the largest possible binding energies of the last three most weakly bound vibrational levels supported by the van der Waals potentials determined by the long-range coefficients C_6 [59]. These positions of molecular levels correspond to infinitely large and negative scattering lengths and true molecular binding energies must be equal to or smaller than them, and lie in such defined bins. The number of mixture's hyperfine energy levels is the largest for $M_{\rm tot} = 0$; therefore, the presented spectra correspond to the richest limiting cases, which are expected to be associated with the largest number of Feshbach resonances. Feshbach resonances can occur at crossings of molecular levels and atomic thresholds.

Interestingly, the most important energy scale for the ^{153}Eu + ^{7}Li system is associated with the vibrational spacing, which is large because of the small reduced mass. At the same time, the hyperfine coupling constants are small for both atoms. In this case, the positions and properties of Feshbach resonances will crucially depend on the background scattering lengths and related binding energies of vibrational levels. For the ^{153}Eu + ^{87}Rb system, the energy scales associated with the vibrational and hyperfine structures are of similar order of magnitude, and the spectrum of Feshbach resonances will be a result of the interplay of both energy scales. For the ^{153}Eu + ^{151}Eu system, the vibrational binding energies are small because of the large reduced mass, and thus the properties of Feshbach resonances will depend crucially on the hyperfine structure, even though the hyperfine coupling constants are small in this system. As a result, it is guaranteed that a large number and density of resonances can be expected

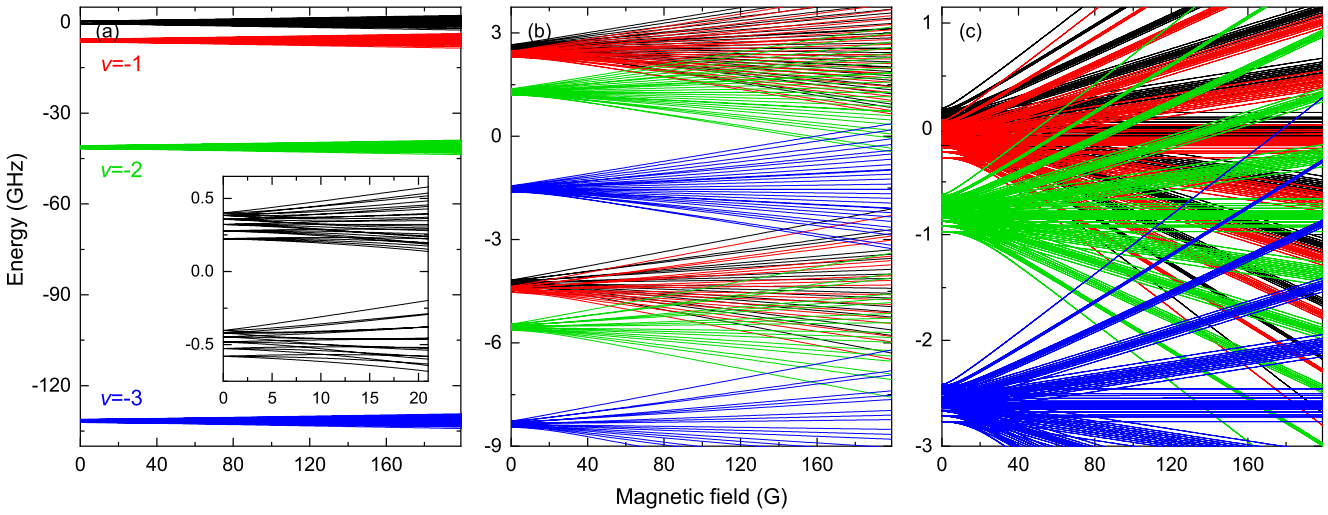

FIG. 2. Hyperfine energy levels for mixtures of (a) ^{153}Eu + ^{7}Li, (b) ^{153}Eu + ^{87}Rb, and (c) ^{153}Eu + ^{151}Eu atoms with $M_{\rm tot} = 0$ as a function of the magnetic field. Black lines show atomic thresholds, whereas colorful (gray scale) lines correspond to the progression of the last three most weakly bound vibrational molecular levels for infinitely large and negative scattering lengths.

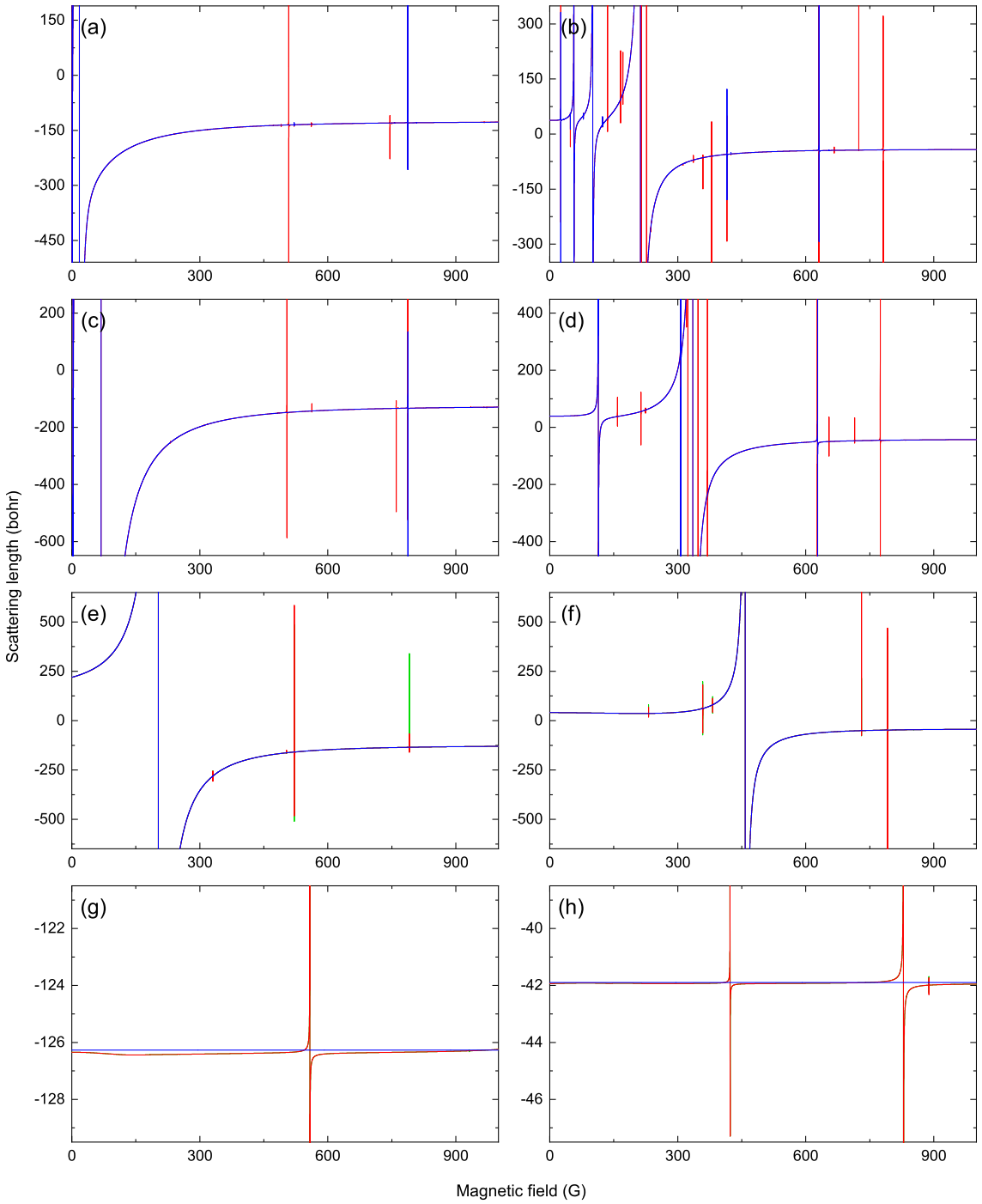

FIG. 3. Scattering lengths for ultracold collisions between ^{153}Eu and ^{7}Li atoms as a function of the magnetic field: (a),(b) for $M_{\rm tot} = 0$, (c),(d) for $M_{\rm tot} = -6$, (e),(f) for $M_{\rm tot} = -7$, and (g),(h) for $M_{\rm tot} = -8$. The following scattering lengths for the potential-energy functions are assumed: (a),(c),(e),(g) $a_{S=3} = 1.5R_6$ and $a_{S=4} = -1.5R_6$; (b),(d),(f),(h) $a_{S=3} = 0.5R_6$ and $a_{S=4} = -0.5R_6$. Blue (dark gray) lines show scattering lengths without the dipole-dipole interaction included and red (gray) and green (light gray) lines show scattering lengths with the dipole-dipole interaction included with $L_{\rm max} = 2$ and 4, respectively. Note different scales for different $M_{\rm tot}$.

at relatively weak magnetic-field strengths below 200 G. The hyperfine spectrum for the homonuclear ^{153}Eu + ^{153}Eu system, which is equivalent to the heteronuclear one restricted to the bosonic sector of the Hilbert space, will have roughly twice smaller number of atomic and molecular levels, but other characteristics will be the same as in the heteronuclear case.

The positions and widths of Feshbach resonances depend on the hyperfine structure, progression of weakly bound rovibrational levels just below atomic thresholds, and background scattering lengths, as discussed above. Unfortunately, even the most accurate potential-energy functions obtained in the most advanced *ab initio* electronic structure calculations do not allow one to predict accurately the scattering lengths

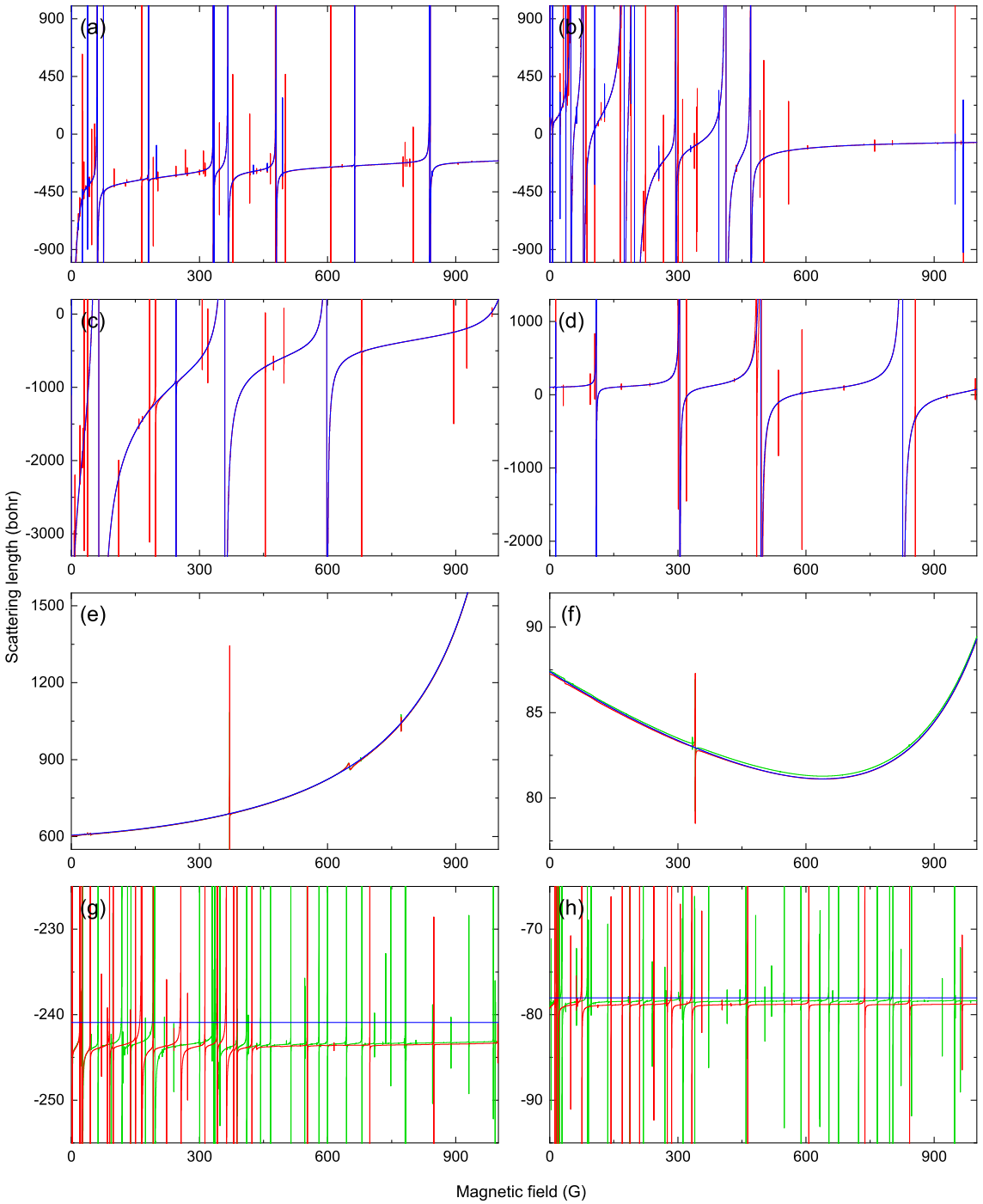

FIG. 4. Scattering lengths for ultracold collisions between ^{153}Eu and ^{87}Rb atoms as a function of the magnetic field: (a),(b) for $M_{\rm tot} = 0$, (c),(d) for $M_{\rm tot} = -6$, (e),(f) for $M_{\rm tot} = -7$, and (g),(h) for $M_{\rm tot} = -8$. The following scattering lengths for the potential-energy functions are assumed: (a),(c),(e),(g) $a_{S=3} = 1.5R_6$ and $a_{S=4} = -1.5R_6$; (b),(d),(f),(h) $a_{S=3} = 0.5R_6$ and $a_{S=4} = -0.5R_6$. Blue (dark gray) lines show scattering lengths without the dipole-dipole interaction included and red (gray) and green (light gray) lines show scattering lengths with the dipole-dipole interaction included with $L_{\rm max} = 2$ and 4, respectively. Note different scales for different $M_{\rm tot}$.

for collisions between many-electron atoms, except for the systems with small number of bound states [60]. Thus, at present, it is impossible to determine all parameters of Feshbach resonances without *a priori* experimental knowledge. Nevertheless, the general characteristics of Feshbach resonances, such as the density of resonances and typical widths, can be learned by tuning the scattering lengths around the values of the characteristic length scales of the underlying van der Waals interactions R_6. Therefore, we have calculated the spectra of magnetic Feshbach resonances for a large number of combinations of scattering lengths and present the most typical ones.

Figures 3–6 show s-wave scattering lengths for ultracold collisions in the ^{153}Eu + ^{7}Li, ^{153}Eu + ^{87}Rb, ^{153}Eu + ^{151}Eu,

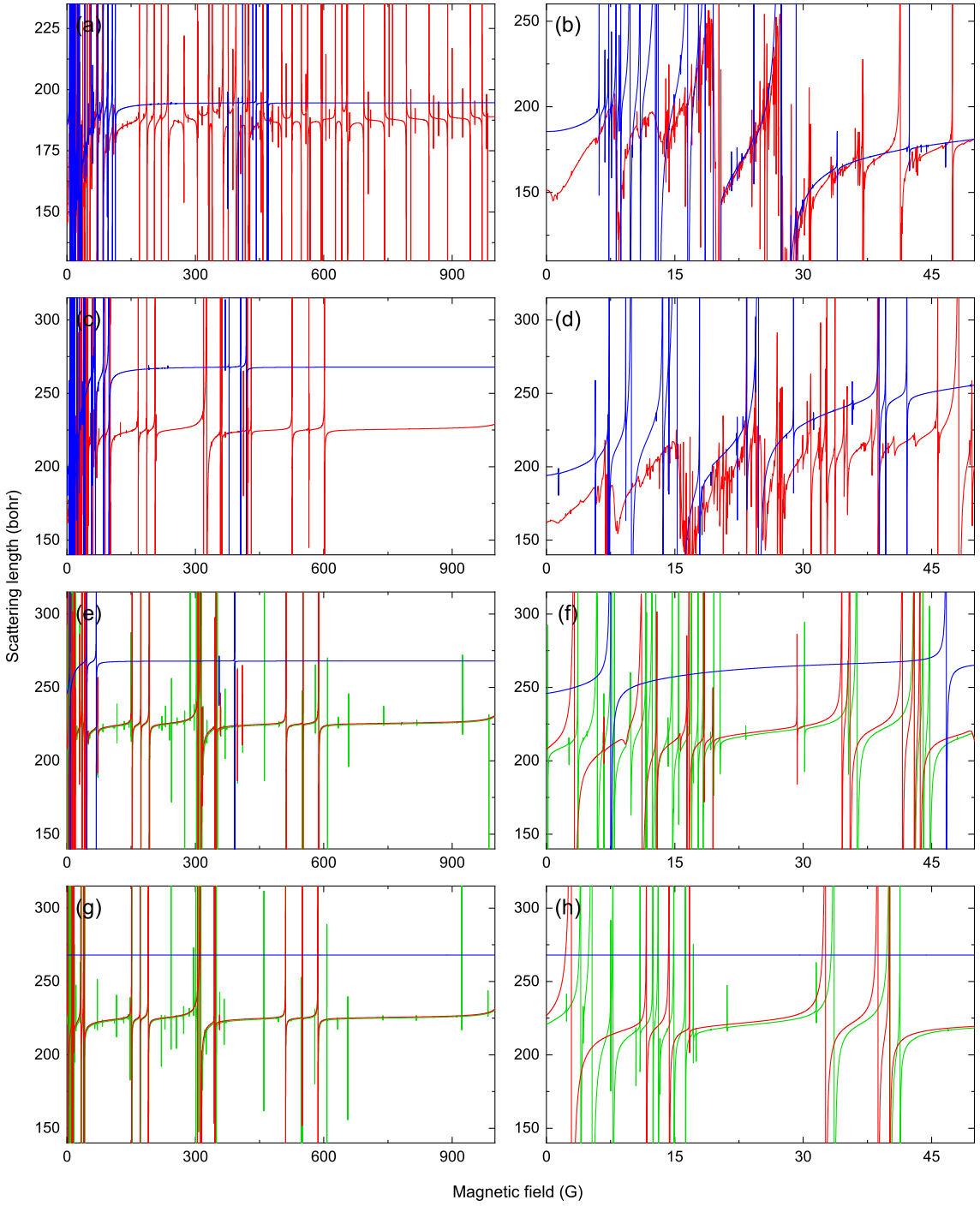

FIG. 5. Scattering lengths for ultracold collisions between ^{153}Eu and ^{151}Eu atoms as a function of the magnetic field: (a),(b) for $M_{\rm tot} = 0$, (c),(d) for $M_{\rm tot} = -5$, (e),(f) for $M_{\rm tot} = -11$, and (g),(h) for $M_{\rm tot} = -12$. Panels (b),(d),(f),(g) are zoomed versions of panels (a),(c),(e),(h). The scattering length of $a_{S=7} = 1.5R_6$ is assumed for spin-polarized collisions. Blue (dark gray) lines show scattering lengths without the dipole-dipole interaction included and red (gray) and green (light gray) lines show scattering lengths with the dipole-dipole interaction included with $L_{\rm max} = 2$ and 4, respectively.

and ^{153}Eu + ^{153}Eu systems as a function of the magnetic-field strength. Results are presented for several different projections of the total angular momentum on the magnetic field $M_{\rm tot}$, including collisions with $M_{\rm tot} = 0$, which correspond to the largest number of channels, and ones with maximal possible $|M_{\rm tot}|$ that correspond to maximally spin-stretched states, for which only resonances induced by the dipole-dipole interaction can occur. In all calculations the same step in the magnetic-field strength of 0.01 G is assumed; therefore, the prominence of the resonances can be related to their widths, which can be visually compared between different channels and systems. Different colors encode results without

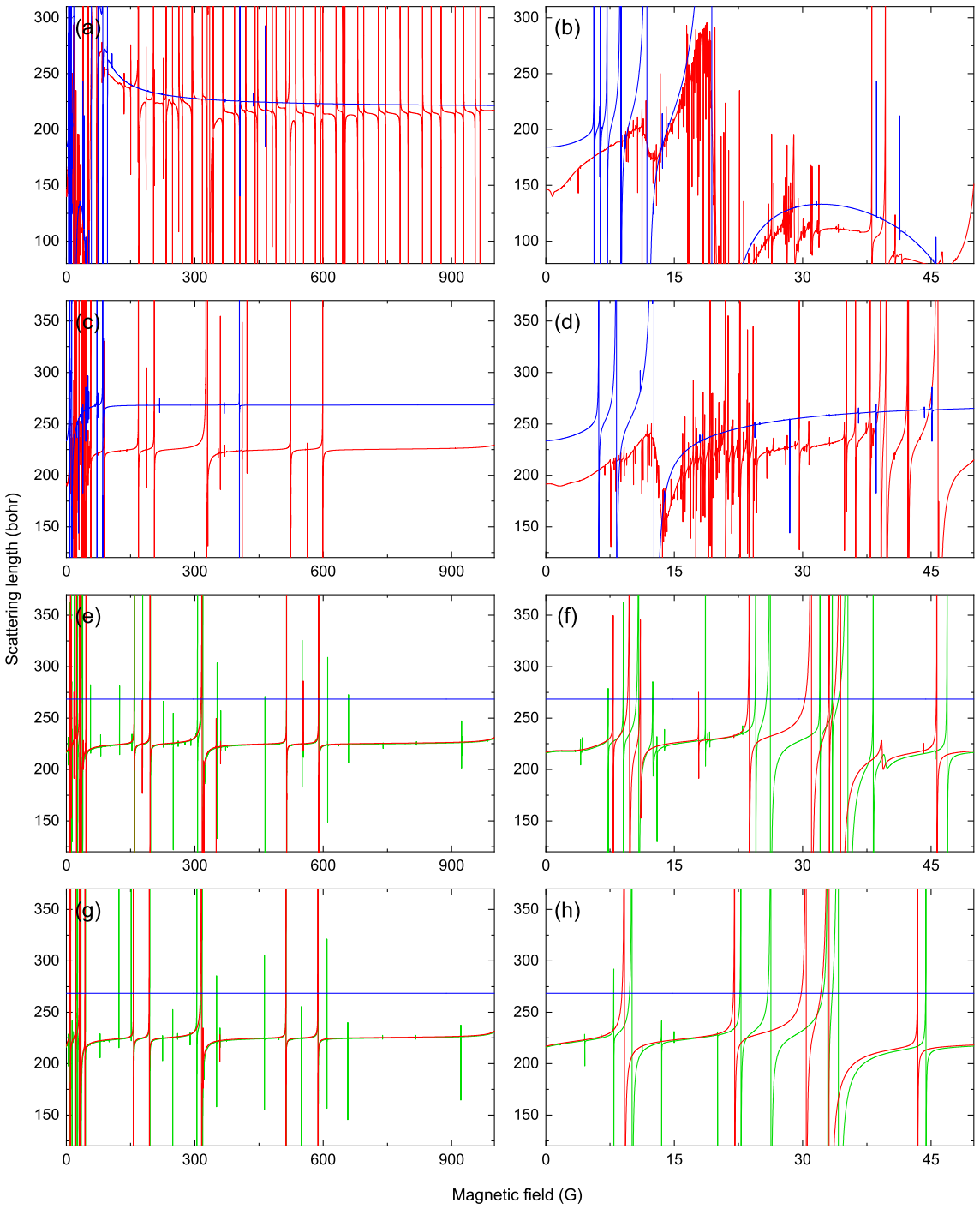

FIG. 6. Scattering lengths for ultracold collisions between ^{153}Eu atoms as a function of the magnetic field: (a),(b) for $M_{\rm tot} = 0$, (c),(d) for $M_{\rm tot} = -5$, (e),(f) for $M_{\rm tot} = -11$, and (g),(h) for $M_{\rm tot} = -12$; panels (b),(d),(f),(g) are zoomed versions of panels (a),(c),(e),(h). The scattering length of $a_{S=7} = 1.5R_6$ is assumed for spin-polarized collisions. Blue (dark gray) lines show scattering lengths without the dipole-dipole interaction included and red (gray) and green (light gray) lines show scattering lengths with the dipole-dipole interaction included with $L_{\rm max} = 2$ and 4, respectively.

the dipole-dipole interaction included, that are obtained by restricting the basis set given by Eq. (4) to $L_{\rm max} = 0$, and with the dipole-dipole interaction included when $L_{\rm max} = 2$ or 4. For $L_{\rm max} = 2$ d-wave resonances appear, and for $L_{\rm max} = 4$ additionally g-wave resonances emerge. These resonances are a result of coupling of the s-wave entrance channel with d-wave and g-wave bound molecular levels in closed channels. The coupling with d-wave bound levels is direct, whereas the coupling with g-wave bound levels is indirect via d-wave channels. Calculations including $L_{\rm max} = 4$ are presented only for channels with large $|M_{\rm tot}|$ for the clarity and because the g-wave resonances are at least an order of magnitude narrower

than the d-wave ones. At the same time, the number of channels increases fast with $L_{\max}$. For example, for $M_{\rm tot} = 0$ of the ^{153}Eu + ^{7}Li or ^{153}Eu + ^{87}Rb system the number of channels is 46, 258, and 582 for $L_{\max} = 0$, 2, and 4, respectively, whereas for $M_{\rm tot} = 0$ of the ^{153}Eu + ^{151}Eu system the number of channels is 218, 1252, and 2916 for $L_{\max} = 0$, 2, and 4, respectively.

The dipole-dipole interaction not only couples different partial waves but it also modifies the long-range character of the interatomic interaction potential in higher partial waves from $1/R^6$ to $1/R^3$ [61–63]. Thus, in the zero collision energy limit, not only s-wave scattering length but also d-wave one can have a finite value. We present only s-wave scattering lengths for brevity and because they are at least an order of magnitude larger than d-wave ones in the present case.

Figures 3 and 4 show s-wave scattering lengths for ultracold collisions in the ^{153}Eu + ^{7}Li and ^{153}Eu + ^{87}Rb systems as a function of the magnetic-field strength. Results are presented for two sets of scattering lengths: $a_{S=3} = 1.5R_6$ and $a_{S=4} = -1.5R_6$ and $a_{S=3} = 0.5R_6$ and $a_{S=4} = -0.5R_6$. The first set corresponds to rather large and favorable for broad resonances scattering lengths, whereas the second one corresponds to rather small and less favorable scattering lengths. As expected, the largest number of resonances is observed for collisions with $M_{\rm tot} = 0$, counting around 10 and 30 s-wave resonances, and 30 and 100 d-wave resonances below 1000 G for the ^{153}Eu + ^{7}Li and ^{153}Eu + ^{87}Rb mixtures, respectively. The number of resonances decreases with increasing $|M_{\rm tot}|$ and there are no s-wave resonances for fully spin-polarized collisions with $M_{\rm tot} = -8$ for which, however, higher wave resonances exist. Interestingly, for the spin-polarized ^{153}Eu + ^{87}Rb mixture, there are around 30 d-wave resonances and around 200 g-wave resonances below 1000 G. The broad s-wave Feshbach resonances have widths around 10–100 G for ^{153}Eu + ^{7}Li and around 1–10 G for ^{153}Eu + ^{87}Rb. The d-wave Feshbach resonances have widths around 10–100 mG and g-wave Feshbach resonances have widths below 10 mG for both systems. The s-wave resonances in mixtures of europium and alkali-metal atoms have a very similar nature to the resonances between alkali-metal atoms because the exchange-interaction-induced splitting between two electronic states is relatively large. At the same time, higher wave resonances are expected to be broader in the present case because the dipole-dipole interaction is seven times stronger between europium and alkali-metal atoms than between alkali-metal atoms.

Figures 5 and 6 show s-wave scattering lengths for ultracold collisions in the ^{153}Eu + ^{151}Eu and ^{153}Eu + ^{153}Eu systems as a function of the magnetic-field strength. The scattering length for the electronic potential-energy curve with the total electronic spin of $S = 7$, which governs the spin-polarized collisions, is set to $a_{S=7} = 1.5R_6$. There are around 100 s-wave and 200 d-wave Feshbach resonances below 1000 G for the collisions with $M_{\rm tot} = 0$, and this number slowly decreases with increasing $|M_{\rm tot}|$. At the same time, two-thirds of resonances are located below 200 G because of the small hyperfine coupling constants for Eu atoms [cf. Fig. 2(c)]. For small $|M_{\rm tot}|$, the spectra below 200 G are very dense with many overlapping resonances and the density of resonances approaches one per Gauss. The number of resonances for the homonuclear combination is smaller than for the heteronuclear mixture, but the reduction in the number of visible resonances is smaller than the reduction in the number of channels. The typical widths of both s-wave and d-wave resonances are between 10 mG and 100 mG, whereas the widths of g-wave resonances are below 10 mG for both homonuclear and heteronuclear collisions. The inclusion of g-wave channels noticeably moves positions of d-wave resonances at small magnetic-field strengths. Additionally, the dipole-dipole interaction visibly modifies the background scattering length (by up to around 20%). Interestingly, the widths of s-wave resonances induced by the relatively weak short-range spin-exchange interaction and the widths of d-wave resonances induced by the relatively strong long-range magnetic dipole-dipole interaction are of the same order of magnitude. In fact, the spin-exchange interaction between Eu atoms counts below 0.1% of the total electronic interaction energy at the equilibrium geometry and was classified as extremely weak as compared to typical energy scales of the exchange interaction in other molecular systems [52].

Due to its very small value and computational complexity, the spin-exchange interaction calculated for the Eu + Eu system [52] is the most uncertain parameter of our model. It was already shown that its actual value is crucial to determine correctly the Zeeman relaxation rates for collisions of magnetically trapped Eu atoms [36]. Therefore, we have also evaluated ultracold collisions between Eu atoms as a function of the magnetic-field strength for several values of the scaling parameter λ_J, where linear scaling of the spin-exchange interaction $J(R) \to \lambda_J J(R)$ was assumed. An exemplary dependence of the scattering lengths for ultracold collisions between ^{153}Eu and ^{151}Eu atoms with $M_{\rm tot} = 0$ at the magnetic-field strength of $B = 50$ G on the scaling parameter λ_J is presented in Fig. 7(a). For $\lambda_J = 1$ the dependence is weak and linear, only interrupted by d-wave resonances. That suggests the perturbative impact of the spin-exchange interatomic interaction on the collisions and s-wave resonances. The nonperturbative regime can be identified for the spin-exchange interaction increased three times or more. For $\lambda_J > 3$ the number and density of resonances increase by a factor of two and stop to depend on λ_J. For example, for $\lambda_J = 5$ the number of s-wave and d-wave resonances below 1000 G for ultracold collisions between ^{153}Eu and ^{151}Eu atoms with $M_{\rm tot} = 0$ is 300 and 300, respectively. For comparison, Fig. 7(b) presents the dependence of the scattering lengths on the scaling of the isotropic part of the interaction potential which, as expected, is very strong.

We have observed similar characteristics as those presented in Figs. 3–7 also for different sets of scattering lengths. Only accidentally very close values of the background scattering lengths for the potential-energy curves with $S = 3$ and 4 can significantly reduce the widths of s-wave Feshbach resonances in mixtures of europium and alkali-metal atoms, while the widths of higher wave resonances can be reduced in all atomic combinations only if the scattering lengths for all the potential-energy curves are very close to zero. This is very improbable and can be resolved by changing the used isotopes. Thus, for all the investigated systems, for a broad range of possible scattering lengths, there should exist, at least

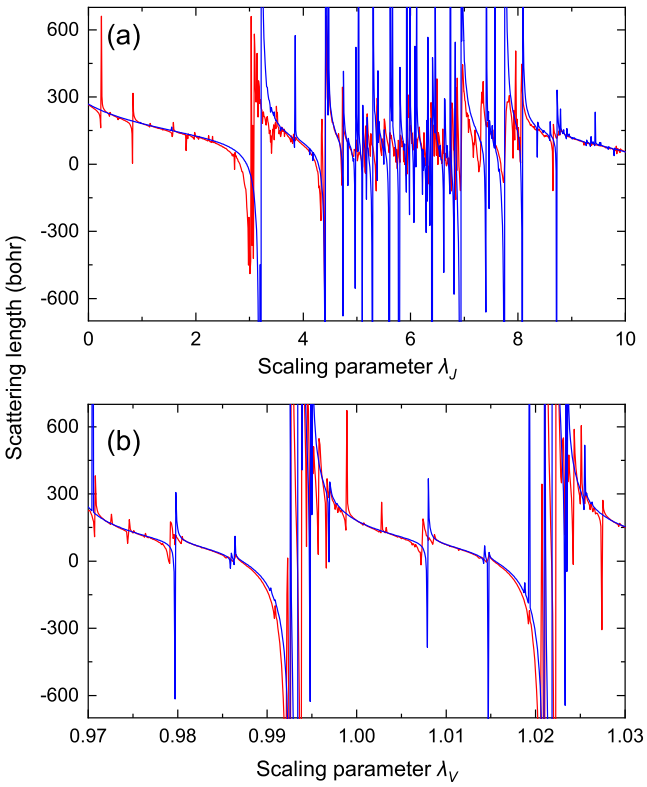

FIG. 7. Scattering lengths for ultracold collisions between ^{153}Eu and ^{151}Eu atoms with $M_{\rm tot} = 0$ at the magnetic field $B = 50$ G as a function of the parameters scaling the anisotropic (a) $J(R) \to \lambda_J J(R)$ and isotropic (b) $V_{S=7}(R) \to \lambda_V V_{S=7}(R)$ interatomic electronic interaction potential functions. The scattering length of $a_{S=7} = 1.5R_6$ is assumed. Blue (dark gray) lines show scattering lengths without the dipole-dipole interaction included and red (gray) lines show scattering lengths with the dipole-dipole interaction included.

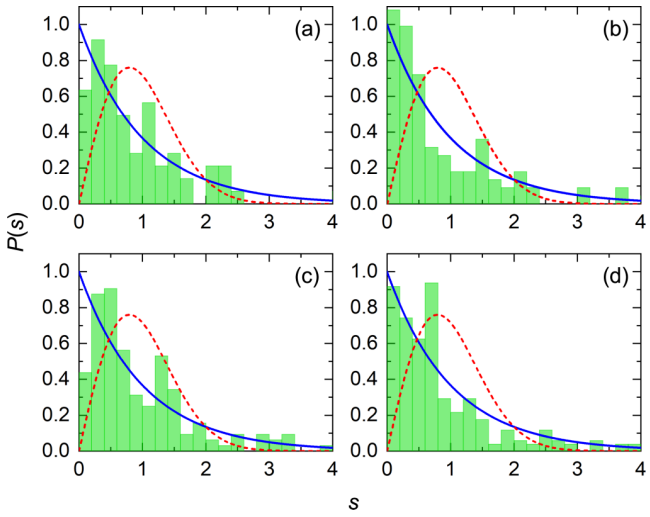

FIG. 8. Nearest-neighbor spacing distributions of s-wave (a),(c) and both s-wave and d-wave (b),(d) resonance positions for ultracold collisions between ^{153}Eu and ^{151}Eu atoms with $M_{\rm tot} = 0$ at magnetic-field strengths between 0 and 100 G with the spin-exchange interaction as obtained in *ab initio* calculations (a),(b) and scaled to the nonperturbative regime by $\lambda_J = 5$ (c),(d). The Poisson (solid blue) and Wigner-Dyson (dashed red) distribution curves are plotted for comparison.

for some $M_{\rm tot}$, favorable resonances for controlling ultracold collisions and magnetoassociation at magnetic-field strengths below 1000 G. For mixtures of europium and alkali-metal atoms s-wave resonances as broad as between alkali-metal atoms (with widths much over 1 G) can be expected. For ultracold homo- and heteronuclear gases of europium atoms a large number of useful s-wave and d-wave resonances (with widths reaching 100 mG) can be expected even at magnetic-field strengths below 100 G. At the same time, it should be possible to find magnetic-field strengths at which independent control of scattering properties in different scattering channels can be realized without being disturbed by accidental resonances. This should be a favorable condition for investigating magnetic polaron and similar phenomena in ultracold highly magnetic gases.

The complex spectra of many overlapping Feshbach resonances observed in Figs. 5(a) and 5(b) and Figs. 6(a) and 6(b) raise a question of whether the investigated systems exhibit a quantum chaotic behavior. For ultracold collisions of Dy and Er atoms it was measured [16,25] and theoretically confirmed [16,44,64–67] that the interplay of anisotropic electronic and dipolar interactions leads to the chaotic spectra of Feshbach resonances being the signature of the level repulsion following the predictions of the Gaussian orthogonal ensemble of random matrices [68]. Similar results were predicted for atom-molecule collisions [69–71]. To verify the above hypothesis in the considered case, in Fig. 8 we present nearest-neighbor spacing distributions of Feshbach resonance positions for ultracold collisions between ^{153}Eu and ^{151}Eu atoms with $M_{\rm tot} = 0$ at the magnetic-field strengths between zero and 100 G, for which the density of overlapping resonances is the largest and chaotic behavior is the most probable. Although we have selected the most dense part of the spectrum, the number of resonances is still relatively small, which makes our analysis semiquantitative. The distribution of uncorrelated energy levels should be described by the Poisson distribution, $P_{\rm P}(s) = \exp(-s)$, whereas the quantum chaotic distribution should be described by the Wigner-Dyson distribution, $P_{\rm WD}(s) = \frac{\pi s}{2}\exp(-\pi s^2/4)$, where the distance between adjacent levels s is in the units of mean resonance spacing [68]. The transition between Poissonian and quantum chaotic Wigner-Dyson distributions can be quantified by the intermediate Brody distribution, $P_{\rm B}(s,\eta) = b(1+\eta)s^\eta \exp(-bs^{\eta+1})$, with associated Brody parameter η [72], which is zero for Poisson and 1 for Wigner-Dyson distribution. In the present case, for the distribution of s-wave resonance positions, the level repulsion can be noticed, but the Brody parameter does not exceed 0.25. When d-wave resonances are included in the spectra, the level repulsion is less pronounced with the Brody parameter not exceeding 0.1. Very similar results are obtained for both native and increased spin-exchange interaction, with only very slight increase of the Brody parameter in the second case. This suggests that the Heisenberg model describing the interatomic spin-exchange interaction in the Eu + Eu system does not support quantum chaotic behavior and the anisotropic interaction related to

the nonzero electronic orbital angular momentum, as in Dy and Er, is needed [16]. The decrease of the level repulsion when the resonances induced by the dipole-dipole interaction are included agrees with previous theoretical works [16,66], which show that the magnetic dipole moment of Dy and Er, and so of Eu, is too small to support quantum chaotic behavior on its own. For larger $|M_{\mathrm{tot}}|$ and for mixtures of europium with alkali-metal atoms the resonance spectra are too simple to expect quantum chaotic signatures.

IV. SUMMARY AND CONCLUSIONS

Motivated by recent advances in production and application of ultracold highly dipolar atoms in complex electronic states, such as Er and Dy [11–17], we have considered ultracold collisions involving Eu atoms as another lanthanide candidate for the realization and application of dipolar atomic and molecular quantum gases in many-body physics. Dy and Er atoms are excellent systems for experiments exploiting dipolar interactions, but their very complex internal structure resulting in very rich, dense, and chaotic spectra of unavoidable magnetic Feshbach resonances [17] can limit applications based on the precision control of internal degrees of freedom, such as magnetoassociation, optical stabilization to deeply bound states, or magnetic polaron physics investigations.

Therefore, we have investigated magnetically tunable Feshbach resonances between ultracold europium atoms and between europium and alkali-metal atoms using multichannel quantum scattering calculations. We have studied both homonuclear $^{153}\mathrm{Eu} + {}^{153}\mathrm{Eu}$ and heteronuclear $^{151}\mathrm{Eu} + {}^{153}\mathrm{Eu}$ systems of europium atoms and $^{153}\mathrm{Eu} + {}^{87}\mathrm{Rb}$ and $^{153}\mathrm{Eu} + {}^{7}\mathrm{Li}$ combinations. We have analyzed the prospects for the control of scattering properties, observation of quantum chaotic behavior, and magnetoassociation into ultracold polar and paramagnetic molecules.

The most important of our findings can be summarized as follows.

(1) Favorable resonances are expected at experimentally feasible magnetic-field strengths below 1000 G for all investigated atomic combinations.

(2) The density of resonances depends strongly on the projection of the total angular momentum on the magnetic field (the degree of polarization).

(3) The dipole-dipole interaction between europium and alkali-metal atoms is weaker than the spin-exchange interaction; therefore, s-wave resonances are more favorable than d-wave ones in these systems.

(4) The dipole-dipole interaction between europium atoms is comparable to relatively weak short-range spin-exchange interaction, but strong enough to induce favorable resonances.

(5) Large number and density of s-wave and d-wave resonances is expected in ultracold gases of europium atoms.

(6) Especially large number and density of resonances is expected at magnetic-field strengths below 200 G, but signatures of quantum chaotic behavior measured by level repulsion are limited.

The present results draw attention to Eu atoms as an interesting and favorable candidate for dipolar many-body physics and pave the way towards experimental studies and application at ultralow temperatures.

ACKNOWLEDGMENTS

We would like to thank Mariusz Semczuk and Anna Dawid for useful discussions, and Alexei Buchachenko for providing us numerical values of the potential energy curves for the Eu_2 dimer. We acknowledge financial support from the Foundation for Polish Science within the Homing programme co-financed by the European Union under the European Regional Development Fund, the National Science Centre Poland (Grants No. 2016/23/B/ST4/03231 and No. 2017/25/B/ST4/01486), and the PL-Grid Infrastructure. The work reported here was initiated during The Toruń Physics Summer Program 2017.

[1] K. M. Jones, E. Tiesinga, P. D. Lett, and P. S. Julienne, Rev. Mod. Phys. **78**, 483 (2006).
[2] C. Chin, R. Grimm, P. S. Julienne, and E. Tiesinga, Rev. Mod. Phys. **82**, 1225 (2010).
[3] I. Bloch, J. Dalibard, and W. Zwerger, Rev. Mod. Phys. **80**, 885 (2008).
[4] I. Bloch, J. Dalibard, and S. Nascimbène, Nat. Phys. **8**, 267 (2012).
[5] S. Inouye, M. Andrews, J. Stenger, H.-J. Miesner, D. Stamper-Kurn, and W. Ketterle, Nature (London) **392**, 151 (1998).
[6] J. Werner, A. Griesmaier, S. Hensler, J. Stuhler, T. Pfau, A. Simoni, and E. Tiesinga, Phys. Rev. Lett. **94**, 183201 (2005).
[7] A. Griesmaier, J. Werner, S. Hensler, J. Stuhler, and T. Pfau, Phys. Rev. Lett. **94**, 160401 (2005).
[8] Z. Pavlović, R. V. Krems, R. Côté, and H. R. Sadeghpour, Phys. Rev. A **71**, 061402 (2005).
[9] T. Lahaye, T. Koch, B. Fröhlich, M. Fattori, J. Metz, A. Griesmaier, S. Giovanazzi, and T. Pfau, Nature (London) **448**, 672 (2007).
[10] T. Koch, T. Lahaye, J. Metz, B. Fröhlich, A. Griesmaier, and T. Pfau, Nat. Phys. **4**, 218 (2008).
[11] M. Lu, N. Q. Burdick, S. H. Youn, and B. L. Lev, Phys. Rev. Lett. **107**, 190401 (2011).
[12] M. Lu, N. Q. Burdick, and B. L. Lev, Phys. Rev. Lett. **108**, 215301 (2012).
[13] K. Aikawa, A. Frisch, M. Mark, S. Baier, A. Rietzler, R. Grimm, and F. Ferlaino, Phys. Rev. Lett. **108**, 210401 (2012).
[14] K. Aikawa, A. Frisch, M. Mark, S. Baier, R. Grimm, and F. Ferlaino, Phys. Rev. Lett. **112**, 010404 (2014).
[15] A. Petrov, E. Tiesinga, and S. Kotochigova, Phys. Rev. Lett. **109**, 103002 (2012).
[16] T. Maier, H. Kadau, M. Schmitt, M. Wenzel, I. Ferrier-Barbut, T. Pfau, A. Frisch, S. Baier, K. Aikawa, L. Chomaz, M. J. Mark, F. Ferlaino, C. Makrides, E. Tiesinga, A. Petrov, and S. Kotochigova, Phys. Rev. X **5**, 041029 (2015).
[17] T. Maier, I. Ferrier-Barbut, H. Kadau, M. Schmitt, M. Wenzel, C. Wink, T. Pfau, K. Jachymski, and P. S. Julienne, Phys. Rev. A **92**, 060702 (2015).

[18] S. Kato, S. Sugawa, K. Shibata, R. Yamamoto, and Y. Takahashi, Phys. Rev. Lett. **110**, 173201 (2013).

[19] M. Höfer, L. Riegger, F. Scazza, C. Hofrichter, D. R. Fernandes, M. M. Parish, J. Levinsen, I. Bloch, and S. Fölling, Phys. Rev. Lett. **115**, 265302 (2015).

[20] A. Khramov, A. Hansen, W. Dowd, R. J. Roy, C. Makrides, A. Petrov, S. Kotochigova, and S. Gupta, Phys. Rev. Lett. **112**, 033201 (2014).

[21] V. Barbé, A. Ciamei, B. Pasquiou, L. Reichsöllner, F. Schreck, P. S. Żuchowski, and J. M. Hutson, Nat. Phys. **14**, 881 (2018).

[22] P. S. Żuchowski, J. Aldegunde, and J. M. Hutson, Phys. Rev. Lett. **105**, 153201 (2010).

[23] T. Lahaye, C. Menotti, L. Santos, M. Lewenstein, and T. Pfau, Rep. Prog. Phys. **72**, 126401 (2009).

[24] M. A. Baranov, M. Dalmonte, G. Pupillo, and P. Zoller, Chem. Rev. **112**, 5012 (2012).

[25] A. Frisch, M. Mark, K. Aikawa, F. Ferlaino, J. L. Bohn, C. Makrides, A. Petrov, and S. Kotochigova, Nature (London) **507**, 475 (2014).

[26] K. Aikawa, S. Baier, A. Frisch, M. Mark, C. Ravensbergen, and F. Ferlaino, Science **345**, 1484 (2014).

[27] M. Schmitt, M. Wenzel, F. Böttcher, I. Ferrier-Barbut, and T. Pfau, Nature (London) **539**, 259 (2016).

[28] H. Kadau, M. Schmitt, M. Wenzel, C. Wink, T. Maier, I. Ferrier-Barbut, and T. Pfau, Nature (London) **530**, 194 (2016).

[29] S. Baier, M. Mark, D. Petter, K. Aikawa, L. Chomaz, Z. Cai, M. Baranov, P. Zoller, and F. Ferlaino, Science **352**, 201 (2016).

[30] Y. Ashida, R. Schmidt, L. Tarruell, and E. Demler, Phys. Rev. B **97**, 060302 (2018).

[31] L. A. Peña Ardila and T. Pohl, arXiv:1804.06390.

[32] D. Sukachev, A. Sokolov, K. Chebakov, A. Akimov, S. Kanorsky, N. Kolachevsky, and V. Sorokin, Phys. Rev. A **82**, 011405 (2010).

[33] J. Miao, J. Hostetter, G. Stratis, and M. Saffman, Phys. Rev. A **89**, 041401 (2014).

[34] J. Kim, B. Friedrich, D. P. Katz, D. Patterson, J. D. Weinstein, R. DeCarvalho, and J. M. Doyle, Phys. Rev. Lett. **78**, 3665 (1997).

[35] C. Hancox, S. Doret, M. Hummon, L. Luo, and J. Doyle, Nature (London) **431**, 281 (2004).

[36] Y. V. Suleimanov, Phys. Rev. A **81**, 022701 (2010).

[37] R. Inoue, Y. Miyazawa, and M. Kozuma, Phys. Rev. A **97**, 061607 (2018).

[38] L. D. Carr, D. DeMille, R. V. Krems, and J. Ye, New J. Phys. **11**, 055049 (2009).

[39] G. Quemener and P. S. Julienne, Chem. Rev. **112**, 4949 (2012).

[40] J. L. Bohn, A. M. Rey, and J. Ye, Science **357**, 1002 (2017).

[41] Z. Pavlović, H. R. Sadeghpour, R. Côté, and B. O. Roos, Phys. Rev. A **81**, 052706 (2010).

[42] M. Tomza, Phys. Rev. A **88**, 012519 (2013).

[43] M. Tomza, Phys. Rev. A **90**, 022514 (2014).

[44] M. L. González-Martínez and P. S. Żuchowski, Phys. Rev. A **92**, 022708 (2015).

[45] A. Frisch, M. Mark, K. Aikawa, S. Baier, R. Grimm, A. Petrov, S. Kotochigova, G. Quéméner, M. Lepers, O. Dulieu, and F. Ferlaino, Phys. Rev. Lett. **115**, 203201 (2015).

[46] J. Rührig, T. Bäuerle, P. S. Julienne, E. Tiesinga, and T. Pfau, Phys. Rev. A **93**, 021406 (2016).

[47] C. Ravensbergen, V. Corre, E. Soave, M. Kreyer, S. Tzanova, E. Kirilov, and R. Grimm, Phys. Rev. Lett. **120**, 223001 (2018).

[48] P. Ilzhöfer, G. Durastante, A. Patscheider, A. Trautmann, M. J. Mark, and F. Ferlaino, Phys. Rev. A **97**, 023633 (2018).

[49] S. Kotochigova, Rep. Prog. Phys. **77**, 093901 (2014).

[50] E. Arimondo, M. Inguscio, and P. Violino, Rev. Mod. Phys. **49**, 31 (1977).

[51] P. Sandars and G. Woodgate, Proc. R. Soc. London A **257**, 269 (1960).

[52] A. A. Buchachenko, G. Chalasinski, and M. M. Szczesniak, J. Chem. Phys. **131**, 241102 (2009).

[53] L. M. C. Janssen, A. van der Avoird, and G. C. Groenenboom, Phys. Rev. Lett. **110**, 063201 (2013).

[54] M. Tomza, R. González-Férez, C. P. Koch, and R. Moszynski, Phys. Rev. Lett. **112**, 113201 (2014).

[55] M. Tomza, Phys. Rev. A **92**, 062701 (2015).

[56] J. M. Hutson, E. Tiesinga, and P. S. Julienne, Phys. Rev. A **78**, 052703 (2008).

[57] B. R. Johnson, J. Chem. Phys. **69**, 4678 (1978).

[58] R. J. LeRoy, Y. Huang, and C. Jary, J. Chem. Phys. **125**, 164310 (2006).

[59] B. Gao, Phys. Rev. A **62**, 050702 (2000).

[60] S. Knoop, P. S. Żuchowski, D. Kędziera, Ł. Mentel, M. Puchalski, H. P. Mishra, A. S. Flores, and W. Vassen, Phys. Rev. A **90**, 022709 (2014).

[61] M. Marinescu and L. You, Phys. Rev. Lett. **81**, 4596 (1998).

[62] V. S. Melezhik and C.-Y. Hu, Phys. Rev. Lett. **90**, 083202 (2003).

[63] M. A. Baranov, Phys. Rep. **464**, 71 (2008).

[64] K. Jachymski and P. S. Julienne, Phys. Rev. A **92**, 020702 (2015).

[65] D. G. Green, C. L. Vaillant, M. D. Frye, M. Morita, and J. M. Hutson, Phys. Rev. A **93**, 022703 (2016).

[66] B. C. Yang, J. Pérez-Ríos, and F. Robicheaux, Phys. Rev. Lett. **118**, 154101 (2017).

[67] C. Makrides, M. Li, E. Tiesinga, and S. Kotochigova, Sci. Adv. **4**, 8308 (2018).

[68] F. Haake, *Quantum Signatures of Chaos*, Springer Series in Synergetics Vol. 54 (Springer-Verlag, Berlin, 2010).

[69] M. D. Frye, M. Morita, C. L. Vaillant, D. G. Green, and J. M. Hutson, Phys. Rev. A **93**, 052713 (2016).

[70] J. Croft, C. Makrides, M. Li, A. Petrov, B. Kendrick, N. Balakrishnan, and S. Kotochigova, Nat. Commun. **8**, 15897 (2017).

[71] J. F. E. Croft, N. Balakrishnan, and B. K. Kendrick, Phys. Rev. A **96**, 062707 (2017).

[72] T. A. Brody, Lett. Nuovo Cimento **7**, 482 (1973).

3.2 Paper II: *Van der Waals molecules consisting of a zinc or cadmium atom interacting with an alkali-metal or alkaline-earth-metal atom*

Paper II

"Van der Waals molecules consisting of a zinc or cadmium atom interacting with an alkali-metal or alkaline-earth-metal atom"

Klaudia Zaremba-Kopczyk and Michał Tomza

Phys. Rev. A 104, 042816 (2021)

Commentary

Ultracold molecules containing alkaline-earth-type atoms are promising candidates for high-precision measurements. Transition-metal Zn and Cd atoms ($^1S_0$ ground state) possess a richer structure of excited electronic states (as compared to the alkaline-earth-metal atoms, also with $^1S_0$ ground state) due to the possibility of electron excitations from the d subshell, and may be utilized to explore potential spatio-temporal variations in the fundamental constants [259]. Additionally, Zn or Cd atom interacting with other atoms may form weakly-bound van der Waals molecules that may potentially be used as precise probes of new gravity-like forces [185]. Moreover, optical lattice clocks based on group-IIB atoms, such as Zn, Cd, and Hg, have been shown to exhibit reduced susceptibility to the blackbody radiation as compared to currently operational Sr and Yb clocks [260].

In the work presented in [Paper II], we calculated the potential energy curves, permanent electric dipole moments, and spectroscopic constants for molecules consisting of a Zn or Cd atom interacting with an alkali-metal (Li, Na, K, Rb, Cs, Fr) or alkaline-earth-metal (Be, Mg, Ca, Sr, Ba, Ra) atom using the *ab initio* coupled-clusters method. We found out that the investigated molecules in the ground electronic state form weakly bound van der Waals complexes with small permanent electric dipole moments and are chemically reactive. In this work, the PhD Candidate: generated all numerical data presented in the article, participated in the results analysis and interpretation, prepared all figures and tables, wrote the first draft and edited subsequent drafts of the manuscript.

Van der Waals molecules consisting of a zinc or cadmium atom interacting with an alkali-metal or alkaline-earth-metal atom

Klaudia Zaremba-Kopczyk [*] and Michał Tomza [†]
Faculty of Physics, University of Warsaw, Pasteura 5, 02-093 Warsaw, Poland

(Received 22 April 2021; accepted 14 July 2021; published 25 October 2021)

Alkaline-earth-like transition-metal atoms such as Zn and Cd are promising candidates for precision measurements and quantum many-body physics experiments. Here, we theoretically investigate the properties of diatomic molecules containing these closed-shell atoms. We calculate potential-energy curves, permanent electric dipole moments, and spectroscopic constants for molecules consisting of either a Zn or Cd atom interacting with an alkali-metal (Li, Na, K, Rb, Cs, Fr) or alkaline-earth-metal (Be, Mg, Ca, Sr, Ba, Ra) atom. We use the *ab initio* electronic-structure coupled-cluster method with single, double, and triple excitations combined with large Gaussian basis sets and small-core relativistic energy-consistent pseudopotentials for heavier atoms. We predict that the studied molecules in the ground electronic state are chemically reactive weakly bound van der Waals complexes with small permanent electric dipole moments. The present results may be useful for spectroscopy and application of the studied molecules in modern ultracold physics and chemistry experiments.

DOI: 10.1103/PhysRevA.104.042816

I. INTRODUCTION

Ultracold molecules have emerged in recent years as a versatile platform for studies of complex quantum phenomena [1–3]. The rich internal molecular structure and intermolecular interactions have been employed in studies of quantum many-body physics, allowing for the realization of many-body Hamiltonians of yet unexplored complexity [4,5]. The controllability of molecular collisions with external magnetic or electric fields, along with precise control over molecular quantum states, have enabled research on ultracold controlled chemical reactions [6–8]. Furthermore, the complexity of molecular structure provides novel possibilities for precision tests of fundamental physics, which include tests of fundamental symmetries, searches for spatiotemporal variations of fundamental constants, tests of quantum electrodynamics, and tests of general relativity, among others [9,10].

Ultracold molecules containing alkaline-earth-type atoms are promising candidates for high-precision measurement experiments [11] and emerging quantum technologies [12], while alkaline-earth-type atoms have already served as important building blocks of high-precision physics [13]. For example, optical lattice clocks based on the $^1S_0 \rightarrow {}^3P_0$ transition in alkaline-earth-type atoms have played a substantial role in establishing current time and frequency standards [14–17]. Here, the main focus has been put on optical lattice clocks based on strontium [14,15,17], ytterbium [16,18], and mercury [19–21] atoms; however, recent proposals have brought attention to two other suitable candidates, zinc and cadmium atoms [22–25]. Optical lattice clocks based on group-IIB atoms, such as Zn, Cd, and Hg, have been shown to exhibit reduced susceptibility to the blackbody radiation (BBR) compared to Sr- or Yb-based clocks [19–22,24,26]. With BBR being the major factor limiting the accuracy of atomic clocks, Zn and Cd atoms serve as promising alternatives to the currently operational Sr and Yb clocks [23,25]. In addition, optical lattice clocks based on alkaline-earth-type atoms are excellent systems for quantum simulations of many-body physics [27,28]. Finally, optical clock transitions in divalent atoms have been suggested as a tool to explore potential variations in the fine-structure constant [19,29] or establishing constraints on the value of the electron's electric dipole moment (EDM) [19].

The use of ultracold molecules based on alkaline-earth-type atoms provides further enhancement of sensitivities to the variations of fundamental constants or EDM effects [10]. In this context, one potentially interesting class of molecules is heteronuclear molecules composed of a closed-shell alkaline-earth-like atom interacting with an open-shell atom, such as an alkali-metal atom [30] or a halide [31]. Such molecules have been proposed to be useful for measuring the variations in the proton-to-electron mass ratio [32] and suggested as appealing candidates for searches of the electron's EDM [31,33–36]. Moreover, homonuclear dimers of alkaline-earth-type atoms also show prospects for precise measurements of the proton-to-electron mass ratio [37,38], while heteronuclear $^2\Sigma$-symmetry molecules have been proposed as quantum simulators with prospects for creating topologically ordered states [39]. $^2\Sigma$-state molecules can be formed from ultracold mixtures of closed-shell and open-shell atoms, following recent experimental advances in studies of Yb+Rb [40], Sr+Rb [41], Yb+Li [42], and Yb+Cs [43] combinations.

In this work, we propose the formation of ultracold heteronuclear molecules composed of a transition-metal zinc or cadmium atom interacting with an alkali-metal or alkaline-earth-metal atom. The electronic structure of homonuclear dimers of group-IIB atoms, such as Zn_2, Cd_2, and Hg_2, has

[*] klaudia.zaremba-kopczyk@fuw.edu.pl
[†] michal.tomza@fuw.edu.pl

been the subject of theoretical studies [44–47], while heteronuclear molecules composed of a Hg atom interacting with an alkali-metal atom have been investigated both theoretically [48,49] and experimentally [50–52]. To the best of our knowledge, molecules composed of a Zn or Cd atom interacting with an alkali-metal or alkaline-earth-metal atom have not yet been investigated in the literature. Transition-metal zinc and cadmium atoms, compared to the alkaline-earth-metal atoms, possess a richer structure of excited electronic states due to the possibility of electron excitations from the d subshell. While the ground-state electronic structure of such zinc- or cadmium-containing molecules resembles the electronic structure of alkaline-earth-metal or alkali-metal–alkaline-earth-metal molecules, the richer electronic structure of constituent atoms would have its reflection in a more complex structure of excited electronic states, which may find application in precision measurements [10]. Additionally, zinc or cadmium atom interacting with other atoms may form weakly bound van der Waals molecules that may potentially be used as precise probes of new gravitylike forces [53,54]. The ongoing progress in laser cooling and trapping of cadmium atoms [24,55–57] further motivates our investigation.

Here, we theoretically investigate the ground-state properties of diatomic molecules composed of either a Zn or Cd atom interacting with an alkali-metal (Li, Na, K, Rb, Cs, Fr) or alkaline-earth-metal (Be, Mg, Ca, Sr, Ba, Ra) atom. We use state-of-the-art electronic structure methods to calculate the potential-energy curves (PECs) and spectroscopic constants for the investigated molecules. We predict that the considered molecules in the ground electronic state are weakly bound van der Waals complexes, which are chemically reactive. They possess rather small permanent electric dipole moments, despite Zn and Cd atoms having electronegativity significantly larger than that of alkali-metal and alkaline-earth-metal atoms. In this way, the present study extends the range of species available for ultracold molecular studies.

This paper is constructed as follows. Section II introduces the *ab initio* electronic structure methods employed in our calculations. Section III presents and analyzes the obtained numerical data, including the potential-energy curves and electric properties of the investigated molecules. Finally, Sec. IV summarizes our paper.

II. COMPUTATIONAL DETAILS

In order to calculate the potential-energy curves within the Born-Oppenheimer approximation, we employ the closed-shell and the spin-restricted open-shell coupled-cluster methods restricted to single, double, and noniterative triple excitations [CCSD(T)]. Next, we include the full iterative triple-excitation correction, ΔT, calculated with the use of the coupled-cluster method restricted to single, double, and full triple excitations (CCSDT). We obtain the counterpoise-corrected interaction energies within the supermolecule approach [58].

We use the small-core scalar-relativistic energy-consistent pseudopotentials from the Stuttgart/Köln library, ECPnMDF, to describe n inner-shell electrons of studied transition-metal atoms and heavier alkali-metal and alkaline-earth-metal atoms (ECP10MDF for Zn, K, and Ca; ECP28MDF for Cd, Rb, and Sr; ECP46MDF for Cs and Ba; and ECP78MDF for Fr and Ra) [59–61]. This approach treats only the electrons from the two outermost shells of a given atom explicitly [i.e., $3s^2 3p^6 3d^{10} 4s^2$ from Zn, $4s^2 4p^6 4d^{10} 5s^2$ from Cd, $(n-1)s^2(n-1)p^6 ns^1$ from alkali-metal, and $(n-1)s^2(n-1)p^6 ns^2$ from alkaline-earth-metal atoms], and hence, it allows us to use larger basis sets for more accurate molecular calculations. We correlate all remaining electrons. For the presented computations at the CCSD(T) level of theory, we employ the corresponding correlation-consistent polarized weighed core-valence quintuple-ζ quality basis sets (aug-cc-pwCV5Z-PP [44,62] with ECP and aug-cc-pwCV5Z [63] for Li, Na, Be, and Mg) augmented by the set of the $[3s3p2d2f1g]$ bond functions. To account for the full triple-excitation correction (ΔT), we perform electronic structure calculations at the CCSDT level of theory with the use of valence-only triple-ζ quality basis sets (aug-cc-pVTZ for Li, Na, Be, and Mg atoms and aug-cc-pVTZ-PP for the remaining atoms).

Additionally, for two representative systems, an open-shell RbZn molecule and a closed-shell SrZn molecule, we carry out convergence tests to analyze the accuracy of the obtained interaction energies and confirm the optimal method and basis sets for the remaining calculations. To this end, we compute interaction energies using the CCSD(T) method and aug-cc-pwCVnZ-PP basis sets with n = D, T, Q, 5. We use these basis sets to extrapolate the interaction energies to the complete-basis-set (CBS) limit and show that adding a bond function (BF) to aug-cc-pwCV5Z-PP basis sets allows us to reproduce the CBS limit accurately. Next, we obtain the full iterative triple-excitation correction (ΔT), given as a difference between interaction energies calculated at the CCSDT and CCSD(T) levels of theory, in smaller basis sets (aug-cc-pVnZ-PP, with n = D, T, Q, and aug-cc-pwCVDZ-PP). Analogously, we estimate the magnitude of noniterative and iterative quadruple excitations [Δ(Q) and ΔQ] using the CCSDT(Q) and CCSDTQ methods, respectively, with the aug-cc-pVDZ-PP and aug-cc-pVTZ-PP basis sets. For completeness, we also compare the PECs obtained within the coupled-cluster method with the ones calculated using the multireference configuration interaction method restricted to single and double excitations (MRCISD).

The permanent electric dipole moments and static electric dipole polarizabilities are calculated using the finite-field method at the CCSD(T)/aug-cc-pwCV5Z level of theory. The z axis is chosen along the internuclear axis and oriented from a Zn or Cd atom to an alkali-metal or alkaline-earth-metal atom.

All electronic structure calculations are performed using the MOLPRO package of *ab initio* programs [64,65]. The full triple and quadruple contributions are computed using the MRCC code embedded in MOLPRO [66]. Vibrational eigenstates are calculated numerically by employing the exact diagonalization of the nuclear motion Hamiltonian within the discrete-variable representation (DVR) on the nonequidistant grid [67]. Atomic masses of the most abundant isotopes are assumed.

III. RESULTS AND DISCUSSION

A. Potential-energy curves

We consider interactions between a zinc or cadmium atom and an alkali-metal AM (AM = Li, Na, K, Rb, Cs, Fr) or

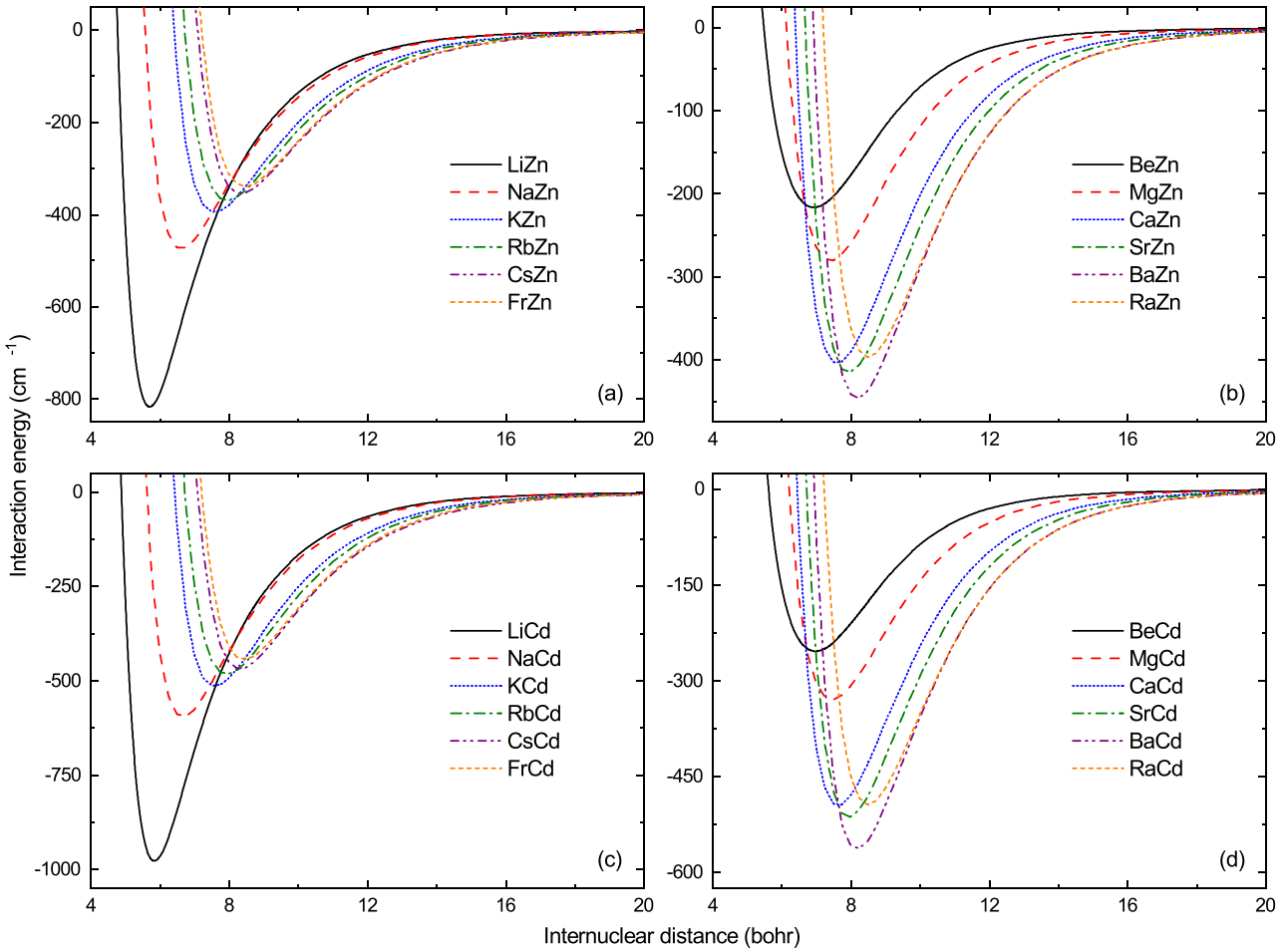

FIG. 1. Potential-energy curves of (a) the *AM*-Zn molecules in the $X^2\Sigma^+$ electronic state, (b) the *AEM*-Zn molecules in the $X^1\Sigma^+$ electronic state, (c) the *AM*-Cd molecules in the $X^2\Sigma^+$ electronic state, and (d) the *AEM*-Cd molecules in the $X^1\Sigma^+$ electronic state.

alkaline-earth-metal *AEM* (*AEM* = Be, Mg, Ca, Sr, Ba, Ra) atom in their electronic ground states. The ground-state Zn and Cd atoms, as well as alkaline-earth-metal atoms, are described with the $^1S_0$ electronic term, while the alkali-metal atoms are described with the $^2S_{1/2}$ electronic term. This yields the $^2\Sigma^+$ molecular electronic states for the ground-state open-shell molecules composed of a Zn or Cd atom and an alkali-metal atom and the $^1\Sigma^+$ molecular electronic states for the ground-state closed-shell molecules composed of a Zn or Cd atom and an alkaline-earth-metal atom.

For the above molecules, we compute the potential-energy curves and provide spectroscopic characteristics: the equilibrium bond lengths R_e, potential-well depths D_e, harmonic constants ω_e, first anharmonicity constants $\omega_e x_e$, numbers of bound vibrational states N_v, and rotational constants B_e. We also report the permanent electric dipole moments d_e and parallel and perpendicular components of the static electric dipole polarizabilities, $\alpha_e^{\parallel}$ and $\alpha_e^{\perp}$, respectively, at equilibrium distances. The computed curves are presented in Fig. 1, and obtained characteristics are collected in Table I. We estimate the number of bound vibrational states N_v with the use of the DVR method, in which we employ the computed PECs, describing the short-range part of the interaction, smoothly connected with the long-range part of the interaction, $-C_6/R^6$, where the dispersion-interaction coefficients C_6 are taken from Ref. [68] and presented in Table I for completeness. We also provide the results for the ground-state homonuclear Zn_2 and Cd_2 dimers described with the $^1\Sigma_g^+$ molecular term and the ZnCd molecule in the $^1\Sigma^+$ electronic ground state.

Figure 1 presents the potential-energy curves of the *AM*-Zn and *AM*-Cd molecules in the $X\ ^2\Sigma^+$ electronic ground state and *AEM*-Zn and *AEM*-Cd molecules in the $X\ ^1\Sigma^+$ electronic ground state calculated at the CCSD(T)+ΔT level of theory. All PECs exhibit a smooth behavior with well-defined minima. For the *AM*-Zn and *AM*-Cd molecules, the well depths systematically decrease with the increasing atomic number of the alkali-metal atoms (a deviation from the trend is observed for radium-containing molecules), while for the *AEM*-Zn and *AEM*-Cd molecules, the well depths systematically increase with the increasing atomic number of the alkaline-earth-metal atoms. The opposite trends can be explained by different characters of bonding within molecules containing alkali-metal and alkaline-earth-metal atoms: the open-shell *AM*-Zn and *AM*-Cd molecules are bound chemically (with a bond order of $\frac{1}{2}$), while the closed-shell *AEM*-Zn and *AEM*-Cd molecules are bound solely by the dispersion forces. All considered molecules are of van der Waals character, with moderate equilibrium distances and well depths

TABLE I. Spectroscopic characteristics of the *AM*-Zn and *AM*-Cd molecules in the $X\ ^2\Sigma^+$ electronic state and *AEM*-Zn and *AEM*-Cd molecules in the $X\ ^1\Sigma^+$ electronic state: equilibrium bond length R_e, well depth D_e, harmonic constant ω_e, first anharmonicity constant $\omega_e x_e$, number of bound vibrational states N_v, rotational constant B_e, permanent electric dipole moment d_e, parallel and perpendicular components of the static electric dipole polarizability $\alpha_e^{\parallel}$ and $\alpha_e^{\perp}$, and long-range dispersion-interaction coefficient C_6. The results for the Zn_2, Cd_2, and ZnCd molecules are also presented.

Molecule	State	R_e (bohr)	D_e (cm^{-1})	ω_e (cm^{-1})	$\omega_e x_e$ (cm^{-1})	N_v	B_e (cm^{-1})	d_e (D)	$\alpha_e^{\parallel}$ (a.u.)	$\alpha_e^{\perp}$ (a.u.)	C_6 (a.u.) [68]
LiZn	$X\ ^2\Sigma^+$	5.67	827	131	6.84	17	0.296	0.30	375	164	541
NaZn	$X\ ^2\Sigma^+$	6.61	474	50.9	1.51	24	0.081	0.20	315	173	597
KZn	$X\ ^2\Sigma^+$	7.57	395	34.8	0.35	28	0.043	0.18	457	291	837
RbZn	$X\ ^2\Sigma^+$	7.93	368	26.6	0.45	34	0.026	0.16	481	321	959
CsZn	$X\ ^2\Sigma^+$	8.33	354	23.4	0.62	37	0.020	0.12	558	390	1129
FrZn	$X\ ^2\Sigma^+$	8.45	339	21.5	0.41	39	0.017	0.11	467	331	1056
BeZn	$X\ ^1\Sigma^+$	6.91	218	39.9	1.88	11	0.159	−0.03	101	69	270
MgZn	$X\ ^1\Sigma^+$	7.39	280	33.2	0.46	18	0.063	−0.003	148	99	450
CaZn	$X\ ^1\Sigma^+$	7.60	404	33.4	0.30	28	0.042	−0.08	271	175	771
SrZn	$X\ ^1\Sigma^+$	7.92	415	27.4	0.23	35	0.026	−0.07	321	215	916
BaZn	$X\ ^1\Sigma^+$	8.17	446	25.7	0.70	40	0.021	−0.12	417	287	1138
RaZn	$X\ ^1\Sigma^+$	8.49	396	22.2	0.21	41	0.017	−0.02	373	266	1044
LiCd	$X\ ^2\Sigma^+$	5.80	988	134	5.41	19	0.270	0.54	409	165	708
NaCd	$X\ ^2\Sigma^+$	6.66	596	53.2	1.19	28	0.071	0.40	350	175	783
KCd	$X\ ^2\Sigma^+$	7.58	515	36.4	1.50	34	0.036	0.44	511	288	1090
RbCd	$X\ ^2\Sigma^+$	7.92	482	26.6	0.30	44	0.020	0.42	537	318	1251
CsCd	$X\ ^2\Sigma^+$	8.32	467	22.7	0.33	50	0.014	0.40	624	383	1470
FrCd	$X\ ^2\Sigma^+$	8.43	443	20.1	0.31	54	0.011	0.34	519	328	1381
BeCd	$X\ ^1\Sigma^+$	6.95	255	42.2	1.59	12	0.149	−0.03	115	75	365
MgCd	$X\ ^1\Sigma^+$	7.44	329	33.8	0.48	21	0.055	0.02	164	105	605
CaCd	$X\ ^1\Sigma^+$	7.62	496	34.5	1.38	33	0.035	−0.02	299	179	1023
SrCd	$X\ ^1\Sigma^+$	7.93	513	26.7	0.12	44	0.019	0.01	352	219	1212
BaCd	$X\ ^1\Sigma^+$	8.17	563	24.7	0.10	53	0.014	−0.02	456	290	1499
RaCd	$X\ ^1\Sigma^+$	8.49	494	20.4	0.20	55	0.011	0.08	406	269	1335
Zn_2	$X\ ^1\Sigma_g^+$	7.23	231	23.4	0.62	22	0.036	0	97	70	359
ZnCd	$X\ ^1\Sigma^+$	7.28	275	22.6	0.53	27	0.028	0.01	110	76	495
Cd_2	$X\ ^1\Sigma_g^+$	7.32	330	21.1	0.24	35	0.020	0	124	83	686

not exceeding $1000\,cm^{-1}$. We also notice that molecules containing cadmium are more strongly bound than molecules containing zinc due to the larger polarizability of the cadmium atom.

The well depths of the *AM*-Zn molecules in the ground $X\ ^2\Sigma^+$ electronic state range from $827\,cm^{-1}$ for LiZn to $339\,cm^{-1}$ for FrZn, systematically decreasing with the atomic number of the alkali-metal atom *AM*. The equilibrium distances range from 5.67 bohrs for LiZn to 8.45 bohrs for FrZn, systematically increasing with the atomic number of *AM*. We observe the same trend for the *AM*-Cd molecules in the ground $X\ ^2\Sigma^+$ electronic state, whose well depths range from $988\,cm^{-1}$ for LiCd to $433\,cm^{-1}$ for FrCd, and equilibrium distances increase from 5.80 bohrs for LiCd to 8.43 bohrs for FrCd. The computed number of vibrational levels increases with the reduced mass of the molecule, from 17 and 19 for LiZn and LiCd to 39 and 54 for FrZn and FrCd, respectively.

For the *AEM*-Zn molecules in the ground $X\ ^1\Sigma^+$ electronic state, the well depth systematically increases from $218\,cm^{-1}$ for BeZn to $446\,cm^{-1}$ for BaZn and slightly drops to $396\,cm^{-1}$ for RaZn. *AEM*-Cd molecules in the ground $X\ ^1\Sigma^+$ electronic state are characterized by well depths which also systematically increase with the atomic number of *AEM*, ranging from $255\,cm^{-1}$ for BeCd to $563\,cm^{-1}$ for BaCd and $494\,cm^{-1}$ for RaCd. The equilibrium distance systematically increases from 6.91 bohrs for BeZn to 8.49 bohrs for RaZn and from 6.95 bohrs for BeCd to 8.49 bohrs for RaCd. The estimated number of vibrational levels amounts to 11 and 12 for BeZn and BeCd and increases with the reduced mass of the molecule up to 41 and 55 for RaZn and RaCd, respectively.

The observed trends in the studied molecules are similar to those reported for analogous alkali-metal–alkaline-earth-metal and alkaline-earth-metal molecules [69–71]. However, the potential-well depths are smaller, and equilibrium distances are larger in the present case due to smaller polarizabilities of the Zn and Cd atoms than those of alkaline-earth-metal atoms.

For completeness, we also provide results for the homonuclear Zn_2 and Cd_2 and heteronuclear ZnCd molecules in their ground $X\ ^1\Sigma_g^+$ and $X\ ^1\Sigma^+$ electronic states, respectively. The calculated spectroscopic characteristics are collected in Table I. Figure 2 presents the PECs, which were calculated at the CCSD(T)+ΔT + Δ(Q) level of theory. The potential-well depths amount to 231, 275, and $330\,cm^{-1}$ for Zn_2, ZnCd, and Cd_2, respectively, and the respective equilibrium distances are 7.23, 7.28, and 7.32 bohrs. The estimated number of vibrational levels is equal to 22 for Zn_2, 27 for ZnCd, and 35 for Cd_2. The values of the well depths D_e and harmonic constants ω_e obtained for homonuclear dimers are in good agreement with the results of previous theoretical calculations and

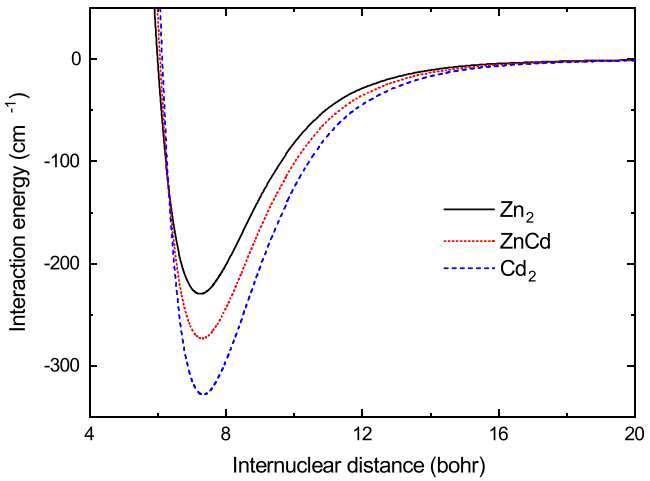

FIG. 2. Potential-energy curves of the Zn_2 and Cd_2 molecules in the $X\ ^1\Sigma_g^+$ electronic state and the ZnCd molecule in the $X\ ^1\Sigma^+$ electronic state.

spectroscopic measurements, which are compared in Table II. Like previous theoretical works, we observe discrepancies between the calculated equilibrium distances and their experimental values, especially for Zn_2.

B. Permanent electric dipole moments and static electric dipole polarizabilities

The permanent electric dipole moments of the *AM*-Zn and *AM*-Cd molecules in the $X\ ^2\Sigma^+$ electronic state and the *AEM*-Zn and *AEM*-Cd molecules in the $X\ ^1\Sigma^+$ electronic states as functions of the internuclear distance are presented in Fig. 3. The values of permanent electric dipole moments at equilibrium distances are collected in Table I. They govern the strength of the intermolecular dipolar interaction and coupling with an external static electric field.

The *AM*-Zn and *AM*-Cd molecules in the $X\ ^2\Sigma^+$ electronic state have small permanent EDMs, not exceeding 0.54 debye at equilibrium distances. The values of the EDMs at equilibrium distances systematically decrease with the increasing atomic number of the alkali-metal atom, ranging from 0.30 debye for LiZn to 0.11 debye for FrZn and from 0.54 for LiCd to 0.34 for FrCd.

The permanent EDMs of the *AEM*-Zn and *AEM*-Cd molecules in the $X\ ^1\Sigma^+$ electronic state take even smaller values, not exceeding 0.12 debye at equilibrium distances. The equilibrium-distance EDMs take values ranging from 0.003 debye for MgZn to 0.12 debye for BaZn and from 0.01 for SrCd to 0.08 for RaCd, with no distinct systematics of atomic number dependence. In contrast to the *AM*-Zn molecules, the permanent electric dipole moments of the *AEM*-Zn molecules point from the alkaline-earth-metal atom to the zinc atom. For BeCd, CaCd, and BaCd molecules, the dipoles are oriented from the alkaline-earth-metal atom to the cadmium atom, while for MgCd, SrCd, and RaCd, the dipoles are oriented from the cadmium atom to the alkaline-earth-metal atom.

The permanent electric dipole moments of all the studied molecules take very small values despite relatively large electronegativity differences between involved atoms. The electronegativity by the Pauling scale of the Zn (1.65) and Cd (1.69) atoms is almost two times larger than that of the alkali-metal (0.79–0.98) and alkaline-earth-metal (0.89–1.57) atoms [74]. For such large differences, significant permanent EDMs, larger than those for analogous alkali-metal–alkaline-earth-metal and alkaline-earth-metal molecules [69–71], could be expected (similar to what was recently reported for molecules containing Cu and Ag atoms [75]). Unfortunately, the present values are significantly smaller, partially as a result of weak interatomic interactions and van der Waals nature of the studied molecules and partially because around minima the permanent EDMs cross zero and change sign. At large distances, the permanent EDMs present an expected systematic dependence on the electronegativity differences.

We also calculate the parallel, $\alpha_e^{\parallel}$, and perpendicular, $\alpha_e^{\perp}$, components of the static electric dipole polarizability tensor, which play an important role in the evaluation of intermolecular interactions and coupling of molecular rovibrational dynamics with a laser field. The values of the parallel and perpendicular components of static electric dipole polarizabilities at equilibrium distances are collected in Table I.

TABLE II. Spectroscopic constants of the Zn_2 and Cd_2 molecules in the $X\ ^1\Sigma_g^+$ electronic state: Comparison with previous studies.

Molecule	Source	R_e (bohr)	D_e (cm^{-1})	ω_e (cm^{-1})
Zn_2	This work	7.23	231	23.4
	Theory [44]	7.27	226	23.9
	Theory [45]	7.23	226	24.0
	Theory [46]	7.32	242	25.65
	Experiment [72]	7.92	242	25.9
Cd_2	This work	7.32	330	21.1
	Theory [44]	7.36	325	20.2
	Theory [45]	7.32	319	21.3
	Theory [46]	7.75	328	21.5
	Experiment [73]	7.14 ± 0.06	328 ± 3	21.4 ± 0.2

C. Convergence and accuracy analysis

In order to investigate the uncertainty of the present molecular electronic structure calculations, we first examine whether the employed *ab initio* methods describe the atomic properties accurately. To this end, we employ the CCSD(T) method to calculate the atomic static electric dipole polarizabilities and ionization potentials of the Zn and Cd atoms using the aug-cc-pwCV5Z-PP basis sets. The obtained atomic polarizabilities of the zinc and cadmium atoms amount to 37.7 and 45.8 a.u. and agree well with the recommended combined experimental-theoretical values of 38.7 ± 0.3 and 46 ± 2 a.u. [76], respectively. The calculated ionization potentials of 75 848 cm^{-1} for Zn and 72 526 cm^{-1} for Cd are also in good agreement with respective experimental values of 75 769 cm^{-1} [77] and 72 540 cm^{-1} [78]. The atomic polarizabilities and ionization potentials of the alkali-metal and alkaline-earth-metal atoms obtained with the used theoretical methods are also in good agreement with experimental data, as confirmed in Ref. [75].

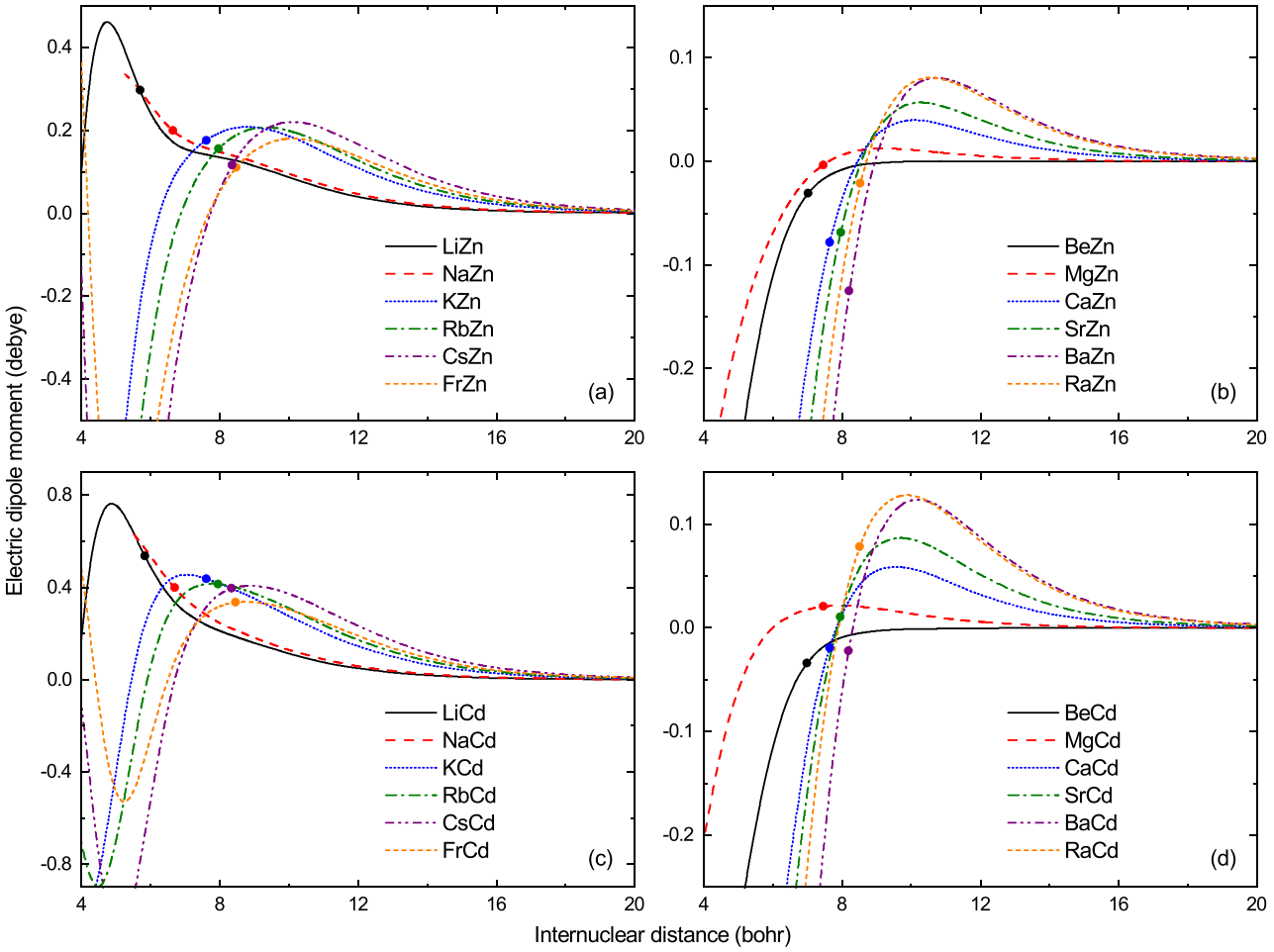

FIG. 3. Permanent electric dipole moments of (a) the *AM*-Zn molecules in the $X\,^2\Sigma^+$ electronic state, (b) the *AEM*-Zn molecules in the $X\,^1\Sigma^+$ electronic state, (c) the *AM*-Cd molecules in the $X\,^2\Sigma^+$ electronic state, and (d) the *AEM*-Cd molecules in the $X\,^1\Sigma^+$ electronic state. The points mark the permanent electric dipole moments at equilibrium distances.

Next, we analyze the convergence of the interatomic interaction energy with the size of the employed basis sets. Figure 4 presents the potential-energy curves for the representative RbZn and SrZn molecules in the $X\,^2\Sigma^+$ and $X\,^1\Sigma^+$ electronic states, respectively, obtained with different basis sets. An inspection of Fig. 4 allows us to conclude that the inclusion of inner-shell electron correlation is crucial for an accurate description of the interatomic interactions and the core-core and core-valence contributions are significant, especially for the *AM*-Zn and *AM*-Cd molecules. The addition of a bond function to the aug-cc-pwCV5Z-PP basis set allows describing the complete-basis-set-limit energy accurately.

Finally, we analyze the convergence of the interatomic interaction energy with the quality of employed wave-function representation. Figure 5 presents the potential-energy curves for the representative RbZn and SrZn molecules in the $X\,^2\Sigma^+$ and $X\,^1\Sigma^+$ electronic states, respectively, calculated at different levels of theory: RHF (spin-restricted Hartree-Fock), MRCISD, MRCISD+Q, MP2 (second-order Møller-Plesset perturbation theory), CCSD, CCSD(T), CCSD(T)+ΔT, and CCSD(T)+ΔT + ΔQ. The aug-cc-pwCV5Z-PP+BF basis set is used in the CCSD(T) calculations, aug-cc-pVTZ-PP is used in the calculation of the full triple correction ΔT, and aug-cc-pVDZ-PP is used in the calculation of the full quadruple correction ΔQ.

In the coupled-cluster calculations, the inclusion of higher-order excitations significantly improves the description of the interaction energies. The obtained potential-well depths for the RbZn and SrZn molecules are equal to, respectively, 352 and 391 cm^{-1} at the CCSD(T) level, 368 and 415 cm^{-1} at the CCSD(T)+ΔT level, and 372 and 435 cm^{-1} at the CCSD(T)+ΔT + ΔQ level. Hence, the full triple correction increases the well depth by about 4% for RbZn and about 6% for SrZn, while the full quadruple correction introduces a further 1% well-depth increase for RbZn and about 5% for SrZn. Moreover, for the Zn_2, ZnCd, and Cd_2 dimers, the perturbative quadruple correction Δ(Q) (calculated with the use of the aug-cc-pVTZ-PP basis set) increases the potential-well depths obtained at the CCSD(T)+ΔT level by 5% to 7%.

Therefore, an accurate description of the interatomic interactions between closed-shell transition-metal atoms, like zinc and cadmium, and alkali-metal or alkaline-earth-metal atoms has to take into consideration higher-order electron correlation, in contrast to alkali-metal dimers with two valence electrons [79]. The triple-excitation contribution is signifi-

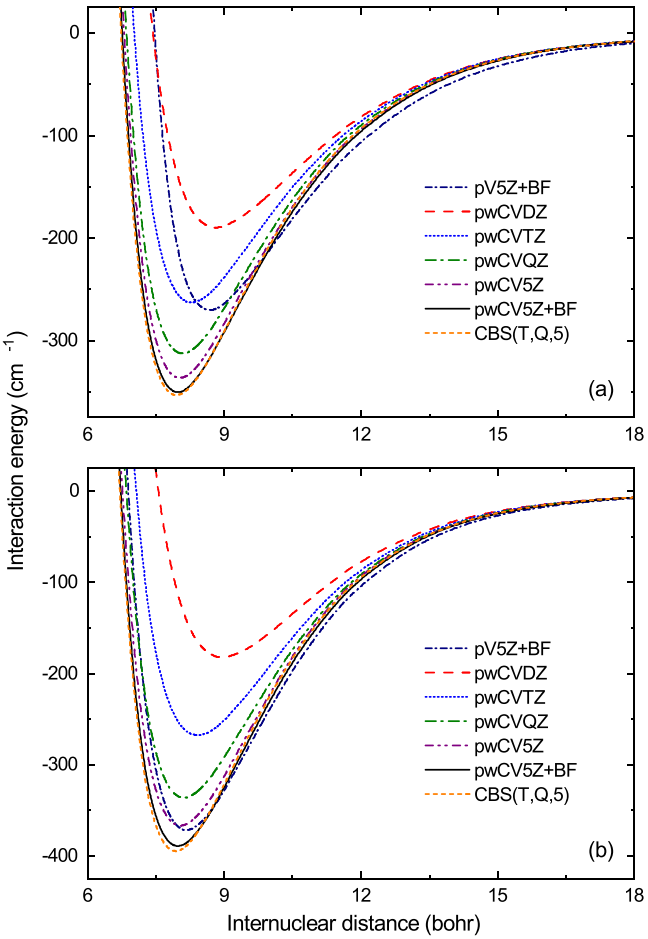

FIG. 4. Potential-energy curves of (a) the RbZn molecule in the $X\ ^2\Sigma^+$ electronic state and (b) the SrZn molecule in the $X\ ^1\Sigma^+$ electronic state, computed with the CCSD(T) method, using different-sized Gaussian basis sets. CBS limit energy for the aug-cc-pwCVnZ basis sets is also presented.

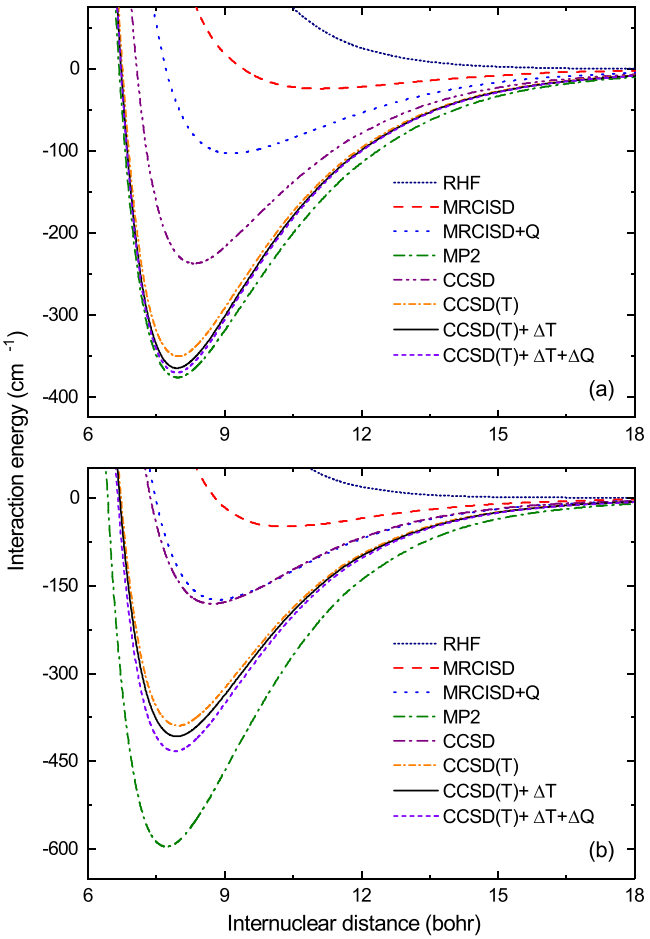

FIG. 5. Potential-energy curves of (a) the RbZn molecule in the $X\ ^2\Sigma^+$ electronic state and (b) the SrZn molecule in the $X\ ^1\Sigma^+$ electronic state computed at different levels of theory: RHF, MRCISD, MRCISD+Q, MP2, CCSD, CCSD(T), CCSD(T)+ΔT, and CCSD(T)+ΔT + ΔQ. See the text for details.

cant for both open-shell AM-Zn and AM-Cd and closed-shell AEM-Zn and AEM-Cd molecules, while the quadruple-excitation contribution is particularly large for closed-shell AEM-Zn and AEM-Cd molecules. It is in agreement with the fact that the CCSDT method for the AM-Zn and AM-Cd molecules with three valence electrons already provides the description of valence electrons at the full configuration interaction level, while the AEM-Zn and AEM-Cd molecules with four valence electrons require the CCSDTQ method for the same.

We also find that the values of the full-iterative triple and full-iterative quadruple corrections systematically decrease with the increasing size of the basis sets, leading us to conclude that the calculated corrections may be slightly overestimated. Overall, we estimate that the uncertainty of our calculations should be at most 5% for molecules containing alkali-metal atoms and slightly more for molecules containing alkaline-earth atoms.

In the MRCISD calculations, the full-valence active space is used. The well depths of the potential-energy curves obtained at the MRCISD level amount to 22.8 cm^{-1} for RbZn and 51.5 cm^{-1} for SrZn. The addition of the Davidson correction, MRCISD+Q, yields deeper PECs, with the well depths of 103 and 175 cm^{-1}, respectively, for RbZn and SrZn, yet the results are still not comparable to those obtained with the coupled-cluster method. We also calculate the PECs within the MRCISD method with $4p$ Zn orbitals and $5p$ Rb/Sr orbitals included in the active space; however, this approach leads to almost identical results. Interestingly, those PECs do not differ significantly from the ones obtained at the CISD level, meaning that the ground electronic states of RbZn and SrZn are well described by a single reference, and higher-order excitations need to be taken into account to reproduce the coupled-cluster results. We also see that the energies obtained within the second-order Møller-Plesset perturbation theory (MP2) are overestimated, particularly for the SrZn molecule.

D. Chemical reactions

We use the calculated potential-well depths D_e to assess the stability of the investigated molecules against atom-exchange chemical reactions [80–82]. A ground-state heteronuclear

molecule AB can undergo an atom-exchange chemical reaction,

$$AB + AB \rightarrow A_2 + B_2, \tag{1}$$

provided that the sum of the dissociation energies D_0 of the products, A_2 and B_2, is larger than or equal to the sum of the dissociation energies of the reactants, $2AB$,

$$D_0(A_2) + D_0(B_2) \geqslant 2D_0(AB). \tag{2}$$

The dissociation energy D_0 is related to the potential-well depth D_e, $D_0 \approx D_e - \frac{1}{2}\omega_e$.

All the studied AM-Zn, AM-Cd, AEM-Zn, and AEM-Cd molecules in the ground rovibrational levels of their ground electronic states are chemically unstable, and atom-exchange reactions are energetically possible,

$$\begin{aligned}
2AM\text{-Zn}(X\,^2\Sigma^+) &\rightarrow \text{Zn}_2(X\,^1\Sigma_g^+) + AM_2(X\,^1\Sigma_g^+),\\
2AM\text{-Cd}(X\,^2\Sigma^+) &\rightarrow \text{Cd}_2(X\,^1\Sigma_g^+) + AM_2(X\,^1\Sigma_g^+),\\
2AEM\text{-Zn}(X\,^1\Sigma^+) &\rightarrow \text{Zn}_2(X\,^1\Sigma^+) + AEM_2(X\,^1\Sigma_g^+),\\
2AEM\text{-Cd}(X\,^1\Sigma^+) &\rightarrow \text{Cd}_2(X\,^1\Sigma_g^+) + AEM_2(X\,^1\Sigma_g^+),
\end{aligned} \tag{3}$$

because the well depths of alkali-metal AM_2 and alkaline-earth-metal AEM_2 dimers [80] are significantly larger than those of the present molecules.

The atom-exchange chemical reactions for the AM-Zn and AM-Cd molecules could potentially be suppressed by restricting the collision dynamic to the high-spin potential-energy surfaces by fully spin polarizing the molecules in an external magnetic field [81]. Unfortunately, only channels leading to alkali-metal dimers in the $a\,^3\Sigma_u^+$ electronic state are closed, while ones leading to Cd_2 and Zn_2 in the $a\,^3\Sigma_u^+$ electronic state are open,

$$\begin{aligned}
2AM\text{-Zn}(X\,^2\Sigma^+) &\not\rightarrow \text{Zn}_2(X\,^1\Sigma_g^+) + AM_2(a\,^3\Sigma_u^+),\\
2AM\text{-Cd}(X\,^2\Sigma^+) &\not\rightarrow \text{Cd}_2(X\,^1\Sigma_g^+) + AM_2(a\,^3\Sigma_u^+),\\
2AM\text{-Zn}(X\,^2\Sigma^+) &\rightarrow \text{Zn}_2(a\,^3\Sigma_u^+) + AM_2(X\,^1\Sigma_g^+),\\
2AM\text{-Cd}(X\,^2\Sigma^+) &\rightarrow \text{Cd}_2(a\,^3\Sigma_u^+) + AM_2(X\,^1\Sigma_g^+).
\end{aligned} \tag{4}$$

Finally, most likely, the trimer formation reactions are another path of chemical losses for all considered molecules [80–82],

$$AB + AB \rightarrow A_2B + B, \tag{5}$$

but their detailed study is out of the scope of this work.

IV. SUMMARY AND CONCLUSIONS

Motivated by the recent progress in laser cooling and trapping of cadmium atoms [24,55–57] and experimental realizations of ultracold mixtures of closed-shell and open-shell atoms [40–43], in this paper, we brought attention to diatomic molecules composed of a closed-shell zinc or cadmium atom interacting with an alkali-metal (Li, Na, K, Rb, Cs, Fr) or alkaline-earth-metal (Be, Mg, Ca, Sr, Ba, Ra) atom. Such molecules are potential candidates for ultracold quantum physics and chemistry experiments, ranging from controlled chemical reactions to precision measurements. To this end, we have carried out state-of-the-art *ab initio* calculations of the potential-energy curves, permanent electric dipole moments, and spectroscopic constants for the molecules in their electronic ground states. We have used the *ab initio* electronic structure coupled-cluster method with single, double, and triple excitations combined with large Gaussian basis sets and small-core relativistic energy-consistent pseudopotentials for heavier atoms. We have predicted that the studied molecules in the ground electronic state are weakly bound van der Waals complexes. We have also found that they have rather small permanent electric dipole moments, despite Zn and Cd atoms having electronegativity significantly larger than that of alkali-metal and alkaline-earth-metal atoms. Finally, we have concluded that they are chemically reactive, and for applications other than studies of ultracold chemical reactions, they should be segregated in an optical lattice, or shielding strategies should be employed [83].

Full potential-energy curves and permanent electric dipole moments as a function of interatomic distance in a numerical form are collected in the Supplemental Material [84].

ACKNOWLEDGMENTS

We acknowledge the financial support from the National Science Centre of Poland (Grant No. 2016/23/B/ST4/03231) and the Foundation for Polish Science within the First Team program cofinanced by the European Union under the European Regional Development Fund. The computational part of this research was partially supported by the PL-Grid Infrastructure.

[1] L. D. Carr, D. DeMille, R. V. Krems, and J. Ye, New J. Phys. **11**, 055049 (2009).
[2] G. Quéméner and P. S. Julienne, Chem. Rev. **112**, 4949 (2012).
[3] J. L. Bohn, A. M. Rey, and J. Ye, Science **357**, 1002 (2017).
[4] S. Baier, M. J. Mark, D. Petter, K. Aikawa, L. Chomaz, Z. Cai, M. Baranov, P. Zoller, and F. Ferlaino, Science **352**, 201 (2016).
[5] C. Gross and I. Bloch, Science **357**, 995 (2017).
[6] S. Ospelkaus, K.-K. Ni, D. Wang, M. H. G. de Miranda, B. Neyenhuis, G. Quéméner, P. S. Julienne, J. L. Bohn, D. S. Jin, and J. Ye, Science **327**, 853 (2010).
[7] M. Tomza, Phys. Rev. Lett. **115**, 063201 (2015).
[8] M.-G. Hu, Y. Liu, D. D. Grimes, Y.-W. Lin, A. H. Gheorghe, R. Vexiau, N. Bouloufa-Maafa, O. Dulieu, T. Rosenband, and K.-K. Ni, Science **366**, 1111 (2019).
[9] D. DeMille, J. M. Doyle, and A. O. Sushkov, Science **357**, 990 (2017).

[10] M. S. Safronova, D. Budker, D. DeMille, D. F. J. Kimball, A. Derevianko, and C. W. Clark, Rev. Mod. Phys. **90**, 025008 (2018).

[11] M. McDonald, B. H. McGuyer, F. Apfelbeck, C.-H. Lee, I. Majewska, R. Moszynski, and T. Zelevinsky, Nature (London) **535**, 122 (2016).

[12] S. S. Kondov, C.-H. Lee, K. H. Leung, C. Liedl, I. Majewska, R. Moszynski, and T. Zelevinsky, Nat. Phys. **15**, 1118 (2019).

[13] A. Derevianko and H. Katori, Rev. Mod. Phys. **83**, 331 (2011).

[14] H. Katori, M. Takamoto, V. G. Pal'chikov, and V. D. Ovsiannikov, Phys. Rev. Lett. **91**, 173005 (2003).

[15] A. D. Ludlow, T. Zelevinsky, G. K. Campbell, S. Blatt, M. M. Boyd, M. H. G. de Miranda, M. J. Martin, J. W. Thomsen, S. M. Foreman, J. Ye, T. M. Fortier, J. E. Stalnaker, S. A. Diddams, Y. Le Coq, Z. W. Barber, N. Poli, N. D. Lemke, K. M. Beck, and C. W. Oates, Science **319**, 1805 (2008).

[16] N. D. Lemke, A. D. Ludlow, Z. W. Barber, T. M. Fortier, S. A. Diddams, Y. Jiang, S. R. Jefferts, T. P. Heavner, T. E. Parker, and C. W. Oates, Phys. Rev. Lett. **103**, 063001 (2009).

[17] R. Le Targat, L. Lorini, Y. Le Coq, M. Zawada, J. Guéna, M. Abgrall, M. Gurov, P. Rosenbusch, D. G. Rovera, B. Nagórny, R. Gartman, P. G. Westergaard, M. E. Tobar, M. Lours, G. Santarelli, A. Clairon, S. Bize, P. Laurent, P. Lemonde, and J. Lodewyck, Nat. Commun. **4**, 2109 (2013).

[18] N. Poli, Z. W. Barber, N. D. Lemke, C. W. Oates, L. S. Ma, J. E. Stalnaker, T. M. Fortier, S. A. Diddams, L. Hollberg, J. C. Bergquist, A. Brusch, S. Jefferts, T. Heavner, and T. Parker, Phys. Rev. A **77**, 050501(R) (2008).

[19] H. Hachisu, K. Miyagishi, S. G. Porsev, A. Derevianko, V. D. Ovsiannikov, V. G. Pal'chikov, M. Takamoto, and H. Katori, Phys. Rev. Lett. **100**, 053001 (2008).

[20] J. J. McFerran, L. Yi, S. Mejri, S. Di Manno, W. Zhang, J. Guéna, Y. Le Coq, and S. Bize, Phys. Rev. Lett. **108**, 183004 (2012).

[21] K. Yamanaka, N. Ohmae, I. Ushijima, M. Takamoto, and H. Katori, Phys. Rev. Lett. **114**, 230801 (2015).

[22] V. D. Ovsiannikov, S. I. Marmo, V. G. Palchikov, and H. Katori, Phys. Rev. A **93**, 043420 (2016).

[23] V. A. Dzuba and A. Derevianko, J. Phys. B **52**, 215005 (2019).

[24] A. Yamaguchi, M. S. Safronova, K. Gibble, and H. Katori, Phys. Rev. Lett. **123**, 113201 (2019).

[25] S. G. Porsev and M. S. Safronova, Phys. Rev. A **102**, 012811 (2020).

[26] M. S. Safronova, S. G. Porsev, U. I. Safronova, M. G. Kozlov, and C. W. Clark, Phys. Rev. A **87**, 012509 (2013).

[27] S. Kolkowitz, S. L. Bromley, T. Bothwell, M. L. Wall, G. E. Marti, A. P. Koller, X. Zhang, A. M. Rey, and J. Ye, Nature (London) **542**, 66 (2017).

[28] A. Goban, R. B. Hutson, G. E. Marti, S. L. Campbell, M. A. Perlin, P. S. Julienne, J. P. D'Incao, A. M. Rey, and J. Ye, Nature (London) **563**, 369 (2018).

[29] E. J. Angstmann, V. A. Dzuba, and V. V. Flambaum, Phys. Rev. A **70**, 014102 (2004).

[30] P. S. Żuchowski, J. Aldegunde, and J. M. Hutson, Phys. Rev. Lett. **105**, 153201 (2010).

[31] M. G. Kozlov and A. Derevianko, Phys. Rev. Lett. **97**, 063001 (2006).

[32] M. Kajita, G. Gopakumar, M. Abe, and M. Hada, Phys. Rev. A **84**, 022507 (2011).

[33] E. R. Meyer and J. L. Bohn, Phys. Rev. A **80**, 042508 (2009).

[34] V. S. Prasannaa, A. C. Vutha, M. Abe, and B. P. Das, Phys. Rev. Lett. **114**, 183001 (2015).

[35] A. Sunaga, V. S. Prasannaa, M. Abe, M. Hada, and B. P. Das, Phys. Rev. A **98**, 042511 (2018).

[36] M. Verma, A. M. Jayich, and A. C. Vutha, Phys. Rev. Lett. **125**, 153201 (2020).

[37] T. Zelevinsky, S. Kotochigova, and J. Ye, Phys. Rev. Lett. **100**, 043201 (2008).

[38] S. Kotochigova, T. Zelevinsky, and J. Ye, Phys. Rev. A **79**, 012504 (2009).

[39] A. Micheli, G. K. Brennen, and P. Zoller, Nat. Phys. **2**, 341 (2006).

[40] N. Nemitz, F. Baumer, F. Münchow, S. Tassy, and A. Görlitz, Phys. Rev. A **79**, 061403(R) (2009).

[41] V. Barbé, A. Ciamei, B. Pasquiou, L. Reichsöllner, F. Schreck, P. S. Żuchowski, and J. M. Hutson, Nat. Phys. **14**, 881 (2018).

[42] A. Green, H. Li, J. H. See Toh, X. Tang, K. C. McCormick, M. Li, E. Tiesinga, S. Kotochigova, and S. Gupta, Phys. Rev. X **10**, 031037 (2020).

[43] K. E. Wilson, A. Guttridge, J. Segal, and S. L. Cornish, Phys. Rev. A **103**, 033306 (2021).

[44] K. A. Peterson and C. Puzzarini, Theor. Chem. Acc. **114**, 283 (2005).

[45] E. Pahl, D. Figgen, A. Borschevsky, and P. Peterson, and K. A. Schwerdtfeger, Theor. Chem. Acc. **129**, 651 (2011).

[46] L. M. Wei, P. Li, L. W. Qiao, and K. T. Tang, J. Chem. Phys. **139**, 154306 (2013).

[47] T. Urbańczyk, M. Strojecki, M. Krośnicki, A. Kedziorski, P. S. Żuchowski, and J. Koperski, Int. Rev. Phys. Chem. **36**, 541 (2017).

[48] L. Thiel, H. Hotop, and W. Meyer, J. Chem. Phys. **119**, 9008 (2003).

[49] A. Sunaga, V. S. Prasannaa, M. Abe, M. Hada, and B. P. Das, Phys. Rev. A **99**, 040501(R) (2019).

[50] M. Witkowski, B. Nagórny, R. Munoz-Rodriguez, R. Ciuryło, P. S. Żuchowski, S. Bilicki, M. Piotrowski, P. Morzyński, and M. Zawada, Opt. Express **25**, 3165 (2017).

[51] M. Witkowski, R. Munoz-Rodriguez, A. Raczyński, J. Zaremba, B. Nagórny, P. S. Żuchowski, R. Ciuryło, and M. Zawada, Phys. Rev. A **98**, 053444 (2018).

[52] M. Borkowski, R. Muñoz Rodriguez, M. B. Kosicki, R. Ciuryło, and P. S. Żuchowski, Phys. Rev. A **96**, 063411 (2017).

[53] E. J. Salumbides, J. C. J. Koelemeij, J. Komasa, K. Pachucki, K. S. E. Eikema, and W. Ubachs, Phys. Rev. D **87**, 112008 (2013).

[54] M. Borkowski, A. A. Buchachenko, R. Ciuryło, P. S. Julienne, H. Yamada, Y. Kikuchi, Y. Takasu, and Y. Takahashi, Sci. Rep. **9**, 14807 (2019).

[55] H. L. Xu, A. Persson, S. Svanberg, K. Blagoev, G. Malcheva, V. Pentchev, E. Biémont, J. Campos, M. Ortiz, and R. Mayo, Phys. Rev. A **70**, 042508 (2004).

[56] K.-A. Brickman, M.-S. Chang, M. Acton, A. Chew, D. Matsukevich, P. C. Haljan, V. S. Bagnato, and C. Monroe, Phys. Rev. A **76**, 043411 (2007).

[57] Y. Kaneda, J. M. Yarborough, Y. Merzlyak, A. Yamaguchi, K. Hayashida, N. Ohmae, and H. Katori, Opt. Lett. **41**, 705 (2016).

[58] S. Boys and F. Bernardi, Mol. Phys. **19**, 553 (1970).

[59] D. Figgen, G. Rauhut, M. Dolg, and H. Stoll, Chem. Phys. **311**, 227 (2005).

[60] I. S. Lim, P. Schwerdtfeger, B. Metz, and H. Stoll, J. Chem. Phys. **122**, 104103 (2005).
[61] I. S. Lim, H. Stoll, and P. Schwerdtfeger, J. Chem. Phys. **124**, 034107 (2006).
[62] J. G. Hill and K. A. Peterson, J. Chem. Phys. **147**, 244106 (2017).
[63] B. P. Prascher, D. E. Woon, K. A. Peterson, T. H. Dunning, and A. K. Wilson, Theor. Chem. Acc. **128**, 69 (2011).
[64] H.-J. Werner, P. J. Knowles, G. Knizia, F. R. Manby, and M. Schütz, Wiley Interdiscip. Rev.: Comput. Mol. Sci. **2**, 242 (2012).
[65] H.-J. Werneret al., MOLPRO, version 2019.2, a package of *ab initio* programs, https://www.molpro.net.
[66] M. Kállay, P. R. Nagy, D. Mester, Z. Rolik, G. Samu, J. Csontos, J. Csóka, P. B. Szabó, L. Gyevi-Nagy, B. Hégely, I. Ladjánszki, L. Szegedy, B. Ladóczki, K. Petrov, M. Farkas, P. D. Mezei, and Á. Ganyecz, J. Chem. Phys. **152**, 074107 (2020).
[67] E. Tiesinga, C. J. Williams, and P. S. Julienne, Phys. Rev. A **57**, 4257 (1998).
[68] L. W. Qiao, P. Li, and K. T. Tang, J. Chem. Phys. **137**, 084309 (2012).
[69] R. Guérout, M. Aymar, and O. Dulieu, Phys. Rev. A **82**, 042508 (2010).
[70] M. C. Heaven, V. E. Bondybey, J. M. Merritt, and A. L. Kaledin, Chem. Phys. Lett. **506**, 1 (2011).
[71] J. V. Pototschnig, A. W. Hauser, and W. E. Ernst, Phys. Chem. Chem. Phys. **18**, 5964 (2016).
[72] M. Strojecki, M. Ruszczak, M. Krośnicki, M. Łukomski, and J. Koperski, Chem. Phys. **327**, 229 (2006).
[73] M. Strojecki, M. Krośnicki, P. Zgoda, and J. Koperski, Chem. Phys. Lett. **489**, 20 (2010).
[74] L. Pauling, *The Nature of the Chemical Bond* (Cornell University Press, Ithaca, NY, 1960).
[75] M. Smialkowski and M. Tomza, Phys. Rev. A **103**, 022802 (2021).
[76] P. Schwerdtfeger and J. K. Nagle, Mol. Phys. **117**, 1200 (2019).
[77] J. Sugar and A. Musgrove, J. Phys. Chem. Ref. Data **24**, 1803 (1995).
[78] A. G. Shenstone and J. T. Pittenger, J. Opt. Soc. Am. **39**, 219 (1949).
[79] M. Gronowski, A. M. Koza, and M. Tomza, Phys. Rev. A **102**, 020801(R) (2020).
[80] P. S. Żuchowski and J. M. Hutson, Phys. Rev. A **81**, 060703(R) (2010).
[81] M. Tomza, K. W. Madison, R. Moszynski, and R. V. Krems, Phys. Rev. A **88**, 050701(R) (2013).
[82] M. Smialkowski and M. Tomza, Phys. Rev. A **101**, 012501 (2020).
[83] L. Anderegg, S. Burchesky, Y. Bao, S. S. Yu, T. Karman, E. Chae, K.-K. Ni, W. Ketterle, and J. M. Doyle, Science **373**, 779 (2021).
[84] See Supplemental Material at http://link.aps.org/supplemental/10.1103/PhysRevA.104.042816 for the calculated potential-energy curves and permanent electric dipole moments in a numerical form.

3.3 Paper III: *Ultracold mixtures of Cr and Li atoms: theoretical prospects for controlled atomic collisions, LiCr molecule formation, and molecular precision measurements*

Paper III

"Ultracold mixtures of Cr and Li atoms: theoretical prospects for controlled atomic collisions, LiCr molecule formation, and molecular precision measurements"

Klaudia Zaremba-Kopczyk, Marcin Gronowski, and Michał Tomza

Preprint (2023)

Commentary

Motivated by the ongoing experiment on the ^{53}Cr+^{6}Li ultracold Fermi-Fermi mixture realized by the group of M. Zaccanti [67; 68], we have theoretically investigated interatomic interactions and ultracold atom-atom collisions between chromium and lithium atoms. The project has involved calculations of the potential energy curves for both the ground and excited states of LiCr molecule with the use of *ab initio* quantum chemistry methods, as well as quantum scattering calculations, followed by the analysis of the prospects for magnetoassociation via magnetic Feshbach resonances and photoassociation of chromium and lithium into polar and highly magnetic LiCr molecules. We have also proposed precision measurements of the variation of the proton-to-electron mass ratio using ultracold LiCr molecules. To our knowledge, this work tackles for the first time (in the context of ultracold studies) the calculation of excited electronic states of a molecule containing an atom with a more complex internal structure than that of an alkali-metal or alkaline-earth-metal atom.

In the work presented in Paper III, the PhD Candidate: calculated the potential energy curves and the permanent and transition electric dipole moments for the quartet, sextet, and octet electronic states of the LiCr molecule correlated to the four lowest atomic dissociation limits, analyzed chemical reactivity of the LiCr molecule in the $X\,^{6}\Sigma^{+}$ and $a\,^{8}\Sigma^{+}$ electronic states, analyzed the prospects for precision measurements of the variation of m_p/m_e using ultracold LiCr molecules, computed the scattering lengths for ultracold collisions between different isotopes of Cr and Li atoms as a function of the system's reduced mass for the $X\,^{6}\Sigma^{+}$ and $a\,^{8}\Sigma^{+}$ potential energy curves, and calculated magnetically tunable Feshbach resonances for ultracold ^{52}Cr+^{6}Li and ^{53}Cr+^{6}Li collisions to assess prospects for magnetoassociation into polar and highly magnetic LiCr molecules. The results obtained by the PhD Candidate are presented in Sections III.A, III.C, and III.E-G of Paper III. The PhD Candidate also prepared all figures and tables presented in Paper III and wrote the first version of the manuscript. The submission of the manuscript has been postponed due to the ongoing collaboration with the experimental group of M. Zaccanti.

Ultracold mixtures of Cr and Li atoms: theoretical prospects for controlled atomic collisions, LiCr molecule formation, and molecular precision measurements

Klaudia Zaremba-Kopczyk,[1] Marcin Gronowski,[1] and Michał Tomza[1,*]

[1]*Faculty of Physics, University of Warsaw, Pasteura 5, 02-093 Warsaw, Poland*

(Dated: July 31, 2023)

We theoretically investigate interatomic interactions and ultracold collisions between chromium and lithium atoms. We use the coupled cluster and multireference configuration interaction methods to calculate the potential energy curves and the permanent and transition electric dipole moments for the quartet, sextet, and octet electronic states of the LiCr molecule correlated to the four lowest atomic dissociation limits. We find that the LiCr molecule in the $X\,^6\Sigma^+$ ground electronic state is strongly bound with the well depth of 8406(150) cm^{-1} and has a large permanent electric dipole moment of 3.3 D at an equilibrium distance of 4.87 bohr, while the $a\,^8\Sigma^+$ first excited electronic states is weakly bound with the well depth of 565(18) cm^{-1} and has a noticeable permanent electric dipole moment of 0.7 D at the equilibrium distance of 6.48 bohr. We also report fine and hyperfine coupling constants for ground-state interactions. Next, we employ the electronic structure data in nuclear dynamics calculations. We investigate the optical paths of forming deeply-bound LiCr molecules via photoassociation and stimulated Raman adiabatic passage. We propose precision measurements of the variation of electron-to-proton mass ratio using ultracold LiCr molecules. We predict the scattering lengths for the ultracold spin-polarized Cr+Li collisions (37^{+29}_{-22} bohr for ^{53}Cr+^{6}Li) governed by the $a\,^8\Sigma^+$ electronic state without any adjustment to experimental data and in good agreement with recent experimental measurements. Finally, we calculate magnetically tunable Feshbach resonances for ultracold ^{52}Cr+^{6}Li and ^{53}Cr+^{6}Li collisions and assess prospects for magnetoassociation into polar and highly magnetic LiCr molecules. Present theoretical results may guide and explain ongoing experimental studies on ultracold strongly-interacting mass-imbalanced Li+Cr mixtures and LiCr molecules.

I. INTRODUCTION

Recent years have seen remarkable progress in atom cooling and trapping techniques, enabling to reach the ultralow temperature regime with species of more and more complex internal structure. In this direction, one substantial achievement was the realization of ultracold samples of highly magnetic transition-metal or lanthanide atoms, such as Cr ($^7S_3$) [1–3], Dy ($^5I_8$) [4, 5], Er ($^3H_6$) [6, 7], and Eu ($^8S_{7/2}$) [8] while magneto-optical cooling and trapping of Tm ($^2F_{7/2}$) [9, 10], Ho ($^4I_{15/2}$) [11], and In ($^2P_{3/2}$) [12] have also been demonstrated. The large electronic angular momenta of these atoms are the source of their high magnetic moments that, in turn, give rise to strong dipole-dipole interatomic interactions.

Ultracold quantum gases of highly magnetic atoms have set the stage for the investigation of the interplay between tunable short-range contact interactions and long-range anisotropic dipole-dipole interactions (DDIs), leading to the observation of many intriguing phenomena [13]. The pioneering experimental works on dipolar quantum gases involved the use of chromium atoms, whose high magnetic moment of 6 Bohr magnetons (μ_B) stems solely from their large electronic spin angular momentum. In the chromium Bose-Einstein condensate, the magnetic DDIs were already strong enough to manifest themselves in the condensate stability dependent on the magnetic moments' orientation [14–16]. Further experiments have employed lanthanide erbium and dysprosium atoms, whose even higher magnetic moments of around 7 μ_B and 10 μ_B, respectively, combined with their larger atomic masses, have allowed observing even more pronounced dipolar effects, such as the Fermi surface deformation [17], Rosensweig instability of a quantum ferrofluid [18], self-bound quantum droplets [19], or supersolidity [20–22]. Additionally, the anisotropy of electronic interactions introduced by the large orbital angular momenta of these atoms has been shown to induce a chaotic character of their ultracold collisions [23, 24]. Dipolar quantum gases have moreover enabled the realization of complex spin models [25].

The majority of the aforementioned experiments utilized magnetic Feshbach resonances to tune the ratio between contact interaction and magnetic dipole-dipole interaction strengths. Magnetically tunable Feshbach resonances serve as an unprecedented tool to control the collisional properties of ultracold quantum gases and are crucial for the formation of ultracold molecules via magnetoassociation [26–28]. There is currently an increased interest in the production of ultracold molecules as their richer internal structure, as compared to atoms, offers new insights into many-body physics, quantum chemistry, or fundamental physics [28–30].

Quantum mixtures of highly magnetic transition-metal or lanthanide atoms with open-shell or closed-shell S-state atoms are favorable systems to study, offering prospects for the formation of ground-state polar molecules with large both electric and

* michal.tomza@fuw.edu.pl

magnetic dipole moments. The additional degrees of freedom in the molecular internal structure and an interplay of long-range electric and magnetic interactions would allow for novel applications in quantum computation and quantum simulations, controlled chemistry, and more [28–31]. Moreover, heteronuclear quantum mixtures serve as a promising platform for studies of impurity physics, magnetic polarons, Efimov physics, or exotic regimes of superfluidity [32–51]. Therefore, cold and ultracold mixtures of Dy+Er [52], Dy+K [53–55], Cr+Li [56–58], Er+Li [59, 60], and Er+Yb [61] are currently being investigated experimentally, while magnetoassociation into weakly-bound homonuclear Er_2 [62] and heteronuclear KDy [63] dimers as well as photoassocation into spin-polarized Cr_2 homonuclear dimers [64] have already been demonstrated. Regarding theoretical studies, the electronic structure of ground-state chromium–alkali-metal-atom molecules [65–67] and chromium–alkaline-earth-metal-atom molecules and their ions [68, 69], or the electronic structure of ground-state europium–alkali-metal-atom and europium–alkaline-earth-metal-atom molecules [70] have been investigated, along with collisional properties of Cr+Rb [65], Cr+Ca^+/Sr^+/Ba^+/Yb^+ [69], Er+Li [71], Eu+Li/Rb [72], Er+Yb [73], Er+Sr, or Dy+Yb [74] ultracold mixtures.

Ultracold Fermi-Fermi mixtures such as ^{161}Dy+^{40}K [53, 54] or ^{53}Cr+^{6}Li [56–58] possess another favorable feature, which is the peculiar mass imbalance between constituent species that, according to theoretical predictions, should allow for the access to novel superfluid states with exotic pairing mechanisms, such as the Fulde-Ferrell-Larkin-Ovchinnikov or Sarma phases [45–50]. Among the few two-component Fermi mixtures that have been realized experimentally: ^{40}K+^{6}Li [75, 76], ^{173}Yb+^{6}Li [77, 78], ^{161}Dy+^{40}K [53, 54], and ^{53}Cr+^{6}Li [56–58], only the latter two combine the prerequisites to reach the strongly interacting regime: collisional stability, tunability of interactions, and a mass ratio below 13.6 [41]. In addition, mass-imbalanced fermionic mixtures offer exotic few-body effects like p-wave atom-dimer interactions [42, 44] or non-Efimovian weakly-bound trimer, tetramer, and pentamer states [41, 51].

While cold and ultracold gases of ^{52}Cr or ^{53}Cr isotopes have already been subject to successful experimental studies [1–3, 14–16, 64], initially little progress has been made towards heteronuclear mixtures of chromium with alkali-metal atoms since the realization of a two-species magnetooptical trap (MOT) for ^{52}Cr and ^{87}Rb in 2004 [79], where the operation of superimposed MOTs was limited by the photoionization of the excited state of the Rb atoms by the Cr cooling-laser light. Only recently, the production of a cold fermionic mixture of ^{53}Cr and ^{6}Li atoms was reported [56] and paved the way for the very recent investigation of ultracold collisions and magnetically tunable Feshbach resonances in Fermi-Fermi mixture of ^{53}Cr and ^{6}Li atoms [57, 58]. This experimental progress further motivates the present study.

In this communication, we bring attention to ultracold mixtures of chromium and lithium atoms and related diatomic molecules. We show that a heteronuclear diatomic molecule composed of chromium and lithium atoms possesses both large magnetic and electric dipole moments, similar to the RbCr molecule that was already investigated theoretically [65]. We explore the electronic structure of the LiCr molecule both in the ground and excited electronic states using state-of-the-art electronic structure methods. We provide more accurate potential energy curves for the ground-state asymptote than previously reported in the literature [66, 67]. We also analyze the magnitude of fine and hyperfine interactions between Cr and Li atoms in their ground electronic states. We calculate for the first time in the context of ultracold studies the potential energy curves for the excited states of a heteronuclear molecule comprising a highly magnetic atom. We predict the optical formation of deeply-bound LiCr molecules using photoassociation and stimulated Raman adiabatic passage. We analyze the chemical stability of the investigated molecules and point out their possible applications in precision measurements of the variation of electron-to-proton mass ratio. Our interaction potential describing spin-polarize collisions is accurate enough to predict the scattering lengths without any adjustment to experimental data for the first time for collisions involving a transition-metal atom. Finally, we investigate magnetically tunable Feshbach resonances between ultracold ^{6}Li and ^{52}Cr or ^{53}Cr isotopes with the use of multichannel quantum scattering calculations and study prospects for magnetoassociation into highly magnetic and polar molecules LiCr.

The paper is organized as follows. Section II introduces the theory underlying *ab initio* electronic structure and quanutm scattering calculations. Section III presents the obtained numerical results and discusses their physical implications. Section IV summarizes our findings.

II. COMPUTATIONAL METHODS

A. Electronic structure calculations

The LiCr molecule consists of an open-shell chromium atom with six valence electrons ($3d^5 4s^1$) interacting with an open-shell lithium atom with one valence electron ($2s^1$). The seven valence electrons of the resulting system give rise to a sextet multiplicity of the ground electronic state, while excited states can be either quartets, sextets, or octets. Here, we consider the electronic states of the LiCr molecule that correlate asymptotically to the atomic states with excitation energies below 20 000 cm^{-1}, i.e., Cr(^7S)+Li(^2S), Cr(^5S)+Li(^2S), Cr(^5D)+Li(^2S), and Cr(^7S)+Li(^2P) (see Tables I and II).

The potential energy curves (PECs) for all electronic states are obtained within the Born-Oppenheimer approximation using the internally contracted multireference configuration interaction method restricted to single and double excitations (MRCISD). The orbitals employed in the MRCISD calculations are optimized using the multi-configurational self-consistent field method (MCSCF) with large active spaces, including molecular orbitals created from the $3d$, $4s$, $4p$, and $4d$ orbitals of the Cr atom and

TABLE I. Atomic excitation energies and ionization potentials of the Cr and Li atoms calculated with the MRCISD+Q and RCCSD(T) methods and compared with experimental data. All energies are in cm^{-1}.

Electronic transition	MRCISD+Q	RCCSD(T)	Exp. [88–90]
$\mathrm{Cr}(^7S \rightarrow {}^5S)$	7293	–	7593
$\mathrm{Cr}(^7S \rightarrow {}^5D)$	8105	8035	8088
$\mathrm{Li}(^2S \rightarrow {}^2P)$	14852	14908	14904
$\mathrm{Li}(^2S) \rightarrow \mathrm{Li}^+(^1S)$	–	43480	43487
$\mathrm{Cr}(^7S) \rightarrow \mathrm{Cr}^+(^6S)$	–	54653	54576

$2s$ and $2p$ orbitals of the Li atom. We also include the Davidson correction (MRCISD+Q). Additionally, the PECs of the ground state and the lowest-lying excited electronic states in each irreducible representation of the C_{2v} symmetry are computed with the use of the spin-restricted open-shell coupled-cluster method restricted to single, double, and noniterative triple excitations, RCCSD(T). The counterpoise-corrected interaction energies are computed within the supermolecule approach [80]:

$$V_{\mathrm{int}}(R) = E_{\mathrm{LiCr}}(R) - E_{\mathrm{Cr}}(R) - E_{\mathrm{Li}}(R)\,, \tag{1}$$

where $V_{\mathrm{int}}(R)$ is the interaction energy at an internuclear distance R, $E_{\mathrm{LiCr}}(R)$ is the total energy of the LiCr molecule, and $E_{\mathrm{Cr}}(R)$ and $E_{\mathrm{Li}}(R)$ are the total energies of the atoms calculated in the diatom's basis set.

We employ large Gaussian basis sets to describe all 27 electrons of the LiCr molecule. The scalar relativistic effects are included by the third-order Douglas-Kroll-Hess (DKH) relativistic Hamiltonian [81, 82] while the relativistic spin-orbit coupling is neglected. The augmented correlation-consistent polarized valence and (weighted) core-valence quintuple-ζ quality basis sets optimized with the DKH Hamiltonian are used to describe the 24 electrons of the Cr atom (aug-cc-pV5Z-DK and aug-cc-pwCV5Z-DK) [83] and the 3 electrons of the Li atom (aug-cc-pV5Z-DK and aug-cc-pCV5Z-DK) [84]. For the aug-cc-pV5Z-DK basis sets, we correlate only the valence electrons, while for aug-cc-pCV5Z-DK basis sets, we correlate electrons from the two outermost shells of the considered atoms. The atomic basis sets are additionally augmented by a set of bond functions (BF) [85, 86] to accelerate the convergence toward the complete basis set limit (CBS).

The interaction potential between two neutral atoms in the electronic ground state at large internuclear distances R is dominated by the dispersion interaction of the form $-C_6/R^6$, where the leading dispersion (van der Waals) coefficient C_6 is given by:

$$C_6 = \frac{3}{\pi}\int_0^\infty \alpha_{\mathrm{Cr}}(i\omega)\alpha_{\mathrm{Li}}(i\omega)\mathrm{d}\omega, \tag{2}$$

i.e., the integral over the product of dynamic polarizabilities of the Cr(Li) atom at an imaginary frequency, $\alpha_{\mathrm{Cr(Li)}}(i\omega)$. The dynamic polarizability $\alpha_{\mathrm{Li}}(i\omega)$ is taken from Ref. [87], while $\alpha_{\mathrm{Cr}}(i\omega)$ from Ref. [68].

In order to assess the uncertainty of the molecular electronic structure calculations, we first examine whether the employed *ab initio* methods reproduce the atomic properties accurately. To this end, we first compare the calculated theoretical excitation energies and ionization potentials (IPs) of the chromium and lithium atoms with experimental data found in Refs. [88–90] (see Table I). We neglect the spin-orbit coupling in all electronic structure calculations, hence the excitation energies presented in Table I were averaged out over the energy shifts for different values of the total angular momentum. The excitation energies and IPs are computed with the use of both MRCISD+Q with the aug-cc-pV5Z-DK basis sets and RCCSD(T) with the aug-cc-p(w)CV5Z-DK basis sets. We observe that for the excitation energy of Cr to the lowest excited state, $\mathrm{Cr}(3d^54s\,{}^7S \rightarrow 3d^54s\,{}^5S)$, the value obtained at the MRCI+Q level of theory agrees with the experimental value within 4%, exhibiting the lowest accuracy. The excitation energy of Cr to the lowest D state, $\mathrm{Cr}(3d^54s\,{}^7S \rightarrow 3d^44s^2\,{}^5D)$, and the ionization potential, $\mathrm{Cr}(3d^54s\,{}^7S) \rightarrow \mathrm{Cr}^+(3d^5\,{}^6S)$, agree within 1% with the experimental values, both for the MRCI+Q and RCCSD(T) calculations. For the lithium

TABLE II. Asymptotic energies (in cm^{-1}) from molecular calculations with the MRCISD+Q and RCCSD(T) methods and molecular states arising from the interaction of the chromium and lithium atom in different electronic states.

Asymptote	MRCISD+Q	RCCSD(T)	Exp. [88, 90]	Molecular states
$\mathrm{Cr}(^7S)$+$\mathrm{Li}(^2S)$	0	0	0	$X\,{}^6\Sigma^+ \equiv (1)\,{}^6\Sigma^+$, $a\,{}^8\Sigma^+ \equiv (1)\,{}^8\Sigma^+$
$\mathrm{Cr}(^5S)$+$\mathrm{Li}(^2S)$	7274	–	7593	$(1)\,{}^4\Sigma^+$, $(2)\,{}^6\Sigma^+$
$\mathrm{Cr}(^5D)$+$\mathrm{Li}(^2S)$	7740	8035	8088	$(2)\,{}^4\Sigma^+$, $(1)\,{}^4\Pi$, $(1)\,{}^4\Delta$, $(3)\,{}^6\Sigma^+$, $(1)\,{}^6\Pi$, $(1)\,{}^6\Delta$
$\mathrm{Cr}(^7S)$+$\mathrm{Li}(^2P)$	15039	14908	14904	$(4)\,{}^6\Sigma^+$, $(2)\,{}^6\Pi$, $(2)\,{}^8\Sigma^+$, $(1)\,{}^8\Pi$

atom, the errors of both the excitation energy to the first excited state, Li($2s\,^2S \rightarrow 2p\,^2P$), and the ionization potential, Li($2s\,^2S$) $\rightarrow$ $Li^+(1s^2\,^1S)$, do not exceed 0.3% with respect to the experimental data, for both the MRCI+Q and RCCSD(T) methods.

Next, for the ground molecular electronic state $X\,^6\Sigma^+ \equiv (1)\,^6\Sigma^+$ and the energetically lowest excited state $a\,^8\Sigma^+ \equiv (1)\,^8\Sigma^+$ that correlate to the Cr(^7S) and Li(^2S) dissociation asymptote, we compute the interaction energies at different levels of theory: spin-restricted Hartree-Fock (RHF), multi-configurational self-consistent field (MCSCF), configuration interaction restricted to single and double excitations (CISD), multireference configuration interaction restricted to single and double excitations (MRCISD) along its version with the Davidson correction (MRCISD+Q), open-shell second-order Møller-Plesset perturbation theory (RMP2), spin-restricted open-shell coupled cluster restricted to single and double excitations (RCCSD), and its version with and noniterative triple excitations [RCCSD(T)]. Additionally, we compute the interaction energies, including the correction for the full triple excitations CCSDT with the aug-cc-pVTZ+bf basis set (RCCSD(T)+ΔT) and the full quadruple excitations CCSDTQ with the aug-cc-pVTZ+BF basis set (RCCSD(T)+ΔT+ΔQ).

We also compute the permanent electric dipole moments and static electric dipole polarizabilities of the $X\,^6\Sigma^+$ and $a\,^8\Sigma^+$ electronic states. We use the finite-field method at the RCCSD(T)/aug-cc-pCV5Z-DK and MRCISD/aug-cc-pV5Z-DK levels of theory. The z axis is chosen along the internuclear axis and oriented from the chromium atom to the lithium atom. The vibrationally averaged dipole moments are calculated as expectation values of R-dependent dipole moment functions with radial vibrational wave functions.

All electronic structure calculations described above are performed with the MOLPRO package of *ab initio* programs [91, 92]. The full triple and quadruple contributions are computed using the MRCC code embedded in MOLPRO [93]. Vibrational eigenstates are calculated numerically with the exact diagonalization of the Hamiltonian for the nuclear motion within the discrete variable representation (DVR) on the non-equidistant grid [94].

B. Quantum scattering calculations

We consider scattering between ground-state chromium atoms Cr($^7S_3$) and ground-state lithium atoms Li($^2S_{1/2}$). Chromium atoms in their ground electronic state do not have any electronic orbital angular momentum ($l_{\rm Cr} = 0$), and their large magnetic dipole moment stems solely from the large electronic spin angular momentum ($s_{\rm Cr} = 3$) of the six unpaired electrons occupying $3d$ and $4s$ orbitals. Lithium atoms have a simple electronic structure, with one valence electron giving rise to the electronic spin angular momentum of $s_{\rm Li} = 1/2$ and no orbital angular momentum ($l_{\rm Li} = 0$). We consider the bosonic ^{52}Cr and fermionic ^{53}Cr chromium isotopes with respective nuclear spins $i = 0$ and $i = 3/2$, and the fermionic lithium isotope ^{6}Li with nuclear spin $i = 1$. The coupling between electronic and nuclear spins results in the hyperfine splitting of the energy levels of ^{53}Cr and ^{6}Li isotopes. The ^{52}Cr isotope has no hyperfine structure. The hyperfine coupling constant for ^{53}Cr is negative and amounts to $a_{\rm hf}^{^{53}{\rm Cr}} = -82.5994(16)$ MHz [95], while the hyperfine coupling constant for ^{6}Li equals to $a_{\rm hf}^{^6{\rm Li}} = 152.137$ MHz [96]. Hence, ^{53}Cr atoms are characterized by the inverse order of hyperfine levels and the hyperfine ground state of angular momentum $f = 9/2$.

The nuclear motion Hamiltonian describing the scattering between Cr and Li atoms reads:

$$\hat{H} = -\frac{\hbar^2}{2\mu}\frac{1}{R}\frac{d^2}{dR^2}R + \frac{\hat{L}^2}{2\mu R^2} + \sum_{S,M_S} V_S(R)|S,M_S\rangle\langle S,M_S| + \hat{H}_{\rm Cr} + \hat{H}_{\rm Li} + \hat{V}_{ss}\,, \tag{3}$$

where R is the internuclear distance, $\hat{L}$ is the rotational angular momentum operator, μ denotes the reduced mass of the colliding atoms, $V_S(R)$ is the Born-Oppenheimer potential energy curve for the state with total electronic spin S, and $|S,M_S\rangle\langle S,M_S|$ is the projection operator onto a state with the total spin S and its space-fixed projection M_S. The atomic Hamiltonians $\hat{H}_j$ with $j =$ Cr, Li describe the hyperfine and Zeeman interactions:

$$\hat{H}_j = a_{\rm hf}^j \hat{s}_j \cdot \hat{i}_j + \left(g_e\mu_{\rm B}\hat{s}_{j,z} + g_j\mu_{\rm N}\hat{i}_{j,z}\right)B_z\,, \tag{4}$$

where $a_{\rm hf}^j$ is the hyperfine coupling constant, $\hat{s}_j$ and $\hat{i}_j$ denote the electron and nuclear spin operators, $g_{e/j}$ – the electron/nuclear g factors, $\mu_{\rm B/N}$ are the Bohr/nuclear magnetons, and B_z is the magnetic field strength. The nuclear magnetons of the considered atoms are taken from Ref. [97]. The last term of the Hamiltonian (3) describes the effective dipolar-like interaction between the electronic spins:

$$\hat{V}_{ss} = \left(\frac{\alpha^2}{R^3} - \lambda_{\rm SO}(R)\right)\left(\hat{s}_{\rm Cr}\cdot\hat{s}_{\rm Li} - 3\hat{s}_{{\rm Cr},z}\hat{s}_{{\rm Li},z}\right)\,, \tag{5}$$

where α^2/R^3 is the contribution due to the direct magnetic dipole-dipole interaction and $\lambda_{\rm SO}(R)$ is the effective dipole-dipole interaction in the second order of perturbation theory with the spin-orbit operator. The latter term is smaller than the former one for light atoms, therefore, we neglect it in our scattering calculations. α denotes the fine structure constant.

TABLE III. Parameter values of the MLR potential energy functions fitted to the computed *ab initio* data for the $X\,^6\Sigma^+$ and $a\,^8\Sigma^+$ electronic states of the LiCr molecule. D_e is in cm^{-1}, and other parameters are in atomic units or are dimensionless.

V_S	D_e (cm^{-1})	R_e (bohr)	φ_0	φ_1	φ_2	φ_3	φ_4	C_6
$V_{S=5/2}$	8406.1	4.8654	-1.6472	-0.7801	-1.0455	-2.6313	-2.8868	954
$V_{S=7/2}$	564.95	6.4753	-1.1049	0.4317	-0.4696	-2.3948	-2.5846	954

We carry out quantum scattering calculations within the coupled-channel formalism [27]. The total scattering wave function is constructed in a fully uncoupled basis set,

$$|s_{\rm Cr}, m_{s_{\rm Cr}}\rangle|i_{\rm Cr}, m_{i_{\rm Cr}}\rangle|s_{\rm Li}, m_{s_{\rm Li}}\rangle|i_{\rm Li}, m_{i_{\rm Li}}\rangle|L, m_L\rangle\,, \tag{6}$$

where m_j is the projection of angular momentum j on the space-fixed z axis, and assuming that the projection of the total angular momentum $M_{\rm tot} = m_{s_{\rm Cr}} + m_{i_{\rm Cr}} + m_{s_{\rm Li}} + m_{i_{\rm Li}} + m_L$ is conserved. The Hamiltonian is then transformed to the asymptotically diagonal basis of hyperfine eigenstates. The coupled-channel equations are solved using the renormalized Numerov propagator [98] with step-size doubling and about 100 step points per de Broglie wavelength as implemented in Ref. [72]. The K and S matrices are obtained by imposing the long-range scattering boundary conditions in terms of the Bessel functions. The scattering lengths are then extracted from the S matrices for the lowest entrance channels $a_0 = (1 - S_{00})(1 + S_{00})/(ik)$, where $k = \sqrt{2\mu E/\hbar^2}$ with E being the collision energy. The collision energy in our scattering calculations is fixed at 100 nK.

We use the most accurate PECs of the $X\,^6\Sigma^+$ and $a\,^8\Sigma^+$ electronic molecular states calculated with the use of *ab initio* methods as described in Sec. III A. Next, we numerically fit the Morse/Long-range (MLR) potential energy functions [99] to the *ab initio* points to represent $V_S(R)$ in Eq. (3). The MLR potential energy functions are given by:

$$V_S(R) = D_e \left[1 - \frac{u_{\rm LR}(R)}{u_{\rm LR}(R_e)} \exp\left(-\phi(R) y_p(R)\right)\right]^2 - D_e, \tag{7}$$

where D_e is the well depth and R_e is the equilibrium distance of the interaction potential, $u_{\rm LR}(R)$ describes the long-range part of the potential,

$$u_{\rm LR}(R) = -\frac{C_6}{R^6}\,, \tag{8}$$

and the remaining functions take the form:

$$\begin{aligned} y_p(R) &= \frac{R^p - R_e^p}{R^p + R_e^p}\,, \\ \phi(R) &= \varphi_\infty\, y_p(R) + \Big(1 - y_p(R)\Big) \sum_{i=0}^{4} \varphi_i y_q^i(R)\,, \end{aligned} \tag{9}$$

with $\varphi_\infty = \ln\left(\frac{-2D_e}{u_{\rm LR}(R_e)}\right)$, $p = 4$, and $q = 4$. The fitted parameter values are collected in Table III.

For many-electron systems, even the most accurate potential energy curves obtained using *ab initio* electronic structure methods do not allow for an accurate prediction of scattering lengths. Therefore, we use the assignment of scattering lengths a_S of the electronic potentials $V_S(R)$ based on recent experimental data, $a_{S=5/2} = 15.5$ bohr and $a_{S=7/2} = 41.5$ bohr [57]. We set the scattering lengths a_S of the employed Morse/Long-range PECs by scaling them with appropriate factors λ, $V_S(R) \to \lambda V_S(R)$. Magnetic Feshbach resonances are characterized by their positions B_0, widths Δ, and background scattering lengths $a_{\rm bg}$ that can be determined by numerical fitting of the expression $a(B) = a_{\rm bg}\,(1 - \Delta/(B - B_0))$ [100] to the computed scattering lengths in the vicinity of the resonance pole.

C. Molecular fine and hyperfine interactions

Electromagnetic interactions of different electric and magnetic moments related to diferent angular momenta present in a molecule, such as electronic and nuclear spins, electronic orbital angular momenta, molecular rotation, and other, result in molecular fine and hyperfine structures [101, 102]. Typical energies of fine and hyperfine interactions are much smaller than electronic energies, therefore they can be treated and included perturbatively. Additionally, nuclear hyperfine couplings are usually much smaller than electronic fine couplings. We study fine and hyperfine interactions for the $X\,^6\Sigma^+$ and $a\,^8\Sigma^+$ electronic states, only. For those states, there is no first-order spin-orbit coupling.

1. Zero-field splitting (electron spin–spin coupling)

The effective Hamiltonian describing the electron spin–spin interaction for a molecule with the total electronic spin S is:

$$\hat{H}_{SS} = D\left[\hat{S}_z^2 - \frac{1}{3}\hat{S}^2\right] + E(\hat{S}_x^2 + \hat{S}_y^2)\,, \tag{10}$$

where $\hat{S}_z$, $\hat{S}_x$, $\hat{S}_z$ are the components of the total electronic spin operator $\hat{S} = \hat{s}_{\mathrm{Cr}} + \hat{s}_{\mathrm{Li}}$. D has two contributions: direct magnetic spin–spin interaction and a second-order spin-orbit term and is connected to the spin–spin coupling constant in Eq. (5) by $D = [\frac{\alpha^2}{R^3} - \lambda_{\mathrm{SO}}(R)]/2$. The direct magnetic interaction can be approximated by $\alpha^2/2R^3$; however, the whole electronic wave function is desired for an accurate description. We use the multireference averaged quadratic coupled-cluster (MR-AQCC) electronic wave-function [103] to obtain the magnetic spin–spin contribution to D, and the MRCISD method to obtain the second-order spin-orbit contribution to D. The scalar relativistic effects are included within the Douglas-Kroll-Hess Hamiltonian [81]. We use the DKH versions of augmented correlation-consistent polarized weighted core-valence basis sets (aug-cc-pwCVDZ-DK, aug-cc-pwCVTZ-DK, aug-cc-pwCVQZ-DK) [83] as available in the ORCA software [104, 105]. We use the method developed by Ganyushin and Neese [106] to obtain D and E from the electronic wave function. We check that E is at least four orders of magnitude smaller than D, which allows us to comclude that E is negligible and can be neglected.

2. Magnetic hyperfine splitting (nuclear spin–electron spin coupling)

The effective Hamiltonian for the electron spin–nuclear spin interaction is:

$$\hat{H}_{nSeS} = \sum_j \left(A_{fc}^j \hat{S}\cdot\hat{i}_j + \hat{S}\cdot\boldsymbol{A}_{sd}^j\cdot\hat{i}_j\right)\,. \tag{11}$$

The summation is over all nuclei j possessing a non-zero spin. The nuclear spin–electron spin interaction is the sum of the Fermi contact term (described by A_{fc}^j) and magnetic dipolar interaction (represented by $\boldsymbol{A}_{sd}^j$). The equivalent form of Eq. (11) is:

$$\hat{H}_{nSeS} = \sum_j \left(A_{fc}^j \hat{S}\cdot\hat{i}_j + \frac{1}{3}c(3\hat{S}_z\hat{i}_{j,z} - \hat{S}\cdot\hat{i}_j) - \frac{1}{2}d(\hat{S}_+\hat{i}_{j,+} + \hat{S}_-\hat{i}_{j,-})\right)\,. \tag{12}$$

The total magnetic hyperfine Hamiltonian also contains a nuclear-spin–electron-orbit term, which we neglect. We check that the Fermi contact term dominates the nuclear-spin–electron-spin interaction and the components of A_{sd}^j matrix (or c and d parameters) are smaller than A_{fc}^j.

We employ the domain-based local pair natural orbital CCSD (DLPNO-CCSD) method [107–115]. The basis set, treatment of relativistic effects and software are the same as for the electron-spin–electron-spin interaction. We neglect the second-order contribution from the spin-orbit coupling.

3. Electron spin–rotation coupling

The electron spin–rotation coupling ε is connected with the electronic g-tensor [116], and for diatomic molecules, the relation has a simple form:

$$\varepsilon = 2B_0\Delta g_\perp\,. \tag{13}$$

$\Delta g_\perp$ describes the difference between the component of the electronic g-tensor perpendicular to the interatomic axis and the free-electron g-factor. B_0 is the rotational constant. The relation in Eq. (13) is correct only in the first order of perturbation theory; however, it works well for most deeply bound diatomic molecules [117, 118]. Based on our experience, we expect that for a weekly bound system the relation can give only a rough estimation of the order of magnitude of ε. We use the ORCA software to obtain $\Delta g_\perp$. We use the same electronic structure method as for the spin-orbit contribution to the electron spin–spin coupling.

4. Nuclear quadrupole coupling

In order to compute the nuclear quadrupole coupling constant (NQC), we use the CCSD method and the CFOUR 2.1 [119] software. We describe the relativistic effects by the one-electron variant of the Spin-free Exact Two-component Theory [120].

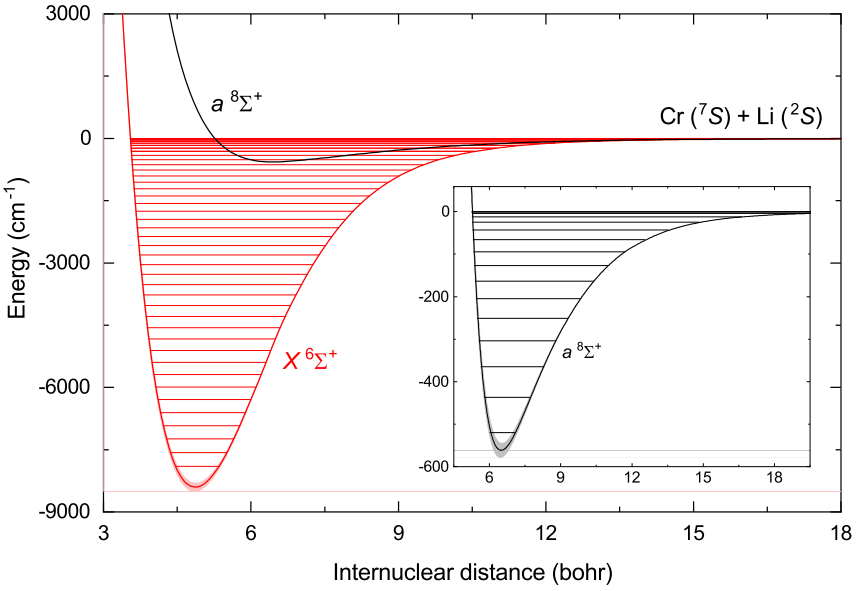

FIG. 1. Potential energy curves of the LiCr molecule in the $X\,^6\Sigma^+$ and $a\,^8\Sigma^+$ electronic states together with corresponding vibrational energy levels. The inset shows the enlarged $a\,^8\Sigma^+$ electronic state. Shaded areas represent the theoretical uncertainty of the presented potential energy curves.

We use all-electron weighted core-valence relativistic triple-zeta basis set (aug-cc-pwCVTZ-DK) for Cr and all-electron core-valence triple-zeta basis set (aug-cc-pCVTZ) for Li [121, 122]. The electronic structure computations provide the electric field gradient tensor at a given nucleus, whereas the nuclear quadrupole moments are taken from the literature [123].

5. *Other components of hyperfine structure*

The isotropic nuclear spin–spin [124, 125] and nuclear spin-rotation [126, 127] coupling constants are estimated at the CCSD level of theory as implemented in CFOUR 2.1 [119]. We neglect the relativistic effects. We ignore the spin-dipole and spin-orbit contributions to the nuclear-spin–nuclear-spin coupling constants. The basis sets are the same as for the nuclear quadrupole coupling constant calculations.

III. NUMERICAL RESULTS AND DISCUSSION

A. Potential energy curves

1. *Potential energy curves and permanent electric dipole moments for the $X\,^6\Sigma^+$ and $a\,^8\Sigma^+$ electronic states*

The $X\,^6\Sigma^+$ and $a\,^8\Sigma^+$ molecular electronic states arise from the interaction of ground-state Cr(^7S) and Li(^2S) atoms. The $a\,^8\Sigma^+$ state is well described by single-reference methods at all internuclear distances, while the $X\,^6\Sigma^+$ state has a single-reference character at small internuclear distances and takes on multireference character at intermediate and large internuclear distances due to the open-shell nature of the interacting atoms. Hence, we compute the interaction energies for the $a\,^8\Sigma^+$ electronic state using the RCCSD(T) method at all internuclear distances, and for the $X\,^6\Sigma^+$ state we use the RCCSD(T) method to compute the interaction energies at short to midrange distances. As the RCCSD(T) method fails to describe properly the dissociation of the molecule in the $X\,^6\Sigma^+$ state into the correct atomic limit, we combine the obtained interaction energies for small to intermediate internuclear distances with the interaction energies for intermediate to large internuclear distances obtained at the MRCISD+Q level. For the MRCISD calculations, we use the active space of all orbitals necessary to describe the valence electrons: $3d$ and $4s$ for the Cr atom and $2s$ for the Li atom, and additionally the $2p$ orbital for the Li atom. We smoothly merge the coupled-cluster interaction energies with the energies calculated with the MRCI method at a distance of around 10 bohr. The MRCI results are prior shifted so that the asymptote for the $X\,^6\Sigma^+$ state overlaps with the asymptote for the $a\,^8\Sigma^+$ state as the

TABLE IV. Spectroscopic characteristics of the ^{6}Li^{53}Cr molecule in the $X\,^6\Sigma^+$ and $a\,^8\Sigma^+$ electronic states: equilibrium bond length R_e, well depth D_e, and harmonic constant ω_e, calculated at different levels of theory.

Method	Basis	R_e (bohr)	D_e (cm^{-1})	ω_e (cm^{-1})
	$X\,^6\Sigma^+$			
MRCISD	aug-cc-pV5Z+BF	4.97	6546	309.7
MRCISD+Q	aug-cc-pV5Z+BF	4.88	7935	333.1
CCSD(T)	aug-cc-pCV5Z+BF	4.87	8406	343.7
CCSD(T)	CBS(Q,5)/aug-cc-pCVnZ	4.86	8435	344.0
CCSD(T)+ΔT	" + aug-cc-pV5Z+BF	4.86	8382	343.8
CCSD(T)+ΔT+ΔQ	" + aug-cc-pVTZ	4.86	8376	343.8
	$a\,^8\Sigma^+$			
MRCISD	aug-cc-pV5Z+BF	7.56	219.5	43.75
MRCISD+Q	aug-cc-pV5Z+BF	6.92	473.5	75.55
CCSD(T)	aug-cc-pV5Z+BF	6.58	565.2	85.10
CCSD(T)	aug-cc-pVXZ CBS(Q,5)	6.58	568.3	85.11
CCSD(T)	aug-cc-pCV5Z+BF	6.54	531.5	82.94
CCSD(T)	CBS(Q,5)/aug-cc-pCVnZ	6.54	530.9	82.58
CCSD(T)+ΔT	" + aug-cc-pV5Z+BF	6.49	561.4	85.29
CCSD(T)+ΔT+ΔQ	" + aug-cc-pVTZ	6.48	565.0	86.19

MRCI method is not size consistent.

The final, most accurate potential energy curves for the $X\,^6\Sigma^+$ and $a\,^8\Sigma^+$ electronic states of the LiCr molecule are presented in Fig. 1. The $X\,^6\Sigma^+$ PEC is computed at the CCSD(T)+ΔT+ΔQ level at short range and combined with the MRCISD+Q results at around 10 bohr, while the $a\,^8\Sigma^+$ PEC is computed at the CCSD(T)+ΔT+ΔQ level of theory at all distances. The obtained potential energy curves are smooth and have well-defined minima. The LiCr molecule in the $X\,^6\Sigma^+$ electronic state is strongly bound with the well depth of 8376 cm^{-1} at the equilibrium distance of 4.86 bohr, similar to the experimental well depth of the Li_2 dimer in its $X\,^1\Sigma_g^+$ ground electronic state with the well depth of 8516.7 cm^{-1} at $R_e = 5.05$ bohr [128]. For comparison, the well depths for the Cr_2 dimer corresponding to the Cr(^7S)+Cr(^7S) dissociation limit range from about 15500 cm^{-1} at around 3.5 bohr in the $X\,^1\Sigma_g^+$ ground state to about 550 cm^{-1} at around 6 bohr in the maximally spin-stretched state $(1)\,^{13}\Sigma_g^+$ [129]. The LiCr molecule in the spin-polarized $a\,^8\Sigma^+$ electronic state is weakly bound with the well depth of 565 cm^{-1} at equilibrium distance of 6.48 bohr. This can be compared to the experimental well depth of the Li_2 dimer in the $a\,^3\Sigma_u^+$ electronic state with the well depth of 333.7 cm^{-1} at $R_e = 7.88$ bohr [130].

Estimating the uncertainty of molecular calculations is challenging but important for reliable guiding and explaining experimental results. Therefore, to access the accuracy of our final calculations, we analyze their convergence with the quality of wavefunction representation, the size of atomic orbitals basis set, and the inclusion of relativistic effects and core electron correlation. Table IV collects the main spectroscopic characteristics: equilibrium bond lengths R_e, well depths D_e, and harmonic constants ω_e (calculated assuming the mass of ^{6}Li^{53}Cr) of the PECs for the $X\,^6\Sigma^+$ and $a\,^8\Sigma^+$ electronic states calculated with the use of MRCISD, MRCISD+Q, and RCCSD(T) methods and the largest basis sets employed in our calculations (aug-cc-pV5Z-DK+BF for MRCI and aug-cc-pCV5Z-DK+BF for CC), compared to the results for the two-point CBS extrapolation of the interaction energies. Additionally, we also calculate the full iterative triple excitations correction (ΔT), given as the difference between interaction energies calculated at the CCSDT and CCSD(T) levels of theory, computed with the use of smaller basis sets, aug-cc-pV5Z-DK+BF. In the same manner, we calculate the full quadruple excitation correction (ΔQ), given as the difference between CCSTQ and CCSDT energies, calculated with the aug-cc-pVTZ-DK basis sets. The PECs for the $a\,^8\Sigma^+$ state computed at different levels of theory: RHF, MRCISD, MRCISD+Q, MP2, CCSD, CCSD(T), CCSD(T)+ΔT, and CCSD(T)+ΔT+ΔQ are presented in Fig. 2 (a) (all PECs are computed with the use of the aug-cc-pCV5Z-DK+BF basis sets except for the MRCISD and MRCISD+Q calculations, where the aug-cc-pV5Z-DK+BF basis sets were used). We also provide the spectroscopic characteristics of PECs for the $a\,^8\Sigma^+$ state calculated at the CCSD(T) level and using different-sized basis sets in Appendix A.

For the LiCr molecule in the $X\,^6\Sigma^+$ electronic state, the potential well depth calculated at the MRCISD level amounts to 6546 cm^{-1} at the equilibrium distance of 4.97 bohr, and for the MRCISD+Q calculations the well depth is increased by 21% to 7935 cm^{-1} at the equilibrium distance of 4.88 bohr. The well depth of the PEC calculated at the CCSD(T) level equals to 8406 cm^{-1} at the equilibrium distance of 4.87 bohr. The addition of full triple excitations correction further improves the description of the interaction energies and decrease the well depth by 24.1 cm^{-1} with respect to the CCSD(T) curve, and the full quadruple

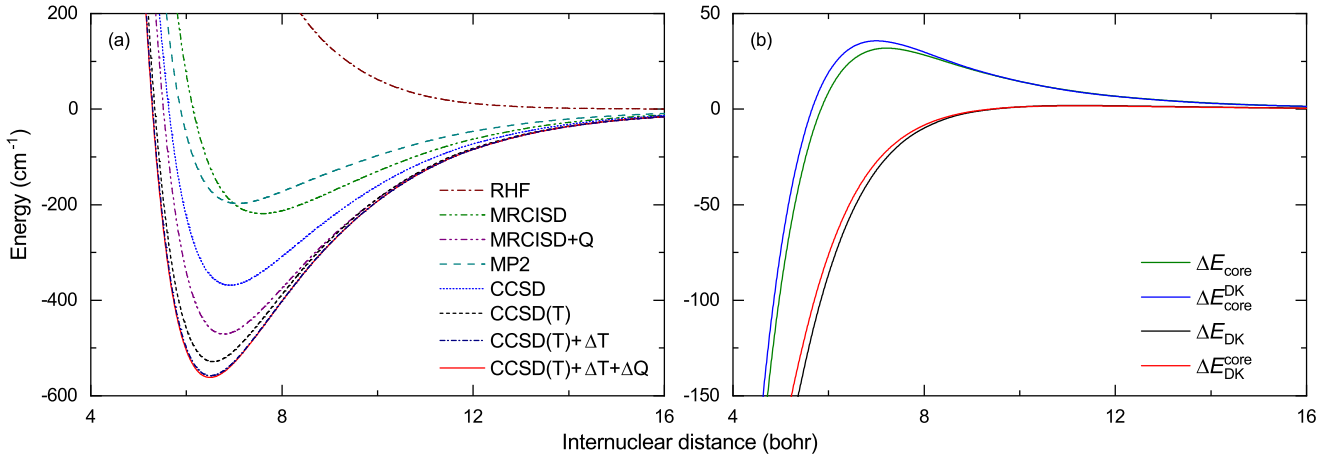

FIG. 2. (a) Potential energy curves for the LiCr molecule in the $a\,^8\Sigma^+$ electronic state computed at different levels of theory: RHF, MRCISD, MRCISD+Q, MP2, CCSD, CCSD(T), CCSD(T)+ΔT, and CCSD(T)+ΔT+ΔQ. (b) Corrections to the interaction energy in the $a\,^8\Sigma^+$ electronic state introduced by the core correlation and scalar relativistic effects computed at the CCSD(T) level. See the text for details.

excitations correction decrease the well depth by 5.4 cm^{-1} with respect to the CCSD(T)+ΔT curve. The well depth obtained at the CCSD(T)+ΔT+ΔQ level amounts to 8376 cm^{-1} at the equilibrium distance of 4.86 bohr with a 0.3% contribution from the full-iterative triple excitations correction and a 0.06% contribution from the full-iterative quadruple excitations correction.

The PECs for the $a\,^8\Sigma^+$ electronic state computed at different levels of theory are presented in Fig. 2(a). As mentioned earlier in the text, we use the aug-cc-pV5Z-DK basis sets augmented by bond functions for the MRCI method, and aug-cc-pCV5Z-DK basis sets augmented by bond functions for the CC method. The use of core-valence basis sets does not provide a good description of the interaction energies within the MRCI method. For the MRCISD method, the well depth amounts to 219.5 cm^{-1} at the equilibrium distance of 7.56 bohr. The inclusion of the Davidson correction significantly improves the description of the interaction energies, and the well depth increases by over 100% to 473.5 cm^{-1} at the equilibrium distance of 6.92 bohr for the MRCISD+Q method. The well depth of 198.5 cm^{-1} at $R_e = 7.05$ bohr obtained at the MP2 level is significantly underestimated. For the coupled-cluster calculations, the well depth computed at the CCSD level amounts to 370.8 cm^{-1} at the equilibrium distance of 6.89 bohr, and the inclusion of non-iterative triple excitations increases the well depth by 70% to 531.5 cm^{-1} at $R_e = 6.54$ bohr. The addition of full triple excitations correction further improves the description of the interaction energies and increases the well depth by 29.8 cm^{-1} with respect to the CCSD(T) curve, and the full quadruple excitations correction increases the well depth by 3.6 cm^{-1} with respect to the CCSD(T)+ΔT curve. The well depth obtained at the CCSD(T)+ΔT+ΔQ level amounts to 565 cm^{-1} at the equilibrium distance of 6.48 bohr with a 5% contribution from the full-iterative triple excitations correction and a 0.6% contribution from the full-iterative quadruple excitations correction. Triple excitations are therefore non-negligible for an accurate calculation of interaction energies, while quadruple excitations do not contribute significantly to the interaction energy, allowing us to conclude that the CCSDT method already provides a description of the LiCr molecule close to the full configuration interaction level.

In Fig. 2(b) we present the core correlation and scalar relativistic corrections to the interaction energy for the $a\,^8\Sigma^+$ electronic state computed at the CCSD(T) level. To this end, we calculate the differences between interaction energies: computed with the aug-cc-pCV5Z basis sets and computed with the aug-cc-pV5Z basis sets, $\Delta E_{\rm core}$; computed with the aug-cc-pCV5Z-DK basis sets and computed with the aug-cc-pV5Z-DK basis sets (and including the DKH correction in both cases), $\Delta E^{\rm DK}_{\rm core}$; computed with the aug-cc-pV5Z-DK basis sets and including the DKH correction and computed with the aug-cc-pV5Z basis sets, $\Delta E_{\rm DK}$; computed with the aug-cc-pCV5Z-DK basis sets and including the DKH correction and computed with the aug-cc-pCV5Z basis sets, $\Delta E^{\rm core}_{\rm DK}$. Hence, $\Delta E_{\rm core}$ describes the effect of the core-core (cc) and core-valence (cv) electron correlations, $\Delta E^{\rm DK}_{\rm core}$ describes the effect of cc and cv correlations in the presence of the DKH relativistic correction, $\Delta E_{\rm DK}$ describes the scalar relativistic effects within the DKH framework while considering only the valence-valence (vv) electron correlations, and $\Delta E^{\rm core}_{\rm DK}$ describes the scalar relativistic effects within the DKH framework computed while taking into account all cc, cv, and vv electron correlations. An inspection of Fig. 2(b) shows that the scalar relativistic correction increases the interaction energies at all internuclear distances, while the cc and cv electron correlations decrease the interaction energies for small internuclear distances in the vicinity the PEC minimum and at intermediate internuclear distances, and increase the interaction energies for small internuclear distances in the repulsive region. As shown in Table VIII in Appendix A, core electron correlations slightly decrease the potential well depths as compared to the corresponding calculations with valence-only active space, and shift the potential minima towards smaller internuclear distances.

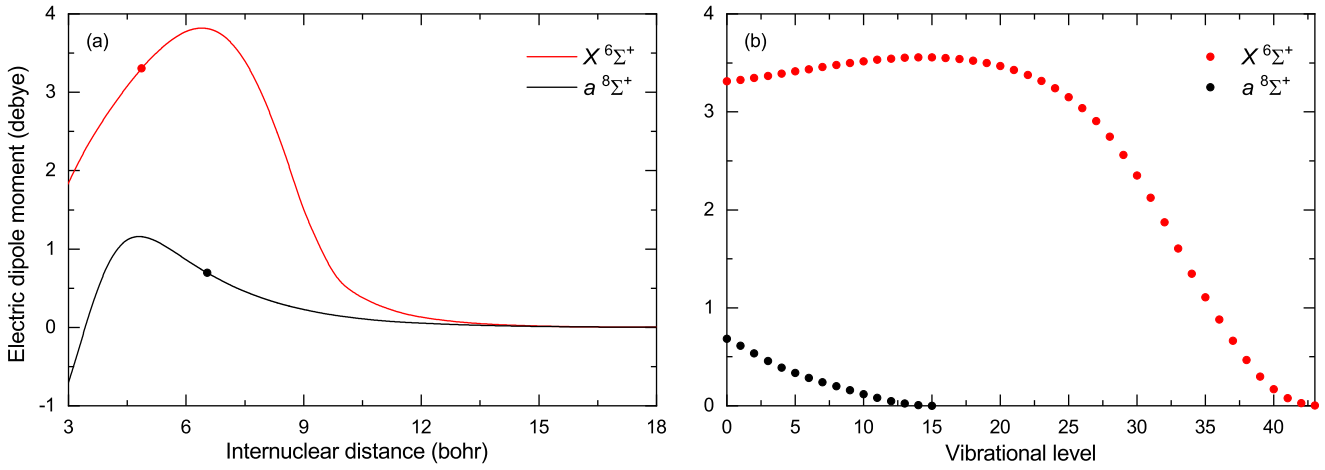

FIG. 3. (a) Permanent electric dipole moments as a function of the internuclear distance for the LiCr molecule in the $X\,^6\Sigma^+$ and $a\,^8\Sigma^+$ electronic states. The points mark the permanent electric dipole moments at equilibrium distances. (b) Permanent electric dipole moments calculated for each vibrational level supported by the $X\,^6\Sigma^+$ and $a\,^8\Sigma^+$ electronic states.

The above convergence analysis and our previous experience [137] allow us to estimate the numerical uncertainty of our final PECs. The uncertainty of the well depth for the $X\,^6\Sigma^+$ state is around 150 cm^{-1} (2 %) and is dominated by the uncertainty of the leading CCSD(T) calculation, including the basis set incompetence and approximate treatment of relativistic effects. The uncertainty of the well depth for the $a\,^8\Sigma^+$ state is around 18 cm^{-1} (3 %), where the largest contribution of 13 cm^{-1} originates from the uncertainty of the leading CCSD(T) part, while the uncertainty of full-triple and higher excitations calculations is 3 cm^{-1} and 2 cm^{-1}, respectively. In this way, the results presented in this work are more accurate than those reported in previous theoretical studies: D_e = 6499 cm^{-1} and $R_e = 5$ bohr for the $X\,^6\Sigma^+$ state, and D_e = 291 cm^{-1} and $R_e = 6.8$ bohr for the $a\,^8\Sigma^+$ state [66]; D_e = 7840 cm^{-1} and $R_e = 4.96$ bohr for the $X\,^6\Sigma^+$ state, and D_e = 847 cm^{-1} and $R_e = 6.28$ bohr for the $a\,^8\Sigma^+$ state [67], where no uncertainty and convergence analysis was provided.

At large internuclear distances the interaction between Cr(^7S) and Li(^2S) atoms is dominated by the van der Waals interaction of Eq. (8). The computed value of the C_6 coefficient is $954\,E_h a_0^6$. It agrees well both with result of recent experimental fit to Feshbach resonances spectrum, $C_6^{\mathrm{FR}} = 922(6)\,E_h a_0^6$ [57], and with the value of the van der Waals coefficient obtained by fitting

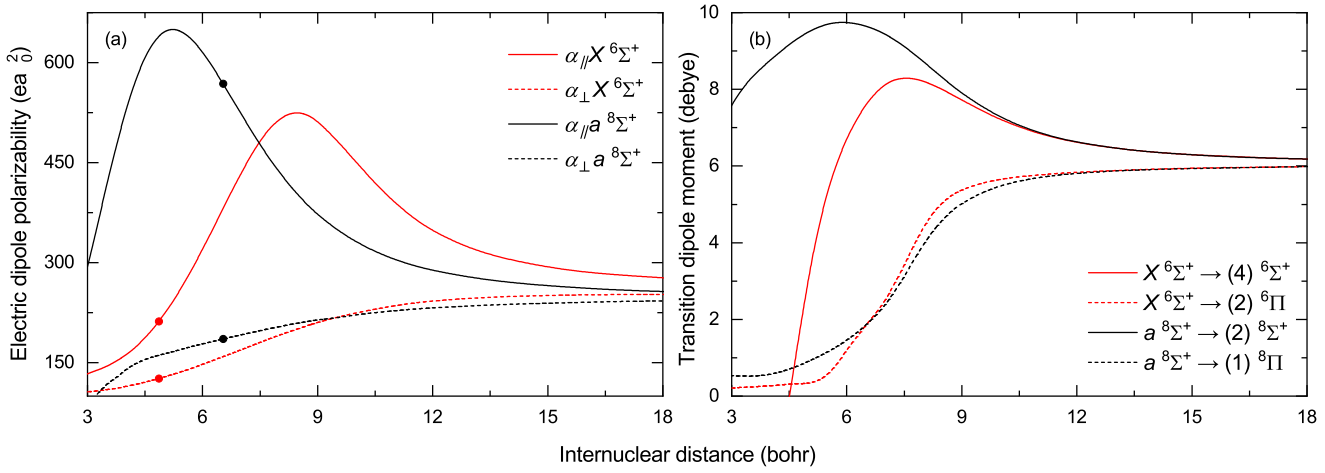

FIG. 4. (a) Parallel, $\alpha_{\|}$, and perpendicular, $\alpha_\perp$, components of the static electric dipole polarizability tensor for the $X\,^6\Sigma^+$ and $a\,^8\Sigma^+$ electronic states of the LiCr molecule as a function of the internuclear distance. The points mark the static electric dipole polarizabilities at equilibrium distances. (b) Transition dipole moments from $X\,^6\Sigma^+$ to $(4)\,^6\Sigma^+$ and to $(2)\,^6\Pi$ electronic states, and from $a\,^8\Sigma^+$ to $(2)\,^8\Sigma^+$ and to $(1)\,^8\Pi$ electronic states.

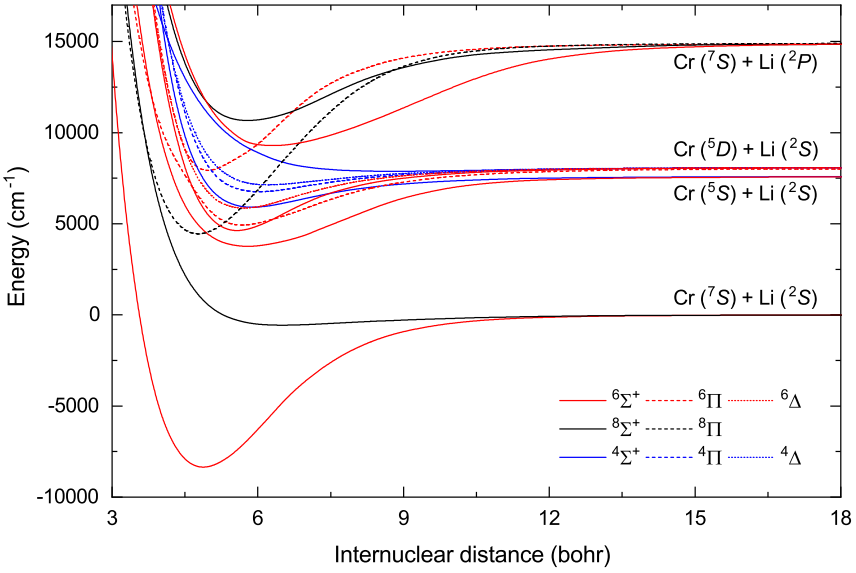

FIG. 5. Potential energy curves of the LiCr molecule in the ground and excited electronic states (in the Hund's case (a) representation).

the analytic form of Eq. (8) to the calculated potential energy curve for the $a\,^8\Sigma^+$ electronic state at large internuclear distances, $C_6^{\rm fit} = 995\,E_h a_0^6$. The larger value of the fitted coefficient may be explained by our single-parameter fit compensating for the omitted higher-order terms. When the next dispersion term is included in the formula of Eq. (8), we get $\tilde{C}_6^{\rm fit} = 927\,E_h a_0^6$ and $\tilde{C}_8^{\rm fit} = 7.0 \times 10^4\,E_h a_0^6$, in much better agreement with the recent experimental values [57].

The permanent electric dipole moments (EDMs) of the LiCr molecule in the $X\,^6\Sigma^+$ and $a\,^8\Sigma^+$ electronic states states as functions of the internuclear distance are presented in Fig. 3 (a). The permanent EDMs, as well as static electric dipole polarizabilities described further in the text, are computed at the CCSD(T) level, and for the $X\,^6\Sigma^+$ state the CCSD(T) and MRCISD results are merged similarly as the potential energy curves. The permanent EDM at the equlibrium distance is relatively large for the $X\,^6\Sigma^+$ state and amounts to 3.30 D. For the $a\,^8\Sigma^+$ state, the permanent EDM is smaller and is equals to 0.70 D at the equilibrium distance. We use the DVR method to estimate the number of vibrational levels (for $j = 0$) for both $X\,^6\Sigma^+$ and $a\,^8\Sigma^+$ electronic states, in which we employ the calculated potential energy curves to describe the short-range part of the interaction, smoothly connected with the long-range part of the interaction given by Eq. (8). The obtained number of bound vibrational states is: 44 for the $X\,^6\Sigma^+$ state and 16 for the $a\,^8\Sigma^+$ state. Next, for each vibrational level we compute the expected value of the EDM, as presented in Fig. 3 (b). For the $X\,^6\Sigma^+$ state, the EDM first increases, reaches the maximum value of 3.56 debyes for the vibrational level $v = 14$ and subsequently decreases, while for the $a\,^8\Sigma^+$ state the permanent EDM decreases monotonically, taking the maximum value of 0.68 debyes for $v = 0$.

Figure 4 (a) shows the computed parallel, $\alpha_\parallel$, and perpendicular, $\alpha_\perp$, components of the static electric dipole polarizability tensor for the $X\,^6\Sigma^+$ and $a\,^8\Sigma^+$ electronic states as a function of the internuclear distance. At equilibrium distances, these amount to: $\alpha_\parallel(R_e) = 212.2\,e^2a_0^2/E_h$ and $\alpha_\perp(R_e) = 126.5\,e^2a_0^2/E_h$ for the $X\,^6\Sigma^+$ state, and $\alpha_\parallel(R_e) = 568.3\,e^2a_0^2/E_h$ and $\alpha_\perp(R_e) = 185.7\,e^2a_0^2/E_h$ for the $a\,^8\Sigma^+$ state. At large internuclear distances, the polarizabilites correctly converge to the sum of atomic polarizabilities: $\alpha = 82.42\,e^2a_0^2/E_h$ for Cr(^7S) and $\alpha = 164.2\,e^2a_0^2/E_h$ for Li(^2S) (computed with the CCSD(T) method).

2. *Potential energy curves and transition electric dipole moments for excited electronic states*

We calculate the potential energy curves and their spectroscopic characteristics for the quartet, sextet, and octet electronic states of the LiCr molecule corresponding to the four lowest dissociation limits: Cr(^7S)+Li(^2S), Cr(^5S)+Li(^2S), Cr(^5D)+Li(^2S), and Cr(^7S)+Li(^2P). The spin-orbit coupling in excited electronic states in neglected thus potential energy curves in the Hund's case (a) are reported in this work. All possible molecular electronic states are listed in Tab. II, along with the computed asymptotic energies. All calculated PECs are shifted to match the experimental asymptotic atomic energies. The MRCI excitation energies are determined as a difference between asymptotic energies of molecular states computed with the same MCSCF wave functions used as reference in the MRCI calculations.

Calculation of the potential energy curves for excited states of the LiCr molecule is numerically and technically challenging

TABLE V. Spectroscopic characteristics of the ^{6}Li^{53}Cr molecule in the ground and excited electronic states: equilibrium bond length R_e, well depth D_e, and harmonic constant ω_e, calculated using the various approaches discussed in the text.

State	Method	Basis	R_e (bohr)	D_e (cm^{-1})	ω_e (cm^{-1})
$X\,^6\Sigma^+$	MRCISD	aug-cc-pV5Z+BF	4.97	6546	309.7
	MRCISD+Q	aug-cc-pV5Z+BF	4.88	7935	333.1
	CCSD(T)	aug-cc-pCV5Z+BF	4.87	8406	343.7
	CCSD(T)+ΔT	" + aug-cc-pV5Z+BF	4.86	8382	343.8
	CCSD(T)+ΔT+ΔQ	" + aug-cc-pVTZ	4.86	8376	343.8
$a\,^8\Sigma^+$	MRCISD	aug-cc-pV5Z+BF	7.56	219.5	43.75
	MRCISD+Q	aug-cc-pV5Z+BF	6.92	473.5	75.55
	CCSD(T)	aug-cc-pCV5Z+BF	6.54	531.5	82.94
	CCSD(T)+ΔT	" + aug-cc-pV5Z+BF	6.49	561.4	85.29
	CCSD(T)+ΔT+ΔQ	" + aug-cc-pVTZ	6.48	565.0	86.19
$(1)\,^4\Sigma^+$	MRCISD	aug-cc-pV5Z	6.10	1001	165.3
	MRCISD+Q	aug-cc-pV5Z	5.86	1704	151.0
$(2)\,^6\Sigma^+$	MRCISD	aug-cc-pV5Z	5.83	3463	157.6
	MRCISD+Q	aug-cc-pV5Z	5.77	3844	173.9
$(2)\,^4\Sigma^+$	MRCISD	aug-cc-pV5Z	9.68	102.8	25.88
	MRCISD+Q	aug-cc-pV5Z	8.78	208.4	37.48
$(1)\,^4\Pi$	MRCISD	aug-cc-pV5Z+BF	6.23	861.6	161.4
	MRCISD+Q	aug-cc-pV5Z+BF	5.99	1340	172.2
$(1)\,^4\Delta$	MRCISD	aug-cc-pV5Z+BF	6.43	616.3	111.9
	MRCISD+Q	aug-cc-pV5Z+BF	6.18	960.7	139.4
$(3)\,^6\Sigma^+$	MRCISD	aug-cc-pV5Z	5.56	3494	281.0
	MRCISD+Q	aug-cc-pV5Z	5.69	3384	224.5
$(1)\,^6\Pi$	MRCISD	aug-cc-pV5Z	5.51	3761	315.4
	MRCISD+Q	aug-cc-pV5Z	5.64	3187	239.6
	CCSD(T)	aug-cc-pCV5Z+BF	5.65	2528	253.2
$(1)\,^6\Delta$	MRCISD	aug-cc-pV5Z	5.60	2303	235.3
	MRCISD+Q	aug-cc-pV5Z	5.97	2650	159.4
	CCSD(T)	aug-cc-pCV5Z+BF	5.70	2242	191.2
$(4)\,^6\Sigma^+$	MRCISD	aug-cc-pV5Z	6.31	4595	154.5
	MRCISD+Q	aug-cc-pV5Z	6.31	5624	158.2
$(2)\,^6\Pi$	MRCISD	aug-cc-pV5Z+BF	4.92	5831	373.9
	MRCISD+Q	aug-cc-pV5Z+BF	4.93	7037	387.4
$(2)\,^8\Sigma^+$	MRCISD	aug-cc-pV5Z+BF	5.74	3781	197.8
	MRCISD+Q	aug-cc-pV5Z+BF	5.75	4259	195.0
$(1)\,^8\Pi$	MRCISD	aug-cc-pV5Z+BF	4.94	8742	335.9
	MRCISD+Q	aug-cc-pV5Z+BF	4.92	9225	338.6
	CCSD(T)	aug-cc-pCV5Z+BF	4.76	10512	343.8

and requires the elaboration of a specific computational scheme for each molecular symmetry and spin multiplicity, including restarts from different geometries, reference states, or active spaces with different hyperparameters controlling the convergence. In Fig. 5 we present the PECs obtained within the most accurate method available – MRCISD+Q for the majority of states and, if possible, RCCSD(T). The characteristics of the obtained PECs are collected in Tab. V.

The computational scheme for the calculation of the interaction energies in the two lowest molecular states was described in detail in the previous section. Here we will focus on the molecular states correlating to the three higher dissociation limits: Cr(^5S)+Li(^2S), Cr(^5D)+Li(^2S), and Cr(^7S)+Li(^2P). There are 3 molecular states with the octet multiplicity: $a\,^8\Sigma^+$, $(2)\,^8\Sigma^+$, and $(1)\,^8\Pi$. As the calculation of the octet states does not pose significant computational challenges, we obtain the PECs with the use of MRCISD and MRCISD+Q methods and aug-cc-pV5Z-DK+BF basis sets. We use the active space composed of the $3d$ and $4s$ orbitals of the Cr atom and $2s$ and $2p$ orbitals of the Li atom. Next, we calculate the quartet and sextet states in the

Π and Δ symmetries. We perform separate MRCI calculations for each symmetry with the use of the aug-cc-pV5Z-DK+BF basis sets and calculate the energies for both spin multiplicities at the same time. We use the minimum active space of $3d$ and $4s$ orbitals of the Cr atom and $2s$ orbital of the Li atom. For the remaining MRCI calculations, we use the aug-cc-pV5Z-DK basis sets without the augmentation by bond functions. In order to compute the quartet states in the Σ symmetry, we use the same minimum active space as described above for the Π and Δ states. For the calculation of the $^6\Sigma^+$ potential energy curves, we first use the active space composed of the $3d$, $4s$, $4p$ and $4d$ orbitals of the Cr atom and $2s$ and $2p$ orbitals of the Li atom to obtain the wave functions at the MCSCF level. Next, we decrease the active space to the $3d$ and $4s$ orbitals of the Cr atom and $2s$ and $2p$ orbitals of the Li atom to perform the MRCI calculations. In the same manner we obtain the $^6\Pi$ potential energy curves, however, for the Π symmetry multiple restarts of MCSCF were necessary to obtain the convergence. For the $(1)\,^6\Pi$, $(1)\,^6\Delta$, and $(1)\,^8\Pi$ states we additionally obtain the PECs with the CCSD(T) method and aug-cc-pCV5Z-DK+BF basis sets.

Based on the MRCI+Q and CCSD(T) results, we identify that the molecular states correlating to the fourth asymptote, Cr(^7S)+Li(^2P), are most strongly bound with the well depths of 5624, 7037, 4259, and 10512 cm^{-1} for the $(4)\,^6\Sigma^+$, $(2)\,^6\Pi$, $(2)\,^8\Sigma^+$, and $(1)\,^8\Pi$ states, respectively. The equilibrium distances are smaller for the Π states, 4.96 and 4.76 bohr for the $(2)\,^6\Pi$ and $(1)\,^8\Pi$ states, and slightly larger for the Σ states, 6.31 bohr for the $(4)\,^6\Sigma^+$ state and 5.75 for the $(2)\,^8\Sigma^+$ state. The molecular states correlating to the Cr(^5S)+Li(^2S) asymptote exhibit moderate binding energies. The $(2)\,^6\Sigma^+$ potential energy curve has a well with depth of 3844 cm^{-1} at 5.77 bohr, and the $(1)\,^4\Sigma^+$ potential well depth is 1704 cm^{-1} at 5.86 bohr. The sextet electronic states correlating to the Cr(^5D)+Li(^2S) asymptote have potential well depths of 3384, 2528, and 2242 cm^{-1} for the $(3)\,^6\Sigma^+$, $(1)\,^6\Pi$, and $(1)\,^6\Delta$, at respective equilibrium distances of 5.69, 5.65, and 5.70 bohr. It needs to be noted here that for the $(1)\,^6\Pi$ state the MRCI and MRCI+Q well depths have relative differences of 48% and 26% with respect to the CCSD(T) result. Similarly, the MRCI+Q well depth for the $(1)\,^6\Delta$ state has a relative error of 18% with respect to the CCSD(T) value. Therefore, MRCI calculations with the use of large active spaces might have led to slightly overestimated results. The quartet electronic states corresponding to the third dissociation asymptote have the smallest binding energies. The $(1)\,^4\Pi$ potential curve has a well of 1340 cm^{-1} at 5.99 bohr and the $(1)\,^4\Delta$ potential curve has a well of 961 cm^{-1} at 6.18 bohr. The $(2)\,^4\Sigma^+$ electronic state is predicted to be most weakly bound, with $D_e = 208$ cm^{-1} at the equilibrium distance of 8.78 bohr.

The weakest binding of molecular electronic states corresponding to the Cr(^5D)+Li(^2S) asymptote may be explained by the fact that the interaction occurs between an electron occupying the $2s$ orbital of lithium and electrons occupying the $3d$ orbital of chromium which is screened by its fully occupied $4s$ orbital. The molecular states correlating to the Cr(^7S)+Li(^2P) have largest binding energies because the $2p$ orbital of lithium is more spatially extended than its $2s$ orbital and stronger overlapping and mixing of valence orbitals can be expected.

For many-electron systems, estimating the uncertainty of *ab initio* calculations is a difficult task, as the accuracy depends on multiple factors, such as convergence with the basis set size or proper treatment of electron correlation and relativistic effects. For the two lowest electronic states, we were able to analyze the convergence in detail and estimate the uncertainty of interaction energy calculations. For higher excited states, it is much harder. Due to the lack of experimental knowledge of dissociation and excitation energies for the LiCr molecule and limitations of the applied theoretical methods, we estimate the uncertainty of the calculated interaction energies for the higher excited states to be up to 30%. Therefore, our description of some excited electronic states may have a partially qualitative character. The order of states, magnitude of interactions, and other characteristics should, however, be correct.

In Fig. 4 (b) we present the transition dipole moments between the electronic states correlating to the Cr(^7S)+Li(^2S) and Cr(^7S)+Li(^2P) asymptotes, i.e., the transition dipole moment from the electronic ground state $X\,^6\Sigma^+$ to the $(4)\,^6\Sigma^+$ and $(2)\,^6\Pi$ electronics states, and the transition dipole moment from the first excited state $a\,^8\Sigma^+$ to the $(2)\,^8\Sigma^+$ and $(1)\,^8\Pi$ electronic states obtained at the MRCISD level. We employ the computed transition moments to study prospects for photoassociation and stabilization of ground-state chromium and lithium atoms into LiCr molecules, as described in Sec. III D.

B. Fine and hyperfine interactions

The results of the electron spin–nuclear spin interaction calculations are collected in Tab. VI. The hyperfine coupling constants A^{fc}_{Cr}, $A^{fc}_{^7\mathrm{Li}}$, and $A^{fc}_{^6\mathrm{Li}}$ are only slightly affected by interatomic interaction in the weakly bound spin-polarized $a\,^8\Sigma^+$ state, while for the deeply bound $X\,^6\Sigma^+$ state the variation of the hyperfine structure is significant.

The value of $\Delta g_\perp$ (13) is about -0.0008 and -0.0003 for $a\,^8\Sigma^+$ and $X\,^6\Sigma^+$, respectively. ε of Eq. (13) describing the electron spin-rotation coupling is roughly -10 MHz for both states. We expect that the nuclear quadrupole coupling constant of ^{53}Cr in LiCr is around 4 MHz for the $a\,^8\Sigma^+$ state and 1 MHz for the $X\,^6\Sigma^+$ state. A significant uncertainty of the nuclear quadrupole moment of ^{53}Cr (around 30%) limits the precision of the computed NQCC. However, a precise spectroscopy of LiCr combined with our predictions of the electric field gradient may provide a more reliable value of the nuclear quadrupole moment of ^{53}Cr. The NQCC of ^{6}Li is about 10^3 lower than the NQCC of ^{53}Cr. The isotropic nuclear spin–spin and nuclear-spin–rotation interactions are below 1 kHz.

TABLE VI. Hyperfine coupling constants A^{fc} (in MHz) for the ground-state Li and Cr atoms and the LiCr molecule in the $X\,^6\Sigma^+$ and $a\,^8\Sigma^+$ electronic states.

System	State	Method	^{6}Li	^{7}Li	^{53}Cr
Li	^2S	non-relativistic DLPNO-CCSD/aug-cc-pwCV5Z-DK	153.2	404.6	-
Li	^2S	DLPNO-CCSD/aug-cc-pwCVQZ-DK	148.8	392.9	-
Li	^2S	DLPNO-CCSD/aug-cc-pwCV5Z-DK	150.3	396.8	-
Li	^2S	Exp. [96]	152.1368407(20)	401.7520433(5)	-
Cr	^7S	non-relativistic DLPNO-CCSD/aug-cc-pwCVQZ-DK	-	-	-119.9
Cr	^7S	DLPNO-CCSD/aug-cc-pwCVTZ-DK	-	-	-81.9
Cr	^7S	DLPNO-CCSD/aug-cc-pwCVQZ-DK	-	-	-83.4
Cr	^7S	Exp. [131]	-	-	-83.5985(15)
LiCr	$X\,^6\Sigma^+$	DLPNO-CCSD/aug-cc-pwCVQZ-DK at R_e	5.7	15.0	3.2
LiCr	$X\,^6\Sigma^+$	DLPNO-CCSD/aug-cc-pwCVQZ-DK at $R\to\infty$	29.8	78.6	-100.1
LiCr	$X\,^6\Sigma^+$	at $R\to\infty$ based on Exp. [96, 131]	30.427368	80.350408	-100.318
LiCr	$a\,^8\Sigma^+$	DLPNO-CCSD/aug-cc-pwCVQZ-DK at R_e	20.7	54.6	-69.3
LiCr	$a\,^8\Sigma^+$	DLPNO-CCSD/aug-cc-pwCVQZ-DK at $R\to\infty$	21.3	56.1	-71.5
LiCr	$a\,^8\Sigma^+$	at $R\to\infty$ based on Exp. [96, 131]	21.733834	57.393149	-71.655

C. Chemical reactivity of ground-state molecules

We use the computed potential well depths, D_e, and related dissociation energies, $D_0 \approx D_e - \frac{1}{2}\omega_e$, to assess the stability of the ground-state LiCr molecules against atom-exchange chemical reactions. For a ground-state heteronuclear molecule AB, an atom-exchange chemical reaction,

$$2\,AB \longrightarrow A_2 + B_2, \tag{14}$$

is energetically possible provided that the sum of dissociation energies of the products is larger than or equal to the sum of the dissociation energies of the reactants:

$$D_0(A_2) + D_0(B_2) \geq 2D_0(AB). \tag{15}$$

As the calculation of the potential energy curves for the Cr_2 dimer poses a significant challenge, accurate values of the binding energies within the Cr_2 dimer have not been yet provided in the literature. However, based on the available data, we can assess that the deeply-bound ground-state $X\,^6\Sigma^+$ LiCr molecules may be chemically stable against atom-exchange reactions if the collision complex dynamics is restricted to higher total spin projectsion M_S manifolds in magnetic field, i.e.,

$$2\,\mathrm{LiCr}\,(X\,^6\Sigma^+) \not\longrightarrow \mathrm{Cr_2}\,((1)\,^9\Sigma_g^+) + \mathrm{Li_2}\,(a\,^3\Sigma_g^+), \tag{16}$$

$$2\,\mathrm{LiCr}\,(X\,^6\Sigma^+) \not\longrightarrow \mathrm{Cr_2}\,((1)\,^{11}\Sigma_u^+) + \mathrm{Li_2}\,(X\,^1\Sigma_g^+), \tag{17}$$

because the Cr_2 [129] and Li_2 dimers [132] have considerably smaller binding energies than the one of the $X\,^6\Sigma^+$ LiCr molecule (except for $X\,^1\Sigma_g^+$ Li_2, for which the dissociation energy is comparable).

The LiCr molecule can be also prepared in the spin-polarized $a\,^8\Sigma^+$ state, for which the atom-exchange reactions are most probably energetically possible:

$$2\,\mathrm{LiCr}\,(a\,^8\Sigma^+) \longrightarrow \mathrm{Cr_2}\,((1)\,^{13}\Sigma_g^+) + \mathrm{Li_2}\,(a\,^3\Sigma_g^+). \tag{18}$$

We estimate that the reaction is close thermoneutral.

D. Photoassociation spectroscopy and STIRAP

The ground-state LiCr molecules can be produced by associating pairs of atoms in an ultracold Cr+Li mixture. Either photoassociation to excited electronic states followed by spontaneous or stimulated stabilization to the ground state or magnetoassociation followed by optical stabilization using the Stimulated Raman Adiabatic Passage (STIRAP) can be employed. Both

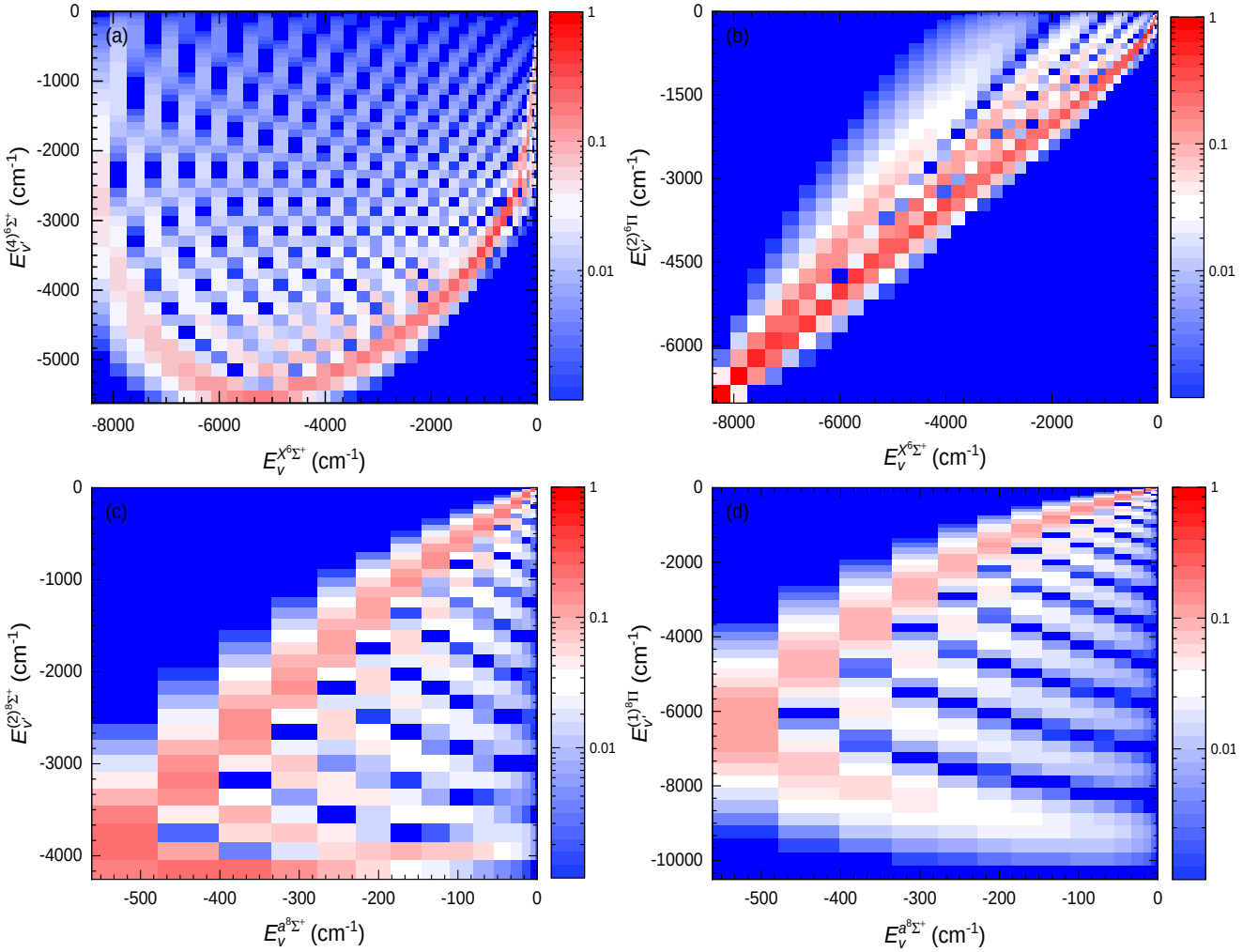

FIG. 6. Franck-Condon factors between vibrational levels of the LiCr molecule in the electronic states dissociating into Cr(^7S)+Li(^2S) and Cr(^7S)+Li(^2P): (a) $X\,^6\Sigma^+ \rightarrow (4)\,^6\Sigma^+$, (b) $X\,^6\Sigma^+ \rightarrow (2)\,^6\Pi$, (c) $a\,^8\Sigma^+ \rightarrow (2)\,^8\Sigma^+$, and (d) $a\,^8\Sigma^+ \rightarrow (1)\,^8\Pi$.

approaches are governed by the transition dipole moments between vibrational levels of the ground and excited electronic states. For the successful production of deeply-bound ground-state molecules, the excited-state vibrational levels having a significant overlap with both scattering or weekly-bound states and deeply-bound levels are needed.

The initial insight and approximation description of possible optical transitions in molecules are given by Franck-Condon factors (FCFs) between vibrational levels supported by the ground and excited electronic states. Figure 6 presents the Franck-Condon factors between vibrational levels of the LiCr molecule in the electronic states dissociating into Cr(^7S)+Li(^2S) and Cr(^7S)+Li(^2P). Molecular states associated with the Cr(^7S)+Li(^2P) asymptote have been selected because this asymptote is relatively well separated from other atomic thresholds and related molecular states should be accessible by strong transition dipole moments borrowed from the strong atomic transition $^2S \rightarrow ^2P$ in Li. The relevant transition dipole moments are presented in Fig. 4(b). The overall scheme involving those states would be similar as in heteronuclear alkali-metal molecules. The overview of Fig. 6 suggests the $X\,^6\Sigma^+ \rightarrow (4)\,^6\Sigma^+$ transitions as the most promising path for the formation of ground-state molecules. Similarly as in alkali-metal dimers, the characteristic bent shape of largest FCFs shows the existence of intermediate levels of the excited $(4)\,^6\Sigma^+$ state having noticeable overlap with both weakly and deeply bound levels of the ground $X\,^6\Sigma^+$ state. In contrast, the FCFs for the $X\,^6\Sigma^+ \rightarrow (2)\,^6\Pi$ transitions are visibly diagonal, that is not preferable pattern for the STIRAP formation, but may allow for direct optical imaging of ground-state LiCr molecules.

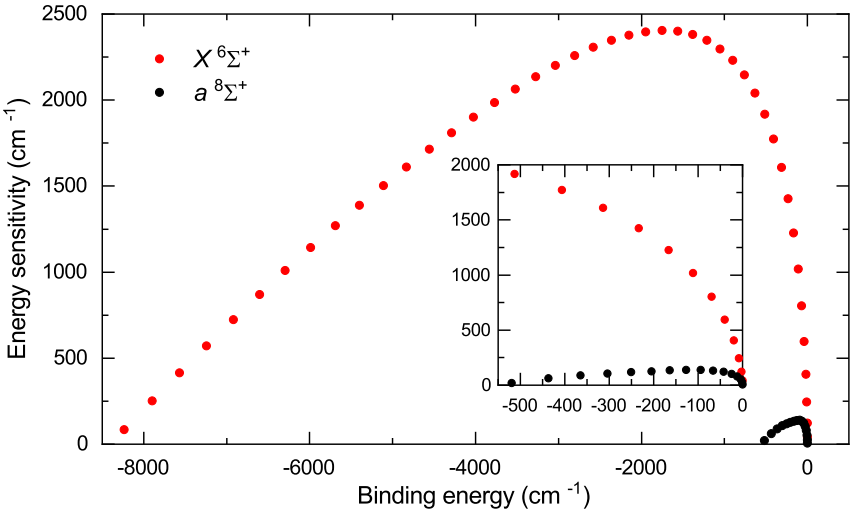

FIG. 7. Vibrationl energy sensitivity $\partial_\mu E_v$ to the proton-to-electron mass ration μ as a function of the binding energy of the vibrational levels of the LiCr molecule in the $X\,^6\Sigma^+$ and $a\,^8\Sigma^+$ electronic states.

E. Application in precision measurements

The electronic, vibrational, and rotational levels within the molecular energetic structure exhibit different sensitivities to fundamental constants, such as the fine-structure constant or the proton-to-electron mass ratio. Therefore, ultracold molecules have been proposed as sensitive probes to study possible variations of fundamental constants [133], and high resolution molecular spectroscopy with homonuclear Cs_2 [134] and Sr_2 [135] dimers, as well as heteronuclear dimer KRb [136] has already been applied in the searches of temporal variation of the proton-to-electron mass ratio, m_p/m_e.

We examine the sensitivity of the vibrational levels associated with the $X\,^6\Sigma^+$ and $a\,^8\Sigma^+$ electronic states of the LiCr molecule to the m_p/m_e ratio. The sensitivity of a vibrational energy level E_v to the system's reduced mass μ (which corresponds to the variation of m_p, assuming that m_e remains constant), $\partial_\mu E_v$, can be expressed as [134]:

$$\partial_\mu E_v \equiv \frac{\partial E_v}{\partial(\ln \mu)} = \frac{v+\frac{1}{2}}{2\rho(E_v)}\,, \tag{19}$$

where $\rho(E_v)$ is the density of states at energy E_v, $\rho(E_v) = (\partial E_v/\partial v)^{-1} \approx (E_v - E_{v-1})^{-1}$. The maximum energy sensitivity $\partial_\mu E_v$ is expected for $v \approx N_v/2$, with N_v denoting the total number of vibrational levels, while vibrational states at the bottom and at the top of a potential well are least sensitive to variations in m_p/m_e. We use Eq. (19) to explicitly calculate the energy sensitivity for each vibrational level of the $X\,^6\Sigma^+$ and $a\,^8\Sigma^+$ electronic states obtained with the use of the DVR method.

Figure 7 presents the results of this calculation. The maximum sensitivity $\partial_\mu E_v^{(\max)} = 2405$ cm^{-1} for the $X\,^6\Sigma^+$ state is associated with the vibrational level $v = 24$, while for the $a\,^8\Sigma^+$ state $\partial_\mu E_v^{(\max)} = 138.7$ cm^{-1} corresponds to $v = 8$. The most sensitive vibrational levels of the $X\,^6\Sigma^+$ state lie near the least sensitive, most deeply-bound levels of the $a\,^8\Sigma^+$ state. The highest sensitivity can be obtained by precision measurements of the energy difference between most and last sensitive levels within the same or two different electronic states. Direct or Raman transitions between such levels of the $X\,^6\Sigma^+$ state would pose a challenge for present day laser technology. A solution and a compromise between the sensitivity and laser techniques accessibility may be the measurement between the lowest level of the $a\,^8\Sigma^+$ state and lying nearby level of the $X\,^6\Sigma^+$ state.

Heteronuclear dimers may offer higher sensitivities of vibrational levels to the proton-to-electron mass ratio as compared to homonuclear dimers [134, 135]. However, their sensitivity to the black-body radiation, presence of hyperfine structure may lead to systematic shifts that may affect the preparation of the system and precision of measurements.

F. Scattering lengths and vibrational levels for spin-polarized interaction

The magnetic Feshbach resonances in the ^{53}Cr+^{6}Li mixture have been recently measured in the group of Matteo Zaccanti [57]. In this work we perform scattering calculations using the electronic potentials $V_{S=5/2}$ and $V_{S=7/2}$ rescaled by $\lambda_{5/2} = 0.9932$ and $\lambda_{7/2} = 1.0069$ to match the experimentally determined values of $a_{S=5/2} = 15.53(7)$ and $a_{S=7/2} = 41.49(3)$ bohr. The

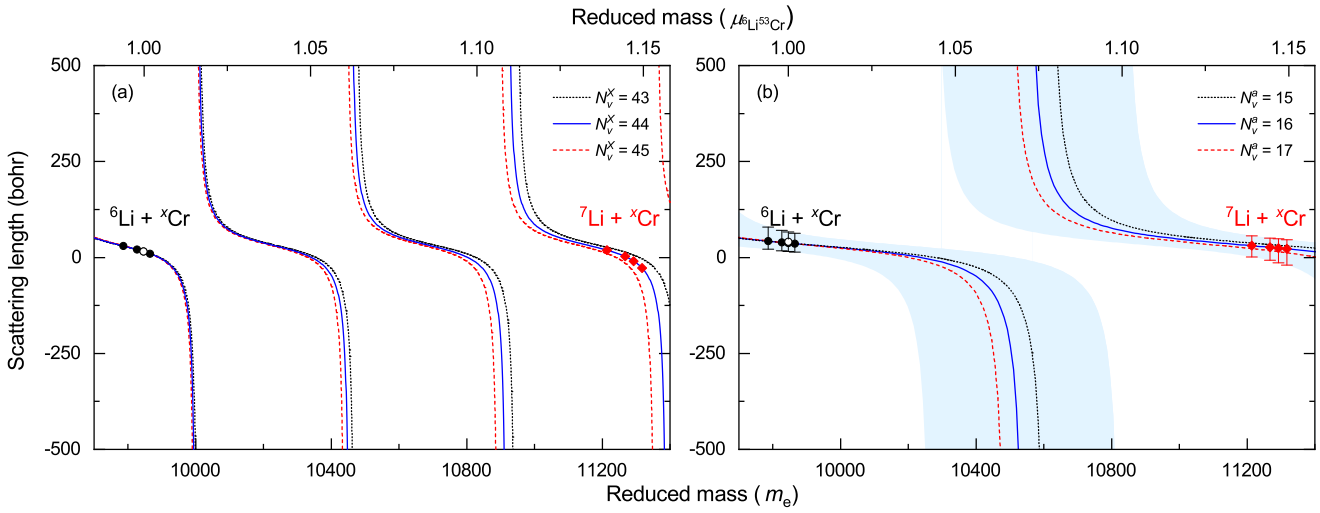

FIG. 8. Scattering lengths for ultracold collisions between ground-state Cr and Li atoms as a function of the system's reduced mass for the (a) $X\,^6\Sigma^+$ and (b) $a\,^8\Sigma^+$ potential energy curves. The full points mark the reduced masses of mixtures comprising subsequent chromium isotopes: $x = 50, 52, 53, 54$, where x is the atomic mass number. The empty points are experimental values from Ref. [57]. In panel (a), the original PEC for $X\,^6\Sigma^+$ is rescaled to fix the scattering length measured in the ^{53}Cr+^{6}Li combination. In panel (b), no scaling is applied and the scattering length obtained from the original *ab initio* PEC (blue solid line) is presented. Dotted and dashed lines show the scattering lenghts assuming different number of vibrational levels (± 1) supported by the PECs with the scattering lengths fixed to be the same for the ^{53}Cr+^{6}Li combination. The blue-shaded area in panel (b) shows the uncertainty of the calculated scattering length related to the uncertainty of the underlying PEC.

TABLE VII. The scattering lengths a_s (in bohr) for the spin-polarized ^{n}Cr+^{m}Li collisions in the $a\,^8\Sigma^+$ electronic state.

^{m}Li / ^{n}Cr	^{50}Cr	^{52}Cr	^{53}Cr	^{54}Cr
^{6}Li	42.5^{+37}_{-21}	39.0^{+32}_{-22}	37.4^{+29}_{-22}	35.9^{+27}_{-22}
^{7}Li	30.5^{+26}_{-29}	26.4^{+24}_{-34}	24.4^{+24}_{-38}	22.4^{+24}_{-42}

scattering lengths for the Cr+Li system have been previously reported in Ref. [66], but they do not have any physical meaning due to the high inaccuracy of the employed electronic structure methods.

In Fig. 8 we present the computed scattering lengths for ultracold collisions between different isotopes of chromium and lithium atoms as a function of the system's reduced mass for (a) $X\,^6\Sigma^+$ and (b) $a\,^8\Sigma^+$ potential energy curves in order to analyse the prospects for controlling the magnetic Feshbach resonance spectrum with different combinations of isotopes. We use the fitted MLR potential energy functions and initially fix the scattering lengths associated with the $X\,^6\Sigma^+$ and $a\,^8\Sigma^+$ interaction potentials at $a_{S=5/2}$ and $a_{S=7/2}$ by using the respective scaling λ factors. We apply the semiclassical formula to express the dependence of the scattering length, a, on a phase shift of the wave function, Φ:

$$a = \bar{a}\,(1 - \tan(\Phi - \pi/8))\,, \tag{20}$$

where $\bar{a}$ is the mean scattering length given by:

$$\bar{a} = \frac{2\pi R_6}{\Gamma(\frac{1}{4})^2}, \tag{21}$$

and the phase shift Φ reads:

$$\Phi = \int_{R_0}^{\infty} \left(-\frac{2\mu V_S(R)}{\hbar^2} \right) \mathrm{d}R, \tag{22}$$

where we integrate from the inner classical turingn point R_0.

An inspection of Fig. 8 reveals that the variability of the scattering length with reduced mass is more rapid for the $X\,^6\Sigma^+$ state than for the $a\,^8\Sigma^+$ state due to the larger number of supported vibrational levels by the $X\,^6\Sigma^+$ electronic potential. It also shows

that the change of lithium isotope from ^{6}Li to ^{7}Li leads to a phase shift of around π for $a\,^8\Sigma^+$ and multiples of π for $X\,^6\Sigma^+$. As the computed potential energy curve for the $X\,^6\Sigma^+$ electronic state is not accurate enough to assign the corresponding scattering length, Fig. 8 (a) has a rather tentative character. The $a\,^8\Sigma^+$ PEC on the other hand is accurate enough to allow for the assignment of the associated scattering length and Fig. 8 (b) allows us to infer about the dependence of the scattering length on the reduced mass of the system. Accidentally, the actual reduced masses of available isotopic mixtures fall into the plateau region of the plot. Since the reduced mass of the Cr+Li system is dominated by the mass of lithium, the use of different chromium isotopes does not introduce a significant change in the value of the scattering length for the $a\,^8\Sigma^+$ interaction potential. We observe the same behaviour of scattering lengths calculated for the $a\,^8\Sigma^+$ potential energy curve rescaled so that it supports ±1 vibrational level as compared to the initial PEC. The corresponding scattering lengths are depicted in Fig. 8 (b) as a blue-shaded area. We conclude that the scattering length of the $a\,^8\Sigma^+$ electronic potential cannot be significantly altered by a different choice of both chromium or lithium isotopes.

G. Magnetically tunable Feshbach resonances

Before we analyse the magnetically tunable Feshbach resonances for Bose-Fermi ^{52}Cr+^{6}Li and Fermi-Fermi ^{53}Cr+^{6}Li mixtures, let us first discuss the impact of the mixtures' hyperfine structures on their scattering properties. Figure 9 presents the hyperfine energy levels of ^{6}Li, ^{52}Cr, and ^{53}Cr atoms and their mixtures: ^{52}Cr+^{6}Li and ^{53}Cr+^{6}Li as a function of the magnetic field strength. Panels (c)-(f) show the hyperfine energy levels summing to selected values of $M_{\rm tot}$: panels (c) and (d) present the energy levels of ^{52}Cr+^{6}Li and ^{53}Cr+^{6}Li mixtures in their absolute ground states with $M_{\rm tot}=-2.5$ and $M_{\rm tot}=-4$, respectively, while panels (e,g) and (f,h) are plotted for $M_{\rm tot}=-0.5$ and $M_{\rm tot}=0$ corresponding to the largest possible numbers of hyperfine energy levels for the respective mixtures. The blue solid lines in panels (c)-(f) present the atomic thresholds being a combination of the atomic hyperfine energy levels with zero binding energy. The red dashed-dotted lines in panels (g) and (h) are the atomic thresholds shifted by the largest possible binding energy of the most weakly bound vibrational level $v=-1$ supported by the van der Waals potential [138]. These red lines set the maximum binding energy of the $v=-1$ level that is determined for infinitely large and negative scattering lengths, hence the actual molecular binding energy must lay between these lines and the atomic thresholds. Feshbach resonances can occur when atomic thresholds and molecular levels cross.

The main energy scale that governs the positions and properties of magnetic Feshbach resonances for the Cr+Li mixtures is the vibrational level spacing, which is large because of the small reduced mass of the colliding atoms. Therefore, the resonance spectrum will primarily depend on the background scattering lengths and binding energies of vibrational levels.

Figure 10 shows s-wave scattering lengths for ultracold collisions in the (a,c,e,g) ^{6}Li+^{52}Cr and (b,d,f,h) ^{6}Li+^{53}Cr mixtures as a function of the magnetic field strength. The results are presented assuming the experimentally assigned scattering lengths $a_{S=5/2}=15.53(7)$ and $a_{S=7/2}=41.49(3)$ bohr [57]. We show results for several different projections of the total angular momentum on the magnetic field $M_{\rm tot}$, including collisions with: (a) $M_{\rm tot}=-0.5$ and (b) $M_{\rm tot}=0$, which correspond to the largest number of channels, (c) $M_{\rm tot}=-2.5$ and (d) $M_{\rm tot}=-4$, which correspond to the absolute ground states of ^{6}Li+^{52}Cr and ^{6}Li+^{53}Cr systems, respectively, and (g) $M_{\rm tot}=-4.5$ and (h) $M_{\rm tot}=-6$ that correspond to maximally spin-stretched states, for which only resonances induced by the dipole-dipole interaction can occur. We assume the step in the magnetic field strength of 0.01 G in all calculations. Different colours represent results without the dipole-dipole interaction included (blue lines) that are obtained by restricting the basis set (6) to $L_{\rm max}=0$, and with the dipole-dipole interaction included with $L_{\rm max}=2$, for which d-wave resonances emerge (red lines). d-wave resonances are a result of a coupling between the s-wave entrance channels and d-wave bound molecular levels in the closed channels.

As expected, the largest number of Feshbach resonances is observed for collisions with $M_{\rm tot}=-0.5$ and $M_{\rm tot}=0$ for Fermi-Bose ^{6}Li+^{52}Cr and Fermi-Fermi ^{6}Li+^{53}Cr mixtures, respectively, amounting to around 4 and 16 s-wave resonances, and 5 and 23 d-wave resonances below 1500 G. The number of resonances decreases with increasing value of $|M_{\rm tot}|$ and there are no s-wave resonances for the fully spin-polarized cases with $M_{\rm tot}=-4.5$ and $M_{\rm tot}=-6$ respectively for ^{6}Li+^{52}Cr and ^{6}Li+^{53}Cr collisions. Unfortunately, almost all of the predicted s-wave resonances are narrow with widths of several mG. The widest s-wave resonances are expected to be located between 1000 and 1500 G and have widths of 0.1-0.65 G. The d-wave Feshbach resonances have widths below 10 mG for both systems.

IV. SUMMARY AND CONCLUSIONS

Advancements in atom cooling and trapping techniques in recent years have allowed for reaching ultralow temperature regimes with atoms that have increasingly complex internal structures. Significant progress has been made in creating ultracold samples of highly magnetic transition-metal or lanthanide atoms such as Cr, Dy, Er, and Eu. These atoms' large electronic angular momenta are a source of their high magnetic moments, which give rise to strong dipole-dipole interatomic interactions. Recently, ultracold mixtures of such atoms with alkali-metal atoms, including Cr+Li, have become experimentally accessible and motivated the present work.

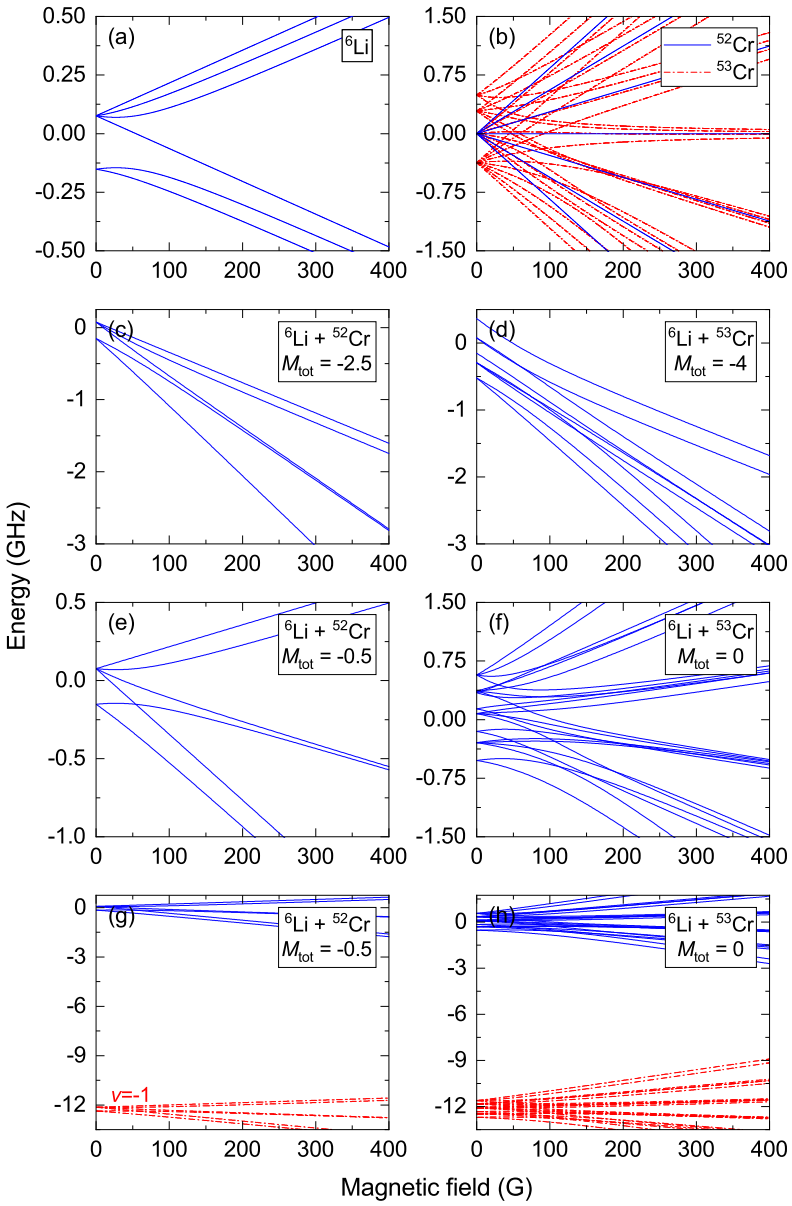

FIG. 9. Hyperfine energy levels for (a) ^{6}Li, (b) ^{52}Cr and ^{53}Cr atoms, and for mixtures of (c,e,g) ^{6}Li+^{52}Cr and (d,f,h) ^{6}Li+^{53}Cr atoms as a function of the magnetic field. Panels (c) and (d) are plotted for $M_{\rm tot} = -2.5$ and $M_{\rm tot} = -4$, respectively, corresponding to the absolute ground states of the mixtures. Panels (e,g) are plotted for $M_{\rm tot} = 0.5$ and panels (f,h) are plotted for $M_{\rm tot} = 0$ corresponding to the largest number of channels. Blue solid lines represent atomic thresholds, while red dash-dotted lines on panels (g,h) correspond to the progression of the most weakly bound vibrational molecular level for infinitely large and negative scattering lengths.

In this work, we have provided a comprehensive theoretical exploration of the interactions and ultracold collisions between chromium and lithium atoms. Advanced computational methods, including coupled cluster and multireference configuration interaction, have been employed to calculate the potential energy curves, as well as the permanent and transition electric dipole moments of various electronic states of the LiCr molecule. The study has revealed that the LiCr molecule, in its ground electronic state, is stable with a deep well depth and a sizable permanent electric dipole moment. Conversely, the molecule's first excited electronic state is only weakly bound with a lesser well depth and a lower permanent electric dipole moment. Fine and hyperfine coupling constants have beed reported for the ground-state interactions. Next, we have examined the potential for forming deeply-bound LiCr molecules via photoassociation and stimulated Raman adiabatic passage, and proposed precision measurements of the electron-to-proton mass ratio variation using ultracold LiCr molecules. Scattering lengths for the ultracold,

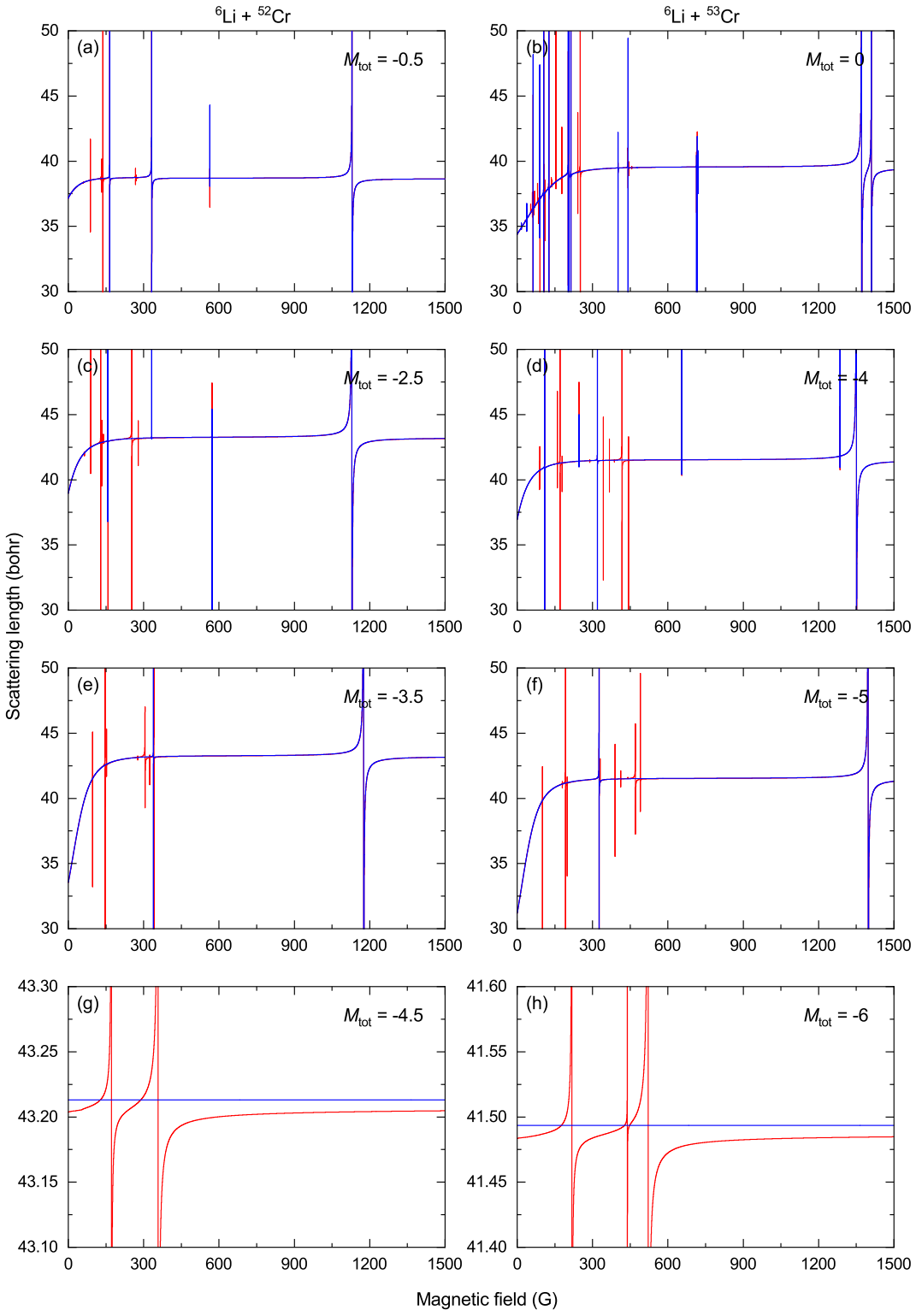

FIG. 10. Scattering lengths for ultracold collisions between (a,c,e,g) ^{6}Li+^{52}Cr and (b,d,f,h) ^{6}Li+^{53}Cr atoms as a function of the magnetic field and different values of $M_{\rm tot}$. The following scattering lengths for the potential-energy functions are assumed: $a_{S=5/2} = 15.5$ and $a_{S=7/2} = 41.5$ bohr. Blue lines show scattering lengths without the dipole-dipole interaction included, and red lines show scattering lengths with the dipole-dipole interaction included with $L_{\rm max} = 2$.

spin-polarized Cr+Li collisions have been predicted, with the results agreeing well with recent experimental measurements. Furthermore, we have provides calculations of magnetically tunable Feshbach resonances for ultracold collisions between certain isotopes of Cr and Li, suggesting the potential for magnetoassociation into polar and highly magnetic LiCr molecules. Our theoretical findings provide valuable insights for current experimental research focusing on ultracold, strongly interacting, mass-imbalanced Li+Cr mixtures and LiCr molecules.

ACKNOWLEDGMENTS

The authors would like to thank Matteo Zaccanti, Alessio Ciamei, and Andrea Simoni for fruitful discussions and providing us with experimental data prior to publication. This research was supported by the Foundation for Polish Science within the Homing program co-financed by the European Regional Development Fund and the National Science Centre Poland (grants no. 2016/23/B/ST4/03231, 2019/35/N/ST4/04504). The computational part of this research was supported by the PL-Grid Infrastructure (grant no. PLG/2023/016115).

Appendix A: Convergence with the basis set size

Table VIII collects the spectroscopic characteristics of the ^{6}Li^{53}Cr molecule in the $a\,^8\Sigma^+$ electronic state calculated with different-sized Gaussian basis sets with and without the DKH correction and with and without the core correlation included.

TABLE VIII. Spectroscopic characteristics of the ^{6}Li^{53}Cr molecule in the $a\,^8\Sigma^+$ electronic state: equilibrium bond length R_e, well depth D_e, and harmonic constant ω_e calculated at the CCSD(T) level of theory and using different-sized Gaussian basis sets (with and without the DKH correction).

Basis	R_e (bohr)	D_e (cm^{-1})	ω_e (cm^{-1})
aug-cc-pVTZ	6.77	487.4	77.14
aug-cc-pVQZ	6.74	510.5	78.77
aug-cc-pV5Z	6.73	516.6	79.08
aug-cc-pV5Z+BF	6.73	519.6	79.30
CBS(Q,5)	6.73	523.0	79.39
aug-cc-pVTZ-DK	6.61	531.3	82.86
aug-cc-pVQZ-DK	6.58	556.1	84.65
aug-cc-pV5Z-DK	6.58	562.0	84.87
aug-cc-pV5Z-DK+BF	6.58	565.2	85.10
CBS(Q,5)	6.58	568.3	85.11
aug-cc-pCVTZ	6.72	466.5	75.72
aug-cc-pCVQZ	6.68	485.1	77.48
aug-cc-pCV5Z	6.69	487.6	77.31
aug-cc-pCV5Z+BF	6.69	490.1	77.43
CBS(Q,5)	6.69	490.3	77.14
aug-cc-pCVTZ-DK	6.57	507.6	81.78
aug-cc-pCVQZ-DK	6.54	527.0	83.06
aug-cc-pCV5Z-DK	6.54	528.9	82.83
aug-cc-pCV5Z-DK+BF	6.54	531.5	82.94
CBS(Q,5)	6.54	530.9	82.58

[1] J. Werner, A. Griesmaier, S. Hensler, J. Stuhler, T. Pfau, A. Simoni, and E. Tiesinga, Phys. Rev. Lett. **94**, 183201 (2005).
[2] A. Griesmaier, J. Werner, S. Hensler, J. Stuhler, and T. Pfau, Phys. Rev. Lett. **94**, 160401 (2005).
[3] B. Naylor, A. Reigue, E. Maréchal, O. Gorceix, B. Laburthe-Tolra, and L. Vernac, Phys. Rev. A **91**, 011603 (2015).
[4] M. Lu, N. Q. Burdick, S. H. Youn, and B. L. Lev, Phys. Rev. Lett. **107**, 190401 (2011).

[5] M. Lu, N. Q. Burdick, and B. L. Lev, Phys. Rev. Lett. **108**, 215301 (2012).
[6] K. Aikawa, A. Frisch, M. Mark, S. Baier, A. Rietzler, R. Grimm, and F. Ferlaino, Phys. Rev. Lett. **108**, 210401 (2012).
[7] K. Aikawa, A. Frisch, M. Mark, S. Baier, R. Grimm, and F. Ferlaino, Phys. Rev. Lett. **112**, 010404 (2014).
[8] Y. Miyazawa, R. Inoue, H. Matsui, G. Nomura, and M. Kozuma, Phys. Rev. Lett. **129**, 223401 (2022).
[9] D. Sukachev, A. Sokolov, K. Chebakov, A. Akimov, S. Kanorsky, N. Kolachevsky, and V. Sorokin, Phys. Rev. A **82**, 011405 (2010).
[10] D. Provorchenko, D. Tregubov, D. Mishin, M. Yaushev, D. Kryuchkov, V. Sorokin, K. Khabarova, A. Golovizin, and N. Kolachevsky, Atoms **11** (2023), 10.3390/atoms11020030.
[11] J. Miao, J. Hostetter, G. Stratis, and M. Saffman, Phys. Rev. A **89**, 041401 (2014).
[12] X. Yu, J. Mo, T. Lu, T. Y. Tan, and T. L. Nicholson, Phys. Rev. A **105**, L061101 (2022).
[13] T. Lahaye, C. Menotti, L. Santos, M. Lewenstein, and T. Pfau, Rep. Prog. Phys. **72**, 126401 (2009).
[14] T. Lahaye, T. Koch, B. Fröhlich, M. Fattori, J. Metz, A. Griesmaier, S. Giovanazzi, and T. Pfau, Nature **448**, 672 (2007).
[15] T. Lahaye, J. Metz, B. Fröhlich, T. Koch, M. Meister, A. Griesmaier, T. Pfau, H. Saito, Y. Kawaguchi, and M. Ueda, Phys. Rev. Lett. **101**, 080401 (2008).
[16] T. Koch, T. Lahaye, J. Metz, B. Fröhlich, A. Griesmaier, and T. Pfau, Nat. Phys. **4**, 218 (2008).
[17] K. Aikawa, S. Baier, A. Frisch, M. Mark, C. Ravensbergen, and F. Ferlaino, Science **345**, 1484 (2014).
[18] H. Kadau, M. Schmitt, M. Wenzel, C. Wink, T. Maier, I. Ferrier-Barbut, and T. Pfau, Nature **530**, 194 (2016).
[19] M. Schmitt, M. Wenzel, F. Böttcher, I. Ferrier-Barbut, and T. Pfau, **539**, 259 (2016).
[20] L. Tanzi, E. Lucioni, F. Famà, J. Catani, A. Fioretti, C. Gabbanini, R. N. Bisset, L. Santos, and G. Modugno, Phys. Rev. Lett. **122**, 130405 (2019).
[21] F. Böttcher, J.-N. Schmidt, M. Wenzel, J. Hertkorn, M. Guo, T. Langen, and T. Pfau, Phys. Rev. X **9**, 011051 (2019).
[22] L. Chomaz, D. Petter, P. Ilzhöfer, G. Natale, A. Trautmann, C. Politi, G. Durastante, R. M. W. van Bijnen, A. Patscheider, M. Sohmen, M. J. Mark, and F. Ferlaino, Phys. Rev. X **9**, 021012 (2019).
[23] A. Frisch, M. Mark, K. Aikawa, F. Ferlaino, J. L. Bohn, C. Makrides, A. Petrov, and S. Kotochigova, Nature **507**, 475 (2014).
[24] T. Maier, H. Kadau, M. Schmitt, M. Wenzel, I. Ferrier-Barbut, T. Pfau, A. Frisch, S. Baier, K. Aikawa, L. Chomaz, M. J. Mark, F. Ferlaino, C. Makrides, E. Tiesinga, A. Petrov, and S. Kotochigova, Phys. Rev. X **5**, 041029 (2015).
[25] S. Baier, M. Mark, D. Petter, K. Aikawa, L. Chomaz, Z. Cai, M. Baranov, P. Zoller, and F. Ferlaino, Science **352**, 201 (2016).
[26] T. Köhler, K. Góral, and P. S. Julienne, Rev. Mod. Phys. **78**, 1311 (2006).
[27] C. Chin, R. Grimm, P. S. Julienne, and E. Tiesinga, Rev. Mod. Phys. **82**, 1225 (2010).
[28] G. Quemener and P. S. Julienne, Chem. Rev. **112**, 4949 (2012).
[29] L. D. Carr, D. DeMille, R. V. Krems, and J. Ye, New J. Phys. **11**, 055049 (2009).
[30] J. L. Bohn, A. M. Rey, and J. Ye, Science **357**, 1002 (2017).
[31] M. A. Baranov, M. Dalmonte, G. Pupillo, and P. Zoller, Chem. Rev. **112**, 5012 (2012).
[32] T.-L. Ho and V. B. Shenoy, Phys. Rev. Lett. **77**, 3276 (1996).
[33] S. Ospelkaus, C. Ospelkaus, O. Wille, M. Succo, P. Ernst, K. Sengstock, and K. Bongs, Phys. Rev. Lett. **96**, 180403 (2006).
[34] D. S. Petrov, G. E. Astrakharchik, D. J. Papoular, C. Salomon, and G. V. Shlyapnikov, Phys. Rev. Lett. **99**, 130407 (2007).
[35] S. Will, T. Best, S. Braun, U. Schneider, and I. Bloch, Phys. Rev. Lett. **106**, 115305 (2011).
[36] N. Spethmann, F. Kindermann, S. John, C. Weber, D. Meschede, and A. Widera, Phys. Rev. Lett. **109**, 235301 (2012).
[37] N. B. Jørgensen, L. Wacker, K. T. Skalmstang, M. M. Parish, J. Levinsen, R. S. Christensen, G. M. Bruun, and J. J. Arlt, Phys. Rev. Lett. **117**, 055302 (2016).
[38] M.-G. Hu, M. J. Van de Graaff, D. Kedar, J. P. Corson, E. A. Cornell, and D. S. Jin, Phys. Rev. Lett. **117**, 055301 (2016).
[39] Y. Ashida, R. Schmidt, L. Tarruell, and E. Demler, Phys. Rev. B **97**, 060302 (2018).
[40] L. A. P. Ardila and T. Pohl, J. Phys. B: At. Mol. Opt. Phys. **52**, 015004 (2018).
[41] O. I. Kartavtsev and A. V. Malykh, J. Phys. B: At. Mol. Opt. Phys. **40**, 1429 (2007).
[42] J. Levinsen, T. G. Tiecke, J. T. M. Walraven, and D. S. Petrov, Phys. Rev. Lett. **103**, 153202 (2009).
[43] C. J. M. Mathy, M. M. Parish, and D. A. Huse, Phys. Rev. Lett. **106**, 166404 (2011).
[44] M. Jag, M. Zaccanti, M. Cetina, R. S. Lous, F. Schreck, R. Grimm, D. S. Petrov, and J. Levinsen, Phys. Rev. Lett. **112**, 075302 (2014).
[45] K. B. Gubbels, M. W. J. Romans, and H. T. C. Stoof, Phys. Rev. Lett. **97**, 210402 (2006).
[46] K. B. Gubbels, J. E. Baarsma, and H. T. C. Stoof, Phys. Rev. Lett. **103**, 195301 (2009).
[47] L. Radzihovsky and D. E. Sheehy, Rep. Prog. Phys. **73**, 076501 (2010).
[48] K. Gubbels and H. Stoof, Phys. Rep. **525**, 255 (2013).
[49] J. Wang, Y. Che, L. Zhang, and Q. Chen, Sci. Rep. **7**, 39783 (2017).
[50] M. Pini, P. Pieri, R. Grimm, and G. C. Strinati, Phys. Rev. A **103**, 023314 (2021).
[51] B. Bazak and D. S. Petrov, Phys. Rev. Lett. **118**, 083002 (2017).
[52] A. Trautmann, P. Ilzhöfer, G. Durastante, C. Politi, M. Sohmen, M. J. Mark, and F. Ferlaino, Phys. Rev. Lett. **121**, 213601 (2018).
[53] C. Ravensbergen, V. Corre, E. Soave, M. Kreyer, E. Kirilov, and R. Grimm, Phys. Rev. A **98**, 063624 (2018).
[54] C. Ravensbergen, E. Soave, V. Corre, M. Kreyer, B. Huang, E. Kirilov, and R. Grimm, Phys. Rev. Lett. **124**, 203402 (2020).
[55] Z.-X. Ye, A. Canali, E. Soave, M. Kreyer, Y. Yudkin, C. Ravensbergen, E. Kirilov, and R. Grimm, Phys. Rev. A **106**, 043314 (2022).
[56] E. Neri, A. Ciamei, C. Simonelli, I. Goti, M. Inguscio, A. Trenkwalder, and M. Zaccanti, Phys. Rev. A **101**, 063602 (2020).
[57] A. Ciamei, S. Finelli, A. Trenkwalder, M. Inguscio, A. Simoni, and M. Zaccanti, Phys. Rev. Lett. **129**, 093402 (2022).
[58] A. Ciamei, S. Finelli, A. Cosco, M. Inguscio, A. Trenkwalder, and M. Zaccanti, Phys. Rev. A **106**, 053318 (2022).
[59] F. Schäfer, N. Mizukami, and Y. Takahashi, Phys. Rev. A **105**, 012816 (2022).
[60] F. Schäfer, Y. Haruna, and Y. Takahashi, J. the Physical Society of Japan **92**, 054301 (2023).
[61] F. Schäfer, Y. Haruna, and Y. Takahashi, Phys. Rev. A **107**, L031306 (2023).

[62] A. Frisch, M. Mark, K. Aikawa, S. Baier, R. Grimm, A. Petrov, S. Kotochigova, G. Quéméner, M. Lepers, O. Dulieu, and F. Ferlaino, Phys. Rev. Lett. **115**, 203201 (2015).
[63] E. Soave, A. Canali, Z.-X. Ye, M. Kreyer, E. Kirilov, and R. Grimm, arXiv preprint arXiv:2304.07921 (2023).
[64] J. Rührig, T. Bäuerle, P. S. Julienne, E. Tiesinga, and T. Pfau, Phys. Rev. A **93**, 021406 (2016).
[65] Z. Pavlović, H. R. Sadeghpour, R. Côté, and B. O. Roos, Phys. Rev. A **81**, 052706 (2010).
[66] G.-H. Jeung, D. Hagebaum-Reignier, and M. J. Jamieson, J. Phys. B: At. Mol. Opt. Phys. **43**, 235208 (2010).
[67] L. Deng, D. Gou, and J. Chai, Chem. Phys. Lett. **650**, 69 (2016).
[68] M. Tomza, Phys. Rev. A **88**, 012519 (2013).
[69] M. Tomza, Phys. Rev. A **92**, 062701 (2015).
[70] M. Tomza, Phys. Rev. A **90**, 022514 (2014).
[71] M. L. González-Martínez and P. S. Żuchowski, Phys. Rev. A **92**, 022708 (2015).
[72] K. Zaremba-Kopczyk, P. S. Żuchowski, and M. Tomza, Phys. Rev. A **98**, 032704 (2018).
[73] M. B. Kosicki, M. Borkowski, and P. S. Żuchowski, New J. Phys. **22**, 023024 (2020).
[74] M. D. Frye, S. L. Cornish, and J. M. Hutson, Phys. Rev. X **10**, 041005 (2020).
[75] M. Taglieber, A.-C. Voigt, T. Aoki, T. W. Hänsch, and K. Dieckmann, Phys. Rev. Lett. **100**, 010401 (2008).
[76] E. Wille, F. M. Spiegelhalder, G. Kerner, D. Naik, A. Trenkwalder, G. Hendl, F. Schreck, R. Grimm, T. G. Tiecke, J. T. M. Walraven, S. J. J. M. F. Kokkelmans, E. Tiesinga, and P. S. Julienne, Phys. Rev. Lett. **100**, 053201 (2008).
[77] H. Hara, Y. Takasu, Y. Yamaoka, J. M. Doyle, and Y. Takahashi, Phys. Rev. Lett. **106**, 205304 (2011).
[78] A. Green, H. Li, J. H. See Toh, X. Tang, K. C. McCormick, M. Li, E. Tiesinga, S. Kotochigova, and S. Gupta, Phys. Rev. X **10**, 031037 (2020).
[79] S. Hensler, A. Griesmaier, J. Werner, A. Görlitz, and T. Pfau, J. Mod. Opt. **51**, 1807 (2004).
[80] S. Boys and F. Bernardi, Mol. Phys. **19**, 553 (1970).
[81] M. Douglas and N. M. Kroll, Ann. Phys. **82**, 89 (1974).
[82] B. A. Hess, Phys. Rev. A **33**, 3742 (1986).
[83] N. B. Balabanov and K. A. Peterson, J. Chem. Phys. **123**, 064107 (2005).
[84] B. P. Prascher, D. E. Woon, K. A. Peterson, T. H. Dunning, and A. K. Wilson, Theor. Chem. Acc. **128**, 69 (2011).
[85] K. Zaremba-Kopczyk and M. Tomza, Phys. Rev. A **104**, 042816 (2021).
[86] M. Śmiałkowski and M. Tomza, Phys. Rev. A **103**, 022802 (2021).
[87] A. Derevianko, S. G. Porsev, and J. F. Babb, Atomic Data and Nuclear Data Tables **96**, 323 (2010).
[88] J. Sugar and C. Corliss, J. Phys. Chem. Ref. Data **14**, Suppl. 2 (1985).
[89] R. L. Kelly, J. Phys. Chem. Ref. Data **16**, Suppl. 1 (1987).
[90] L. J. Radziemski, R. Engleman, and J. W. Brault, Phys. Rev. A **52**, 4462 (1995).
[91] H.-J. Werner, P. J. Knowles, G. Knizia, F. R. Manby, and M. Schütz, WIREs Comput Mol Sci **2**, 242 (2012).
[92] H.-J. Werner, P. J. Knowles, G. Knizia, F. R. Manby, M. Schütz, P. Celani, W. Györffy, D. Kats, T. Korona, R. Lindh, A. Mitrushenkov, G. Rauhut, K. R. Shamasundar, T. B. Adler, R. D. Amos, S. J. Bennie, A. Bernhardsson, A. Berning, D. L. Cooper, M. J. O. Deegan, A. J. Dobbyn, F. Eckert, E. Goll, C. Hampel, A. Hesselmann, G. Hetzer, T. Hrenar, G. Jansen, C. Köppl, S. J. R. Lee, Y. Liu, A. W. Lloyd, Q. Ma, R. A. Mata, A. J. May, S. J. McNicholas, W. Meyer, T. F. Miller III, M. E. Mura, A. Nicklass, D. P. O'Neill, P. Palmieri, D. Peng, K. Pflüger, R. Pitzer, M. Reiher, T. Shiozaki, H. Stoll, A. J. Stone, R. Tarroni, T. Thorsteinsson, M. Wang, and M. Welborn, "Molpro, version 2019.2, a package of ab initio programs," (2019), https://www.molpro.net.
[93] M. Kállay, P. R. Nagy, D. Mester, Z. Rolik, G. Samu, J. Csontos, J. Csóka, P. B. Szabó, L. Gyevi-Nagy, B. Hégely, I. Ladjánszki, L. Szegedy, B. Ladóczki, K. Petrov, M. Farkas, P. D. Mezei, and Á. Ganyecz, J. Chem. Phys. **152**, 074107 (2020).
[94] E. Tiesinga, C. J. Williams, and P. S. Julienne, Phys. Rev. A **57**, 4257 (1998).
[95] J. M. Pendlebury and K. F. Smith, Proc. Phys. Soc. **84**, 849 (1964).
[96] E. Arimondo, M. Inguscio, and P. Violino, Rev. Mod. Phys. **49**, 35 (1977).
[97] N. Stone, At. Data Nucl. Data Tables **90**, 75 (2005).
[98] B. R. Johnson, J. Chem. Phys. **69**, 4678 (1978).
[99] R. J. LeRoy, Y. Huang, and C. Jary, J. Chem. Phys. **125**, 164310 (2006).
[100] A. J. Moerdijk, B. J. Verhaar, and A. Axelsson, Phys. Rev. A **51**, 4852 (1995).
[101] J. M. Brown, J. M. Brown, and A. Carrington, *Rotational spectroscopy of diatomic molecules* (Cambridge university press, 2003).
[102] C. Puzzarini, J. F. Stanton, and J. Gauss, Int. Rev. Phys. Chem. **29**, 273 (2010).
[103] Chem. Phys. Lett. **214**, 481 (1993).
[104] F. Neese, WIREs Computational Molecular Science **2**, 73 (2012).
[105] F. Neese, WIREs Computational Molecular Science **8**, e1327 (2018).
[106] D. Ganyushin and F. Neese, J. Chem. Phys. **125**, 024103 (2006).
[107] F. Neese, A. Hansen, and D. G. Liakos, J. Chem. Phys. **131**, 064103 (2009).
[108] F. Neese, A. Hansen, F. Wennmohs, and S. Grimme, Acc. Chem. Res. **42**, 641 (2009).
[109] F. Neese, F. Wennmohs, and A. Hansen, J. Chem. Phys. **130**, 114108 (2009).
[110] D. G. Liakos, A. Hansen, and F. Neese, J. Chem. Theory Comput. **7**, 76 (2011).
[111] A. Hansen, D. G. Liakos, and F. Neese, J. Chem. Phys. **135**, 214102 (2011).
[112] C. Riplinger and F. Neese, J. Chem. Phys. **138**, 034106 (2013).
[113] C. Riplinger, B. Sandhoefer, A. Hansen, and F. Neese, J. Chem. Phys. **139**, 134101 (2013).
[114] C. Riplinger, P. Pinski, U. Becker, E. F. Valeev, and F. Neese, J. Chem. Phys. **144**, 024109 (2016).
[115] M. Saitow, U. Becker, C. Riplinger, E. F. Valeev, and F. Neese, J. Chem. Phys. **146**, 164105 (2017).
[116] R. C. Jr., Mol. Phys. **9**, 585 (1965).

[117] A. Robinson, J. Brown, J. Flores-Mijangos, L. Zink, and M. Jackson, Mol. Phys. **105**, 639 (2007).
[118] G. Tarczay, P. G. Szalay, and J. Gauss, J. Phys. Chem. A **114**, 9246 (2010), pMID: 20684654.
[119] D. A. Matthews, L. Cheng, M. E. Harding, F. Lipparini, S. Stopkowicz, T.-C. Jagau, P. G. Szalay, J. Gauss, and J. F. Stanton, J. Chem. Phys. **152**, 214108 (2020).
[120] L. Cheng and J. Gauss, J. Chem. Phys. **135**, 084114 (2011).
[121] B. P. Prascher, D. E. Woon, K. A. Peterson, T. H. Dunning, and A. K. Wilson, Theor. Chem. Acc. **128**, 69–82 (2011).
[122] J. G. Hill and K. A. Peterson, J. Chem. Phys. **147**, 244106 (2017).
[123] P. Pyykkö, Mol. Phys. **116**, 1328 (2018).
[124] J. Gauss and J. F. Stanton, J. Chem. Phys. **102**, 251 (1995).
[125] J. Gauss and J. F. Stanton, J. Chem. Phys. **103**, 3561 (1995).
[126] J. Gauss, K. Ruud, and T. Helgaker, J. Chem. Phys. **105**, 2804 (1996).
[127] D. SUNDHOLM and J. GAUSS, Mol. Phys. **92**, 1007 (1997).
[128] J. A. Coxon and T. C. Melville, J. Mol. Spectrosc. **235**, 235 (2006).
[129] Z. Pavlović, B. O. Roos, R. Côté, and H. R. Sadeghpour, Phys. Rev. A **69**, 030701 (2004).
[130] M. Semczuk, X. Li, W. Gunton, M. Haw, N. S. Dattani, J. Witz, A. K. Mills, D. J. Jones, and K. W. Madison, Phys. Rev. A **87**, 052505.
[131] T. Reinhardt, J. Maichel, M. Baumann, and J. Krüger, Z. Phys. D **39**, 87 (1995).
[132] M. Musiał and S. A. Kucharski, J. Chem. Theory Comput. **10**, 1200 (2014).
[133] C. Chin, V. V. Flambaum, and M. G. Kozlov, New J. Phys. **11**, 055048 (2009).
[134] D. DeMille, S. Sainis, J. Sage, T. Bergeman, S. Kotochigova, and E. Tiesinga, Phys. Rev. Lett. **100**, 043202 (2008).
[135] T. Zelevinsky, S. Kotochigova, and J. Ye, Phys. Rev. Lett. **100**, 043201 (2008).
[136] J. Kobayashi, A. Ogino, and S. Inouye, Nat. Commun. **10**, 3771 (2019).
[137] M. Gronowski, A. M. Koza, and M. Tomza, Phys. Rev. A **102**, 020801 (2020).
[138] B. Gao, Phys. Rev. A **62**, 050702 (2000).

3.4 Paper IV: *Van der Waals coefficients for interactions of dysprosium and erbium atoms with alkali-metal and alkaline-earth-metal atoms*

Paper IV

"Van der Waals coefficients for interactions of dysprosium and erbium atoms with alkali-metal and alkaline-earth-metal atoms"

Klaudia Zaremba-Kopczyk, Michał Tomza, and Maxence Lepers

Preprint (2023)

Commentary

The strong long-range and anisotropic dipole-dipole interactions present in ultracold quantum gases of highly magnetic atoms yielded the observation of many unprecedented phenomena as discussed in Sec. 1.4. At ultralow temperatures, neutral atoms interact mainly via short-range van der Waals interactions whose leading term scales as $1/R^6$ with internuclear distance R, and, for atoms with magnetic moments, also via long-range and anisotropic magnetic DDIs that scale as $1/R^3$. In the case of atoms whose electronic state is not spherically symmetric (like Dy($^5I_8$) and Er($^3F_4$)), the vdW interactions are also anisotropic.

Since the long-range interactions are a dominant form of interactions in ultracold gases, their proper description is essential for the modeling of ultracold collisions. At the same time, for molecules containing heavy, multielectron atoms (such as highly magnetic lanthanides) it is impossible to compute BO potential energy curves covering the full range of internuclear distances with the accuracy needed to precisely predict the scattering properties of an ultracold gas. Therefore, simplified models for the ultracold atom-atom collisions have been developed, in which the tail of the interaction potential plays the most significant role, while the effect of short-range spin-exchange interactions is included within the phase of the scattering wave function [74].

The aim of the study presented in Paper IV was to compute the leading van der Waals coefficients, C_6, for Dy and Er atoms in their two lowest electronic states interacting with ground-state alkali-metal (Li, Na, K, Rb, Cs, Fr) and alkaline-earth-metal (Be, Mg, Ca, Sr, Ba) atoms. In this work, the PhD Candidate derived the analytical formulas for the matrix elements of the Hamiltonian describing the vdW interactions in a system composed of two neutral atoms using the angular momentum algebra. First, the derivation was made for the general case, and then for the particular case in which one of the atoms has both a non-zero electron spin and a non-zero orbital angular momentum, while the other atom is in an S state and can only have a non-zero electron spin. Next, the PhD Candidate implemented the derived formulas in the form of a computer code and performed numerical calculations of the C_6 coefficients. The PhD Candidate also wrote the first version of the manuscript, which is presented below.

Van der Waals coefficients for interactions of dysprosium and erbium atoms with alkali-metal and alkaline-earth-metal atoms

Klaudia Zaremba-Kopczyk,[1,*] Michał Tomza,[1] and Maxence Lepers[2,†]

[1] *Faculty of Physics, University of Warsaw, Pasteura 5, 02-093 Warsaw, Poland*
[2] *Laboratoire Interdisciplinaire Carnot de Bourgogne, CNRS, Université de Bourgogne Franche-Comté, 21078 Dijon, France*

(Dated: June 15, 2023)

Long-range part of the interatomic interactions plays a substantial role in the collisional dynamics of ultracold gases. Here, we report on the calculation of the C_6 coefficients characterizing the van der Waals interaction between dysprosium or erbium atoms in the two lowest energy levels and the ground-state alkali-metal (Li, Na, K, Rb, Cs, Fr) or alkaline-earth-metal (Be, Mg, Ca, Sr, Ba) atoms. The calculated van der Waals coefficients are essential for the modeling of collisional properties of heteronuclear quantum mixtures containing highly-magnetic dysprosium or erbium atoms and alkali-metal or alkaline-earth-metal atoms.

I. INTRODUCTION

Dipolar quantum gases have been experiencing a surge in interest over the last years, driven by the experimental breakthroughs in reaching quantum degeneracy with ultracold gases of highly-magnetic atoms [1–7] and continuous advances in the production of ultracold polar molecules [8, 9]. Ultracold gases composed of particles possessing a large intrinsic magnetic or/and electric dipole moment are characterized by the unique combination of tunable short-range contact interactions and long-range anisotropic dipole-dipole interactions, offering exceptional controllability with external electromagnetic fields. This feature of dipolar quantum gases has opened up new possibilites for exploring many-body physics of strongly correlated systems [10, 11], controlled chemistry [12, 13], quantum information [14, 15], and physics beyond the Standard Model [16].

Numerous fascinating phenomena have already been observed with dipolar gases composed of highly-magnetic lanthanide atoms, dysprosium and erbium, just to mention the chaotic spectra of Feshbach resonances [17], Fermi surface deformation [18], and quantum-stabilized states – self-bound droplets [19, 20] and supersolids [21–23]. While the experimental studies of ultracold polar molecules have been focused so far mainly on heteronuclear bialkali molecules [24–29], the production of dimers possessing much more complex internal structure, such as Er_2 [30] and DyK [31], has also been demonstrated. The ongoing advances in the production and manipulation of ultracold dipolar molecules hold promise for the realization of novel exotic states of quantum matter, like molecular superfluids and supersolids [32–34].

Recently, there has been a growing interest in degenerate mixtures containing highly-magnetic atoms, such as Cr ($^7S_3$; magnetic dipole moment of 6 Bohr magnetons, μ_B), Eu ($^8S_{7/2}$; $7\,\mu_B$), Er ($^3H_6$; $7\,\mu_B$), Ho ($^4I^o_{15/2}$; $9\,\mu_B$), or Dy ($^5I_8$; $10\,\mu_B$), as they offer great versatility in exploring novel physical phenomena. Heteronuclear molecules formed via magneto- or photoassociation will posses large both electric and magnetic dipole moments, combining strong anisotropic interactions of both electric and magnetic nature with the complexity of molecular electronic structure. Aside from the formation of molecules in non-trivial electronic states, such heteronuclear mixtures can be employed in studies of polaron physics in systems with dominant dipolar interactions [35–37], Efimov physics [38], exotic Fulde-Ferrell-Larkin-Ovchinnikov states in systems with significant mass imbalance [39, 40], and binary supersolids [41]. With current experiments on degenerate mixtures of Dy and K atoms [42–44], Dy and Er atoms [45–47], Er and Li atoms [48], Cr and Li atoms [49, 50], and Er and Yb atoms [51], the realization of theoretical proposals is becoming more and more feasible. Therefore, the electronic structure of molecules containing highly-magnetic transition-metal and lanthanide atoms, such as Cr– [52, 53] and Eu–alkali-metal and alkaline-earth-metal dimers [54] have been theoretically investigated alongside the collisional properties of ultracold heteronuclear mixtures: Cr+Li [55], Cr+Rb [52], Cr+Ca^+/Sr^+/Ba^+/Yb^+ [56], Eu+Li/Rb [57], Er+Li [58], Er+Yb [59, 60], Er+Sr [60], and Dy+Sr/Yb [60]. Additionally, the *ab initio* studies of interatomic interactions in homonuclear dimers of highly-magnetic lanthanide atoms such as Eu_2 [61], Er_2 [62], and Tm_2 [62] have also been reported.

Despite the significant increase in computational power and development of computational methods for electronic structure calculations over the last decades, a full *ab initio* approach to characterize the interatomic interactions in dimers containing heavy atoms in non-trivial electronic states would require the use of an enormous active space to account for all possible electron configurations, and that far exceeds currently available computational resources. In the case of lanthanide atoms, the unpaired electrons occupying the $4f$ or $5d$ shells, submerged under a closed $6s$ shell, give rise to large magnetic moments and

* klaudia.zaremba-kopczyk@fuw.edu.pl
† maxence.lepers@u-bourgogne.fr

large electronic orbital angular momenta of the atoms, which in turn lead to highly anisotropic interatomic interactions. Large basis sets would need to be employed in electronic structure calculations for dimers involving these atoms to ensure proper description of interactions at large internuclear distances. It is therefore impossible to compute Born-Oppenheimer potential-energy curves covering the full range of internuclear distances with the accuracy needed to precisely predict the scattering properties in ultracold systems containing highly-magnetic lanthanides.

At ultralow temperatures, neutral atoms interact mainly via short-range van der Waals (vdW) interactions, whose leading term scales as $1/R^6$ with internuclear distance R, and, for atoms with magnetic moments, also via long-range and anisotropic magnetic dipole-dipole interactions (DDI) that scale as $1/R^3$. In the case of atoms whose electronic state is not spherically symmetric, the vdW interactions are also anisotropic. This anisotropy of interactions induces couplings between the scattering states in the open channels and bound molecular states in the closed channels, significantly modifying the collisional properties of an ultracold quantum gas containing magnetic atoms in non-S states. Due to the large number of scattering channels involved, a full coupled-channels approach to quantum scattering calculations would be extremely computationally demanding. Therefore, simplified models for the ultracold atom-atom collisions have been developed [63]. Since the tail of the interaction potential plays the most significant role in the two-body dynamics, it is crucial to know accurate values of the van der Waals (or dispersion) C_6 coefficients that enter the leading term of the multipole expansion, $-C_6/R^6$, while the effect of short-range spin-exchange interactions can be included within the phase of the scattering wave function.

The aim of the present study is to compute the leading van der Waals coefficients, C_6, for Dy and Er atoms in their two lowest electronic states interacting with ground-state alkali-metal (Li, Na, K, Rb, Cs, Fr) and alkaline-earth-metal (Be, Mg, Ca, Sr, Ba) atoms. To this end, we employ the sum-over-states method to calculate the dynamic electric dipole polarizabilities, which are further used to compute the C_6 coefficients with the Gaussian quadrature method. We derive the formulas for the C_6 coefficients in the basis of fine atomic levels and present the numeric values of the isotropic $C_{6,0}$ and anisotropic $C_{6,2}$ coefficients.

The outline of this paper is as follows. In Section II, we introduce the electronic structure of the considered atoms, define the dynamic electric dipole polarizability, recall the formula for the second-order energy correction resulting from the vdW interactions between two neutral atoms and, finally, we provide the formulas for the C_6 coefficients: isotropic $C_{6,00}$ and anisotropic $C_{6,20}$. In Section III, we present the computed values of $C_{6,00}$ and $C_{6,20}$ coefficients for Dy/Er+alkali-metal/ alkaline-earth-metal atom pairs and discuss the obtained results. Section IV contains a summary of our findings and concluding remarks.

II. METHODOLOGY

A. Electronic structure

The electronic configuration of ground-state dysprosium Dy($^5I_8$) is [Xe]$4f^{10}6s^2$ with total electronic angular momentum $J = 8$, orbital angular momentum $L = 6$ and spin angular momentum $S = 2$. The first excited level Dy($^5I_7$) with $J = 7$ has the same electronic configuration and belongs to the same LS manifold as the ground state. The lowest electronic configuration of erbium is [Xe]$4f^{12}6s^2$ with the ground state Er($^3H_6$) ($J = 6$, $L = 5$, $S = 1$) and first excited state Er($^3F_4$) ($J = 4$, $L = 3$, $S = 1$). Ground-state alkali-metal atoms AM and ground-state alkaline-earth-metal atoms AEM posses a much simpler electronic structure, with spherically-symmetric ground states described by $^2S_{1/2}$ ($J = 1/2$, $L = 0$, $S = 1/2$) and $^1S_0$ ($J = 0$, $L = 0$, $S = 0$) terms, respectively. The total angular momenta J and their projections on the quantization axis M are good quantum numbers in the presence of a spin-orbit coupling and we use them to label the atomic energy levels throughout our derivations in Sec. II B – D.

B. Long-range potential energy

The multipolar expansion of the interaction energy between two distant charge distributions A and B, whose centers of mass are separated by distance R, can be written as (in spherical coordinates; Hartree atomic units are used throughout the paper):

$$V_{\rm AB}(R) = \sum_{l_A,l_B=0}^{+\infty} \sum_{m=-l_<}^{+l_<} \frac{f_{l_A l_B m}}{R^{1+l_A+l_B}} Q_{l_A,m}(A) Q_{l_B,-m}(B)\,, \tag{1}$$

where l_A and l_B describe the tensor rank related to the multipole moments $Q_{l_A,m}(A)$ and $Q_{l_B,-m}(B)$ of the charge distributions A and B, respectively, and $-l_< \leq m \leq l_<$, where $l_< = \min(l_A, l_B)$. The number factor $f_{l_A l_B m}$ equals to:

$$f_{l_A l_B m} = (-1)^{l_B} \sqrt{\frac{(2l_A+2l_B)!}{(2l_A)!(2l_B)!}} C^{l_A+l_B,0}_{l_A m l_B -m} \tag{2}$$

with $C^{a\alpha}_{b\beta c\gamma}$ denoting a Clebsch-Gordan (CG) coefficient.

Let A and B be two distant atoms. The matrix element describing the second-order energy correction resulting

from their interaction reads:

$$
\begin{aligned}
&\langle \beta_A J_A M'_A \beta_B J_B M'_B | \hat{V}^{(2)}_{\rm AB} | \beta_A J_A M_A \beta_B J_B M_B \rangle \\
&= - \sum_{l_A l_B l'_A l'_B} \frac{(-1)^{l_B + l'_B + 2J_A + 2J_B}}{R^{2+l_A+l_B+l'_A+l'_B}} \\
&\times \sqrt{\frac{(2l_A+2l_B+1)!(2l'_A+2l'_B+1)!}{(2l_A)!(2l_B)!(2l'_A)!(2l'_B)!}} \\
&\times \sum_{k_A k_B k q} (-1)^{k_A+k_B} (2k_A+1)(2k_B+1) \\
&\times C^{k0}_{l_A+l_B,0,l'_A+l'_B,0} C^{k0}_{k_A q k_B -q} \\
&\times \begin{Bmatrix} l'_B & l_B & k_B \\ l'_A & l_A & k_A \\ l'_A+l'_B & l_A+l_B & k \end{Bmatrix} \sum_{\beta''_A J''_A \beta''_B J''_B} \\
&\times \frac{\langle \beta_A J_A || \hat{Q}_{l_A} || \beta''_A J''_A \rangle \langle \beta''_A J''_A || \hat{Q}_{l'_A} || \beta_A J_A \rangle}{E_{\beta''_A J''_A} - E_{\beta_A J_A} + E_{\beta''_B J''_B} - E_{\beta_B J_B}} \\
&\times \langle \beta_B J_B || \hat{Q}_{l_B} || \beta''_B J''_B \rangle \langle \beta''_B J''_B || \hat{Q}_{l'_B} || \beta_B J_B \rangle \\
&\times \begin{Bmatrix} l'_A & l_A & k_A \\ J_A & J_A & J''_A \end{Bmatrix} \begin{Bmatrix} l'_B & l_B & k_B \\ J_B & J_B & J''_B \end{Bmatrix} \\
&\times \frac{C^{J_A M'_A}_{J_A M_A k_A q_A} C^{J_B M'_B}_{J_B M_B k_B q_B}}{\sqrt{(2J_A+1)(2J_B+1)}} \,,
\end{aligned}
\tag{3}
$$

where the subscripts denote values corresponding to atoms A and B, respectively, $E_{\beta_{\{A,B\}} J_{\{A,B\}}}$ ($E_{\beta''_{\{A,B\}} J''_{\{A,B\}}}$) is the energy of level $|\beta_{\{A,B\}} J_{\{A,B\}}\rangle$ ($|\beta''_{\{A,B\}} J''_{\{A,B\}}\rangle$) ($\beta$ denotes all remaining quantum numbers describing the state of an atom), and $\langle \beta_{\{A,B\}} J_{\{A,B\}} || \hat{Q}_{l_{\{A,B\}}} || \beta''_{\{A,B\}} J''_{\{A,B\}} \rangle$ is the reduced transition multipole moment between $|\beta_{\{A,B\}} J_{\{A,B\}}\rangle$ and $|\beta''_{\{A,B\}} J''_{\{A,B\}}\rangle$ levels. The selection rules impose that $M_A + M_B = M'_A + M'_B$. The pairs (k_A, k_B) and the value of k are constrained by the values of (l_A, l'_A, l_B, l'_B) and define the possible ranks of the tensorial terms; q_A, q_B, and q are limited by the values of k_A, k_B, and k [64]. The first curly brackets contain a Wigner 9-j symbol, whereas the latter two contain a Wigner 6-j symbol.

In this paper, we consider only the induced-dipole–induced-dipole interaction term ($l_A = l_B = l'_A = l'_B = 1$) and neglect higher-order terms as they decay faster than R^{-6}. In our particular case, atom $A = \{\mathrm{Dy}(^5I_8), \mathrm{Dy}(^5I_7), \mathrm{Er}(^3H_6), \mathrm{Er}(^3F_4)\}$ and atom $B = \{AM(^2S_{1/2}), AEM(^1S_0)\}$. Therefore, $k_A = \{0, 2\}$ and $k_B = 0$, which implies that $k = k_A = \{0, 2\}$ and $q_A = q_B = q = 0$. The CG coefficient $C^{\alpha a}_{\alpha a 00}$ equals to 1. With the above assumptions, the matrix element from Eq. (3) reads:

$$
\begin{aligned}
&\langle \beta_A J_A M'_A \beta_B J_B M'_B | \hat{V}^{(2)}_{\rm AB} | \beta_A J_A M_A \beta_B J_B M_B \rangle \\
&= -\frac{30}{R^6} \sum_{\beta''_A J''_A \beta''_B J''_B} \frac{(-1)^{J_A+J''_A} (-1)^{J_B+J''_B}}{\sqrt{(2J_A+1)(2J_B+1)}} \\
&\times \frac{|\langle \beta_A J_A || \hat{Q}_1 || \beta''_A J''_A \rangle|^2 |\langle \beta_B J_B || \hat{Q}_1 || \beta''_B J''_B \rangle|}{E_{\beta''_A J''_A} - E_{\beta_A J_A} + E_{\beta''_B J''_B} - E_{\beta_B J_B}} \\
&\times \sum_{k_A=0,2} (2k_A+1) C^{k_A 0}_{2020} C^{k_A 0}_{k_A 000} C^{J_A M'_A}_{J_A M_A k_A 0} \\
&\times \begin{Bmatrix} 1 & 1 & 0 \\ 1 & 1 & k_A \\ 2 & 2 & k_A \end{Bmatrix} \begin{Bmatrix} 1 & 1 & k_A \\ J_A & J_A & J''_A \end{Bmatrix} \begin{Bmatrix} 1 & 1 & 0 \\ J_B & J_B & J''_B \end{Bmatrix} \\
&\times \delta_{M_A, M'_A} \delta_{M_B, M'_B} \,,
\end{aligned}
\tag{4}
$$

which can be written as $-C_6/R^6$ with the leading van der Waals C_6 coefficient equal to:

$$
\begin{aligned}
C_6 &= 30 \sum_{\beta''_A J''_A \beta''_B J''_B} \frac{(-1)^{J_A+J''_A} (-1)^{J_B+J''_B}}{\sqrt{(2J_A+1)(2J_B+1)}} \\
&\times \frac{|\langle \beta_A J_A || \hat{Q}_1 || \beta''_A J''_A \rangle|^2 |\langle \beta_B J_B || \hat{Q}_1 || \beta''_B J''_B \rangle|^2}{E_{\beta''_A J''_A} - E_{\beta_A J_A} + E_{\beta''_B J''_B} - E_{\beta_B J_B}} \\
&\times \sum_{k_A=0,2} (2k_A+1) C^{k_A 0}_{2020} C^{k_A 0}_{k_A 000} C^{J_A M_A}_{J_A M_A k_A 0} \\
&\times \begin{Bmatrix} 1 & 1 & 0 \\ 1 & 1 & k_A \\ 2 & 2 & k_A \end{Bmatrix} \begin{Bmatrix} 1 & 1 & k_A \\ J_A & J_A & J''_A \end{Bmatrix} \begin{Bmatrix} 1 & 1 & 0 \\ J_B & J_B & J''_B \end{Bmatrix} .
\end{aligned}
\tag{5}
$$

C. Dynamic dipole polarizabilities

The dynamic electric dipole polarizability describes the dynamical response of an atom to an external oscillating electric field and, when calculated as a function of imaginary frequencies, it can be employed in calculations of the C_6 coefficients in a straightforward manner that will be discussed in the subsequent subsection. For an atom in a level $|\beta J\rangle$, the zz component of the dynamic electric dipole polarizability α_{zz} at imaginary frequency $i\omega$ can be written as:

$$
\begin{aligned}
&\alpha_{zz}(i\omega; \beta, J, M) = 2 \sum_{(\beta'' J'') \neq (\beta J)} \frac{E_{\beta'' J''} - E_{\beta J}}{(E_{\beta'' J''} - E_{\beta J})^2 + \omega^2} \\
&\times |\langle \beta J || \hat{Q}_1 || \beta'' J'' \rangle|^2 (-1)^{J+J''} \sum_{k=0,2} \sqrt{\frac{2k+1}{2J+1}} C^{k0}_{1010} C^{JM}_{JMk0} \\
&\times \begin{Bmatrix} 1 & 1 & k \\ J & J & J'' \end{Bmatrix} = \sum_{k=0,2} \frac{C^{k0}_{1010} C^{JM}_{JMk0}}{\sqrt{2J+1}} \alpha_k(i\omega; \beta, J) \,.
\end{aligned}
\tag{6}
$$

We can further decompose α_{zz} into isotropic (or scalar) $\alpha^{\rm scal}_{\beta,J}$ ($k = 0$) and anisotropic $\alpha^{\rm aniso}_{\beta,J,M}$ ($k = 2$) components,

expressed in terms of the coupled polarizabilities α_k as:

$$\alpha^{\rm scal}_{\beta,J}(i\omega) = -\frac{1}{\sqrt{3(2J+1)}}\alpha_0(i\omega;\beta,J)\,, \tag{7}$$

$$\alpha^{\rm aniso}_{\beta,J,M}(i\omega) = \frac{\sqrt{2}(3M^2-J(J+1))}{\sqrt{3J(J+1)(2J+3)(4J^2-1)}}\alpha_2(i\omega;\beta,J)\,, \tag{8}$$

where

$$\alpha_k(i\omega;\beta,J) = 2\sqrt{2k+1}\sum_{(\beta''J'')\neq(\beta J)}\frac{E_{\beta''J''}-E_{\beta J}}{(E_{\beta''J''}-E_{\beta J})^2+\omega^2} \times |\langle\beta J||\hat{Q}_1||\beta''J''\rangle|^2(-1)^{J+J''}\begin{Bmatrix}1 & 1 & k\\ J & J & J''\end{Bmatrix}; \tag{9}$$

$\alpha^{\rm aniso}_{\beta,J,M}$ can be further related to the so-called tensor polarizability $\alpha^{\rm tens}_{\beta,J}$ in the following way:

$$\alpha^{\rm aniso}_{\beta,J,M}(i\omega) = \frac{3M^2-J(J+1)}{J(2J-1)}\alpha^{\rm tens}_{\beta,J}(i\omega)\,, \tag{10}$$

where

$$\alpha^{\rm tens}_{\beta,J}(i\omega) = \sqrt{\frac{2J(2J-1)}{3(J+1)(2J+1)(2J+3)}}\alpha_2(i\omega;\beta,J). \tag{11}$$

The anisotropic part of the polarizability is non-zero when $J \geq 1$.

As one can tell from Eq. (6), the calculation of the dynamic electric dipole polarizabilities requires an accurate knowledge of transition energies and transition dipole moments. The atomic data for erbium and dysprosium were previously computed in Refs. [65, 66]. The polarizability data for the alkali-metal $AM(^2S_{1/2})$ and alkaline-earth-metal $AEM(^1S_0)$ atoms used in this paper were taken from Ref. [67].

D. van der Waals C_6 coefficients

The C_6 (5) coefficient can be written as a sum of the isotropic $C_{6,00}$ and anisotropic $\propto C_{6,20}$ contributions ($C_{6,20}$ is the only anisotropic contribution since atom B is spherically symmetric):

$$C_6 = C_{6,00} + \frac{3M_A^2 - J_A(J_A+1)}{2J_A(2J_A-1)}C_{6,20}\,, \tag{12}$$

where $C_{6,00}$ and $C_{6,20}$ can be conveniently expressed in terms of scalar $\alpha^{\rm scal}_{\beta,J}$ and tensor $\alpha^{\rm tens}_{\beta,J}$ dynamic polarizabilities at imaginary frequencies. To this end, we apply the residue theorem to Eq. (5):

$$\frac{1}{a+b} = \frac{2}{\pi}\int_0^\infty \frac{ab}{(a^2+u^2)(b^2+u^2)}{\rm d}u \tag{13}$$

TABLE I. C_6 coefficients (in a.u.) characterizing the van der Waals interactions between dysprosium atoms in the ground $^5I_8$ and first excited electronic state $^5I_7$ and alkali-metal (AM) atoms in the ground electronic state $^2S_{1/2}$.

AM	Dy($^5I_8$)+AM($^2S_{1/2}$)		Dy($^5I_7$)+AM($^2S_{1/2}$)	
	$C_{6,00}$	$C_{6,20}$	$C_{6,00}$	$C_{6,20}$
Li	1725	7.809	1725	8.104
Na	1850	8.033	1850	8.301
K	2857	13.13	2857	13.66
Rb	3139	14.29	3139	14.85
Cs	3762	17.24	3763	17.94
Fr	3372	14.47	3373	14.95

TABLE II. C_6 coefficients (in a.u.) characterizing the van der Waals interactions between dysprosium atoms in the ground $^5I_8$ and first excited electronic state $^5I_7$ and alkaline-earth metal (AEM) atoms in the ground electronic state $^1S_0$.

AEM	Dy($^5I_8$)+AEM($^1S_0$)		Dy($^5I_7$)+AEM($^1S_0$)	
	$C_{6,00}$	$C_{6,20}$	$C_{6,00}$	$C_{6,20}$
Be	671	1.997	671	1.973
Mg	1174	3.822	1174	3.821
Ca	2193	8.250	2193	8.393
Sr	2651	10.21	2651	10.41
Ba	3405	13.69	3406	14.03

where $a, b > 0$: in our case $a = E_{\beta''_A J''_A} - E_{\beta_A J_A}$, $b = E_{\beta''_B J''_B} - E_{\beta_B J_B}$, and $u = \omega$. We find that the isotropic coefficient $C_{6,00}$ can be computed using the integral:

$$C_{6,00} = \frac{3}{\pi}\int_0^\infty {\rm d}\omega\alpha^{\rm scal}_{\beta_A,J_A}(i\omega)\alpha^{\rm scal}_{\beta_B,J_B}(i\omega)\,, \tag{14}$$

while the $C_{6,20}$ coefficient is given by:

$$C_{6,20} = \frac{3}{\pi}\int_0^\infty {\rm d}\omega\alpha^{\rm tens}_{\beta_A,J_A}(i\omega)\alpha^{\rm scal}_{\beta_B,J_B}(i\omega)\,. \tag{15}$$

Following Ref. [67], we compute the C_{6,k_A0} coefficients using the 50-point Gauss-Legendre quadrature method:

$$C_{6,\{0,2\}0} = \frac{3}{\pi}\sum_{\kappa=0}^{50} w_\kappa\alpha^{\{\rm scal,tens\}}_{\beta_A,J_A}(i\omega_\kappa)\alpha^{\rm scal}_{\beta_B,J_B}(i\omega_\kappa)\,. \tag{16}$$

The values of Gaussian quadrature abscissas ω_κ and weights w_κ are provided in Ref. [67].

III. RESULTS AND DISCUSSION

In Tables I – IV we present the computed isotropic $C_{6,00}$ and anisotropic $C_{6,20}$ coefficients characterizing the leading term of van der Waals interactions between: Dy($^5I_8$)/Dy($^5I_7$) and alkali-metal $AM(^2S_{1/2})$

TABLE III. C_6 coefficients (in a.u.) characterizing the van der Waals interactions between erbium atoms in the ground $^3H_6$ and first excited electronic state $^3F_4$ and alkali-metal (AM) atoms in the ground electronic state $^2S_{1/2}$.

AM	Er($^3H_6$)+AM($^2S_{1/2}$)		Er($^3F_4$)+AM($^2S_{1/2}$)	
	$C_{6,00}$	$C_{6,20}$	$C_{6,00}$	$C_{6,20}$
Li	1609	-9.210	1607	0.6894
Na	1729	-8.956	1727	0.6578
K	2664	-15.89	2661	1.169
Rb	2929	-17.13	2925	1.242
Cs	3509	-20.95	3506	1.501
Fr	3156	-16.14	3152	1.105

TABLE IV. C_6 coefficients (in a.u.) characterizing the van der Waals interactions between erbium atoms in the ground $^3H_6$ and first excited electronic state $^3F_4$ and alkaline-earth metal (AEM) atoms in the ground electronic state $^1S_0$.

AEM	Er($^3H_6$)+AEM($^1S_0$)		Er($^3F_4$)+AEM($^1S_0$)	
	$C_{6,00}$	$C_{6,20}$	$C_{6,00}$	$C_{6,20}$
Be	636	-0.8894	636	0.0029
Mg	1110	-2.367	1109	0.0950
Ca	2063	-7.279	2061	0.4608
Sr	2491	-9.435	2489	0.6117
Ba	3195	-13.68	3192	0.9187

atoms (Table I), Dy($^5I_8$)/Dy($^5I_7$) and alkaline-earth-metal AEM($^1S_0$) atoms (Table II), Er($^3H_6$)/Er($^3F_4$) and alkali-metal AM($^2S_{1/2}$) atoms (Table III), and Er($^3H_6$)/Er($^3F_4$) and alkaline-earth-metal AEM($^1S_0$) atoms (Table IV). We can see that the isotropic coefficients strongly dominate the anisotropic ones. Despite their small values, the anisotropic $C_{6,20}$ coefficients are responsible for the coupling between scattering channels and the emergence of Feshbach resonances in ultracold collisions. For both dysprosium and erbium interactions with alkali-metal and alkaline-earth-metal atoms, the C_6 coefficients follow the trend of the static electric dipole polarizabilities – their absolute value increases with the increasing atomic number, and a slight deviation from the trend is observed for the interactions with francium.

IV. SUMMARY AND CONCLUSIONS

In the present work, we have provided analytical expressions for the isotropic and anisotropic C_6 van der Waals coefficients for the interaction between a non-S-state atom and an S-state atom. We have applied the derived formulas to compute the C_6 coefficients for the Dy($^5I_8$)/Dy($^5I_7$)/Er($^3H_6$)/Er($^4F_3$) + AM($^2S_{1/2}$)/AEM($^1S_0$) systems, where AM = Li, Na, K, Rb, Cs, Fr and AEM = Be, Mg, Ca, Sr, Ba.

With the rapid development in the field of dipolar quantum gases and ongoing experiments involving highly-magnetic lanthanide atoms, the present results will be beneficial for studies of collisional properties of heteronuclear quantum mixtures containing dysprosium or erbium atoms and alkali-metal or alkaline-earth metal atoms.

ACKNOWLEDGMENTS

K. Z.-K. acknowledges the financial support from the National Science Center in Poland (Grant No. 2019/35/N/ST4/04504). The work reported here was initiated during K. Z.-K.'s visit at the Université de Bourgogne Franche-Comté funded by the "Excellence Initiative – Research University" Program.

[1] A. Griesmaier, J. Werner, S. Hensler, J. Stuhler, and T. Pfau, Phys. Rev. Lett. **94**, 160401 (2005).
[2] M. Lu, N. Q. Burdick, S. H. Youn, and B. L. Lev, Phys. Rev. Lett. **107**, 190401 (2011).
[3] M. Lu, N. Q. Burdick, and B. L. Lev, Phys. Rev. Lett. **108**, 215301 (2012).
[4] K. Aikawa, A. Frisch, M. Mark, S. Baier, A. Rietzler, R. Grimm, and F. Ferlaino, Phys. Rev. Lett. **108**, 210401 (2012).
[5] K. Aikawa, A. Frisch, M. Mark, S. Baier, R. Grimm, and F. Ferlaino, Phys. Rev. Lett. **112**, 010404 (2014).
[6] B. Naylor, A. Reigue, E. Maréchal, O. Gorceix, B. Laburthe-Tolra, and L. Vernac, Phys. Rev. A **91**, 011603 (2015).
[7] Y. Miyazawa, R. Inoue, H. Matsui, G. Nomura, and M. Kozuma, Phys. Rev. Lett. **129**, 223401 (2022).
[8] B. Gadway and B. Yan, J. Phys. B **49**, 152002 (2016).
[9] S. Moses, J. Covey, M. Miecnikowski, D. Jin, and J. Ye, Nat. Phys. **13**, 13 (2017).
[10] M. A. Baranov, M. Dalmonte, G. Pupillo, and P. Zoller, Chem. Rev. **112**, 5012 (2012).
[11] L. Chomaz, I. Ferrier-Barbut, F. Ferlaino, B. Laburthe-Tolra, B. L. Lev, and T. Pfau, Rep. Prog. Phys. **86**, 026401 (2022).
[12] M. H. G. de Miranda, A. Chotia, B. Neyenhuis, D. Wang, G. Quéméner, S. Ospelkaus, J. L. Bohn, J. Ye, and D. S. Jin, Nat. Phys. **7**, 502 (2011).
[13] J. L. Bohn, A. M. Rey, and J. Ye, Science **357**, 1002 (2017).
[14] D. DeMille, Phys. Rev. Lett. **88**, 067901 (2002).
[15] K.-K. Ni, T. Rosenband, and D. D. Grimes, Chem. Sci. **9**, 6830 (2018).
[16] M. S. Safronova, D. Budker, D. DeMille, D. F. J. Kimball, A. Derevianko, and C. W. Clark, Rev. Mod. Phys. **90**, 025008 (2018).
[17] A. Frisch, M. Mark, K. Aikawa, F. Ferlaino, J. L. Bohn,

C. Makrides, A. Petrov, and S. Kotochigova, Nature **507**, 475 (2014).
[18] K. Aikawa, S. Baier, A. Frisch, M. Mark, C. Ravensbergen, and F. Ferlaino, Science **345**, 1484 (2014).
[19] H. Kadau, M. Schmitt, M. Wenzel, C. Wink, T. Maier, I. Ferrier-Barbut, and T. Pfau, Nature **530**, 194 (2016).
[20] M. Schmitt, M. Wenzel, F. Böttcher, I. Ferrier-Barbut, and T. Pfau, **539**, 259 (2016).
[21] L. Tanzi, E. Lucioni, F. Famà, J. Catani, A. Fioretti, C. Gabbanini, R. N. Bisset, L. Santos, and G. Modugno, Phys. Rev. Lett. **122**, 130405 (2019).
[22] F. Böttcher, J.-N. Schmidt, M. Wenzel, J. Hertkorn, M. Guo, T. Langen, and T. Pfau, Phys. Rev. X **9**, 011051 (2019).
[23] L. Chomaz, D. Petter, P. Ilzhöfer, G. Natale, A. Trautmann, C. Politi, G. Durastante, R. M. W. van Bijnen, A. Patscheider, M. Sohmen, M. J. Mark, and F. Ferlaino, Phys. Rev. X **9**, 021012 (2019).
[24] K.-K. Ni, S. Ospelkaus, M. H. G. de Miranda, A. Pe'er, B. Neyenhuis, J. J. Zirbel, S. Kotochigova, P. S. Julienne, D. S. Jin, and J. Ye, Science **322**, 231 (2008).
[25] S. Ospelkaus, K.-K. Ni, D. Wang, M. H. G. de Miranda, B. Neyenhuis, G. Quéméner, P. S. Julienne, J. L. Bohn, D. S. Jin, and J. Ye, Science **327**, 853 (2010).
[26] P. K. Molony, P. D. Gregory, Z. Ji, B. Lu, M. P. Köppinger, C. R. Le Sueur, C. L. Blackley, J. M. Hutson, and S. L. Cornish, Phys. Rev. Lett. **113**, 255301 (2014).
[27] J. W. Park, S. A. Will, and M. W. Zwierlein, Phys. Rev. Lett. **114**, 205302 (2015).
[28] M. Guo, B. Zhu, B. Lu, X. Ye, F. Wang, R. Vexiau, N. Bouloufa-Maafa, G. Quéméner, O. Dulieu, and D. Wang, Phys. Rev. Lett. **116**, 205303 (2016).
[29] X. Ye, M. Guo, M. L. González-Martínez, G. Quéméner, and D. Wang, Sci. Adv. **4**, eaaq0083 (2018).
[30] A. Frisch, M. Mark, K. Aikawa, S. Baier, R. Grimm, A. Petrov, S. Kotochigova, G. Quéméner, M. Lepers, O. Dulieu, and F. Ferlaino, Phys. Rev. Lett. **115**, 203201 (2015).
[31] E. Soave, A. Canali, Z.-X. Ye, M. Kreyer, E. Kirilov, and R. Grimm, arXiv preprint arXiv:2304.07921 (2023), 10.48550/arXiv.2304.07921.
[32] A. V. Gorshkov, S. R. Manmana, G. Chen, J. Ye, E. Demler, M. D. Lukin, and A. M. Rey, Phys. Rev. Lett. **107**, 115301 (2011).
[33] A. K. Fedorov, S. I. Matveenko, V. I. Yudson, and G. V. Shlyapnikov, Sci. Rep. **6**, 27448 (2016).
[34] M. Schmidt, L. Lassablière, G. Quéméner, and T. Langen, Phys. Rev. Res. **4**, 013235 (2022).
[35] B. Kain and H. Y. Ling, Phys. Rev. A **89**, 023612 (2014).
[36] M. Wenzel, T. Pfau, and I. Ferrier-Barbut, Phys. Scr. **93**, 104004 (2018).
[37] L. A. P. Ardila and T. Pohl, J. Phys. B: At. Mol. **52**, 015004 (2018).
[38] R. Pires, J. Ulmanis, S. Häfner, M. Repp, A. Arias, E. D. Kuhnle, and M. Weidemüller, Phys. Rev. Lett. **112**, 250404 (2014).
[39] L. Radzihovsky and D. E. Sheehy, Rep. Prog. Phys. **73**, 076501 (2010).
[40] J. Wang, Y. Che, L. Zhang, and Q. Chen, Sci. Rep. **7**, 39783 (2017).
[41] T. Bland, E. Poli, L. A. P. n. Ardila, L. Santos, F. Ferlaino, and R. N. Bisset, Phys. Rev. A **106**, 053322 (2022).
[42] C. Ravensbergen, V. Corre, E. Soave, M. Kreyer, E. Kirilov, and R. Grimm, Phys. Rev. A **98**, 063624 (2018).
[43] C. Ravensbergen, E. Soave, V. Corre, M. Kreyer, B. Huang, E. Kirilov, and R. Grimm, Phys. Rev. Lett. **124**, 203402 (2020).
[44] Z.-X. Ye, A. Canali, E. Soave, M. Kreyer, Y. Yudkin, C. Ravensbergen, E. Kirilov, and R. Grimm, Phys. Rev. A **106**, 043314 (2022).
[45] A. Trautmann, P. Ilzhöfer, G. Durastante, C. Politi, M. Sohmen, M. J. Mark, and F. Ferlaino, Phys. Rev. Lett. **121**, 213601 (2018).
[46] G. Durastante, C. Politi, M. Sohmen, P. Ilzhöfer, M. J. Mark, M. A. Norcia, and F. Ferlaino, Phys. Rev. A **102**, 033330 (2020).
[47] C. Politi, A. Trautmann, P. Ilzhöfer, G. Durastante, M. J. Mark, M. Modugno, and F. Ferlaino, Phys. Rev. A **105**, 023304 (2022).
[48] F. Schäfer, N. Mizukami, and Y. Takahashi, Phys. Rev. A **105**, 012816 (2022).
[49] A. Ciamei, S. Finelli, A. Cosco, M. Inguscio, A. Trenkwalder, and M. Zaccanti, Phys. Rev. A **106**, 053318 (2022).
[50] A. Ciamei, S. Finelli, A. Trenkwalder, M. Inguscio, A. Simoni, and M. Zaccanti, Phys. Rev. Lett. **129**, 093402 (2022).
[51] F. Schäfer, Y. Haruna, and Y. Takahashi, Phys. Rev. A **107**, L031306 (2023).
[52] Z. Pavlović, H. R. Sadeghpour, R. Côté, and B. O. Roos, Phys. Rev. A **81**, 052706 (2010).
[53] M. Tomza, Phys. Rev. A **88**, 012519 (2013).
[54] M. Tomza, Phys. Rev. A **90**, 022514 (2014).
[55] K. Zaremba-Kopczyk, M. Gronowski, and M. Tomza, (2023).
[56] M. Tomza, Phys. Rev. A **92**, 062701 (2015).
[57] K. Zaremba-Kopczyk, P. S. Żuchowski, and M. Tomza, Phys. Rev. A **98**, 032704 (2018).
[58] M. L. González-Martínez and P. S. Żuchowski, Phys. Rev. A **92**, 022708 (2015).
[59] M. B. Kosicki, M. Borkowski, and P. S. Żuchowski, New J. Phys. **22**, 023024 (2020).
[60] M. D. Frye, S. L. Cornish, and J. M. Hutson, Phys. Rev. X **10**, 041005 (2020).
[61] A. A. Buchachenko, G. Chalasinski, and M. M. Szczesniak, J. Chem. Phys. **131**, 241102 (2009).
[62] E. Tiesinga, J. Kłos, M. Li, A. Petrov, and S. Kotochigova, New J. Phys. **23**, 085007 (2021).
[63] C. Chin, R. Grimm, P. S. Julienne, and E. Tiesinga, Rev. Mod. Phys. **82**, 1225 (2010).
[64] M. Lepers and O. Dulieu, Phys. Chem. Chem. Phys. **13**, 19106 (2011).
[65] H. Li, J.-F. Wyart, O. Dulieu, S. Nascimbène, and M. Lepers, J. Phys. B: At. Mol. Opt. Phys. **50**, 014005 (2016).
[66] M. Lepers, J.-F. Wyart, and O. Dulieu, Phys. Rev. A **89**, 022505 (2014).
[67] A. Derevianko, S. G. Porsev, and J. F. Babb, At. Data Nucl. Data Tables **96**, 323 (2010).

Chapter 4

Conclusions and outlook

The main goal of the present thesis was theoretical investigation of interatomic interactions and ultracold collisions in mixtures containing transition-metal and lanthanide atoms. In recent years, such systems have been subject to intensified studies, both theoretical and experimental, as they are promising candidates for many future applications.

The results obtained within this PhD work support current experiments on ultracold quantum gases containing highly magnetic atoms (such as Cr, Eu, Dy, and Er) and propose new molecular systems for quantum simulations of many-body physics and precision measurements. The main achievements of the present work can be summarized as follows:

1. Magnetically tunable Feshbach resonances between ultracold europium ^{153}Eu atoms and between europium ^{153}Eu and alkali-metal ^{7}Li and ^{87}Rb atoms have been investigated using multichannel quantum scattering calculations. We have found out that favorable resonances are expected at experimentally feasible magnetic-field strengths below 1000 G for all investigated atomic combinations. A large number and density of s-wave and d-wave resonances is expected in ultracold gases of europium atoms with limited signatures of quantum chaotic behavior. The dipole-dipole interaction between europium and alkali-metal atoms is weaker than the spin-exchange interaction and hence s-wave resonances are more favorable than d-wave ones in these systems.

2. We have carried out state-of-the-art *ab initio* calculations of the potential-energy curves, permanent electric dipole moments, and spectroscopic constants for diatomic molecules composed of a closed-shell Zn or Cd atom interacting with an alkali-metal (Li, Na, K, Rb, Cs, Fr) or alkaline-earth-metal (Be, Mg, Ca, Sr, Ba, Ra) atom in their ground states. We have employed the coupled-clusters method with single, double, and triple excitations combined with large Gaussian basis sets and small-core relativistic energy-consistent pseudopotentials for heavier atoms. We have predicted that the molecules in the ground electronic state are weakly bound van der Waals complexes with rather small permanent electric dipole moments and are chemically reactive. The studied molecules are potential candidates for ultracold quantum physics and chemistry experiments, ranging from controlled chemical reactions to precision measurements.

3. We have investigated interatomic interactions and ultracold collisions between chromium and lithium atoms. We have employed the coupled-clusters and multireference configuration interaction methods to calculate the potential energy curves and the permanent and transition electric dipole moments for the quartet, sextet, and octet electronic states of the LiCr molecule correlated to the four lowest atomic dissociation limits. We have shown that the LiCr molecule is strongly bound in the ground $X\,^6\Sigma^+$ electronic state and possesses a large permanent electric dipole moment of 3.3 D at an equilibrium distance. We have employed multichannel quantum scattering calculations to investigate the magnetically tunable Feshbach resonances in ultracold ^{52}Cr+^{6}Li and ^{53}Cr+^{6}Li mixtures. We

have proposed a way to probe the temporal variation of the proton-to-electron mass ratio using ultracold LiCr molecules. We have investigated the prospects for magnetoassociation and photoassociation of Li and Cr atoms into polar and highly magnetic LiCr molecules. The obtained theoretical results may guide the ongoing experimental studies on ultracold strongly-interacting mass-imbalanced Fermi-Fermi Cr+Li mixtures and LiCr molecules.

4. We have derived analytical expressions for the isotropic and anisotropic C_6 van der Waals coefficients for the interaction between a non-S-state atom and an S-state atom. We have applied the derived formulas to compute the C_6 coefficients for the Dy($^5I_8$)/Dy($^5I_7$) / Er($^3H_6$)/Er($^4F_3$) + $AM(^2S_{1/2})/AEM(^1S_0)$ systems, where AM = Li, Na, K, Rb, Cs, Fr and AEM = Be, Mg, Ca, Sr, Ba. The calculated van der Waals coefficients are essential for the modeling of collisional properties of heteronuclear quantum mixtures containing highly magnetic dysprosium or erbium atoms and alkali-metal or alkaline-earth-metal atoms and may guide future experiments on heteronuclear mixtures containing these atoms.

Therefore, the results presented in the thesis may guide the ongoing and future experimental studies on ultracold quantum mixtures containing transition-metal and lanthanide atoms, including molecule formation and investigation of novel exotic many-body physics or precision measurements.

Symbols and abbreviations

List of abbreviations

AMO	atomic, molecular and optical
BCS	Bardeen-Cooper-Schrieffer
BEC	Bose-Einstein condensate
BO	Born-Oppenheimer
BSSE	basis set superposition error
CI	Configuration Interaction
CBS	complete basis set
CC	coupled clusters
COM	center of mass
DBOC	diagonal Born-Oppenheimer correction
DDI	dipole-dipole interaction
DKH	Douglas-Kroll-Hess
DVR	discrete variable representation
ECP	effective core potential
EDM	electric dipole moment
eEDM	electron electric dipole moment
FCF	Franck-Condon factor
FR	Feshbach resonance
FFLO	Fulde-Ferrell-Larkin-Ovchinnikov
GTO	Gaussian-type orbital
HF	Hartree-Fock
LCAO	linear combination of atomic orbitals
MCSCF	multi-configurational self-consistent field
MRCI	multireference configuration interaction
MO	molecular orbital
MOT	magneto-optical trap
PA	photoassociation
PEC	potential energy curve
SCF	self-consistent field
STIRAP	stimulated Raman adiabatic passage
SO	spin-orbit
STO	Slater-type orbital
vdW	van der Waals

List of symbols

a	s-wave scattering length
a_0	Bohr radius
α	fine-structure constant
c	speed of light
$\boldsymbol{d}$	electric dipole moment
e	electron charge
ϵ_0	vacuum permittivity
$\boldsymbol{\nabla}$	gradient operator
h	Planck constant
$\hbar$	reduced Planck constant, $\hbar = h/2\pi$
g	g-factor
$\boldsymbol{I}$	nuclear spin angular momentum
$\boldsymbol{J}$	total electronic angular momentum
k_B	Boltzmann constant
l	orbital angular momentum quantum number
$\boldsymbol{L}$	electronic orbital angular momentum
m_e	electron mass
m_p	proton mass
$\boldsymbol{\mu}$	magnetic dipole moment
μ_0	vacuum permeability
μ_B	Bohr magneton
μ_N	nuclear magneton
n	phase-space density
ω	angular frequency
$\boldsymbol{S}$	electronic spin angular momentum
T	temperature
v	vibrational quantum number
Z	nuclear charge

Bibliography

[1] M. H. Anderson, J. R. Ensher, M. R. Matthews, C. E. Wieman, and E. A. Cornell, Science **269**, 198 (1995).

[2] K. B. Davis, M. O. Mewes, M. R. Andrews, N. J. van Druten, D. S. Durfee, D. M. Kurn, and W. Ketterle, Phys. Rev. Lett. **75**, 3969 (1995).

[3] C. C. Bradley, C. A. Sackett, J. J. Tollett, and R. G. Hulet, Phys. Rev. Lett. **75**, 1687 (1995).

[4] S. N. Bose, Z. Phys. **26**, 178 (1924).

[5] A. Einstein, Sitzungber. Kgl. Akad. Wiss. , 261 (1924).

[6] S. Chu, Rev. Mod. Phys. **70**, 685 (1998).

[7] C. N. Cohen-Tannoudji, Rev. Mod. Phys. **70**, 707 (1998).

[8] W. D. Phillips, Rev. Mod. Phys. **70**, 721 (1998).

[9] E. A. Cornell and C. E. Wieman, Rev. Mod. Phys. **74**, 875 (2002).

[10] W. Ketterle, Rev. Mod. Phys. **74**, 1131 (2002).

[11] J. L. Hall, Rev. Mod. Phys. **78**, 1279 (2006).

[12] T. W. Hänsch, Rev. Mod. Phys. **78**, 1297 (2006).

[13] R. J. Glauber, Rev. Mod. Phys. **78**, 1267 (2006).

[14] S. Haroche, Rev. Mod. Phys. **85**, 1083 (2013).

[15] D. J. Wineland, Rev. Mod. Phys. **85**, 1103 (2013).

[16] B. DeMarco and D. S. Jin, Science **285**, 1703 (1999).

[17] G. Modugno, G. Ferrari, G. Roati, R. J. Brecha, A. Simoni, and M. Inguscio, Science **294**, 1320 (2001).

[18] A. G. Truscott, K. E. Strecker, W. I. McAlexander, G. B. Partridge, and R. G. Hulet, Science **291**, 2570 (2001).

[19] T. Weber, J. Herbig, M. Mark, H.-C. Nägerl, and R. Grimm, Science **299**, 232 (2003).

[20] K. M. O'Hara, S. L. Hemmer, M. E. Gehm, S. R. Granade, and J. E. Thomas, Science **298**, 2179 (2002).

[21] S. Kraft, F. Vogt, O. Appel, F. Riehle, and U. Sterr, Phys. Rev. Lett. **103**, 130401 (2009).

[22] S. Stellmer, M. K. Tey, B. Huang, R. Grimm, and F. Schreck, Phys. Rev. Lett. **103**, 200401 (2009).

[23] Y. N. M. de Escobar, P. G. Mickelson, M. Yan, B. J. DeSalvo, S. B. Nagel, and T. C. Killian, Phys. Rev. Lett. **103**, 200402 (2009).

[24] B. J. DeSalvo, M. Yan, P. G. Mickelson, Y. N. Martinez de Escobar, and T. C. Killian, Phys. Rev. Lett. **105**, 030402 (2010).

[25] A. Griesmaier, J. Werner, S. Hensler, J. Stuhler, and T. Pfau, Phys. Rev. Lett. **94**, 160401 (2005).

[26] B. Naylor, A. Reigue, E. Maréchal, O. Gorceix, B. Laburthe-Tolra, and L. Vernac, Phys. Rev. A **91**, 011603 (2015).

[27] Y. Takasu, K. Maki, K. Komori, T. Takano, K. Honda, M. Kumakura, T. Yabuzaki, and Y. Takahashi, Phys. Rev. Lett. **91**, 040404 (2003).

[28] T. Fukuhara, Y. Takasu, M. Kumakura, and Y. Takahashi, Phys. Rev. Lett. **98**, 030401 (2007).

[29] S. Sugawa, R. Yamazaki, S. Taie, and Y. Takahashi, Phys. Rev. A **84**, 011610 (2011).

[30] M. Lu, N. Q. Burdick, S. H. Youn, and B. L. Lev, Phys. Rev. Lett. **107**, 190401 (2011).

[31] M. Lu, N. Q. Burdick, and B. L. Lev, Phys. Rev. Lett. **108**, 215301 (2012).

[32] K. Aikawa, A. Frisch, M. Mark, S. Baier, A. Rietzler, R. Grimm, and F. Ferlaino, Phys. Rev. Lett. **108**, 210401 (2012).

[33] K. Aikawa, A. Frisch, M. Mark, S. Baier, R. Grimm, and F. Ferlaino, Phys. Rev. Lett. **112**, 010404 (2014).

[34] Y. Miyazawa, R. Inoue, H. Matsui, G. Nomura, and M. Kozuma, Phys. Rev. Lett. **129**, 223401 (2022).

[35] M. Iskin and C. A. R. S. de Melo, Phys. Rev. Lett. **99**, 080403 (2007).

[36] M. Taglieber, A.-C. Voigt, T. Aoki, T. W. Hänsch, and K. Dieckmann, Phys. Rev. Lett. **100**, 010401 (2008).

[37] R. Wynar, R. S. Freeland, D. J. Han, C. Ryu, and D. J. Heinzen, Science **287**, 1016 (2000).

[38] E. A. Donley, N. R. Claussen, S. T. Thompson, and C. E. Wieman, Nature **417**, 529 (2002).

[39] C. Chin, A. J. Kerman, V. Vuletić, and S. Chu, Phys. Rev. Lett. **90**, 033201 (2003).

[40] C. A. Regal, C. Ticknor, J. L. Bohn, and D. S. Jin, Nature **424**, 47 (2003).

[41] J. Herbig, T. Kraemer, M. Mark, T. Weber, C. Chin, H.-C. Nägerl, and R. Grimm, Science **301**, 1510 (2003).

[42] T. Feldker, H. Fürst, H. Hirzler, N. V. Ewald, M. Mazzanti, D. Wiater, M. Tomza, and R. Gerritsma, Nat. Phys. **16**, 413 (2020).

[43] P. Weckesser, F. Thielemann, D. Wiater, A. Wojciechowska, L. Karpa, K. Jachymski, M. Tomza, T. Walker, and T. Schaetz, Nature **600**, 429 (2021).

[44] S. Ma, A. P. Burgers, G. Liu, J. Wilson, B. Zhang, and J. D. Thompson, Phys. Rev. X **12**, 021028 (2022).

[45] A. Jenkins, J. W. Lis, A. Senoo, W. F. McGrew, and A. M. Kaufman, Phys. Rev. X **12**, 021027 (2022).

[46] I. Bloch, J. Dalibard, and W. Zwerger, Rev. Mod. Phys. **80**, 885 (2008).

[47] I. Bloch, J. Dalibard, and S. Nascimbène, Nat. Phys. **8**, 267 (2012).

[48] C. Gross and I. Bloch, Science **357**, 995 (2017).

[49] R. V. Krems, Phys. Chem. Chem. Phys. **10**, 4079 (2008).

[50] J. L. Bohn, A. M. Rey, and J. Ye, Science **357**, 1002 (2017).

[51] M. S. Safronova, D. Budker, D. DeMille, D. F. J. Kimball, A. Derevianko, and C. W. Clark, Rev. Mod. Phys. **90**, 025008 (2018).

[52] M. G. Kozlov, M. S. Safronova, J. R. Crespo López-Urrutia, and P. O. Schmidt, Rev. Mod. Phys. **90**, 045005 (2018).

[53] B. Kain and H. Y. Ling, Phys. Rev. A **89**, 023612 (2014).

[54] M. Wenzel, T. Pfau, and I. Ferrier-Barbut, Phys. Scr. **93**, 104004 (2018).

[55] L. A. P. Ardila and T. Pohl, J. Phys. B: At. Mol. **52**, 015004 (2018).

[56] R. Pires, J. Ulmanis, S. Häfner, M. Repp, A. Arias, E. D. Kuhnle, and M. Weidemüller, Phys. Rev. Lett. **112**, 250404 (2014).

[57] L. Radzihovsky and D. E. Sheehy, Rep. Prog. Phys. **73**, 076501 (2010).

[58] J. Wang, Y. Che, L. Zhang, and Q. Chen, Sci. Rep. **7**, 39783 (2017).

[59] T. Bland, E. Poli, L. A. P. n. Ardila, L. Santos, F. Ferlaino, and R. N. Bisset, Phys. Rev. A **106**, 053322 (2022).

[60] C. Ravensbergen, V. Corre, E. Soave, M. Kreyer, E. Kirilov, and R. Grimm, Phys. Rev. A **98**, 063624 (2018).

[61] C. Ravensbergen, E. Soave, V. Corre, M. Kreyer, B. Huang, E. Kirilov, and R. Grimm, Phys. Rev. Lett. **124**, 203402 (2020).

[62] Z.-X. Ye, A. Canali, E. Soave, M. Kreyer, Y. Yudkin, C. Ravensbergen, E. Kirilov, and R. Grimm, Phys. Rev. A **106**, 043314 (2022).

[63] A. Trautmann, P. Ilzhöfer, G. Durastante, C. Politi, M. Sohmen, M. J. Mark, and F. Ferlaino, Phys. Rev. Lett. **121**, 213601 (2018).

[64] G. Durastante, C. Politi, M. Sohmen, P. Ilzhöfer, M. J. Mark, M. A. Norcia, and F. Ferlaino, Phys. Rev. A **102**, 033330 (2020).

[65] C. Politi, A. Trautmann, P. Ilzhöfer, G. Durastante, M. J. Mark, M. Modugno, and F. Ferlaino, Phys. Rev. A **105**, 023304 (2022).

[66] F. Schäfer, N. Mizukami, and Y. Takahashi, Phys. Rev. A **105**, 012816 (2022).

[67] A. Ciamei, S. Finelli, A. Cosco, M. Inguscio, A. Trenkwalder, and M. Zaccanti, Phys. Rev. A **106**, 053318 (2022).

[68] A. Ciamei, S. Finelli, A. Trenkwalder, M. Inguscio, A. Simoni, and M. Zaccanti, Phys. Rev. Lett. **129**, 093402 (2022).

[69] F. Schäfer, Y. Haruna, and Y. Takahashi, Phys. Rev. A **107**, L031306 (2023).

[70] K. Zaremba-Kopczyk, P. S. Żuchowski, and M. Tomza, Phys. Rev. A **98**, 032704 (2018).

[71] K. Zaremba-Kopczyk and M. Tomza, Phys. Rev. A **104**, 042816 (2021).

[72] K. M. Jones, E. Tiesinga, P. D. Lett, and P. S. Julienne, Rev. Mod. Phys. **78**, 483 (2006).

[73] T. D. Lee, K. Huang, and C. N. Yang, Phys. Rev. **106**, 1135 (1957).

[74] C. Chin, R. Grimm, P. S. Julienne, and E. Tiesinga, Rev. Mod. Phys. **82**, 1225 (2010).

[75] R. Grimm, M. Weidemüller, and Y. B. Ovchinnikov, Adv. At. Mol. Opt. Phy. **42**, 95 (2000).

[76] E. L. Raab, M. Prentiss, A. Cable, S. Chu, and D. E. Pritchard, Phys. Rev. Lett. **59**, 2631 (1987).

[77] A. L. Migdall, J. V. Prodan, W. D. Phillips, T. H. Bergeman, and H. J. Metcalf, Phys. Rev. Lett. **54**, 2596 (1985).

[78] S. Chu, J. E. Bjorkholm, A. Ashkin, and A. Cable, Phys. Rev. Lett. **57**, 314 (1986).

[79] L. D. Carr, D. DeMille, R. V. Krems, and J. Ye, New J. Phys. **11**, 055049 (2009).

[80] T. Köhler, K. Góral, and P. S. Julienne, Rev. Mod. Phys. **78**, 1311 (2006).

[81] J. Ulmanis, J. Deiglmayr, M. Repp, R. Wester, and M. Weidemüller, Chem. Rev. **112**, 4890 (2012).

[82] N. V. Vitanov, A. A. Rangelov, B. W. Shore, and K. Bergmann, Rev. Mod. Phys. **89**, 015006 (2017).

[83] K.-K. Ni, S. Ospelkaus, M. H. G. de Miranda, A. Pe'er, B. Neyenhuis, J. J. Zirbel, S. Kotochigova, P. S. Julienne, D. S. Jin, and J. Ye, Science **322**, 231 (2008).

[84] J. G. Danzl, E. Haller, M. Gustavsson, M. J. Mark, R. Hart, N. Bouloufa, O. Dulieu, H. Ritsch, and H.-C. Nägerl, Science **321**, 1062 (2008).

[85] K. Aikawa, D. Akamatsu, M. Hayashi, K. Oasa, J. Kobayashi, P. Naidon, T. Kishimoto, M. Ueda, and S. Inouye, Phys. Rev. Lett. **105**, 203001 (2010).

[86] T. Takekoshi, L. Reichsöllner, A. Schindewolf, J. M. Hutson, C. R. Le Sueur, O. Dulieu, F. Ferlaino, R. Grimm, and H.-C. Nägerl, Phys. Rev. Lett. **113**, 205301 (2014).

[87] P. K. Molony, P. D. Gregory, Z. Ji, B. Lu, M. P. Köppinger, C. R. Le Sueur, C. L. Blackley, J. M. Hutson, and S. L. Cornish, Phys. Rev. Lett. **113**, 255301 (2014).

[88] F. Wang, X. He, X. Li, B. Zhu, J. Chen, and D. Wang, New J.Phys. **17**, 035003 (2015).

[89] J. W. Park, S. A. Will, and M. W. Zwierlein, Phys. Rev. Lett. **114**, 205302 (2015).

[90] M. Guo, B. Zhu, B. Lu, X. Ye, F. Wang, R. Vexiau, N. Bouloufa-Maafa, G. Quéméner, O. Dulieu, and D. Wang, Phys. Rev. Lett. **116**, 205303 (2016).

[91] T. M. Rvachov, H. Son, A. T. Sommer, S. Ebadi, J. J. Park, M. W. Zwierlein, W. Ketterle, and A. O. Jamison, Phys. Rev. Lett. **119**, 143001 (2017).

[92] L. D. Marco, G. Valtolina, K. Matsuda, W. G. Tobias, J. P. Covey, and J. Ye, Science **363**, 853 (2019).

[93] S. Stellmer, B. Pasquiou, R. Grimm, and F. Schreck, Phys. Rev. Lett. **109**, 115302 (2012).

[94] V. Barbé, A. Ciamei, B. Pasquiou, L. Reichsöllner, F. Schreck, P. S. Żuchowski, and J. M. Hutson, Nat. Phys. **14**, 881 (2018).

[95] K. H. Leung, E. Tiberi, B. Iritani, I. Majewska, R. Moszynski, and T. Zelevinsky, New J. Phys. **23**, 115002 (2021).

[96] A. Frisch, M. Mark, K. Aikawa, S. Baier, R. Grimm, A. Petrov, S. Kotochigova, G. Quéméner, M. Lepers, O. Dulieu, and F. Ferlaino, Phys. Rev. Lett. **115**, 203201 (2015).

[97] E. Soave, A. Canali, Z.-X. Ye, M. Kreyer, E. Kirilov, and R. Grimm, Phys. Rev. Res. **5**, 033117 (2023).

[98] M. W. Zwierlein, C. A. Stan, C. H. Schunck, S. M. F. Raupach, S. Gupta, Z. Hadzibabic, and W. Ketterle, Phys. Rev. Lett. **91**, 250401 (2003).

[99] S. Jochim, M. Bartenstein, A. Altmeyer, G. Hendl, S. Riedl, C. Chin, J. H. Denschlag, and R. Grimm, Science **302**, 2101 (2003).

[100] K. Xu, T. Mukaiyama, J. R. Abo-Shaeer, J. K. Chin, D. E. Miller, and W. Ketterle, Phys. Rev. Lett. **91**, 210402 (2003).

[101] M. Greiner, C. A. Regal, and D. S. Jin, Nature **426**, 537 (2003).

[102] S. Dürr, T. Volz, A. Marte, and G. Rempe, Phys. Rev. Lett. **92**, 020406 (2004).

[103] E. Wille, F. M. Spiegelhalder, G. Kerner, D. Naik, A. Trenkwalder, G. Hendl, F. Schreck, R. Grimm, T. G. Tiecke, J. T. M. Walraven, S. J. J. M. F. Kokkelmans, E. Tiesinga, and P. S. Julienne, Phys. Rev. Lett. **100**, 053201 (2008).

[104] J. Deiglmayr, A. Grochola, M. Repp, K. Mörtlbauer, C. Glück, J. Lange, O. Dulieu, R. Wester, and M. Weidemüller, Phys. Rev. Lett. **101**, 133004 (2008).

[105] C.-H. Wu, J. W. Park, P. Ahmadi, S. Will, and M. W. Zwierlein, Phys. Rev. Lett. **109**, 085301 (2012).

[106] X. Ye, M. Guo, M. L. González-Martínez, G. Quéméner, and D. Wang, Sci. Adv. **4**, eaaq0083 (2018).

[107] M. Semczuk, X. Li, W. Gunton, M. Haw, N. S. Dattani, J. Witz, A. K. Mills, D. J. Jones, and K. W. Madison, Phys. Rev. A **87**, 052505 (2013).

[108] P. D. Lett, K. Helmerson, W. D. Phillips, L. P. Ratliff, S. L. Rolston, and M. E. Wagshul, Phys. Rev. Lett. **71**, 2200 (1993).

[109] H. Wang, P. L. Gould, and W. C. Stwalley, Phys. Rev. Lett. **80**, 476 (1998).

[110] J. D. Miller, R. A. Cline, and D. J. Heinzen, Phys. Rev. Lett. **71**, 2204 (1993).

[111] A. Fioretti, D. Comparat, A. Crubellier, O. Dulieu, F. Masnou-Seeuws, and P. Pillet, Phys. Rev. Lett. **80**, 4402 (1998).

[112] A. Ridinger, S. Chaudhuri, T. Salez, D. R. Fernandes, N. Bouloufa, O. Dulieu, C. Salomon, and F. Chevy, Europhys. Lett. **96**, 33001 (2011).

[113] S. Dutta, J. Lorenz, A. Altaf, D. S. Elliott, and Y. P. Chen, Phys. Rev. A **89**, 020702 (2014).

[114] J. W. Park, S. A. Will, and M. W. Zwierlein, New J. Phys. **17**, 075016 (2015).

[115] D. Wang, J. Qi, M. F. Stone, O. Nikolayeva, H. Wang, B. Hattaway, S. D. Gensemer, P. L. Gould, E. E. Eyler, and W. C. Stwalley, Phys. Rev. Lett. **93**, 243005 (2004).

[116] A. Wakim, P. Zabawa, and N. P. Bigelow, Phys. Chem. Chem. Phys. **13**, 18887 (2011).

[117] C. Gabbanini and O. Dulieu, Phys. Chem. Chem. Phys. **13**, 18905 (2011).

[118] G. Zinner, T. Binnewies, F. Riehle, and E. Tiemann, Phys. Rev. Lett. **85**, 2292 (2000).

[119] G. Reinaudi, C. B. Osborn, M. McDonald, S. Kotochigova, and T. Zelevinsky, Phys. Rev. Lett. **109**, 115303 (2012).

[120] R. Roy, R. Shrestha, A. Green, S. Gupta, M. Li, S. Kotochigova, A. Petrov, and C. H. Yuen, Phys. Rev. A **94**, 033413 (2016).

[121] N. Nemitz, F. Baumer, F. Münchow, S. Tassy, and A. Görlitz, Phys. Rev. A **79**, 061403 (2009).

[122] A. Guttridge, S. A. Hopkins, M. D. Frye, J. J. McFerran, J. M. Hutson, and S. L. Cornish, Phys. Rev. A **97**, 063414 (2018).

[123] S. Tojo, M. Kitagawa, K. Enomoto, Y. Kato, Y. Takasu, M. Kumakura, and Y. Takahashi, Phys. Rev. Lett. **96**, 153201 (2006).

[124] N. R. Hutzler, H.-I. Lu, and J. M. Doyle, Chem. Rev. **112**, 4803 (2012).

[125] E. S. Shuman, J. F. Barry, and D. DeMille, Nature **467**, 820 (2010).

[126] S. Truppe, H. J. Williams, M. Hambach, L. Caldwell, N. J. Fitch, E. A. Hinds, B. E. Sauer, and M. R. Tarbutt, Nat. Phys. **13**, 1173 (2017).

[127] B. L. Augenbraun, A. Frenett, H. Sawaoka, C. Hallas, N. B. Vilas, A. Nasir, Z. D. Lasner, and J. M. Doyle, Phys. Rev. Lett. **127**, 263002 (2021).

[128] R. Fulton, A. I. Bishop, M. N. Shneider, and P. F. Barker, Nat. Phys. **2**, 465 (2006).

[129] H. L. Bethlem, A. J. A. van Roij, R. T. Jongma, and G. Meijer, Phys. Rev. Lett. **88**, 133003 (2002).

[130] H. L. Bethlem, F. M. H. Crompvoets, R. T. Jongma, S. Y. T. van de Meerakker, and G. Meijer, Phys. Rev. A **65**, 053416 (2002).

[131] J. R. Bochinski, E. R. Hudson, H. J. Lewandowski, G. Meijer, and J. Ye, Phys. Rev. Lett. **91**, 243001 (2003).

[132] M. R. Tarbutt, H. L. Bethlem, J. J. Hudson, V. L. Ryabov, V. A. Ryzhov, B. E. Sauer, G. Meijer, and E. A. Hinds, Phys. Rev. Lett. **92**, 173002 (2004).

[133] E. R. Hudson, C. Ticknor, B. C. Sawyer, C. A. Taatjes, H. J. Lewandowski, J. R. Bochinski, J. L. Bohn, and J. Ye, Phys. Rev. A **73**, 063404 (2006).

[134] S. Y. T. van de Meerakker, Y. Labazan, S. Hoekstra, J. Küpper, and G. Meijer, J. Phys. B: At., Mol. Opt. Phys. **39**, S1077 (2006).

[135] S. Jung, E. Tiemann, and C. Lisdat, Phys. Rev. A **74**, 040701 (2006).

[136] S. K. Tokunaga, J. M. Dyne, E. A. Hinds, and M. R. Tarbutt, New J. Phys. **11**, 055038 (2009).

[137] T. E. Wall, S. K. Tokunaga, E. A. Hinds, and M. R. Tarbutt, Phys. Rev. A **81**, 033414 (2010).

[138] R. Fulton, A. I. Bishop, and P. F. Barker, Phys. Rev. Lett. **93**, 243004 (2004).

[139] T. Cremers, S. Chefdeville, V. Plomp, N. Janssen, E. Sweers, and S. Y. T. van de Meerakker, Phys. Rev. A **98**, 033406 (2018).

[140] V. Plomp, Z. Gao, T. Cremers, and S. Y. T. van de Meerakker, Phys. Rev. A **99**, 033417 (2019).

[141] H. Sawaoka, A. Frenett, A. Nasir, T. Ono, B. L. Augenbraun, T. C. Steimle, and J. M. Doyle, Phys. Rev. A **107**, 022810 (2023).

[142] L. D. van Buuren, C. Sommer, M. Motsch, S. Pohle, M. Schenk, J. Bayerl, P. W. H. Pinkse, and G. Rempe, Phys. Rev. Lett. **102**, 033001 (2009).

[143] D. Patterson, J. Rasmussen, and J. M. Doyle, New J. Phys. **11**, 055018 (2009).

[144] A. C. Vutha, W. C. Campbell, Y. V. Gurevich, N. R. Hutzler, M. Parsons, D. Patterson, E. Petrik, B. Spaun, J. M. Doyle, G. Gabrielse, and D. DeMille, J. Phys. B **43**, 074007 (2010).

[145] N. R. Hutzler, M. F. Parsons, Y. V. Gurevich, P. W. Hess, E. Petrik, B. Spaun, A. C. Vutha, D. DeMille, G. Gabrielse, and J. M. Doyle, Phys. Chem. Chem. Phys. **13**, 18976 (2011).

[146] D. Egorov, W. C. Campbell, B. Friedrich, S. E. Maxwell, E. Tsikata, L. D. van Buuren, and J. M. Doyle, Eur. Phys. J. D **31**, 307 (2004).

[147] J. F. Barry, E. S. Shuman, and D. DeMille, Phys. Chem. Chem. Phys. **13**, 18936 (2011).

[148] H.-I. Lu, J. Rasmussen, M. J. Wright, D. Patterson, and J. M. Doyle, Phys. Chem. Chem. Phys. **13**, 18986 (2011).

[149] W. Bu, T. Chen, G. Lv, and B. Yan, Phys. Rev. A **95**, 032701 (2017).

[150] S. Truppe, M. Hambach, S. M. Skoff, N. E. Bulleid, J. S. Bumby, R. J. Hendricks, E. A. Hinds, B. E. Sauer, and M. R. Tarbutt, J. Mod. Opt. **65**, 648 (2018).

[151] C. D'Errico, M. Zaccanti, M. Fattori, G. Roati, M. Inguscio, G. Modugno, and A. Simoni, New J. Phys. **9**, 223 (2007).

[152] M. T. Cvitaš, P. Soldán, J. M. Hutson, P. Honvault, and J.-M. Launay, Phys. Rev. Lett. **94**, 200402 (2005).

[153] M. Lara, J. L. Bohn, D. Potter, P. Soldán, and J. M. Hutson, Phys. Rev. Lett. **97**, 183201 (2006).

[154] P. S. Żuchowski and J. M. Hutson, Phys. Rev. A **78**, 022701 (2008).

[155] A. O. G. Wallis and J. M. Hutson, Phys. Rev. Lett. **103**, 183201 (2009).

[156] M. L. González-Martínez and J. M. Hutson, Phys. Rev. Lett. **111**, 203004 (2013).

[157] J. Lim, M. D. Frye, J. M. Hutson, and M. R. Tarbutt, Phys. Rev. A **92**, 053419 (2015).

[158] H. Son, J. J. Park, W. Ketterle, and A. O. Jamison, Nature **580**, 197 (2020).

[159] B. K. Stuhl, B. C. Sawyer, D. Wang, and J. Ye, Phys. Rev. Lett. **101**, 243002 (2008).

[160] J. F. Barry, D. J. McCarron, E. B. Norrgard, M. H. Steinecker, and D. DeMille, Nature **512**, 286 (2014).

[161] E. B. Norrgard, D. J. McCarron, M. H. Steinecker, M. R. Tarbutt, and D. DeMille, Phys. Rev. Lett. **116**, 063004 (2016).

[162] D. J. McCarron, M. H. Steinecker, Y. Zhu, and D. DeMille, Phys. Rev. Lett. **121**, 013202 (2018).

[163] L. Anderegg, B. L. Augenbraun, Y. Bao, S. Burchesky, L. W. Cheuk, W. Ketterle, and J. M. Doyle, Nat. Phys. **14**, 890 (2018).

[164] H. J. Williams, L. Caldwell, N. J. Fitch, S. Truppe, J. Rodewald, E. A. Hinds, B. E. Sauer, and M. R. Tarbutt, Phys. Rev. Lett. **120**, 163201 (2018).

[165] J. Lim, J. R. Almond, M. A. Trigatzis, J. A. Devlin, N. J. Fitch, B. E. Sauer, M. R. Tarbutt, and E. A. Hinds, Phys. Rev. Lett. **120**, 123201 (2018).

[166] S. Ding, Y. Wu, I. A. Finneran, J. J. Burau, and J. Ye, Phys. Rev. X **10**, 021049 (2020).

[167] I. Kozyryev, L. Baum, K. Matsuda, B. L. Augenbraun, L. Anderegg, A. P. Sedlack, and J. M. Doyle, Phys. Rev. Lett. **118**, 173201 (2017).

[168] N. B. Vilas, C. Hallas, L. Anderegg, P. Robichaud, A. Winnicki, D. Mitra, and J. M. Doyle, Nature **606**, 70 (2022).

[169] D. Mitra, N. B. Vilas, C. Hallas, L. Anderegg, B. L. Augenbraun, L. Baum, C. Miller, S. Raval, and J. M. Doyle, Science **369**, 1366 (2020).

[170] B. K. Stuhl, M. T. Hummon, M. Yeo, G. Quéméner, J. L. Bohn, and J. Ye, Nature **492**, 396 (2012).

[171] G. Valtolina, K. Matsuda, W. G. Tobias, J.-R. Li, L. De Marco, and J. Ye, Nature **588**, 239 (2020).

[172] A. Schindewolf, R. Bause, X.-Y. Chen, M. Duda, T. Karman, I. Bloch, and X.-Y. Luo, Nature **607**, 677 (2022).

[173] I. Stevenson, A. Z. Lam, N. Bigagli, C. Warner, W. Yuan, S. Zhang, and S. Will, Phys. Rev. Lett. **130**, 113002 (2023).

[174] J. Lin, G. Chen, M. Jin, Z. Shi, F. Deng, W. Zhang, G. Quéméner, T. Shi, S. Yi, and D. Wang, arXiv preprint arXiv:2304.08312 (2023), 10.48550/arXiv.2304.08312.

[175] K.-A. B. Soderberg, N. Gemelke, and C. Chin, New J. Phys. **11**, 055022 (2009).

[176] P. F. Weck and N. Balakrishnan, Int. Rev. Phys. Chem. **25**, 283 (2006).

[177] S. Ospelkaus, K.-K. Ni, D. Wang, M. H. G. de Miranda, B. Neyenhuis, G. Quéméner, P. S. Julienne, J. L. Bohn, D. S. Jin, and J. Ye, Science **327**, 853 (2010).

[178] M.-G. Hu, Y. Liu, D. D. Grimes, Y.-W. Lin, A. H. Gheorghe, R. Vexiau, N. Bouloufa-Maafa, O. Dulieu, T. Rosenband, and K.-K. Ni, Science **366**, 1111 (2019).

[179] M. Greiner, O. Mandel, T. Esslinger, T. W. Hänsch, and I. Bloch, Nature **415**, 39 (2002).

[180] R. Jördens, N. Strohmaier, K. Günter, H. Moritz, and T. Esslinger, Nature **455**, 204 (2008).

[181] A. K. Fedorov, S. I. Matveenko, V. I. Yudson, and G. V. Shlyapnikov, Sci. Rep. **6**, 27448 (2016).

[182] M. Schmidt, L. Lassablière, G. Quéméner, and T. Langen, Phys. Rev. Res. **4**, 013235 (2022).

[183] A. V. Gorshkov, S. R. Manmana, G. Chen, J. Ye, E. Demler, M. D. Lukin, and A. M. Rey, Phys. Rev. Lett. **107**, 115301 (2011).

[184] K. R. A. Hazzard, S. R. Manmana, M. Foss-Feig, and A. M. Rey, Phys. Rev. Lett. **110**, 075301 (2013).

[185] M. Borkowski, A. A. Buchachenko, R. Ciuryło, P. S. Julienne, H. Yamada, Y. Kikuchi, Y. Takasu, and Y. Takahashi, Sci. Rep. **9**, 14807 (2019).

[186] K. Van Tilburg, N. Leefer, L. Bougas, and D. Budker, Phys. Rev. Lett. **115**, 011802 (2015).

[187] C. Chin, V. V. Flambaum, and M. G. Kozlov, New J. Phys. **11**, 055048 (2009).

[188] T. Zelevinsky, S. Kotochigova, and J. Ye, Phys. Rev. Lett. **100**, 043201 (2008).

[189] D. DeMille, S. Sainis, J. Sage, T. Bergeman, S. Kotochigova, and E. Tiesinga, Phys. Rev. Lett. **100**, 043202 (2008).

[190] J. Kobayashi, A. Ogino, and S. Inouye, Nat. Commun. **10**, 3771 (2019).

[191] M. Verma, A. M. Jayich, and A. C. Vutha, Phys. Rev. Lett. **125**, 153201 (2020).

[192] N. J. Fitch, J. Lim, E. A. Hinds, B. E. Sauer, and M. R. Tarbutt, Quantum Sci. Technol. **6**, 014006 (2020).

[193] D. DeMille, S. B. Cahn, D. Murphree, D. A. Rahmlow, and M. G. Kozlov, Phys. Rev. Lett. **100**, 023003 (2008).

[194] J. Kłos, H. Li, E. Tiesinga, and S. Kotochigova, New J. Phys. **24**, 025005 (2022).

[195] M. A. Baranov, M. Dalmonte, G. Pupillo, and P. Zoller, Chem. Rev. **112**, 5012 (2012).

[196] L. Chomaz, I. Ferrier-Barbut, F. Ferlaino, B. Laburthe-Tolra, B. L. Lev, and T. Pfau, Rep. Prog. Phys. **86**, 026401 (2022).

[197] T. Lahaye, T. Koch, B. Fröhlich, M. Fattori, J. Metz, A. Griesmaier, S. Giovanazzi, and T. Pfau, Nature **448**, 672 (2007).

[198] T. Lahaye, J. Metz, B. Fröhlich, T. Koch, M. Meister, A. Griesmaier, T. Pfau, H. Saito, Y. Kawaguchi, and M. Ueda, Phys. Rev. Lett. **101**, 080401 (2008).

[199] T. Koch, T. Lahaye, J. Metz, B. Fröhlich, A. Griesmaier, and T. Pfau, Nat. Phys. **4**, 218 (2008).

[200] A. Frisch, M. Mark, K. Aikawa, F. Ferlaino, J. L. Bohn, C. Makrides, A. Petrov, and S. Kotochigova, Nature **507**, 475 (2014).

[201] T. Maier, H. Kadau, M. Schmitt, M. Wenzel, I. Ferrier-Barbut, T. Pfau, A. Frisch, S. Baier, K. Aikawa, L. Chomaz, M. J. Mark, F. Ferlaino, C. Makrides, E. Tiesinga, A. Petrov, and S. Kotochigova, Phys. Rev. X **5**, 041029 (2015).

[202] K. Aikawa, S. Baier, A. Frisch, M. Mark, C. Ravensbergen, and F. Ferlaino, Science **345**, 1484 (2014).

[203] M. Schmitt, M. Wenzel, F. Böttcher, I. Ferrier-Barbut, and T. Pfau, **539**, 259 (2016).

[204] H. Kadau, M. Schmitt, M. Wenzel, C. Wink, T. Maier, I. Ferrier-Barbut, and T. Pfau, Nature **530**, 194 (2016).

[205] S. Baier, M. Mark, D. Petter, K. Aikawa, L. Chomaz, Z. Cai, M. Baranov, P. Zoller, and F. Ferlaino, Science **352**, 201 (2016).

[206] L. Tanzi, E. Lucioni, F. Famà, J. Catani, A. Fioretti, C. Gabbanini, R. N. Bisset, L. Santos, and G. Modugno, Phys. Rev. Lett. **122**, 130405 (2019).

[207] F. Böttcher, J.-N. Schmidt, M. Wenzel, J. Hertkorn, M. Guo, T. Langen, and T. Pfau, Phys. Rev. X **9**, 011051 (2019).

[208] L. Chomaz, D. Petter, P. Ilzhöfer, G. Natale, A. Trautmann, C. Politi, G. Durastante, R. M. W. van Bijnen, A. Patscheider, M. Sohmen, M. J. Mark, and F. Ferlaino, Phys. Rev. X **9**, 021012 (2019).

[209] A. Petrov, E. Tiesinga, and S. Kotochigova, Phys. Rev. Lett. **109**, 103002 (2012).

[210] J. Miao, J. Hostetter, G. Stratis, and M. Saffman, Phys. Rev. A **89**, 041401 (2014).

[211] D. Sukachev, A. Sokolov, K. Chebakov, A. Akimov, S. Kanorsky, N. Kolachevsky, and V. Sorokin, Phys. Rev. A **82**, 011405 (2010).

[212] T. Lahaye, C. Menotti, L. Santos, M. Lewenstein, and T. Pfau, Rep. Prog. Phys. **72**, 126401 (2009).

[213] K. B. Gubbels, J. E. Baarsma, and H. T. C. Stoof, Phys. Rev. Lett. **103**, 195301 (2009).

[214] K. Gubbels and H. Stoof, Phys. Rep. **525**, 255 (2013).

[215] J. Levinsen, T. G. Tiecke, J. T. M. Walraven, and D. S. Petrov, Phys. Rev. Lett. **103**, 153202 (2009).

[216] M. Jag, M. Zaccanti, M. Cetina, R. S. Lous, F. Schreck, R. Grimm, D. S. Petrov, and J. Levinsen, Phys. Rev. Lett. **112**, 075302 (2014).

[217] C. J. M. Mathy, M. M. Parish, and D. A. Huse, Phys. Rev. Lett. **106**, 166404 (2011).

[218] O. I. Kartavtsev and A. V. Malykh, J. Phys. B: At. Mol. Opt. Phys. **40**, 1429 (2007).

[219] B. Bazak and D. S. Petrov, Phys. Rev. Lett. **118**, 083002 (2017).

[220] M. L. Wall, K. R. A. Hazzard, and A. M. Rey, in *From Atomic to Mesoscale* (World Scientific, 2015) pp. 3–37.

[221] Z. Pavlović, H. R. Sadeghpour, R. Côté, and B. O. Roos, Phys. Rev. A **81**, 052706 (2010).

[222] M. Tomza, Phys. Rev. A **88**, 012519 (2013).

[223] M. Tomza, Phys. Rev. A **90**, 022514 (2014).

[224] M. Tomza, Phys. Rev. A **92**, 062701 (2015).

[225] M. L. González-Martínez and P. S. Żuchowski, Phys. Rev. A **92**, 022708 (2015).

[226] M. B. Kosicki, M. Borkowski, and P. S. Żuchowski, New J. Phys. **22**, 023024 (2020).

[227] M. D. Frye, S. L. Cornish, and J. M. Hutson, Phys. Rev. X **10**, 041005 (2020).

[228] A. A. Buchachenko, G. Chalasinski, and M. M. Szczesniak, J. Chem. Phys. **131**, 241102 (2009).

[229] H. Li, G. Quéméner, J.-F. m. c. Wyart, O. Dulieu, and M. Lepers, Phys. Rev. A **100**, 042711 (2019).

[230] E. Tiesinga, J. Kłos, M. Li, A. Petrov, and S. Kotochigova, New J. Phys. **23**, 085007 (2021).

[231] M. Born and K. Huang, *Dynamical Theory of Crystal Lattices* (Clarendon Press, 1955).

[232] M. P. Bircher, E. Liberatore, N. J. Browning, S. Brickel, C. Hofmann, A. Patoz, O. T. Unke, T. Zimmermann, M. Chergui, P. Hamm, U. Keller, M. Meuwly, H.-J. Woerner, J. Vaníček, and U. Rothlisberger, Struct. Dyn. **4** (2018), 10.1063/1.4996816.

[233] B. Gadway and B. Yan, J. Phys. B: At. Mol. Opt. Phys. **49**, 152002 (2016).

[234] J. T. Muckerman, Chem. Phys. Lett. **173**, 200 (1990).

[235] O. Dulieu and P. S. Julienne, J. Chem. Phys. **103**, 60 (1995).

[236] E. Tiesinga, C. J. Williams, and P. S. Julienne, Phys. Rev. A **57**, 4257 (1998).

[237] J. A. R. Shea, E. Gwin, and E. Neuscamman, J. Chem. Theory Comput. **16**, 1526 (2020).

[238] R. Shepard, Adv. Chem. Phys. **69**, 63 (1987).

[239] F. Plasser and H. Lischka, Quantum Chemistry and Dynamics of Excited States **9**, 277 (2020).

[240] J. C. Slater, Phys. Rev. **36**, 57 (1930).

[241] S. F. Boys and A. C. Egerton, Proc. R. Soc. A: Math. Phys. Eng. Sci. **200**, 542 (1950).

[242] J. Dunning, Thom H., J. Phys. Chem. **90**, 1007 (1989).

[243] J. Almlof, T. Helgaker, and P. R. Taylor, J. Phys. Chem. **92**, 3029 (1988).

[244] S. Boys and F. Bernardi, Mol. Phys. **19**, 553 (1970).

[245] R. E. Moss, *Advanced Molecular Quantum Mechanics* (Springer Dordrecht, 1973).

[246] P. Pyykkö, Adv. Quantum Chem., **11**, 353 (1978).

[247] M. Douglas and N. M. Kroll, Ann. Phys. **82**, 89 (1974).

[248] T. Nakajima and K. Hirao, Chem. Rev. **112**, 385 (2012).

[249] B. A. Hess, Phys. Rev. A **33**, 3742 (1986).

[250] G. Jansen and B. A. Hess, Phys. Rev. A **39**, 6016 (1989).

[251] P. J. Hay and W. R. Wadt, J. Chem. Phys. **82**, 270 (1985).

[252] C. J. Joachain, *Quantum collision theory* (North-Holland Physics Publishing, 1983).

[253] L. M. C. Janssen, P. S. Żuchowski, A. van der Avoird, G. C. Groenenboom, and J. M. Hutson, Phys. Rev. A **83**, 022713 (2011).

[254] L. M. C. Janssen, A. van der Avoird, and G. C. Groenenboom, Phys. Rev. Lett. **110**, 063201 (2013).

[255] B. R. Johnson, J. Chem. Phys. **69**, 4678 (2008).

[256] T. Mukaiyama, J. R. Abo-Shaeer, K. Xu, J. K. Chin, and W. Ketterle, Phys. Rev. Lett. **92**, 180402 (2004).

[257] A. J. Moerdijk, B. J. Verhaar, and A. Axelsson, Phys. Rev. A **51**, 4852 (1995).

[258] M. Lepers and O. Dulieu, Phys. Chem. Chem. Phys. **13**, 19106 (2011).

[259] H. Hachisu, K. Miyagishi, S. G. Porsev, A. Derevianko, V. D. Ovsiannikov, V. G. Pal'chikov, M. Takamoto, and H. Katori, Phys. Rev. Lett. **100**, 053001 (2008).

[260] V. A. Dzuba and A. Derevianko, J. Phys. B **52**, 215005 (2019).